Titre: Title:	Modeling of the Thermo-mechanical behavior of Additively Manufactured Thermoplastic Composites by means of full-field Numerical Homogenization
Auteur: Author:	Facundo Sosa-Rey
Date:	2023
Type:	Mémoire ou thèse / Dissertation or Thesis
Référence: Citation:	Sosa-Rey, F. (2023). Modeling of the Thermo-mechanical behavior of Additively Manufactured Thermoplastic Composites by means of full-field Numerical Homogenization [Thèse de doctorat, Polytechnique Montréal]. PolyPublie. https://publications.polymtl.ca/53361/

URL de PolyPublie: PolyPublie URL:	https://publications.polymtl.ca/53361/
Directeurs de recherche: Advisors:	Martin Lévesque, & Daniel Therriault
Programme: Program:	Génie mécanique

POLYTECHNIQUE MONTRÉAL
affiliée à l'Université de Montréal

Modeling of the thermo-mechanical behavior of additively manufactured thermoplastic composites by means of full-field numerical homogenization

FACUNDO SOSA-REY
Département de génie mécanique

Thèse présentée en vue de l'obtention du diplôme de *Philosophiæ Doctor*
Génie mécanique

Avril 2023

POLYTECHNIQUE MONTRÉAL
affiliée à l'Université de Montréal

Cette thèse intitulée :

Modeling of the thermo-mechanical behavior of additively manufactured thermoplastic composites by means of full-field numerical homogenization

présentée par **Facundo SOSA-REY**
en vue de l'obtention du diplôme de *Philosophiæ Doctor*
a été dûment acceptée par le jury d'examen constitué de :

Alain BATAILLY, président
Martin LÉVESQUE, membre et directeur de recherche
Daniel THERRIAULT, membre et codirecteur de recherche
Michel BORNERT, membre
David JACK, membre externe

DEDICATION

A mis padres, de haber sacrificado tanto por nosotros.

"The world breaks everyone and afterward many are strong at the broken places."
-Ernest Hemingway, A Farewell to Arms

ACKNOWLEDGEMENTS

Tout d'abord, merci aux Prof. Martin Lévesque et Daniel Therriault de m'avoir donné l'opportunité de faire un projet de recherche aussi ambitieux et fascinant, et d'avoir toujours été là pour me soutenir et me pousser plus loin.

Merci à la Phamille, qui avez rendu cette expérience unique et personnelle. Merci à Alessandra, Juliette, J-F, Dogan, Yahya, Anamaria, Gabriel, David, aux deux Oliviers, Rui, Shibo, Florianne, Jean, Paul, Thibault, Mohammadreza, Josué, et Ferran pour toutes les bonnes discussions, beaux moments et nombreux délires.

Merci à Lingyu pour avoir pris le temps de me former aux protocoles de mesure avec la chambre thermale, et pour sa disponibilité à répondre à mes questions. Merci à Kambiz et Yanik pour leur soutien dans les aspects techniques et à Rouhollah pour assurer le fonctionnement quotidien du laboratoire. Merci à Marie-Hélène pour toute son aide pour l'utilisation du µCT et sa patience à régler les problèmes avec l'équipement. Merci à Clément, qui a été un très bon collaborateur.

Merci au CRSNG, FRQNT, et au programme GPS d'avoir fourni un soutien financier considérable, qui à rendu ce projet possible. Merci à Safran et à Sébastien Pautard pour leur rôle dans la chaire FACMO, et l'accompagnement au travers de ce projet.

Merci à tous mes professeurs tout au long de mon parcours scolaire, qui ont été patients avec toutes mes questions parfois tirées par les cheveux.

Merci à Antoine, Charles-Olivier, Sophie, Alexandra, Jean-Romain, Nicolas, Anna, Blandine, Philippe, Jonathan, Yassine, Anais, et bien d'autres, d'être de chers amis, sans quoi la vie n'aurait pas de saveur.

Thank you to Lex Fridman, Jordan Peterson, Eric Weinstein, and Sam Harris, for being sources of great inspiration, and for giving me the courage and humility to keep fighting the good fight. Listening to you all for countless hours makes me feel we are dear friends.

Merci à Pauline mon amoureuse, le soleil de ma vie, sans qui je ne crois pas que j'aurais persévéré. Merci à Dominique et Isabelle, ainsi qu'à Romain et Agathe, pour tous les encouragements et les beaux moments passés ensemble.

Merci à mes parents Hector et Olga, et à Lorenzo, Luisina et Florencia, sur qui je peux toujours compter.

RÉSUMÉ

Grace à la fabrication additive, des pièces d'une géométrie complexe ayant des caractéristiques internes sont possibles sans avoir recours à des moules. Différents prototypes peuvent donc être rapidement réalisés et testés, et pour des séries limitées, l'absence d'outillage rend cette méthode économiquement avantageuse. Dans une méthode telle que la Fabrication par Filament Fondu (FFF), l'utilisation de polymères thermoplastiques et de renfort sous forme de fibres permet d'améliorer les performances mécaniques des pièces produites. Par contre, elles demeurent en deçà de celles de leurs homologues fabriqués par injection. En outre, le processus d'impression confère un ensemble unique de caractéristiques morphologiques qui rendent les propriétés du matériau difficiles à prédire. Le fait de ne disposer que de données limitées et de nature empiriques sur le comportement mécanique des polymères renforcés de fibres courtes et sur leur relation procédé-structure-propriété constitue un problème pour la modélisation des pièces fabriquées par FFF. Si les concepteurs ne peuvent pas prédire les propriétés élastiques et viscoélastiques, et comment celles-ci sont affectées par les changements de température, ils sont obligés d'utiliser des estimés conservateurs comme substitut, et ils pourront dont pas tenir compte de manière fiable de l'anisotropie de la réponse mécanique. Ces difficultés en termes de modélisation constituent une limite à l'adoption de cette technique en industrie. Dans cette thèse, le lien entre le processus et la structure est étudié en prenant des images micro-tomographiques 3D (µCT) de spécimens réels, et en traitant ces données avec un logiciel spécialement conçu pour extraire les constituants individuels (fibres, matrice, vides). À partir de ces données, des modèles d'homogénéisation sont adaptés et mis en œuvre pour permettre la prédiction des propriétés élastiques et viscoélastiques effectives et leur anisotropie. Ces prédictions sont ensuite comparées à des mesures expérimentales prises sur des spécimens fabriqués par FFF.

La méthode d'homogénéisation présentée permet de prédire le module de traction en fonction du diamètre de la buse et du motif d'impression avec une précision de 5% par rapport aux valeurs expérimentales. Il s'agit d'une amélioration significative par rapport aux principales méthodes dans le domaine, qui utilisent principalement des microstructures générées artificiellement. Les propriétés thermo-viscoélastiques anisotropes complètes sont également modélisées via une procédure d'homogénéisation à double échelle qui utilise des relations constitutives pour le polymère pur telles qu'obtenues à partir de données expérimentales. Cette méthode permet de prédire la souplesse en fluage avec une erreur relative moyenne de 3% dans la direction longitudinale par rapport aux mesures expérimentales, à la fois à 21 et 120 °C. En outre, plusieurs caractéristiques morphologiques qui n'avaient jamais été

rapportées auparavant sont présentées, ce qui permet de mieux comprendre pourquoi ces matériaux ont une réponse mécanique aussi unique et variable. La méthodologie présentée peut être étendue à d'autres combinaisons polymère et fibres, et peut être utilisée pour la prédiction d'autres propriétés physiques, telles que la résistance, la ténacité à la rupture, et d'autres phénomènes comme la conductivité thermique ou électrique, et la piézoélectricité.

ABSTRACT

Additive manufacturing offers many possibilities in terms of the part geometry and the internal features that are achievable without using molds. Design iterations can therefore be quickly realized and tested, and for small part counts the absence of tooling makes it economically advantageous. In a method such as Fused Filament Fabrication (FFF), the combination of thermoplastic polymers and fiber reinforcements improves the mechanical performance of the parts produced, but they remain inferior to those seen in their injected counterparts. Furthermore, the printing process imparts a unique set of morphological features that makes the material properties difficult to predict. Having only limited empirical data on the mechanical behavior of short fiber reinforced polymers and their process-structure-property relationship is a problem for modelling of parts fabricated through FFF. If designers cannot predict the elastic and viscoelastic properties, and how those vary with temperature, they are forced to use conservative estimates as a substitute, and they will not be able to reliably account for the anisotropy in the response, limiting the adoption of this technique. In this thesis, the link between process and structure is investigated by taking 3D micro-tomographic (µCT) imaging of real specimens, and processing those data with a specially-built software that extracts individual constituents (fibers, matrix, voids). Using that data, homogenization models are adapted and implemented to enable the prediction of effective elastic and viscoelastic properties, and the anisotropy therein, which is then compared to experimental measurements of 3D printed materials.

The homogenization method presented is demonstrated to enable prediction of tensile modulus as a function of nozzle diameter and printing pattern with an accuracy within 5% compared to experimental values. This is a significant improvement compared to leading methods in the field, which make use of artificially generated microstructure descriptions. The full anisotropic thermo-viscoelastic properties are also modelled via a dual-scale homogenization procedure which uses constitutive relations for the pure polymer as fitted from experimental data, and allows the prediction of creep compliance with a 3% mean relative error in the longitudinal direction compared to experimental measurements, both at 21 and 120°C. In addition, several morphological features that had never been reported before are presented, which provide valuable insight as to why these materials have such unique and variable mechanical response. The methodology presented can be extended to other polymer/fiber combinations, and as a basis for predictive models of other physical properties, such as tensile strength, fracture toughness, and other phenomena like thermal or electrical conductivity, and piezoelectricity.

TABLE OF CONTENTS

LIST OF TABLES

LIST OF FIGURES

LIST OF SYMBOLS AND ACRONYMS

ASTM	American Society for Testing and Materials
CF	Carbon Fiber
CPU	Central Processing Unit
DOI	Digital Object Identifier
FACMO	Fabrication Additive des Composites à Matrice Organique
FE	Finite Element
FFF	Fused Filament Fabrication
FFT	Fast Fourier Transform
FoV	Field of View
FRP	Fiber Reinforced Polymer
GMM	Generalized Maxwell Model
KUBC	Kinematic uniform boundary condition
LM	Levenberg-Marquardt
MADS	Mesh Adaptive Direct Search
NOMAD	Nonlinear Optimization by Mesh Adaptive Direct search
PBC	Periodic boundary conditions
PEEK	Poly-ether ether ketone
PEI	Poly-ether imide
PLA	Poly-Lactic Acid
RoI	Region of Interest
RVE	Representative Volume Element
SCF	Short Carbon Fibers
SEM	Scanning Electron Microscopy
SFRP	Short Fiber Reinforced Polymer
SUBC	Static uniform boundary conditions
UMAT	User-defined MATerial behavior
µCT	Micro-Computed Tomography

LIST OF APPENDICES

CHAPTER 1 INTRODUCTION

Using fiber reinforced polymer composite is a well-established method for reducing the weight of structural components in fields such as the aerospace or automotive industry. Manufacturing those elements from thermoset polymers and weaved continuous carbon fibers offer weight-specific stiffness and strength considerably higher than metals. However, the molding process is subject to many constraints, which limit the complexity of the shapes that are achievable industrially. In addition, the nature of thermoset polymers is such that it allows little repairability and poor end-of-life reuse or recycling potential.

On the other hand, thermoplastic polymers can be remelted, and when used in conjunction with short carbon fibers, achieve significantly improved weight-specific properties, when compared to those of the bulk matrices (though they remain below those of continuous carbon fiber thermoset composites). Those properties make them choice candidates for techniques like Fused Filament Fabrication (FFF), an additive manufacturing method in which parts are constructed layer by layer, by melting the base material and depositing it under computer control. FFF allows a very high design freedom in terms of part geometry and the infill pattern can be controlled and optimized to achieve tailored mechanical, thermal or electrical properties. Complex parts are fabricated in a single step, with little material waste, and minimal post-processing is required.

However, the microscopic morphology of short fiber reinforced polymers (SFRPs) made by FFF is dissimilar to that encountered in injection molding, a common manufacturing technique for this material class. At present, knowledge of the process-structure-property relationship in SFRP made by FFF is limited, and therefore the properties achieved by a set of processing conditions and material combinations are difficult to predict. For instance, the effect of process parameters on the length and orientation of fibers and on pore morphology is not understood, and those are determining factors for the mechanical behavior of SFRPs. Consequently, the ability to predict the elastic and viscoelastic properties of SFRPs is very limited, which makes the mechanical design process largely empirical, which is costly and inefficient. To enable the adoption of this technology for industrial applications, the ability to model and predict those properties for SFRPs and how they are affected by temperature is an area of active research and development.

This doctoral project is part of the FACMO research chair (Fabrication Additive des Composites à Matrice Organique), a research and development partnership between Safran S.A., an aerospace equipment manufacturer from France and the Laboratory for Multi-scale Me-

chanics ($\texttt{LM}^2$) at Polytechnique Montreal. The goal of this multidisciplinary research project is the development of new materials and the advancement of the theoretical and practical knowledge of the use of additively manufactured SFRPs for structural and acoustic applications. Other members of the FACMO chair have developed the processing and manufacturing expertise to create functional parts with this material. In this thesis, the prediction of mechanical properties of additively manufactured high performance SFRPs as a function of processing parameters is addressed. Two main aspects are discussed. First, the development of a specialized microstructure analysis tool that enables the automated processing of imaging data taken from actual specimens is presented. Then, the implementation of numerical modelling techniques to predict the elastic and thermo-viscoelastic properties using those processed data is detailed. Furthermore, the predictions made by these methods are both informed by and validated against experimental tensile testing data.

This thesis is structured in the following way. Chapter 2 presents a literature review on the current work on morphological characterization of SFRPs, and the numerical modelling efforts for elastic and viscoelastic property prediction. Chapter 3 presents a rationale for the project, and the specific objectives to be met. Chapter 4 presents the scientific approach, including the outline of the research papers prepared during this project. Chapter 5 presents the development, validation and testing of OpenFiberSeg, a specialized microstructural characterization tool for SFRPs. Chapter 6 presents a multiscale mechanical modelling methodology, which is used to predict the tensile behavior in five printing configurations and is validated against experimental data. Chapter 7 extends the multiscale method to enable the identification of an anisotropic thermo-viscoelastic behavior law for SFRPs. Chapter 8 presents complimentary work on the determination of the representative volume element from imaging data instead of artificially generated geometries. Chapter 9 presents a general discussion on the overall methodology and the insights gained from the morphological and experimental characterization. The conclusion in Chapter 10 includes the limitations of the present study, and the relevant future avenues of investigation in the modelling of SFRPs made by FFF for industrial applications.

CHAPTER 2 LITERATURE REVIEW

Notation Unless otherwise specified, scalars are represented by lowercase letters (a, b, α, β), vectors by lowercase latin bold letters $(\mathbf{a,b})$, 2^{nd}-order tensors by lowercase bold greek letters: $(\boldsymbol{\varepsilon}, \boldsymbol{\sigma})$, 4^{th}-order tensors by uppercase bold Latin letters: $(\mathbf{C}, \mathbf{S})$. Einstein summation convention is adopted, which reads for the singly contracted product:

$$\mathbf{a} \cdot \mathbf{b} = a_i b_i = \sum_i a_i b_i = \ c \text{ (a scalar)} \tag{2.1}$$

$$\boldsymbol{\alpha} \cdot \boldsymbol{\beta} = \alpha_{ij}\beta_{jk} = \sum_j \alpha_{ij}\beta_{jk} = \ \delta_{ik} = \boldsymbol{\delta} \text{ (a } 2^{nd}\text{-order tensor)} \tag{2.2}$$

2.1 Fused Filament Fabrication

Initially patented by Stratasys under the trademark Fused Deposition Modelling (FDM), Fused Filament Fabrication is an additive manufacturing process in which spools of polymer filaments are deposited by extruding them though a heated nozzle, with computer-driven positioning [4, 10–12]. A common FFF printed configuration is presented in Figure 2.1, where the printhead containing the nozzle has 3 degrees of freedom relatively to the printing surface, or bed. The printhead moves in the x (left-right) and y (forward-backward) direction, and the print bed moves vertically in the z direction. The extrusion of material is performed in a sequence of continuous beads that can have a variety of trajectories, generally in the plane of the bed (non-planar applications also exist). By creating subsequent layers of printed material, many geometries are possible to create, in a more cost-effective manner for small part count than with injection or compression molding for instance.

However, the process-structure-property relationship found in parts made by FFF is much less understood than for those made by molding [11, 13, 14], and the achieved mechanical properties are inferior those seen in injected parts using the same base materials [5, 15]. Those limitation can be mitigated in two ways: by using high performance polymers with superior tensile and strength properties, and by the addition of short fiber reinforcements, as shown in Figure 2.1, which can improve those properties significantly [4, 5, 11, 16]. For instance, neat (pure) poly-ether ether ketone (PEEK) resin has a tensile modulus of 4.1 GPa and a tensile strength of 105 MPa (resin type Victrex 90G [17]). When reinforced with 30 wt.% Zoltek™ PX35 chopped carbon fibers, the tensile modulus and strength of printed specimens were reported at 17.9 GPa and 129 MPa, respectively [18].

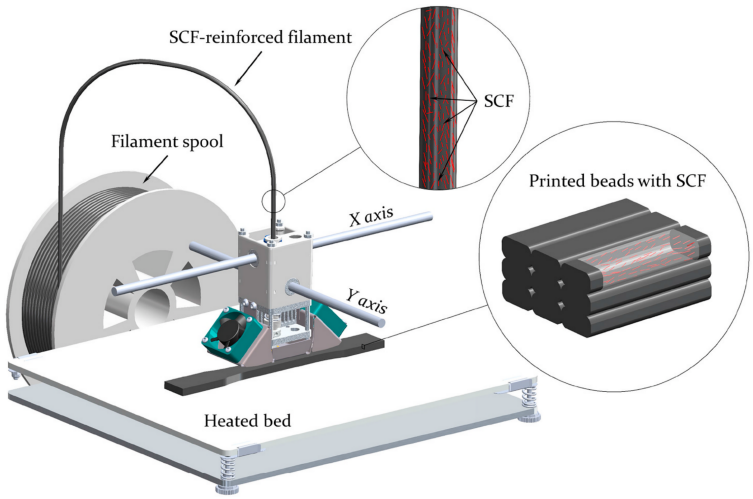

Figure 2.1 Fused Filament Fabrication using short carbon fiber (SCF) reinforced polymer filament. Adapted from [4].

2.2 Elasticity theory

Materials are said to be linearly elastic when there exists a linear relation between individual components of stress ($\boldsymbol{\sigma}$) and strain ($\boldsymbol{\varepsilon}$), or, as is formalized by Hooke's law as: $\boldsymbol{\sigma} = \mathbf{C} : \boldsymbol{\varepsilon}$, where $\mathbf{C}$ is the stiffness tensor for the material. Depending on their internal configurations, all materials fall into a symmetry group. The material symmetries that are relevant to SFRPs are as follows. An isotropic material has the same response regardless of loading direction, and 2 independent constants are required to build its stiffness tensor $\mathbf{C}$. Other materials have a particular axis that, when rotated along it, preserve the same response, but have a different one when loaded in another direction. Those materials are called transversely isotropic and require 5 independent components to fully construct their $\mathbf{C}$ tensor.

2.2.1 Linear viscoelasticity

Materials for which the strain response is time-dependent are called viscoelastic. In polymeric materials, the dominant viscoelastic mechanism is the elongation of the molecular chains [19]. In *linear* viscoelasticity, this process is reversible, with chains gradually returning to their equilibrium state after the loading is removed, and the creep strain being proportional to the applied stress. In general, linearity only holds up to a certain loading level, at which point the proportionality is lost, and phenomena such as visco-hyperelasticity [20] and viscoplasticity [21] (permanent strain) can arise. Aging is the process by which the viscoelastic behavior changes over time, which is accelerated by adverse conditions such as high temperature or

corrosive environment [22]. Aging effects are not considered in this thesis.

The most common expression of the linearly viscoelastic stiffness, that is well-suited to modelling real materials is the Generalized Maxwell Model (GMM) [23–29], where the time-dependence of a material parameter is expressed as a Prony series, i.e.:

$$\mathbf{C}(t) = \mathbf{C}^{(\infty)} + \sum_{i=1}^{N} \mathbf{C}^{(i)} \left(e^{-\omega_i(t)} \right) \tag{2.3}$$

where $\mathbf{C}^{(i)}$ are the stiffness tensors and ω_i their corresponding relaxation times. The instantaneous (or elastic) stiffness is therefore found at $t = 0$, which yields $\mathbf{C}_{elastic} = \mathbf{C}^{(\infty)} + \sum_{i=1}^{N} \mathbf{C}^{(i)}$. The Boltzmann principle, in which "the effect of the compound cause is the sum of the effects of the individual causes" [30, 31], allows is to express the time-dependent relation between components of stress and strain tensors, in a linear, non-ageing viscoelastic material as:

$$\boldsymbol{\sigma}(t) = \mathbf{C}^{(\infty)} : \boldsymbol{\varepsilon}(t) + \int_0^t \sum_{i=1}^{N} \mathbf{C}^{(i)} \left(e^{-\omega_i(t-\tau)} \right) : \frac{\mathrm{d}\boldsymbol{\varepsilon}(\tau)}{\mathrm{d}\tau} \mathrm{d}\tau. \tag{2.4}$$

Here, the time-dependent stiffness $\mathbf{C}(t)$ is composed of $\mathbf{C}^{(\infty)}$, the stiffness at $t \to \infty$, and a sequence of i pairs of relaxations times ω_i and stiffness tensors $\mathbf{C}^{(i)}$. Equation 2.4 is referred to as the integral form of viscoelasticity, the hereditary integral, or the Stieltjes convolution [23, 24, 26, 27, 32].

Time-temperature superposition principle When polymers are exposed to high temperatures, their viscoelastic properties are altered [33]. For so-called thermo-rheologically simple materials, the temperature dependence is expressed via the concept of internal time [34–36], in which real time t is adjusted by a shift factor a_T, which is function of temperature T, such that:

$$\mathbf{C}(t, T) = \mathbf{C} \left(\frac{t}{a_T(T)} \right). \tag{2.5}$$

In polymers, this temperature-dependence has an abrupt transition at the so-called glass transition temperature T_g, at which the material evolves from a glassy state at low temperatures, where it is rigid and brittle, to a rubbery state where it is compliant and plastic. Above the T_g of a polymer, the shift factor can be obtained empirically with the Williams-Landel-Ferry

model [19, 29], for which $\log(\alpha(T))$ is:

$$\log\Big(\alpha(T)\Big) = -\frac{C_1(T - T_g)}{C_2 + (T - T_g)}, \tag{2.6}$$

where C_1 and C_2 are material-specific positive constants. In this research project, only temperatures below T_g are considered, for which the shift factor can be obtained using the Arrhenius law, as per:

$$\log\Big(\alpha(T)\Big) = -\frac{E_a}{2.303R}\left(\frac{1}{T} - \frac{1}{T_0}\right), \tag{2.7}$$

where E_a is the activation energy of the polymer relaxation and R is the ideal gas constant [35, 37].

It is also possible to have a shift factor $\alpha(T)$ which is directionnally dependent [36, 38], i.e. $\alpha_{ijkl}(T)$ or dependent on other application-specific parameters, such as the humidity level or the degree of cure of the (thermoset) polymer [37, 38].

2.3 Material properties

To achieve the highest possible mechanical properties in SFRPs made by FFF, the choice of base materials is decisive. As presented in Figure 2.2, there is a very broad range of achievable mechanical properties of thermoplastic polymers. Among the thermoplastics suitable for FFF, so-called high-performance thermoplastics are of particular research interest. High-performance polymers exhibit high mechanical properties such as stiffness, strength, fracture toughness, etc, and that retain much of those properties under harsh service conditions, such as high temperatures, chemical/physical attacks such as solvents and UV exposure, or high humidity [10, 39, 40]. Those desirable characteristics, notably stability at high temperature, also hinder their processability by FFF, as higher temperatures are required to melt the base material, and larger heat gradients cause warpage during printing [11, 16]. As the material is deposited on previously solidified polymer, the welding at the interlayer region is partial [11, 40]. The thermal retraction during solidification (and the crystallization-induced stress in the case of semi-crystalline polymers) can cause material separation, which manifests as interlayer porosity [15, 41–43].

The other strategy to achieve high mechanical performance is the use of fiber reinforcements, whose stiffness and strength are orders of magnitude higher than those of polymers. Common reinforcement materials are carbon fibers [10, 18], glass fibers [44, 45], natural fibers [46], ceramic [47] and metallic [48] inclusions, which are mixed with the polymer prior to filament spool fabrication. Polyacrylonitrile (PAN)-based carbon fibers (CFs) can be continuous,

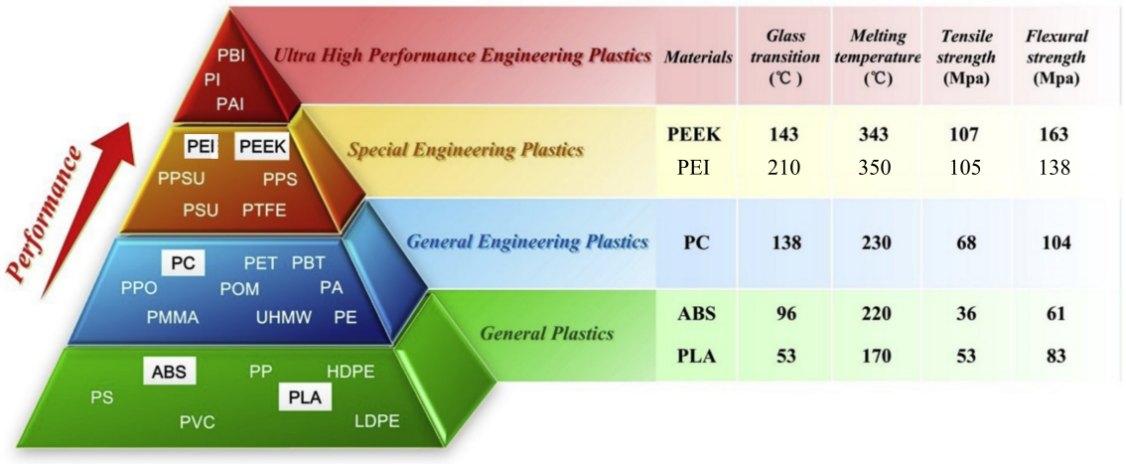

Materials	Glass transition (℃)	Melting temperature (℃)	Tensile strength (Mpa)	Flexural strength (Mpa)
PEEK	**143**	**343**	**107**	**163**
PEI	210	350	105	138
PC	**138**	**230**	**68**	**104**
ABS	**96**	**220**	**36**	**61**
PLA	**53**	**170**	**53**	**83**

Figure 2.2 Properties of several categories of thermoplastics. The mechanical and thermal properties of high-performance special engineering plastics are $2-3\times$ higher than those of common general plastics. Adapted from [5–8].

chopped or milled, and depending on their composition and type, affect the mechanical properties of the composites and their processability in different ways [10, 18]. This research project concentrates on chopped carbon fibers, which have an average length of $50-100$ µm and a diameter of $7-10$ µm. PAN-based CFs are known to be transversely isotropic, with the isotropy axis being the fiber axis, and are linearly elastic up to temperatures of 1400°C [49]. The higher thermal conductivity of CFs means the extrudate cools down faster, leading to less time for polymer chain diffusion at the interlayer, which leads to weakening of this region. The presence of CFs in molten polymers is generally accompanied with increased viscosity, which makes the extrusion more prone to clogging, and leads to increased porosity both when filaments are produced and at deposition [5, 50–52]. Porosity is deleterious to stiffness and strength of the composites and creates crack nucleation sites [42]. Consequently, the use of reinforcements is a compromise between the achieved improvements in mechanical properties and the added challenge in processability and the mitigation of other side-effects.

2.3.1 Thermoplastic polymer matrix: Poly-ether-ether ketone (PEEK)

Poly-ether-ether ketone (PEEK) is a high-performance semi-crystalline thermoplastic polymer, with both a high glass transition temperature ($T_g \approx 145$°C) and a high melting temperature ($T_m \approx 335-384$°C, depending on grade) [53–55]. Due to its high aromatic structure, PEEK presents high chemical as well as thermal resistance [56] and its tensile modulus can be increased by thermal treatments to promote crystallinity [54]. Under certain conditions, the crystallinity of PEEK can be as high as 40% [57, 58]. Furthermore, it is known to have high

adhesion to glass and carbon fibers [56]. All these attributes make it a prime candidate for use in composite materials in high performance applications, where adverse conditions such as a broad range of temperature and humidity levels, and exposure to chemicals is expected.

As for its viscoelastic properties, PEEK has been shown to follow thermo-rheologically simple behavior at temperatures of 20-200°C, with a shift factor following Arrhenius' equations below T_g and William-Landel-Ferry (WLF) equation above [58]. PEEK's creep compliance is known to be much higher in the glass region and to increases markedly above 130°C.

As can be seen in Table 2.1, the threshold at which PEEK was reported as linearly viscoelastic decreases for higher temperatures. These results were all obtained by uniaxial relaxation testing.

In Figure 2.3 from Xiao et al., the creep compliance ($1/C_{11}$) of Victrex 450G PEEK at 90°C measured by uniaxial tensile testing is presented for several loading levels. The authors report that curves for 9.2, 18.4 and 23 MPa are superposable and differ only by an initial constant. At 30 MPa however, there begins to be a divergence, at which point non-linear, stress-dependent behavior laws are required. This suggests that Victrex 450G PEEK exhibits linear viscoelasticity at 90°C up to a loading of 23 MPa.

2.3.2 Morphology of composites made by FFF

The nature of the printing process creates unique morphological attributes, which are separable into 3 distinct length scales [13, 61, 62]. At the microscale, the presence of fibers and intrabead porosity makes for a microstructure that is most likely affected by the processing parameters, although the relationship between the two is scarcely known at present. Secondly, the so-called infill pattern chosen at the design stage creates a regular arrangement of passes, which is at a scale dictated by the nozzle diameter and the specificities of the pattern selected. These meso-scale structures are at a length scale much larger than that at which the microscale constituents (individual fibers and intrabead porosity) are relevant, therefore it can be considered separately. Finally, there is the part geometry scale, which is also orders

Table 2.1 Maximal stress for which PEEK resin exhibits linear viscoelasticity

Temperature (°C)	**Stress Level (MPa)**	**Resin Type**	**Source**
23	25.0	APC-2	Katouzian [59]
90	20.0	Victrex 15G	Xiao [9]
110	16.2	Victrex 450G	Guo [60]
120	14.18	Victrex 450G	Guo [60]
130	12.15	Victrex 450G	Guo [60]

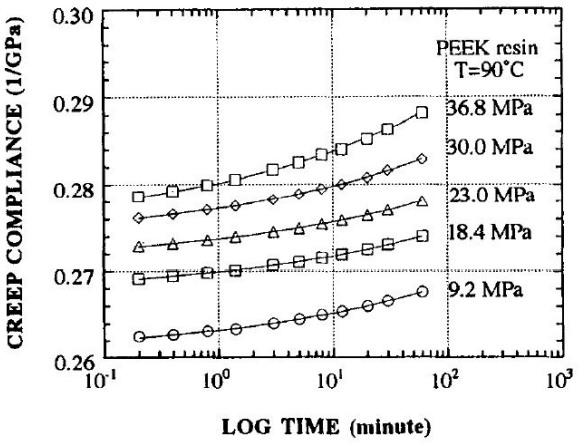

Figure 2.3 Creep compliance of PEEK resin obtained at 90°C, for different creep stress levels [9]

of magnitude larger than the infill pattern.

From a mechanical behavior standpoint, the relevant microscale features are: the distribution of fiber lengths and orientations, the variability in fiber volume fraction v_f, and the distribution of the intrabead porosity [50, 63–67]. At the mesoscale, two infill patterns are considered in this thesis: both are 100% volume occupation, one is with all printing passes aligned, or the 0°-0° pattern, and one with printing passes alternating 0° in one layer, and 90° in the following, meaning printing beads of subsequent layers are perpendicular to each other. Many other patterns exist and can be devised for particular purposes.

At the microscale, several methods exist for obtaining fiber orientation and length distribution. In Scanning Electron Microscopy (SEM) imaging of polished specimen, the cross section of the approximately cylindrical fibers are visible as ellipses. Using the orientation of the major axis of those ellipses, and the minor to major ratio, the 3D orientation relative to printing direction can be inferred [18, 63, 68]. This method is time-consuming, and generally only done on a few images, meaning variations in the volume are not captured. Some authors do repeated polishing or use confocal microscopy [69] to obtain volumetric information [68, 70]. Fiber lengths can be measured experimentally by either dissolving [18] or burning [4, 63] the polymer matrix, then measuring the length of remaining fibers individually. Those experimental methods cannot account for the correlation that exists between length and orientation of fibers [63, 71], as those properties are measured independently on different fibers.

2.4 Tomographic data: acquisition and segmentation

The microstructural features of SFRPs can be investigated directly through imaging methods such as X-ray micro-computed tomography, or µCT imaging [45, 66, 72–74]. In this method, a specimen is mounted on a rotary holder, and a sequence of X-ray projections are taken by rotating the specimen by precise, regular increments. The series of projections thus obtained are then combined mathematically to generate a volumetric description of the inside of the specimen, in which the differential absorption of different materials create image intensity variations [75–78]. In Figure 2.4, a schematic representation of the specimen, X-ray source and detector is presented. This technique enables the resolution of features as small as 0.4 μm under certain conditions. To distinguish individual CFs, which have a diameter in the 5-10 μm range, a resolution (pixel size) of $\approx$ 0.7 μm is required. However, as CFs and matrix have a similar density and elemental composition (mainly carbon), the produced data has low contrast, which makes segmentation more difficult [72, 73, 79].

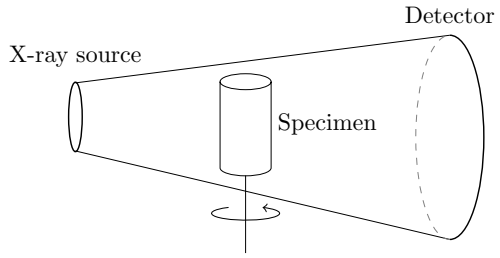

Figure 2.4 Schematic of the µCT imaging procedure. Differential absorption of different materials in the specimen serve to create a volumetric mapping of its interior.

To gain useful insight on morphological properties from µCT imaging, the tomographs produced must be analyzed with specialized tools, so that the constituents, or phases, can be identified inside the volume. The process of discrimination between phases is called segmentation. Due to the amount of data required to analyze data from multiple specimens made with different processing conditions, it is critical that the segmentation procedure be automated, accurate and reproducible.

2.4.1 Segmentation of tomographic data

There are a handful of studies that have attempted microstructure characterization based on imaging data taken on SFRPs used in FFF. It is possible to gain insight about orientation distribution of reinforcements without classification of phases, by computing the local structure tensor from the gradients between neighboring voxels in the volume of data [65, 80–84].

With this simple method, the local orientation of reinforcements can be described, and this information can be used for mechanical modelling via analytical homogenization models. But without separating individual fibers, length information is not available through this method.

Separating fibers is a much more complex task, as a pixel-wise labelling is not sufficient to reconstitute each fiber in its entirety. For that, tracking across the volume is required. In addition, when a large fiber volume fraction v_f is used, fiber contact becomes more frequent, which further complicates the separation of individual fibers. To date, only a few studies perform this level of analysis on SFRPs, such as [66, 73, 85–87].

2.5 Homogenization

Homogenization is the process by which the knowledge of the microscopic structure of a multiphase material is used to generate a fictitious homogeneous solid that approximates its measured macroscopic characteristics. This process is made possible under the condition that the heterogeneous material is statistically homogeneous, meaning that a representative volume element (RVE) can be chosen inside it, larger than typical inclusion dimensions, such that stress or stain fields have the same statistical moments (average, variance, etc.) regardless of where in the solid the RVE is chosen [88]. As a consequence, any field in the solid has the same average over the solid as over the RVE. Under those conditions, we can separate the micro- and macroscopic scales to seek a volumetric average stress $\boldsymbol{\Sigma}$ (or strain $\mathbf{E}$) over the RVE [88, 89], which serves to characterize the behavior of the entire solid. The detailed microscopic elastic equation: $\boldsymbol{\sigma}(\boldsymbol{x}) = \mathbf{C}(\boldsymbol{x}) : \boldsymbol{\varepsilon}(\boldsymbol{x})$, therefore becomes simply: $\boldsymbol{\Sigma} = \tilde{\mathbf{C}} : \mathbf{E}$, where $\tilde{\mathbf{C}}$ denotes the *homogenized* stiffness tensor. It has been shown [89] that for a composite consisting of r distinct phases, $\tilde{\mathbf{C}}$ can be expressed as:

$$\tilde{\mathbf{C}} = \mathbf{C}_1 + \sum_{2}^{r} c_r(\mathbf{C}_r - \mathbf{C}_1) : \mathbf{A}_r \tag{2.8}$$

where $\mathbf{A}$ is the so-called localization tensor, which links the microscopic strain to the average loading as per $\boldsymbol{\varepsilon}(\boldsymbol{x}) = \mathbf{A}(\boldsymbol{x}) : \mathbf{E}$. Every homogenization model provides a method for approximating $\mathbf{A}$.

There are 2 families of homogenization methods. In mean-field, or analytical methods, $\tilde{\mathbf{C}}$ is arrived at by computing $\tilde{\mathbf{C}}$ using global attributes such as the volume fraction of inclusions, their aspect ratio, and their respective stiffnesses. In general, however, their accuracy is known to decrease in certain configurations of inclusions, such as high volume fration, high aspect ratio, and/or high property contrasts between phases [90, 91], which are precisely those of the SFRPs of interest in this thesis. As shown in [91], existing models either over-

or underestimate elastic properties when the volume fraction is high (>20%) or when properties contrast between matrix and inclusions is high (>50). Furthermore, it has been shown in [71] that applying analytical homogenization to micro-tomographs of injection-molded polypropylene with short glass fiber reinforcements (volume fraction of 13%, properties contrast of ≈ 45, aspect ratio ≈ 30), leads to predictions that differ from experiment by 8%-20% in the best cases.

The other family of homogenization methods are full-field, or numerical, methods. In those methods, the geometry is described explicitly, and the stress and strain fields are solved numerically, to then arrive at an average response given a specific microstructure and material parameters. The $\tilde{\mathbf{C}}$ tensor for that configuration is derived from this average response. The success of this methods rests on the ability of arriving at a microstructure description, or representative volume element (RVE) containing sufficient information as to be an adequate stand-in for the real material, but at the same time being of minimal size, such that the computational cost of solving the constitutive laws at each node is practical. The determination of the RVE dimensions is discussed first, then the different types of resolution methods are presented.

2.5.1 Determination of the Representative Volume Element (RVE)

The representative volume element (RVE) is commonly defined as a subvolume of the true solid with the minimum number of heterogeneities as to exhibit the same macroscopic properties as would any arbitrary large subvolume [92, 93]. Various authors proposed different mathematical criteria by which to define the RVE size. For a random media, the theoretical volume element that exactly represents the solid needs an infinity of heterogeneities [94]. In practice, the RVE is defined as satisfying a user-prescribed error on a particular criterion. In a seminal work, Hill states the following twofold condition for RVE determination: first that the sample should be "typical of the whole mixture on average", second that the number of inclusions should be sufficiently large so that the average properties such as moduli are independent of the applied boundary conditions [95] This latter point was formally proved by Sab in [96]. Other authors such as Drugan and Willis [97], Gusev [92], Ostoja-Starzewski [94] proposed mathematical expressions by which the self-similarity of RVE to the infinite media is quantified. The choice of this criterion is not trivial, and a poor choice can lead to a volume smaller than required for representativity, or a volume much larger than necessary, leading to inaccurate results in the first case, and prohibitive computational cost in the second [98]. Note that for a given microstructure, the RVE size will vary depending on the property being investigated, e.g., elastic modulus or thermal conductivity, and is affected

by the property contrast between the phases present, a higher contrast generally leading to larger RVEs [99, 100]. In the case of fiber-like inclusions, a large fiber aspect ratio is also accompanied by a increase in RVE size, and for a randomly oriented microstructure, the convergence can be estimated by the degree of isotropy of the effective property.

In many cases, the response of the infinite media is not known but can only be estimated. To circumvent this problem, Kanit et al. [99] developed a quantitative method by which the RVE size is disambiguated and predicted from the convergence rates of mean properties. Since working at the true RVE for a particular material is not always feasible, a more computationally efficient method consists of taking a set of smaller subvolumes, called realizations, averaging the homogenized results together, to estimate the properties that would be evaluated at the true RVE size. He used the rate of convergence of the mean value as a function of RVE size (number of inclusions) to predict the size of the RVE. Furthermore, he demonstrated that the property obtained through averaging of several realization is statistically equivalent to one single, larger volume of a size commensurate with the sum of realizations sizes, but at reduced computational cost.

To conduct the RVE determination, boundary conditions (BCs) must be set. There are 3 common BCs for elasticity calculations.

Static uniform boundary conditions (SUBCs) (or uniform traction):
$\boldsymbol{\sigma}(\boldsymbol{x}) \cdot \mathbf{n} = \boldsymbol{\Sigma} \cdot \mathbf{n}, \quad \forall \boldsymbol{x} \in \partial V$, where ∂V is the surface of the volume element V, and $\mathbf{n}$ is the normal vector to the surface of V at $\boldsymbol{x}$.

Kinematic uniform boundary conditions (KUBCs) (or uniform displacement):
$\boldsymbol{u}(\boldsymbol{x}) = \mathbf{E} \cdot \boldsymbol{x}, \quad \forall \boldsymbol{x} \in \partial V$, where $\boldsymbol{u}(\boldsymbol{x})$ is the displacement vector, and $\mathbf{E}$ is a symmetrical second order tensor. Huet [101] has shown that in general, the effective properties of the volume elements are bounded by uniform traction (lower bound) and uniform displacement (upper bound), and the distance between these bounds generally increases with property contrast.

Periodic boundary conditions (PBCs):
$\boldsymbol{u}(\boldsymbol{x}) = \mathbf{E} \cdot \boldsymbol{x} + \boldsymbol{u}^*(\boldsymbol{x})$, where $\boldsymbol{u}^*$ is a periodic fluctuation, meaning it takes the same value on points directly opposite each other on the unit cell faces.

In Figure 2.5, approximations of the bulk modulus k^{app} for an artificially generated composite structure made of increasingly larger volumes V as measured by number of voronoi grains. Three boundary conditions are presented, KUBC, SUBC and PBCs, as well as the Voigt and Reuss bounds. It has been shown that the effective properties converge faster using PBCs, in the sense that the asymptotic value is reached for a lower V size, for less computational effort, particularly for high property contrast [92, 99, 102].

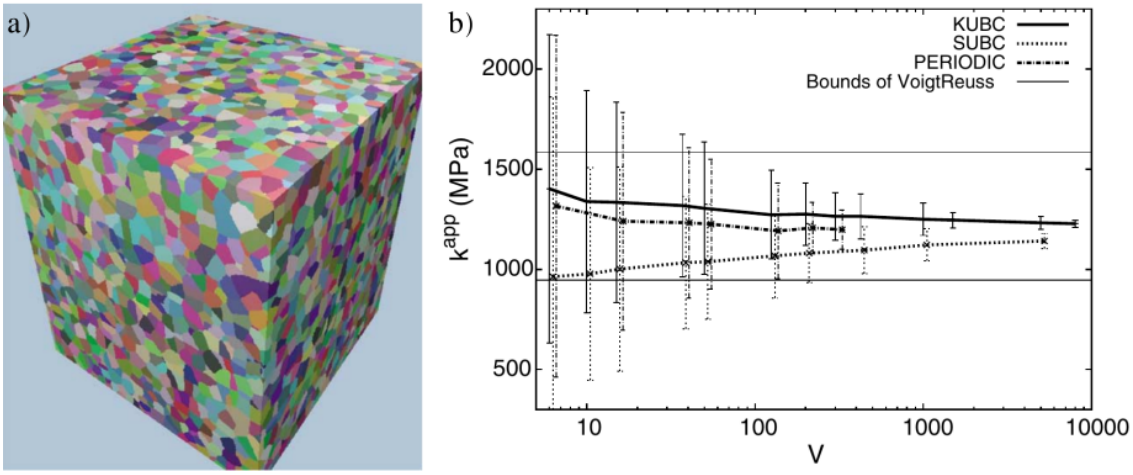

Figure 2.5 Variation of predicted properties as a function of RVE size, for several BCs. a) Example of an artificially generated polycrystal microstructure, as a voronoi mosaic. b) Estimation of the bulk modulus of this microstructure, as a function of number of grains in volume V. For PBCs, the predicted property converges to its asymptotic value for a size of 100, compared to 1000 for KUBCs and SUBCs. Adapted from [99].

As an example of this method applied to SFRPs, Dirrenberger et al. [100] considered the case of inter-penetrating (undifferentiated) randomly-oriented infinitely long fiber network of $v_f = 16\%$. They used a Poisson law to generate artificial volume elements and used Kanit's method to derive a RVE size for thermal and elastic properties. Since fibers are not differentiated, the meshing is significantly simpler than for individual fibers. The largest volume considered in their study contains 800 fibers. Using a relative error tolerance of 5%, they report an RVE size for a single realization of $\sim 1500 - 4000$ fibers for this configuration, depending on the property examined.

2.5.2 Finite elements method (FEM)

The most common method for computing the stress and strain fields inside a heterogeneous microstructure is the finite elements method (FEM) [20, 29, 33, 36, 63, 103–106]. In this method, the domain is represented by a mesh of elements of a particular shape (ex: tetragons, hexahedrons, etc.) that each have a number of degrees of freedom at their nodes. The differential equations describing the problem are then solved by evaluating them in an integral form over each element, thus assigning values to each degree of freedom and allowing the global solution to be constructed [107]. A domain of arbitrary geometry can be used, and a higher node concentration (or level of mesh refinement) can be used in regions of particular interest such as near small features or discontinuities. In the case of heterogeneous domains,

a finer mesh is required at the phase boundaries (i.e., the interfaces), as strong gradients in stress and strain can form in those regions. As presented in Figure 2.6, for fiber-reinforced composites, proximity between fibers causes large stress concentration factors (≈ 7) [108], underscoring the need for a detailled resolution in those areas. While automated solvers can generally execute the meshing automatically, problems arise however when high volume fractions are required. Proximity between inclusions will cause the number of required elements to increase drastically, making the computational cost of solving the problem enormous, and the meshing tools eventually failing to construct a mesh altogether. User input becomes necessary at this point, which is a tedious process, affects the accuracy of results, making them less repeatable [91]. Furthermore, the complexity of the mesh-generation process puts in question the competitiveness of this method [109].

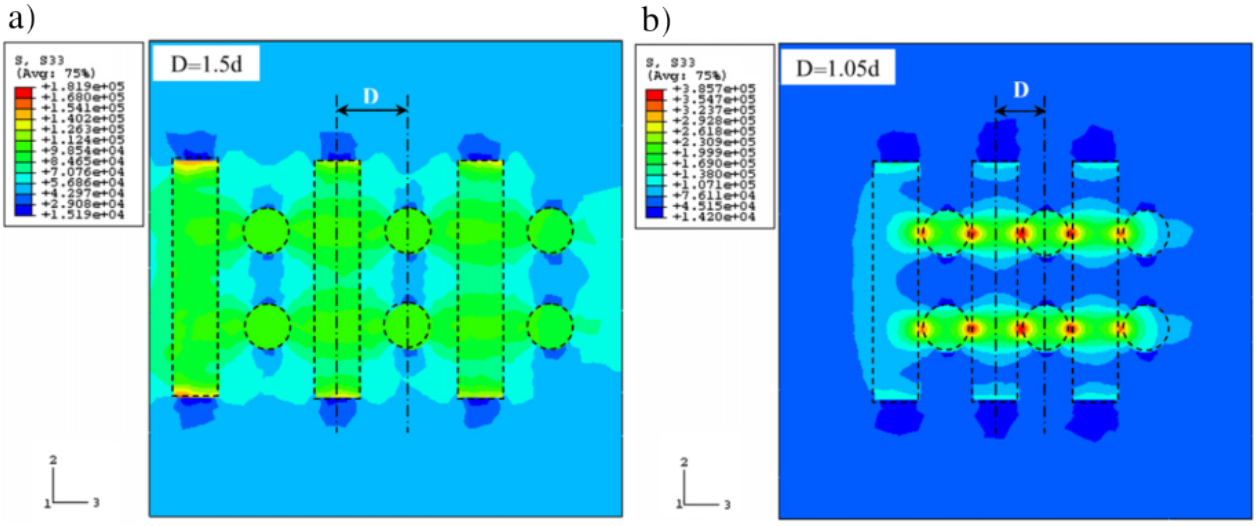

Figure 2.6 Stress field (σ_{33}) for volume containing vertical and out of plane fibers, subjected to a strain $\varepsilon_{33} = 1E-5$. In a) a center-to-center separation of 1.5 fiber diameters d yields a stress concentration factor of 2.14. In b), the stress concentration factor reaches 6.98 for a distance $D = 1.05d$. Proximity between fibers leads to higher overall stiffness and lower toughness, as higher local stresses are reached for the same applied strain. Adapted from [108].

2.6 Moulinec and Suquet's FFT algorithm

To circumvent the limitations of FEM for high volume fraction composites, researchers have sought to develop mesh-free methods for homogenization. Moulinec and Suquet [110] proposed such a method which reformulates the elasticity equations as the Lippmann-Schwinger equation [111], and solves the problem iteratively, with extensive use of the Fourier transform.

The Fourier transform is an integral transform that is used in many physics and engineering contexts to relate a time or space varying function $f(x)$ to a form where its frequency dependence is explicit. The Fourier transform of $f(x)$, noted $\mathcal{F}(f(x))$, is:

$$\mathcal{F}(f(x)) = \hat{f}(\xi) = \frac{1}{\sqrt{2\pi}} \int_{-\infty}^{\infty} f(x) e^{-i2\pi x\xi} \mathrm{d}x \tag{2.9}$$

where $\hat{f}(\xi)$ denotes the expression of the function $f(x)$ in Fourier (or frequency) domain, and $i = \sqrt{\text{-}1}$. We write: $\hat{f}(\xi) = \mathcal{F}\left(f(x)\right)$. Several mathematical relations are simpler to evaluate in the Fourier domain. For instance, the convolution product of two funciton f and g, noted $(f * g)(x)$, defined as:

$$(f * g)(x) = \int_{\infty}^{\infty} f(x - \tau) g(\tau) \mathrm{d}\tau, \tag{2.10}$$

becomes a simple multiplication in the Fourier domain, as per:

$$\mathcal{F}\Big((f * g)(t) \Big) = \hat{f}(\xi)\hat{g}(\xi). \tag{2.11}$$

In a heterogeneous solid, the stiffness is a function of position, i.e. $\mathbf{C}(\boldsymbol{x})$. The local deformation can be written as the sum of a constant term $\mathbf{E}$, and a fluctuating term $\boldsymbol{\varepsilon}(\boldsymbol{u}^*(\boldsymbol{x}))$, as: $\boldsymbol{\varepsilon}(\boldsymbol{u}(\boldsymbol{x})) = \boldsymbol{\varepsilon}(\boldsymbol{u}^*(\boldsymbol{x})) + \mathbf{E}$, or equivalently: $\boldsymbol{u}(\boldsymbol{x}) = \boldsymbol{u}^*(\boldsymbol{x}) + \mathbf{E} \cdot \boldsymbol{x}$. Here $\boldsymbol{u}^*$ is considered periodic, and the stress term $\boldsymbol{\sigma}$ is antiperiodic: $\boldsymbol{\sigma}(L) \cdot \mathbf{n} = -\boldsymbol{\sigma}(-L) \cdot \mathbf{n}$ so that the traction term $\boldsymbol{\sigma} \cdot \mathbf{n} = \mathbf{0}$ at the boundary (equilibrium condition). $\mathbf{n}$ is the vector normal to the boundary, and the unit cell, which is centered at the origin, has a side of length $2L$, as can be seen in Figure 2.7.

The classical elasticity equation becomes:

$$\begin{cases} \boldsymbol{\sigma}(\boldsymbol{x}) = \mathbf{C}(\boldsymbol{x}) : \Big(\boldsymbol{\varepsilon}(\boldsymbol{u}^*(\boldsymbol{x})) + \mathbf{E} \Big) & \forall\ \boldsymbol{x} \in V \\ \nabla \cdot \boldsymbol{\sigma}(\boldsymbol{x}) = \mathbf{0} & \forall\ \boldsymbol{x} \in V \end{cases} \tag{2.12}$$

We pose a reference media with stiffness $\mathbf{C}_0$ and define $\delta_{\mathbf{C}(\boldsymbol{x})} = \mathbf{C}(\boldsymbol{x}) - \mathbf{C}_0$. Inserting $\delta_{\mathbf{C}(\boldsymbol{x})}$ into Equation 2.12 gives:

$$\boldsymbol{\sigma}(\boldsymbol{x}) = (\delta_{\mathbf{C}(\boldsymbol{x})} + \mathbf{C}_0) : \boldsymbol{\varepsilon}(\boldsymbol{u}(\boldsymbol{x})) \tag{2.13}$$

$$= \mathbf{C}_0 : \boldsymbol{\varepsilon}(\boldsymbol{u}(\boldsymbol{x})) + \delta_{\mathbf{C}(\boldsymbol{x})} : \boldsymbol{\varepsilon}(\boldsymbol{u}(\boldsymbol{x})). \tag{2.14}$$

$$\text{We define: } \tau(\boldsymbol{x}) = \delta_{\mathbf{C}(\boldsymbol{x})} : \boldsymbol{\varepsilon}(\boldsymbol{u}(\boldsymbol{x})), \tag{2.15}$$

called the polarization, which contains the position-dependent stiffness through $\delta_{\mathbf{C}(\boldsymbol{x})}$, and

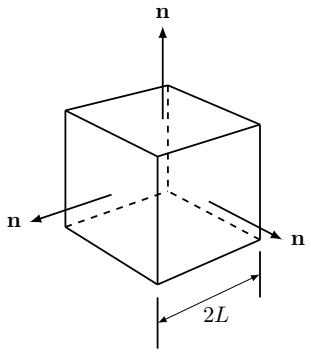

Figure 2.7 Unit cell: cube of side 2L, showing vectors normal to the boundary

the fluctuations in deformation through $\boldsymbol{\varepsilon}(\boldsymbol{u}(\boldsymbol{x}))$. This formulation is termed the periodic Lippmann-Schwinger equation [111]. The Moulinec algorithm iteratively solves for $\tau(\boldsymbol{x})$ through a fixed-point scheme.

Expessing Equation (2.14) in the Fourier domain, it is possible to write the solution as:

$$\boldsymbol{\varepsilon}(\boldsymbol{u}^*(\boldsymbol{x})) = -\boldsymbol{\Gamma}^0 * \tau(\boldsymbol{x}) \tag{2.16}$$

where $\boldsymbol{\Gamma}^0$ is the Green operator corresponding to the reference media $\mathbf{C}_0$, and $*$ denotes a convolution product. In the Fourier domain, $\boldsymbol{\Gamma}^0$ can be derived explicitly, and takes the following form for isotropic symmetries (see Appendix A for derivation):

$$\hat{\boldsymbol{\Gamma}}^0_{khij}(\boldsymbol{\xi}) = \frac{1}{4\mu_0|\boldsymbol{\xi}|^2}\Big(\delta_{ki}\xi_h\xi_j + \delta_{hi}\xi_k\xi_j + \delta_{kj}\xi_h\xi_i + \delta_{hj}\xi_k\xi_i\Big) - \frac{\lambda_0+\mu_0}{\mu_0(\lambda_0+2\mu_0)}\frac{\xi_i\xi_j\xi_k\xi_h}{|\boldsymbol{\xi}|^4} \tag{2.17}$$

where δ_{ij} is the Kroeneker delta, $\boldsymbol{\xi}$ are the frequency domain variables and μ_0 and λ_0 are the Lamé coefficients of the reference material. The work of Mura [112] details the derivation of the Green operator for other material symmetries.

The principle behind the Moulinec algorithm is to use Equations (2.15-2.16), in the real and Fourier space, respectively, to iteratively solve Equation (2.14). A constant deformation $\mathbf{E}$ is applied, and the stiffness tensors $\mathbf{C}(\boldsymbol{x})$ and $\mathbf{C}_0$ are known. we start by computing $\boldsymbol{\sigma}$ and $\tau(\boldsymbol{x})$ from $\mathbf{C}(\boldsymbol{x})$ and $\mathbf{E}$ (Equations (2.20-2.21)). This initial $\tau(\boldsymbol{x})$ will not be accurate, as it only accounts for the average displacement $\mathbf{E}$. It can be used to arrive at a better estimate of $\hat{\boldsymbol{\varepsilon}}$ (Equation (2.23)), which in turn yields a better estimate of $\boldsymbol{\sigma}$ (Equation (2.25). The entire algorithm is repeated until the solution has converged (Equation 2.26), meaning the estimated error is inferior to a prescribed value. The error at iteration i is defined as:

$$e^i = \frac{\left(\left\langle |\nabla \cdot \boldsymbol{\sigma}^i|^2 \right\rangle\right)^{1/2}}{\left\langle |\boldsymbol{\sigma}^i| \right\rangle} = \frac{\left(\left\langle |\boldsymbol{\xi} \cdot \hat{\boldsymbol{\sigma}}^i|^2 \right\rangle\right)^{1/2}}{\left\langle |\hat{\boldsymbol{\sigma}}^i| \right\rangle}, \tag{2.18}$$

where $|\cdot|$ is the Euclidean norm, and $\langle \cdot \rangle$ is the volume average over V. A typical value used as a stopping criterion is $e \leq 10^{-4}$. The main algorithm is as follows:

Initialization (step $i = 0$)

$$\boldsymbol{\varepsilon}^0(\boldsymbol{x}) = \mathbf{E} \quad \forall \boldsymbol{x} \in V \tag{2.19}$$

$$\boldsymbol{\sigma}^0(\boldsymbol{x}) = \mathbf{C}(\boldsymbol{x}) : \boldsymbol{\varepsilon}(\boldsymbol{x})^0 \quad \forall \boldsymbol{x} \in V \tag{2.20}$$

Iteration (steps $i \geq 0$)

$$a)\ \tau^i(\boldsymbol{x}) = \boldsymbol{\sigma}^i(\boldsymbol{x}) - \mathbf{C}_0 : \boldsymbol{\varepsilon}^i(\boldsymbol{x}) \tag{2.21}$$

$$b)\ \hat{\tau}^i(\boldsymbol{\xi}) = \mathcal{F}(\tau(\boldsymbol{x})^i) \tag{2.22}$$

$$c)\ \hat{\boldsymbol{\varepsilon}}^{i+1}(\boldsymbol{\xi}) = -\hat{\boldsymbol{\Gamma}}^0(\boldsymbol{\xi}) : \hat{\tau}^i(\boldsymbol{\xi}) \quad \forall \boldsymbol{\xi} \neq 0, \hat{\boldsymbol{\varepsilon}}^{i+1}(0) = \mathbf{E} \tag{2.23}$$

$$d)\ \boldsymbol{\xi}^{i+1} = \mathcal{F}^{-1}(\hat{\boldsymbol{\varepsilon}}^{i+1}) \tag{2.24}$$

$$e)\ \boldsymbol{\sigma}^{i+1}(\boldsymbol{x}) = \mathbf{C}(\boldsymbol{x}) : \boldsymbol{\varepsilon}^{i+1}(\boldsymbol{x}) \tag{2.25}$$

Convergence test (Equation 2.18)

$$f)\ \text{If } (e^i \leq 10^{-4}) : \text{stop. Else: iterate from a).} \tag{2.26}$$

Once an equilibrium condition has been reached, if the applied strain $\mathbf{E}$ was chosen to be uniaxial and unitary, one column of the homogenized stiffness tensor $\tilde{\mathbf{C}}$ is obtained directly from $\langle \boldsymbol{\sigma}(\boldsymbol{x}) \rangle$.

2.6.1 Comparison of FFT and FEM performances

While the performance comparison of the FEM and FFT based approaches has not been reported for SFRPs, it has been done by a handful of authors for polycrystalline structures, in terms of similarity of predicted results and computational workload. Rovinelli et al. [113] have studied the plasticity of the polycrystalline Ti55531, in the vicinity of a crack tip, using tomographic data of a physical specimen as a starting point. As presented in Figure 2.8, for FFT simulations the volume required needs to be a rectangular prism, so the authors filled the outside of the solid with gas. For the FEM simulation, the mesh was refined in the neighborhood of the crack tip using quadratic tetrahedral elements, and the rest of the volume used linear elements. The use of quadratic elements in the FEM formulation enabled the capturing of sharper transitions of the stress field around the crack tip. The FFT formulation is linear, so this effect is not present.

From a computational standpoint, the FFT formulation is more readily parallelizable, as the resolution of each voxel column in the volume is independent of each other column. The

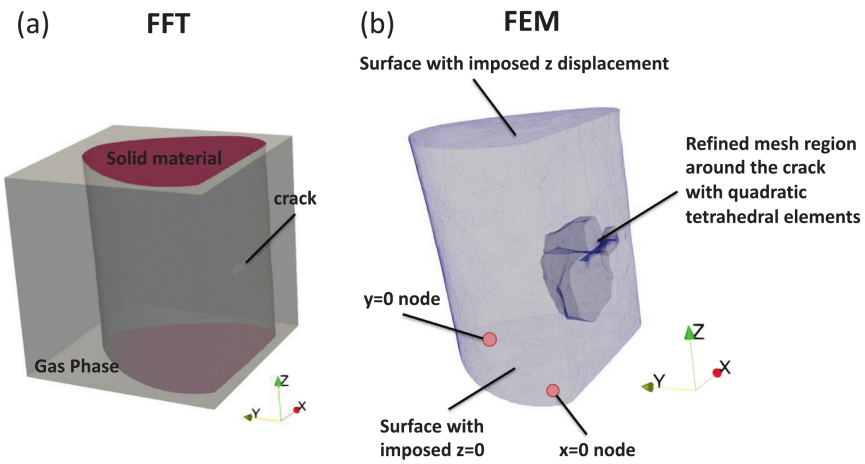

Figure 2.8 Microstructure geometry of an Ti55531 specimen, as used in the a) the FFT and b) the FEM method. In a), the gray and red regions represent the solid and gaseous phase, respectively. In b) the solid is meshed, using linear tetrahedral elements, and quadratic tetrahedral elements near the crack tip. Adapted from [113].

FEM formulation has some degree of parallelizability, but in the model used in the paper (and many commercial solutions) the maximum number of cores allowable cores is 8-12.

The authors report only minor distinctions in the predicted stress fields, except at the crack tip, where the different geometrical representation and handling of boundary conditions causes up to 10% difference in local values of stress, which dissipate at a distance of 7 μm of the crack tip. In term of computational time, when using a comparable number of CPUs, the FFT method is up to 25$\times$ faster than the FEM method, though it is not obvisous how this ratio would be affected by strong property contrasts and anisotropic reinforcements such as those seen in SFRPs.

CHAPTER 3 RATIONALE AND OBJECTIVES

3.1 Rationale

A critical evaluation of the existing literature has revealed the following salient points.

- Successful modelling is dependent on the quality of the microstructure descriptions used, or its fidelity to real materials. The majority of work on this topic focuses on making a statistical description of real materials and producing artificially generated microstructures to match those statistics as closely as possible. The computation burden required to generate artificial microstructures increases significantly with the inclusion's aspect ratio and volume fraction, and if the desired output is one that has a particular length and orientation distribution of fibers. Microstructure characterization from imaging data is a well-developed topic, but its use in direct microstructure description (i.e., not artificially generated) for modelling purposes has only been reported for a few relatively simple cases.

- The use of imaging data for microstructure description requires extensive development of specialized image analysis tools, with the specific goal of producing geometric descriptions compatible with numerical modelling methods, which requires the differentiation of constituents (single fibers and pores). The type of volumetric image processing required is challenging for two reasons: the presence of porosity makes this a 3-phase classification task, and the high volume fraction of fibers produces frequent fiber contact, for which a separation heuristic must be devised.

- The process-structure relationship that exist in SFRPs made with FFF is still largely unknown, in part due to the indirect methods by which fiber lengths and orientation distributions are characterized, and because the use of 3D imaging is much more technically demanding than 2D microscopy for instance. However, important features like the correlation between length and orientations of fibers and the spatial variability of local distributions inside the solid and how it relates to processing parameters can only be revealed through data that is volumetric in nature.

- Most experimental investigations of SFRPs made by FFF concentrate on the relation between process and property directly, with little consideration of morphology. Without a method for discerning the morphological attributes that are produced by the process

parameters and how they in turn affect the mechanical behavior, improving the reliability of the FFF process and thereby part performance remains empirical, without strong fundamental footing. That area of research is nascent for 3D printed composites, and a necessary precondition to establish a knowledge base into the process-structure-property relationship that exists in these materials.

- To date, modelling efforts on SFRPs made with FFF exhibit large error margins ($\sim 20 - 40\%$) as to their predictive accuracy of stiffness for instance. The microstructures used are often simplified into perfectly aligned, or uniform (random) distribution, and analytical methods are often used for microscale homogenization. The imperfect description of the microstructure, paired with the limited ability of analytical modelling to account for fiber-fiber interactions which are more prominent for higher volume fractions, are possible explanations for the poor accuracy of these methods.

- Some attempts at full-field numerical modelling exist, notably with FEM. The creation of a suitable mesh from the geometric description is difficult to automate successfully, and the resulting mesh requires such high levels of refinements at fiber contact points that the computational cost the FEM resolution becomes prohibitive. Mesh-free methods are a better alternative and are only beginning to be applied to SFRPs.

- Homogenization-based modelling of elasticity and viscoelasticity lack experimental validation, and when it is present, the anisotropy of the resulting solid is only addressed in a few studies on pure polymer, and never on reinforced polymers. It has been demonstrated that anisotropy arises from the printing pattern, due to the mesoscale regular arrangement of printing passes. It is expected that the anisotropy would increase with the addition of reinforcements, due to the marked preferential alignment in extruded materials and the fact that carbon fibers are strongly anisotropic. Disentangling the contribution of micro and mesoscale anisotropy would be an important insight to be gained from detailed modelling and multi-axis experimental testing.

- The contribution of specific processing parameters such as nozzle diameter and printing pattern on mechanical properties through their effect on morphology would pave the way to a deeper understanding of processing parameter selection, which is also largely empirical.

- The goal of making SFRPs with higher temperature resistance implies the need for modelling creep compliance, which is more prominent at higher temperatures. A method for identifying a material law that incorporates time and temperature dependence con-

sidering complex microstructure has only been done for a handful of cases involving SFRPs made with FFF.

3.2 Objectives

The general objective of this thesis is to develop a numerical method to predict the elastic and thermo-viscoelastic properties of SFRPs made with FFF. The main objective is broken into the following specific objectives (SO).

SO1: Characterize morphological properties of SFRPs as a function of processing parameters. The objective is to create an image analysis tool to automate the task of µCT data analysis to identify individual constituents (single fibers, pores) within the polymer matrix. This tool should require little to no user input and be able to differentiate individual fibers to extract their length and orientation in space. In addition to the geometric representation of the microstructure in a form that is compatible with modelling methods, statistical representations and visualization methods must be devised to enable comparison of the processed scans between them and gain insight into the process-structure relation. The processing of scans from specimen produced with several manufacturing conditions including nozzle diameter, fiber volume fraction, and printing pattern is required.

SO2: Characterize and model tensile properties of SFRPs made with FFF. The process-property relation is investigated by manufacturing test specimens under different processing conditions and subjecting them to mechanical testing to measure their tensile properties. FFT-based full-field homogenization models are adapted to perform effective elastic property prediction using the morphological description obtained using the image analysis tool. The predictions are validated against the experimental tensile testing data. The predicted properties and the morphological features revealed enable the quantification of the anisotropy of these material properties and to what degree it is affected by processing parameters.

SO3: Formulate a material law incorporating the time and temperature dependence of SFRPs made with FFF. Using experimental creep-recovery data taken on specimens made with neat (pure) polymer, an isotropic constitutive law is generated at two different temperatures. This law, along with the morphological description, is then used as inputs for an anisotropic, temperature-dependent constitutive law identification procedure, which is then compared with the experimental data from reinforced polymer specimens.

CHAPTER 4 SCIENTIFIC APPROACH

Over the course of this research project, three scientific publications were prepared. The achievements of each article are outlined here, as well as their relation to the objectives as stated in Chapter 3.

4.1 Article 1: OpenFiberSeg: open-source segmentation of individual fibers and porosity in tomographic scans of additively manufactured short fiber reinforced composites

This article presents an automated segmentation procedure for µCT imaging of fiber-reinforced composites containing porosity. Using high resolution scans obtained from specimen fabricated from CF-reinforced PEEK at several fiber volume fractions, a pixel-wise labelling was performed by adapting existing machine learning and classical image processing algorithms. Then, a tracking procedure was developed by which pixels are grouped into connex regions, and continuous segments in 3D are identified based on their geometrical properties. An elaborate stitching procedure was created to identify segments likely to belong to a single fiber, and to fill in the gaps between them. Once all fibers present in the volume were individually labelled, characteristics such as the relation between length and orientation were revealed for each level of fiber volume fraction. The tool was validated by reproducing the segmentation and tracking results of two separate studies on FRPs. The total fiber fraction predicted by the segmentation was also compared with that computed from experimental measurements of the density of each specimen. Visual inspection was used to demonstrate that although minimal human input is required, the resulting microstructure description is of high quality, with a mean precision of 93.1% on an individual fiber basis and near perfect precision for porosity detection.

This article was published in the *Composite Science and Technology* journal on July 28$^{\text{th}}$, 2022 (DOI: 10.1016/j.compscitech.2022.109497). This article was almost entirely written by the author of this thesis, who developed the software implementation of the segmentation tool and performed the image acquisition. Dr. Yahya Abderrafai and Dr. Audrey Diouf Lewis provided expertise in material processing and performed filament preparation. Dr. Nicola Piccirelli is our industrial partner representative and provided administrative oversight. Professors Daniel Therriault and Martin Lévesque assured supervision, scientific guidance and review of the manuscript.

4.2 Article 2: Multiscale Fast Fourier Transform homogenization of additively manufactured fiber reinforced composites from component-wise description of morphology

In this paper, the micro and mesoscale microstructure of 3D printed SFRPs was characterized with the OpenFiberSeg, using data collected on specimen manufactured using three different nozzle diameters and three different printing patterns using the nozzle of intermediate size, for a total of five printing configurations. This data was used to generate microstructures description to perform dual-scale FFT-based homogenization and predict the tensile properties directly from the tomographic data. The extraction of richly detailed morphological data also enabled the visual inspection of the spatial variation of local properties such as fiber length and orientation distribution, and fiber and porosity density. The different levels of anisotropy present at the microscale (intrabead) for each printing configuration was revealed by statistical observation of orientation distribution. The dual-scale homogenization prediction of tensile moduli was validated against experimental data and compared to the output of homogenization performed on artificial microstructures, a leading method in the field. The predicted tensile moduli were shown to be within 5% of experimental data, in all but one of the printing configurations.

This article was submitted to the *Composite Science and Technology* journal on January 19$^{\text{th}}$, 2023, and at the time of writing is undergoing peer-review. This article was almost entirely written by the author of this thesis and is the main author of the software implementation of the dual-scale homogenization method and the morphological analysis. Clément Vella participated in the development of the software adaptation of the homogenization method. Alessandra Lingua and Juliette Pierre performed processing parameter optimization, specimen preparation, and tensile testing. Dr. Nicola Piccirelli is our industrial partner representative and provided administrative oversight. Professors Daniel Therriault and Martin Lévesque assured supervision, scientific guidance and review of the manuscript.

4.3 Article 3: Thermo-viscoelastic multiscale homogenization of additively manufactured short fiber reinforced polymers from direct microstructure characterization

In this article, the dual-scale homogenization method was extended to model the time and temperature dependent mechanical properties of SFRPs made by FFF. First, the constitutive law parameter for the neat polymer was identified using experimental creep-recovery testing data. This material law and the microstructure descriptions obtained by OpenFiberSeg were

then used to generate the time dependent mechanical behavior of the composite through FFT-homogenization. The parameters for a material law exhibiting anisotropic and temperature dependent viscoelasticity were then identified, considering the mesoscale structure (the printing pattern). The behavior law is then used to predict the stress strain history of any arbitrary loading, which is compared to multi-axis experimental data. For specimen printed unidirectionally, submitted to axial loading, the mean relative error for a creep-recovery test is <3%, for both 21°C and 120°C.

This article was submitted to the *International Journal of Solids and Structures* on Febuary 22$^{\text{nd}}$, 2023, and at the time of writing is undergoing peer-review. This article was almost entirely written by the author of this thesis and is the main author of the software implementation of the dual-scale homogenization method, and performed the creep-recovery testing under various temperatures. Alessandra Lingua performed processing parameter optimization and specimen preparation. Dr. Nicola Piccirelli is our industrial partner representative and provided administrative oversight. Professors Daniel Therriault and Martin Lévesque assured supervision, scientific guidance and review of the manuscript.

CHAPTER 5 ARTICLE 1: OpenFiberSeg: open-source segmentation of individual fibers and porosity in tomographic scans of additively manufactured short fiber reinforced composites

This article was published in the *Composite Science and Technology* journal on July 28th, 2022 (DOI: 10.1016/j.compscitech.2022.109497).
Sosa-Rey, F., Abderrafai, Y., Lewis, A. D., Therriault, D., Piccirelli, N., & Lévesque, M. (2022). *Composites Science and Technology*, 226, 109497.

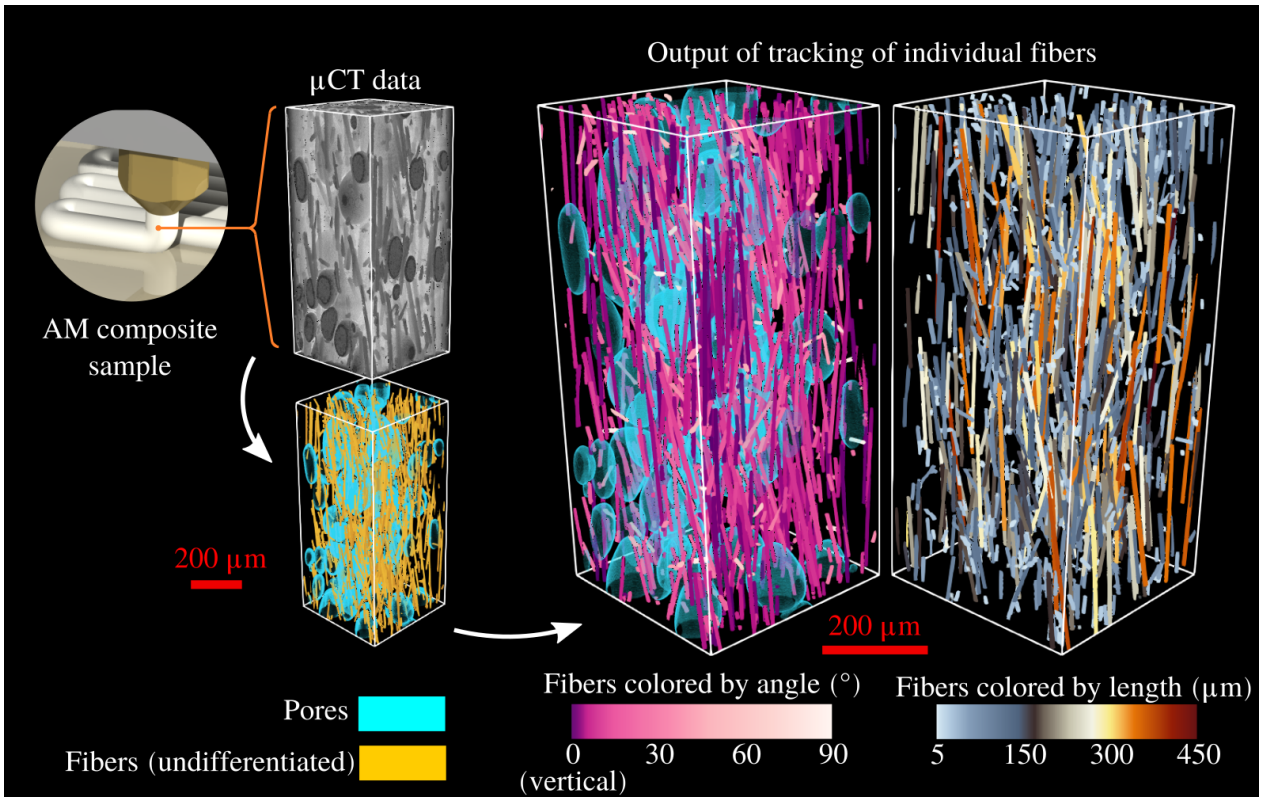

Figure 5.1 Graphical abstract: OpenFiberSeg

5.1 Abstract

From a modelling standpoint, the morphology of additively manufactured (AM) high-performance short fiber reinforced polymer (SFRP) are essential to characterize, yet this task poses great challenges. The method presented extracts individual fibers from tomographic scans and produces a segmentation that is 93.1% precise on average on a per-fiber basis across a large range of fiber filling ratios (5-40 wt.%), needs minimal human input and is scalable to full-

sized datasets containing $\sim 10^5$ individual fibers. In addition, this tool allows the analysis of the correlated length and orientation distribution of fibers, and the quantification of shear-induced alignment and fiber breakage. The method is validated by successfully reproducing the segmentation of (continuous) fiber reinforced composites published in 2 separate studies and by predicting the fiber volume fraction and material density directly from the tomographic data of SFRPs. The output can serve as a basis for constituent-level mechanical modelling, and to gain insight into the relationship between processing parameters, morphology and mechanical behavior of SFRP. The full source code and imaging data are attached to this publication.

5.2 Background

Fused Filament Fabrication (FFF) is an additive manufacturing (AM) method in which parts of arbitrary geometry are built layer-by-layer. The use of materials like polyether-ether ketone (PEEK) in FFF is a very active area of research as its mechanical properties similar to human bone, its chemical and thermal resistance, biocompatibility and transparency to medical imaging methods make it a choice candidate for medical implants and prostheses [15, 39, 41, 114, 115]. When PEEK is used as a short fiber reinforced polymer (SFRP), the reinforcements can be oriented purposefully, enabling the engineering of parts with high weight-specific material properties [11,43,50]. As such, reinforced PEEK parts made by FFF are being investigated as possible replacement for heavier metallic components in the automotive and aerospace industry [11, 15, 43, 51]. However, several technical challenges complicate the printing process with this material and cause it to under-perform when compared to aircraft-grade aluminum parts [16,116]. PEEK resin being semi-crystalline with a high melting point, significant shrinkage occurs during solidification, both of thermal origin and due to density and viscosity changes during crystallization [5, 11, 15, 41, 43]. When used in FFF, process parameters, part geometry and local cooling history can interact to cause warpage of such severity as to cause print failure [11]. Adding reinforcements can reduce warpage [16] and improve mechanical properties like strength and stiffness [5], but have complex effects on crystallization [5], interlayer bonding and flow dynamics [11]. During extrusion, fibers alignment and flow characteristics are mutually dependent, and in turn affect the bonding dynamics, as fibers present at the bead surface modify diffusion conditions and surface tension [11]. Improper bonding between layers is one of the main causes why FFF parts exhibit inferior mechanical properties to molded parts, most notably across the layers [5,15]. Porosity is another important factor, introduced both during filament production and by air trapping between passes and layers at deposition [5, 15, 42]. This reduces the effective cross-section of

the parts, changes flexural properties through pore collapse, and adversely affects strength since pores act as stress concentration sites [11, 42, 117]. The inclusion of fibers has been shown to be accompanied by increased porosity [5, 50–52], measured at 20 vol.% for PEEK with 30 wt.% carbon fibers (CFs) [118]. These combined effects makes mechanical modelling of real parts a yet-unsolved challenge [4,11,12,87,119–121], as all these phenomena need to be considered in concert [11]. To help address this issue, microstructural analysis methods must be developed to enable the extraction of relevant properties from imaging data, particularly at the constituent scale (single fiber and pore).

5.2.1 Microstructural features

In order to serve as a basis for mechanical behavior prediction, the microstructural analysis must extract the main features affecting stiffness and strength of SFRP materials (other than the inherent properties of the matrix and fibers). Those features have been identified as: the distributions of fiber lengths and orientation [75,80,122–125], the uniformity of fibers' spatial dispersion [50, 126], as well as the presence and morphology of porosity and other defects [126–129]. Unlike for the case of continuous fibers, in SFRP those properties are all affected by the processing parameters (both in injection molding or FFF) [50, 119, 123–125, 130], and are therefore crucial to understand the properties of the parts produced. For instance, shear-induced alignment of fibers and fiber breakage during the different processing steps have decisive impact on the mechanical performance of SFRP parts [11, 50].

Recent advances have been made on constituent-level characterization of SFRP used in FFF, for instance in basalt fiber reinforced polylactic acid (PLA) [78], and CF reinforced PEEK [118]. In both cases, proprietary software was used to perform the critical segmentation steps. Yu et al. [78] do differentiate individual fibers, but in a context of little porosity in the feedstock material (so-called inner-voids, of at most 4.2 vol.%), and moderate infill (up to 20 wt.%). As for CF reinforced PEEK, Sommacal et al. [118] centered their study on porosity distribution, and identified the volume occupied by reinforcements generally, not individual fibers.

In this work, we propose a method of automated constituent extraction from imaging data, called OpenFiberSeg. We draw on existing methods and techniques, complementing and adapting them to the specific case of FFF of reinforced PEEK. The presence of significant porosity ($\sim 20 vol.\%$), low contrast in the input data and high filling ratios under consideration (up to 40 wt.%) make for a problem that is uniquely challenging. Once this problem is solved, the solution can be applied to a host of fiber reinforced materials, of equivalent or lesser degree of complexity. The intent of open distribution of both source code and imaging

data guided the development of this tool, to help accelerate progress in the field.

5.3 Literature review

X-ray tomography provides volumetric renderings of the microstructure of these solids. However, since CFs and polymeric matrices have similiar densities and elemental composition, the imaging data is low contrast and has considerable noise amplitude [72, 73]. As imaging apparatus are limited to a voxel size of 0.7 to 0.4 μm, fiber identification must be performed on at best a handful of voxels, as they typically have a diameter ranging from 5 to 10 μm. Manual labelling by an expert is possible, but is a tedious, time-consuming task, and subject to inter and intra-observer variability [131]. Automatic segmentation tools are therefore required. Various groups have produced such tools for fiber-reinforced composites, the majority of which consider only two-phase materials (the phases being matrix and reinforcements) [65, 66, 81, 85, 122]. When dealing with a third phase (the porosity), the segmentation task considered to be much harder [132, 133], especially when the grayscale values from different phases can overlap each other [133, 134] as they do in FFF reinforced PEEK. In [74], 3-phase segmentation (matrix, fibers and voids) is performed by using a stochastic optimization procedure adapted from [135, 136] to segment small regions of data, and training a neural network with the output. The authors avoid the task of manually labelling training data or the computationally prohibitive task of using the stochastic procedure on full-sized dataset. Their method performs well on real data from glass fiber reinforced polypropylene containing voids, though only visual validation is presented. Using synthetic data with no porosity, they report a per-fiber detection precision of 87.0% (651/748 fibers detected).

If orientation characterisation is the only concern, one traditional method is to use scanning electron microscope images of polished specimen, and determine fiber orientations based on the minor and major axes of the ellipses made by their cross-sections on the specimen surface [137]. However, this method is limited to surface level, is time-consuming, and cannot distinguish between the two orientations that produce the same elliptical cross section [73, 82]. A more modern method based on 3D imaging is to compute the local orientation tensor by obtaining the local structure tensor for neighboring voxels via the Hessian matrix [80–82]. While being very general and not requiring fiber separation, this method can produce length information only for very highly resolved scans, and it is quite susceptible to noise [138] (though it can be adapted to process poorly resolved scans [65]). Furthermore, the accuracy of the orientation tensor method drops significantly if the gray intensity profile is not Gaussian inside fibers, or for high filling ratios, where fiber contact is more common [80, 122].

5.3.1 Fiber separation and tracking

To extract richer data pertaining to *individual* fibers, a necessary first step is the segmentation (labelling) of voxels belonging to fibers rather than other phases (matrix, pores, etc). Methods to perform this task include: grayscale value thresholding (Otsu's method) [85] , pattern matching [76,77], supervised machine learning (for instance K-means clustering used by Qim at DTU [79,139,140], or deep learning methods like those implemented in commercial software like Dragonfly™ [72,134,138] or others. One common limitation for all these methods is that for high filling ratios, many fibers will be in close proximity, and their boundary blurred, leaving many missed detections or failing to separate distinct fibers [81,85]. Since computer vision tools and methods are overwhelmingly aimed at 2 dimensional (2D) images, all of the cited methods are 2D-based. Many missed or false detections could be avoided by taking advantage of the 3 dimensional (3D) nature of tomographic data, but only some efforts have been made towards this goal, for instance using convolutional neural network in 3D [141,142].

Extracting individual fibers from the voxel-wise label requires a 3D tracking procedure. A fiber tracking method proposed by Whitacre [143] (companion study of Czabaj [76]), uses template matching as the first segmentation step, then the Global Nearest Neighbor algorithm combined with the Kalman filter to estimate fiber trajectories as they are being constructed. This method also incorporates smoothing, track stitching, and a constraint by which fiber trajectories are only accepted if no volumetric overlap occurs in their paths. Whitacre reports 99.4% accuracy of track assignment, but as is pointed out, this is for a relatively small specimen (629 fibers) of *unidirectional* composite, with high scan quality. The authors recognize that for more complex, larger specimen, this method would "increase the computational cost dramatically" [76] (though mainly for the meshing and mechanical simulation than tracking *per se*). The segmentation procedure itself took 2h for 629 fibers on a desktop workstation, while 1 mm^3 of SFRP can contain up to $\sim 10^5$ individual fibers [85]. Assuming linear scaling, that would translates into nearly two weeks' time.

Another tracking method applied to injected glass fiber SFRP was developed by Agyei and Sangid [85] by which the image quality of the scans are first sharpened, then voxels probably containing fibers are flagged using Otsu's method, and clustered using an iterative watershed algorithm. Ellipsoids are fitted to each cluster, and they are connected across 3D space on the basis of the proximity of their centroids. Post-processing ensures that the remaining fibers have tortuosity below a prescribed threshold. Their method successfully tracks 91 682 fibers with a processing time of 55 hrs on a desktop workstation. However, they selected injection-molded glass fiber reinforced polypropylene because of the higher contrast of glass fibers, and there is no porosity to speak of in their samples.

Partially reconstructed fibers have been stitched in different ways. Altendorf selects stitching candidates on the basis of endpoint distance, the angle between the segments, and the angle between segments and the added connecting line [144]. Creveling implement a method by which fiber tracks all considered for stitching, and the most likely candidates which pass a series of checks are selected, including endpoint distance, potential interference with existing tracks, and other tests [77].

In FFF SFRP, the regions surrounding pores are of particular concern from a tracking standpoint. Artifacts at pore boundaries cause many missed and false detections of fibers (even for manual labelling). Hence, a heuristic that overcomes this difficulty need be more complex than those in tracking tools previously published, focused on materials with negligible porosity.

The ultimate objective being mechanical property inference, it is more important that the reconstructed volume be statistically equivalent to the actual solid, rather than any single fiber being found or not. As long as the proportion of phases present is correct, as well as the lengths and orientation distribution of fibers, the extracted microstructure will serve as a representative volume element [145, 146]. This guiding principle will be useful for selecting empirical parameters for aspects of our method that are probabilistic in nature, most notably the stitching partially tracked fibers.

5.4 Methods

In this work, contrasts in imaging data are first enhanced by histogram equalization. Then 2D-image based pre-segmentation of porosity and specimen boundary (perimeter) is performed with a combination of classical image processing (Otsu's method and Canny edge detection) and fiber regions are located with the use of a machine learning (ML) tool called InSegt [147]. From this voxel-wise labelling, a 3D-based feature extraction is performed: fiber segments are identified by locating centroids and connecting them by the K-nearest neighbor algorithm. Then, a multi-step stitching heuristic is applied to recombine these segments in a manner which can handle not only missing but also false detections. The voxel-wise labelling is then retroactively corrected to include the missing segments, and to successfully label the fiber boundaries which are a source of frequent error for ML tools. The method is shown to be effective across many material compositions (filling ratios), with close to no human input, except at the ML model training stage.

The material specimen under consideration here are produced by free-space extrusion (3D printing nozzle not pressed against the build plate, but extruding in air). This way, phenom-

ena present at the meso scale (inter-bead and inter-layer voids, over- or under-extrusion) and macro scale (infill fraction, infill pattern, stacking of layers of different relative orientation, etc) [4, 12, 119, 148] are removed from consideration, allowing an analysis of the morphology at the microscale in a more pristine state.

5.4.1 Specimen preparation

Pellets of PEEK 90G (Victrex™, UK) were first desiccated in a Cole-Parmer 282A Vacuum Oven (Antylia Scientific, USA) at 150°C for 5 hours. For each specimen, pellets were first introduced in a DSM Xplore Micro 5 cc twin-screw microextruder (Xplore Instruments BV, Netherlands), before introduction of Panex™ 35 Type 83 chopped CFs (Zoltek, USA), with weight fractions from 5 to 40%, by 5% increments (pure polymer was removed from consideration as it shows no porosity and doesn't require tracking). Mixing (while extrusion is shut off) was carried out at a constant speed of 3 mm/s at 360°C. Extrusion was made at a constant speed of 3 mm/s at 390°C. Only sections of the filament with a variation of 100 microns or less as measured with a caliper were kept for extrusion in a 3D printer extruder. Printing of specimen was performed on a AON3D™ industrial 3D printer, extruding through a 0.6 mm diameter nozzle in free space (not pressing on the build plate) with a nozzle temperature of 390°C. The resulting average specimen diameter is 500 μm.

5.4.2 Tomographic data acquisition

Individual filaments specimens were then mounted on a pin vise and placed in a ZEISS Xradia™ 520 micro-computed tomography system. Each specimen was exposed to a source power of 80 KV, with the source at a distance of 10 mm, and the detector at 15 mm, with no filter in the beam line. 1600 projections were acquired for each specimen, for a total acquisition time of ~ 1.75 hour per specimen. Volumetric reconstruction was performed with the parameters obtained automatically by the Zeiss Reconstructor™ software. The resulting voxel dimension is , and the filaments were entirely inside the scanned field of view. Figure 5.2a shows a sample 2D slice of the resulting tomograph, for a PEEK filament (diameter 0.6 mm) with 40 wt.% CF. In Figure 5.2b we can see that the pores (large dark structures) have a light region at their boundary which has the same grey intensity as the fibers (smaller white round shapes), complicating the segmentation task. These artifacts are attributed to sharp changes in refractive index in the specimen, and could be attenuated by imaging in phase-contrast mode, in which source and detector are much farther apart [149]. However, this incurs much longer and therefore more expensive scans.

While OpenFiberSeg can work on larger specimen sizes (up to 1.4 mm in diameter, using 4500

projections and a total exposure time $\sim$ 4 hours), with the contrasts encountered with CF PEEK, pixel sizes >1 μm lead to unsatisfactory performance of InSegt, for which the stitching procedure cannot compensate. This means highly resolved scans are required for this class of materials. Although not presently tested, glass fibers (GF) reinforcements would have a stronger imaging contrast, as they are mainly made of silicon rather than carbon atoms like polymers, have a density of 2.61 g/cm^3 compared to CF at 1.72 g/cm^3 and average diameter of 12 μm against 7 μm for CF [5]. In which case, larger pixel sizes (up to 2 μm) will probably be acceptable.

5.4.3 Global processing flowchart

The data processing is structured in the manner illustrated in Figure 5.3. Starting form the tomographic data, the phases are separated on a voxel-by-voxel basis. Then, for all three reference directions x, y and z, individual fiber regions are separated, and centroids extracted. Tracking of fibers is performed, including stitching of partial detections. From fiber tracks, 3D representations of each fiber are constructed, with gaps identified by the stitching procedures filled. Fibers detected from all 3 directions are then recombined to form the final segmented output. The entire procedure requires minimal input from the user, and accomodates a variety of material types (continuous fiber composites, and FFF SFRP of very different filling ratios, etc). The relevant parameters are scaled with respect to the voxel physical dimension, which depend on scanning parameters.

5.4.4 Initial voxel-wise labelling

Porosity detection

The first labelling steps consists in identifying which voxels contain either polymer matrix, fiber reinforcement, porosity, or are outside the filament (the perimeter). First, the contrasts in the raw data are enhanced using histogram equalization from the OpenCV library (cv.equalizeHist). Then, with the help of the Canny edge detection algorithm (implemented in the Scikit-image library [150]), both the perimeter and the porosity can be identified on each 2D slicing of the volume. This algorithm uses the gradient in the image and two thresholds to identify continuous contours. To identify the perimeter, a binary mapping is first created by thresholding the image with Otsu's method. This mapping makes the specimen stand out from the perimeter, and the boundary is easily identified. The Canny algorithm is used twice: on the binary mapping (to find the specimen boundary), and on the original histogram-equalized image (to identify pore boundaries). The required parameters for the

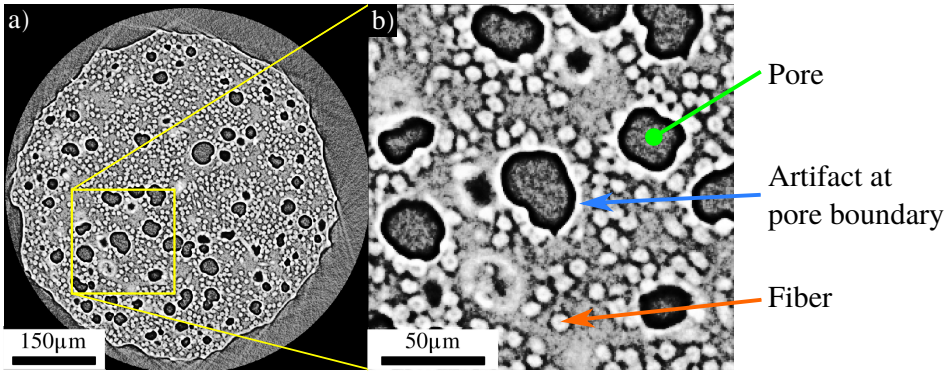

Figure 5.2 Sample 2D slice of tomographic scan of a PEEK 40 wt.% CF filament (after histogram equalization). a) Entire filament cross-section b) Pores and fibers are indicated by arrows, along with the artifacts in the region surrounding pores.

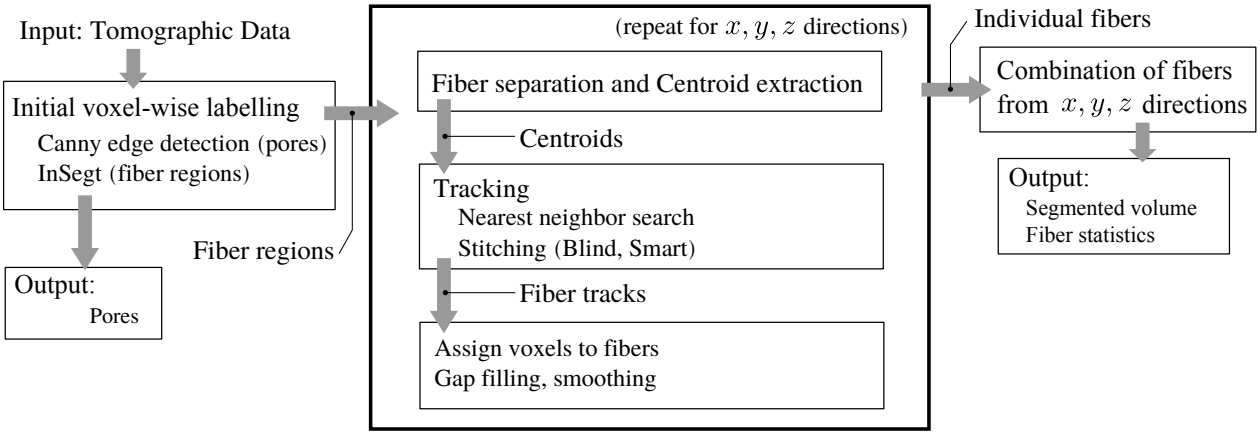

Figure 5.3 Schematic flowchart of the segmentation and tracking procedure. From the tomographic data, voxels containing pores and fibers are first isolated, then fibers are tracked and reconstructed from all 3 reference directions, to be combined in a single segmented microstructure.

Canny algorithm depend on image characteristics. For the datasets used in this study, the following parameters were used: low_threshold ranging from 60-100, high_threshold of 180-200, and sigma=3.0 for the porosity detection, and low_threshold=30, high_threshold=50 and sigma=1.0 for perimeter detection. See attached source code for further details. In order to fill in the closed contours in each case, the floodfill algorithm (cv.floodfill) is used, which labels all the voxels reachable (not bound by a closed contour) from a given seed point. The Canny method was favored over simpler gradient-based methods like Sobel, Roberts or Prewitt edge detection as it more robust against noisy data [151] and it produced closed contours consistently amidst the variety of edge characteristics encountered in the original data. As can be seen in figure 5.2b, pore edge sharpness can vary significantly, making simpler methods unsuitable.

Figure 5.4a shows the result of the porosity extraction by contour filling in a typical region of data. Because the contours are at times too attenuated in a few (typically 1-2) image slices, the volume of pores are interrupted by a few thin missing sections. Small regions are also present, which visual inspection reveals to be false positives (the smallest real pores are much larger than these structures which are < 2 μm thick.)

As shown in Figure 5.4b, both types of artifacts are eliminated by performing the 3D morphological operations of **closing** (filling in missing thin slices) and **opening** (removing structures smaller than the structuring element) as implemented in the N-dimensional image processing library SciPy.ndimage [152]. For both operations, spherical structuring elements of radius 3 and 1 voxels are selected, respectively. These are large enough to handle the encountered artifacts, and small enough to leave the general topology of pores unaffected. The resulting pores after corrections are shown in Figure 5.4c. Relying on classical image processing such as this has the advantage of handling a variety of scanning conditions and morphologies without any intervention, or occasionally requiring the adjustment of a handful of parameters (the two Canny thresholds), rather than the re-training of neural networks encountered in ML. We therefore elected to not investigate ML methods for this particular task.

Fiber detection and separation into convex blobs

The InSegt tool is used to find probable fiber-containing regions. In InSegt, a manual labelling of a small region of the data is used to create an image dictionary based segmentation tool using the machine-learning method called K-means clustering. A specimen image slice is then processed, yielding a probability field giving the likeliness that each voxels belongs to a fiber or not. By inspecting this probability field, the user selects a threshold above which to label pixels as fibers, and checking against the input to ensure the majority of fibers are found,

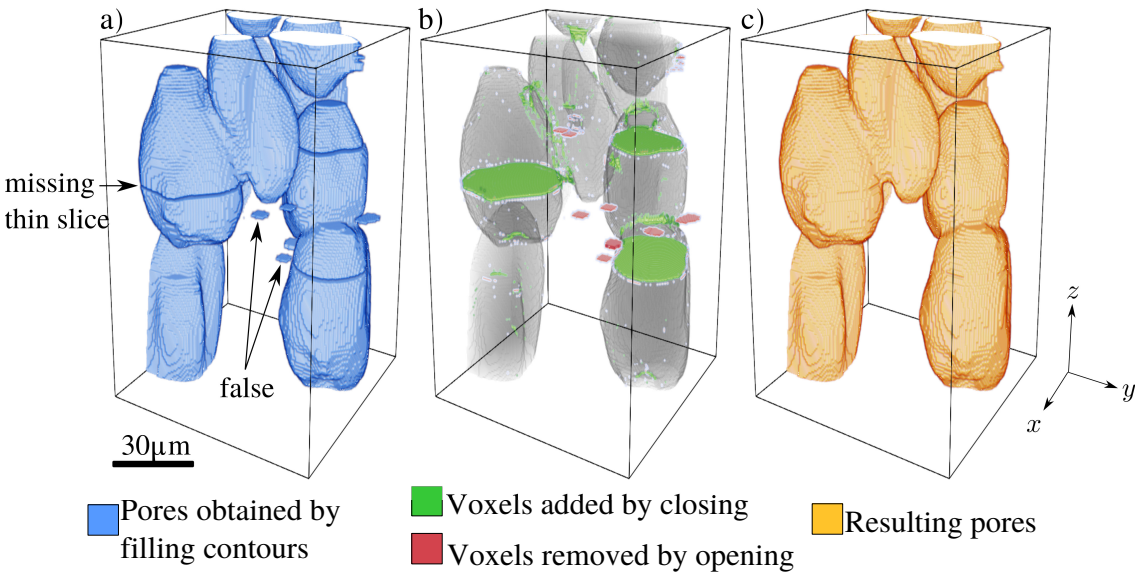

Figure 5.4 Porosity labelling, typical region of data (2D slicing in $x-y$ planes): a) as obtained by filling the closed contours of the Canny algorithm. b) Morphological closing fills in missing thin slices inside well-defined pores, opening removes false detections. c) Resulting pores.

with as little false positives as possible. The full volume is then processed to obtain an initial mapping of all voxels containing fibers. For specimen with low filling fraction (<15 wt.%), the fiber regions were often underestimated in size, because setting the threshold lower to capture the whole perimeter for each fiber also introduced many false detections. This minor effect was corrected with a method presented in Supplementary Materials (Appendix B), involving the Laplacian of the probability field.

As shown in Figure 5.5a, each voxel is now considered either matrix, pore, or fiber. However, the InSegt tool often labels fibers in close proximity as a single connex region, or *blob*. To identify individual fibers across the volume, it is necessary to detect the regions containing more than one fiber, and split them accordingly. First, the watershed algorithm is used to find all the connex regions (using the cv.watershed function, implemented in the manner detailed in [153], with distance parameter of 0.8 pixel). Then, OpenCV functions cv.findContour and cv.convexityDefects are then utilized to flag the blobs that are not convex (defined as a convexity defect size >1.2 pixels). The blobs passing or failing this convexity test are represented in Figure 5.5b as "single fiber" blobs and "rejected" blobs, respectively. To reprocess the "rejected" blobs, the watershed transform is used again, in a recursive manner: the distance parameter of the watershed is increased by 0.1 pixels increments for each individual blob. When the new watershed transform outputs more than one blob, the convexity test is performed on those new blobs. New blobs that are flagged as non-convex are then processed

by themselves in the same manner. The resulting subdivision of each blob into the largest number of convex blobs is illustrated in Figure 5.5c. For these individual fiber blobs, a centroid (analogous to center of mass) is computed with the OpenCV function cv.moments, as shown in red in Figure 5.5d. Note that not all identified centroids belong to real fibers, as some will be false detections, particularly due to light-colored artifacts around pores. The shape of these artifacts is such that those centroids will most likely not form neatly defined chains of sufficient length, and they will be discarded during the tracking procedure.

The fact that detection of pores and perimeter, the splitting of blobs, the convexity tests and the extraction of centroids can be done on a slice-by-slice basis allows these step to be done in parallel, yielding a speedup factor equivalent to the number of cores available.

5.4.5 Tracking

Figure 5.6 shows a schematic of the entire tracking procedure: image slices are imagined as 1 dimensional (1D) projections, shown as dotted lines. Fiber regions were identified (with some missing and false detections, as shown in Figure 5.6b, and centroids were extracted, from which complete fiber objects are sought. When tracking in the vertical direction, the fibers roughly aligned with this direction will have centroids on adjacent slices at a small distance in the transverse plane, when compared to the radius of the fibers. For each pair of adjacent slices, we want to find the pairs of centroids that are mutually closest. The K-nearest neighbor (KNN) algorithm is very efficient and highly scalable in this setting, as it can find the closest neighbor with an $\mathcal{O}(n \log n)$ complexity. For each slice, a K-dimensional tree (KD-tree) is built (in 2D, for x and y coordinates), as implemented in SciPy. The KD-trees are then queried at the coordinates of the centroids for the following slice. We then initialize fiber objects from the continuous chains of closest centroids: centroids on the first slice which are successfully paired to those on the second form initial fiber segments (if they are within a maximum distance). From then, centroids on the following slices are either matched to an existing fiber, to which they are added, or become new fibers themselves, as depicted in Figure 5.6c.

Blind stitching

Due to missing and false centroid detections, the centroid chains are often interrupted segments from a single true fiber. Using only the start- and end-points for each chain, a similar procedure is done: a 3-dimensional KDTree is constructed for the start- and end-points. Both trees are queried with the other set of points, and matching nearest neighbors are found. Three checks are made before selecting fibers for combination: these matches need

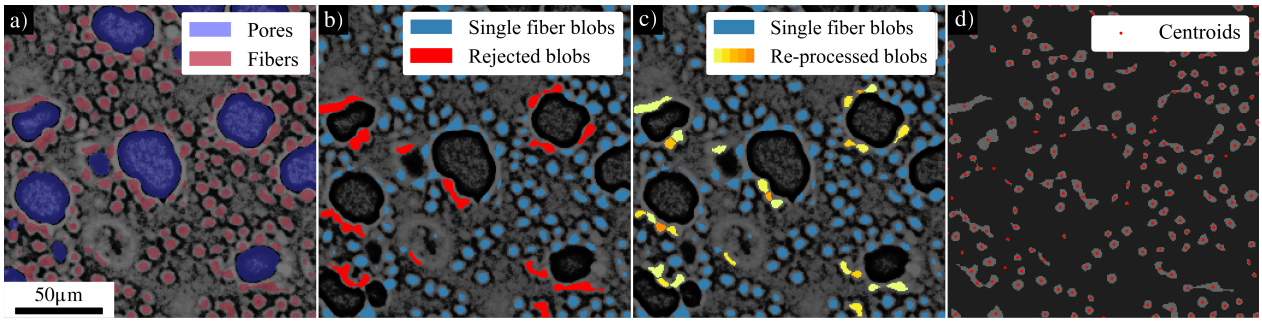

Figure 5.5 Initial labelling and centroid extraction in data from a PEEK 40 wt.% CF specimen. a) Labelling of pores by Canny edge detection and fiber blobs with InSegt. b) Fiber-containing blobs failing convexity test flagged for reprocessing. c) Output of recursive watershed transform on non-convex blobs. d) Extraction of centroids for each fiber blob.

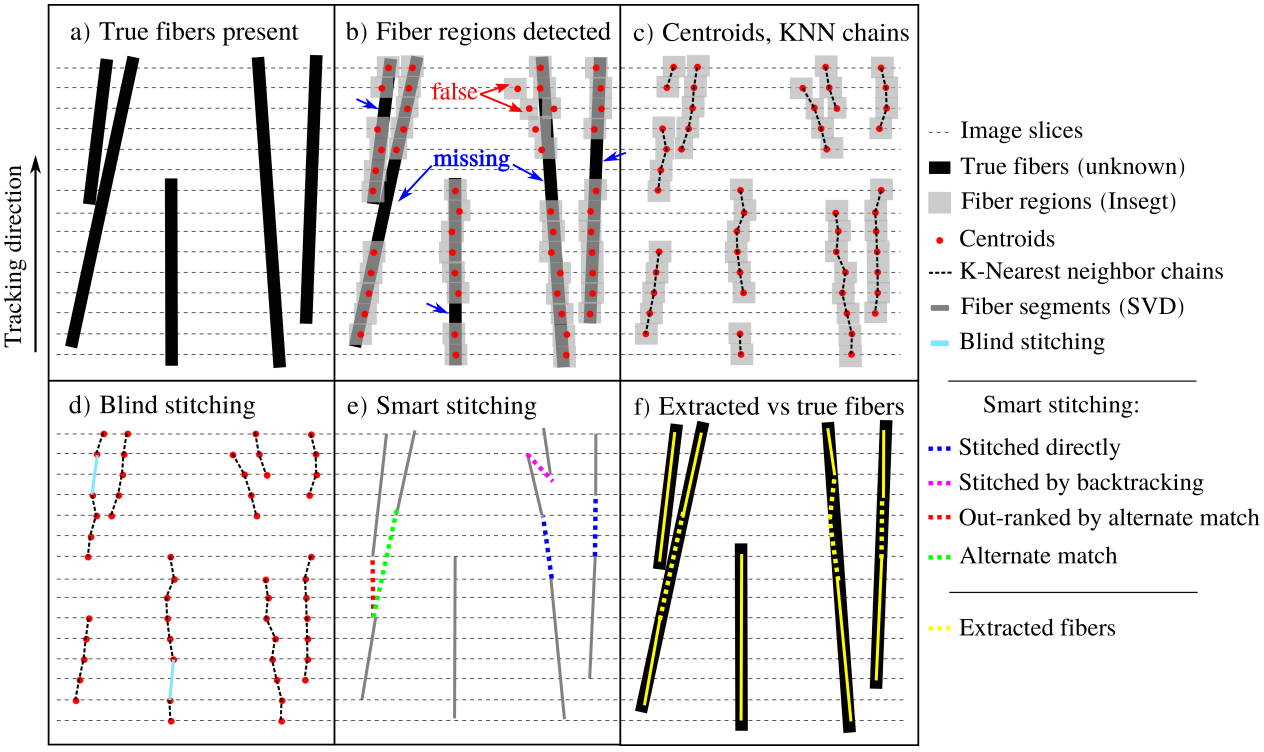

Figure 5.6 Schematic representation of fiber tracking: a) true fibers in the data (unknown). b) Detections by InSegt, with missing and false regions. c) Extracted centroids, linked in chains of nearest neighbors. d) Blind stitching: bridging small gaps of few missing centroids (light blue). e) Fiber segments that are sufficiently aligned in space are combined (blue). Segments that overlap can also be stitched, if backtracking length is below a maximum distance (shown in pink). When more than one stitching candidate is found, better alignment between longer fibers is favored (in green) over first match (in red). f) Extracted fibers overlaid on true (unknown) fibers in data.

be below a prescribed distance, set empirically to 2.5 fiber diameters for CF (or 20 μm) in the stitching direction, and 1 diameter (7.5 μm) in the transverse direction, as well as to not allow backtracking: the end-point of the lowest fiber must be lower in the z direction than the start-point of the higher one. The distance criteria are taken relative to the fiber diameter, which can be measured visually if not known for a particular material. These values allows for some imprecision in the centroid position relative to the true fiber center, without allowing a match to a different fiber that is neighboring the main one. The matching pairs that meet these criteria are combined, linking the corresponding centroid chains. As we can see in Figure (5.6)d-e, for each centroid chain a line segment is obtained that represents its main orientation and length, by the singular value decomposition (SVD) method (numpy.linalg.svd function).

The limitations of the "blind" stitching method are that if a long gap is present in the data for a particular fiber, there isn't enough information to ascertain that the detected segments are really part of the same fiber, or if there are two distinct fibers that are somewhat aligned. Large gaps attributable to many missing centroids are likely to occur in two contexts: in the vicinity of pores, and when fibers that have strong inclination (>45°) relative to the main direction, with an elongated cross-section. Both of these effects lead to interruptions in fiber tracking. With blind stitching alone, an underestimation of long fibers would occur, and since longer fibers contribute the majority of the mechanical load transfer, they are quite significant, especially for those at a strong inclination. To circumvent this limitation, the following method is employed.

Smart stitching

For each fiber segment (shown in grey in Figure 5.6e, two six-dimensional vectors are constructed (one for each end-point): the 3 coordinates of the point, and the 3 components of its normalized orientation vector. Then, a 6-D KDTree is constructed for the end (topmost) points vectors, and the start (lowest) point vectors are the query points. This way, as shown in blue in Figure 5.6e, we simultaneously find the pairs of objects that are closest both in terminal point distance and in terms of relative angle. Here it is possible and desirable to allow the stitching of segments that exhibit backtracking: segments belonging to the same fiber overlap each other quite often, due to the presence of erroneous centroids along the path of the fiber. As shown in purple in Figure 5.6e, allowing the stitching of fiber segments that overlap up to a maximum prescribed distance can be done reliably by assuring that both the relative angle and the start-to-end transverse distance (in the plane normal to the main direction) are sufficiently small.

As shown in red in Figure 5.6e, sometimes a match is made first which satisfies requirements in distance and relative angle, but an alternate match (in green) is also possible, perhaps further away, but with a more perfect alignment. When instances of this scenario were encountered in the real data, predominantly the offending candidate was a short segment, in the vicinity of the endpoint of the main fiber. To avoid these false matches, a ranking function was devised that favors stitches between longer segments (the orientation vector has more statistically significance for a higher centroids count) without deteriorating the relative angle by more than a prescribed value. This way, from all possible candidate matches for a particular segment, the ones between longer segments at acceptable relative inclination were prioritized.

By checking not only the endpoint distance but also relative angle, the distance criteria can be set larger than for the "blind" stitching step, without risking the stitching of non-related fiber segments. Once all segments to be stitched have been identified, two additional checks are made: in the gap between the endpoints that would be connected by the stitching, new centroids are interpolated at each of the z coordinates corresponding to an image slice. Above a certain distance, to avoid connecting fibers which truly aren't related, a majority of those new centroids must be in a region which was labelled as "fiber" by the InSegt tool (rather than "pore"). Secondly, none of the new centroids can be at a distance of less than one fiber diameter from an existing fiber, as they would otherwise physically overlap with the existing fiber. If both tests are passed, stitching is allowed and the interpolated centroids are inserted in the gap between segments. Once all the stitching steps are complete, we update the fiber line segments to account for the presence of partial segments and interpolated centroids.

The fiber objects that have a length below a prescribed minimum are marked as "rejected". Many false positives occur at very short fiber lengths, when a few non-related centroids are connected, but do not represent a real fiber in the data. A length of 1 fiber diameter is chosen as the minimum permissible length, and fibers shorter that that are marked as "rejected". Since the mechanical behavior will be determined mainly by longer fibers, missing a few real fibers at such short length is considered acceptable, so long as the fiber filling fraction remains close to the known value for the material in question. Fibers with strong inclination ($> 55°$ from tracking direction) are also rejected, as they will be more accurately tracked along the direction with which they are most aligned with. (A vector $[1, 1, 1]^T$ forms an angle of $54.7°$ with any of the reference axes, so a larger angle indicates better alignment with another axis). By performing the entire centroid detection and tracking procedure from the 3 reference directions (x, y, z), all possible inclinations are thus captured.

5.4.6 Assigning voxels to fibers

To reconstruct the fiber bodies from the identified centroid chains, we link voxels in the initial labelling to each of them.

For the majority of voxels in the watershed output, assigning a fiber ID number is immediate, as the tracked centroid was obtained from these voxels. However, in the gaps between stitched fiber segments, the centroids created by interpolation are not related to any existing voxels. For those cases, the first step is to check whether the interpolated centroids are squarely inside a closed contour that is not already matched to another fiber, in which case all those voxels are assigned to its fiber. If more than one centroid (either interpolated or present in the initial extraction) are present in the same closed contour, the watershed transform is used to assign the voxels to the closest centroid, assuring the subdivided voxel groups all lie in a single connex region. Remains the case where interpolated centroids lie in regions where no voxels are labelled as fiber. To create this labelling, the following method is used.

5.4.7 Volumetric post-processing: gap filling and artifact removal

As shown in Figure 5.7a, for each fiber identified in tracking, a sub-volume is created which is only large enough to contain the voxels belonging to that fiber. A tube-like structuring element is created by stacking 2D circles (of the same diameter as a fiber) at the same angle and direction as this fiber's orientation vector, for a total height of a few voxels longer than the largest gap created by stitching (or a default value for unstitched fibers). The morphological operation of closing (scipy.ndimage.binary_closing function) is applied using this structuring element. As shown in Figure 5.7b, this has two effects: it smooths the surface of the fiber, and it fills gaps in a manner that is inferred from existing geometry, rather than prescribed. This is preferable because some fibers have an oblong rather than a circular shape, which this method preserves. Also, strongly inclined fibers will have elongated cross-sections. The morphological operation of opening (scipy.ndimage.binary_opening) is used afterwards with a ball structuring element, with a diameter slighly under a fiber diameter. The effect of this is to remove the regions that are erroneously labelled as belonging to this fiber: just for like pores, these false detections will be thin, and are readily removed by opening. In Figure 5.7c, we see the topmost regions of the fiber after removal of such an erroneous shape (i.e., an artifact).

Making this operation on a subset of the entire volume is memory-efficient, and can be done in parallel. A last check is made when projecting it back into the large volume: newly identified voxels should not spill into regions already identified as another fiber, or a pore.

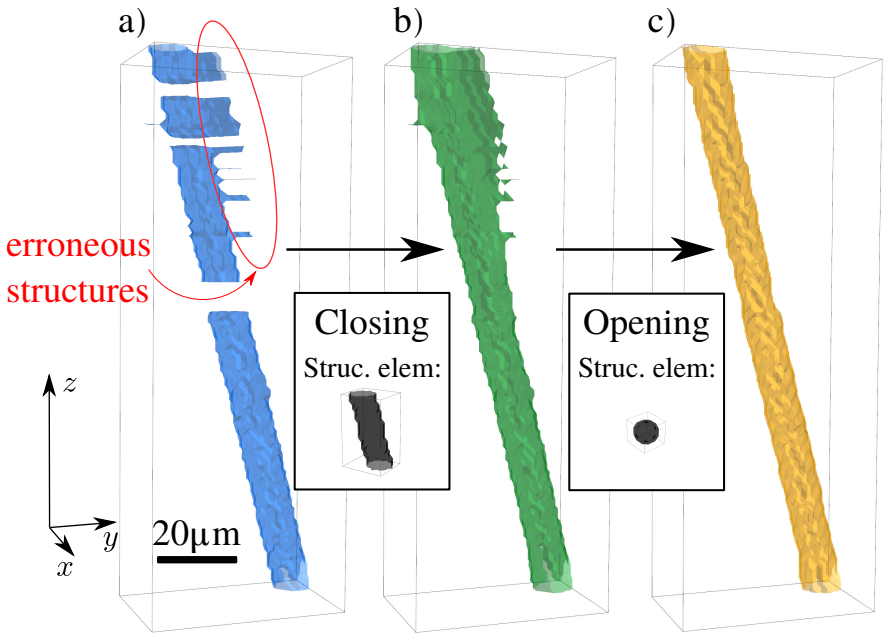

Figure 5.7 Example of post-processing on a single fiber object made up of 4 stitched segments, leaving three gaps (tracking performed along z). a) Fiber from previously labelled voxels, including erroneous structures. b) Output of morphological closing with inclined rod structuring element: gaps are filled, but erroneous regions are expanded. c) Output of morphological opening with ball structuring element: smoothing, removal of erroneous regions.

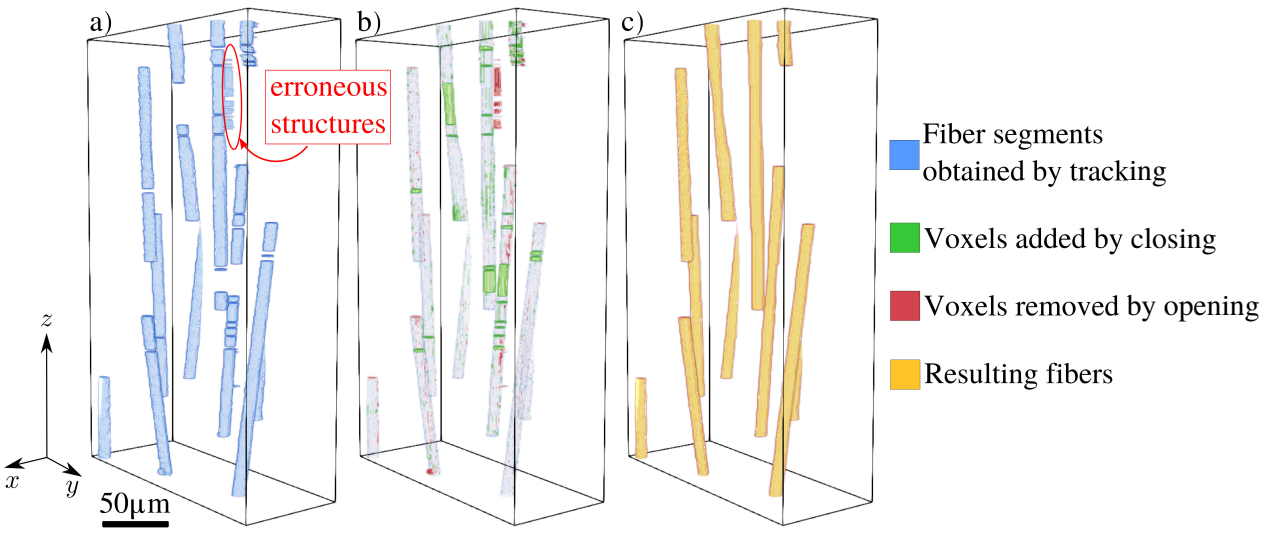

Figure 5.8 Post-processing applied to a larger region showing several distinct fiber objects. a) Fiber segments as obtained by assigning voxels to the tracking output, with several gaps. b) Morphological closing adds missing segments where interpolation has occurred, and opening removes a few erroneous structures. c) Resulting volume of fibers.

In Figure 5.8, we can see the effect of the morphological operations on several fibers at once, in a small region of interest. In Figure 5.8a) are presented the fibers as obtained by tracking and assignment of voxels. We can see interruptions of different sizes, as well as the same erroneous structures previously seen. In Figure 5.8b the effect of closing and opening are highlighted: closing fills in the gaps between interpolated segments, opening removes erroneous regions. The resulting fibers in Figure 5.8c are a much more reliable representation of those present in the data.

5.4.8 Combining fibers from all reference directions (x, y, z)

As strongly inclined fibers are more easily detected by slicing in the transverse plane (x and y directions), the entire segmentation procedure explained above is repeated twice more. Using the labelling obtained in the direction of main alignment (z), all voxels where fibers were successfully identified (and not rejected for being too short or too steep) are first removed from the pre-segmentation volume (substracted from the InSegt output). This way, only new fibers can be found.

After the entire procedure is performed for both x and y directions, the fibers found need to be projected onto the original frame orientation. The most problematic cases are long fibers which are inclined by close to 45° to more than one of the reference directions. This results in partial capture of segments from potentially all three reference frames, which for the x and y directions can potentially interfere with each other. Two more steps are taken to correct these problems. First, colliding voxels are identified and if their corresponding fiber objects are sufficiently aligned, the objects are combined into a single fiber. Then the smart stitching method is called on all the fibers from all the permutations, with the provision that only fibers from two different permutations are eligible to be stitched together. This allows the reconstruction of fiber whose segments were obtained from more than one reference direction. Finally, the volumetric post-processing method is applied again on the fibers that have been combined or stitched in this last step, yielding the final segmentation of fibers present in the data.

5.5 Validation

The segmentation procedure was performed on 2 distinct datasets, whose analysis were previously published by Czabaj [76,143] and Creveling [77], and kindly made available to us. By performing the segmentation on the same input data, we can compare our tracking results to theirs, and verify the degree of accuracy of OpenFiberSeg for the type of materials on which

these scans were performed. The code from these two projects not being public, only the results in the original publications can be discussed.

5.5.1 Data from Czabaj et al, 2014

This dataset is obtained from a specimen of AS4/3501–6 graphite/epoxy unidirectional composite, formed into a thin "matchstick" specimen. The resulting tomograph is presented in Figure 5.9a. The authors of this work used template matching and a sophisticated method involving the Kalman filter and track stitching to track fibers across the volume, and preventing fiber inter-penetration [76, 143].

As can be seen in Figure 5.9b, the shape of the histograms of angles measured with our tool vs that in [76] are quite close, especially when considering the position of the 5^{th}, 25^{th}, 50^{th}, 75^{th} and 95^{th} percentiles, which are all within less than 0.5° between our results and theirs. While the height of the central peak is 9% higher for our method when compared to theirs, several reasons can account for this. When obtaining fiber centroids at each slice, we compute the moments of the fiber blobs, whereas their methods finds the best match for a pre-defined circular template: some variability in centroid positions is likely to occur between the two methods. Secondly, when attempting to reproduce their results, we needed to truncate the dataset as they did, leaving 508 out of 629 fibers, without knowing the exact coordinates. Also, while all fibers presented are found automatically in OpenFiberSeg, in the original paper manual segmentation of 4 missed fibers, and removal of 3 false one was done. They report a processing time of 2 hours on a CPU capable of 4 simultaneous threads. Our method also executes in 2 hours when using 4 threads.

5.5.2 Data from Creveling et al. 2019

This data was obtained on a IM7/8552 carbon/epoxy laminate, from which a 1 mm^3 specimen was extracted. A high-resolution micro-CT scan was performed, yielding a voxels size of 0.41 μm. As shown in Figure 5.10a, this specimen has 3 plies, with fibers oriented at +45°, -60°, and +60°, as measured from the vertical direction. In the original paper, the fibers were extracted using template matching and a more elaborate method of stitching. As can be seen in Figure 5.10b, there is only small deviation between the outputs of our method and theirs, especially when considering the position of the percentiles for each peak. The remaining difference in peak heights can probably be explained by the different method of obtaining centroids, i.e. template matching vs the direct calculation of center of mass of irregularly shaped blobs, used in out method.

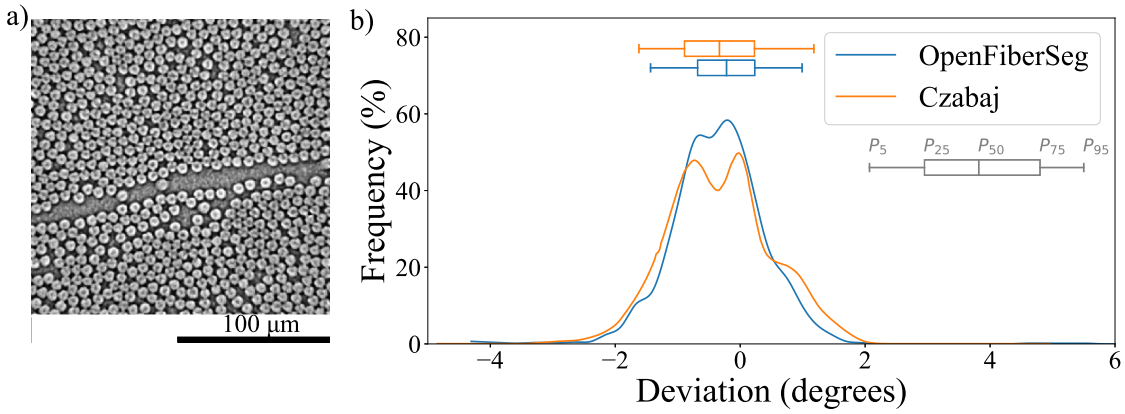

Figure 5.9 Extraction performed on original micro-CT scan of unidirectional graphite/epoxy composite. a) Sample data slice, reproduced with authorization [76]. b) Probability density function of fiber deviation from main direction, as reported by original authors, and as measured with OpenFiberSeg. The box and whisker plots for each peak represent the 5$^{\text{th}}$, 25$^{\text{th}}$, 50$^{\text{th}}$, 75$^{\text{th}}$ and 95$^{\text{th}}$ percentiles for both segmentation methods, which are all within 0.5°, indicating good agreement between the methods.

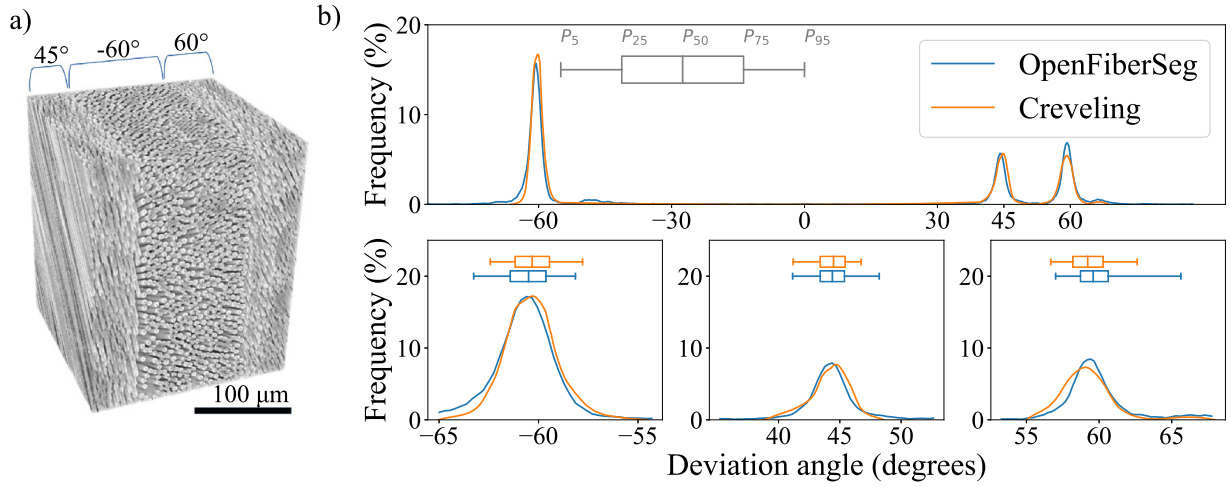

Figure 5.10 Extraction performed on micro-CT scan of carbon/epoxy laminate. a) rendering of original data, showing the main angles of the three layers, relative to the vertical direction [77]. Reproduced with authorization. b) Probability density function of fiber deviation from main direction, as reported in [77], and as measured with OpenFiberSeg. The bottom portion shows zoom around the three main peaks, with generally good agreement between the output of the two methods. The box and whisker plots for each peak represent the 5$^{\text{th}}$, 25$^{\text{th}}$, 50$^{\text{th}}$, 75$^{\text{th}}$ and 95$^{\text{th}}$ percentiles for both segmentation methods, when grouping the data around the three main peaks.

From these two analyses, we can assert that OpenFiberSeg of segmentation yields very similar results to state-of-the art tools, at least when it comes to the tracking of fibers in bi-phasic, continuous fiber reinforced polymers. As we will now show, OpenFiberSeg can handle a much larger number of fibers, with more randomness in orientation (hence more contact between fibers) and to produce accurate results from partial detections, amidst porosity.

5.6 Results

5.6.1 Predicting fiber volume fraction and material density

For SFRP with several tens of thousands of individual fibers, getting a clear appreciation of the quality of the segmentation is not straightforward. One way is using the segmentation data to predict properties such as the specimen density or the fiber volume fraction c_f^v and compare them to values measured experimentally. The c_f^v is obtained directly from segmentation data, and can be calculated experimentally from the knowledge of the mass fractions used at the specimen preparation step, fiber and matrix density (from supplier data), and the pore volume fraction c_p^v measured by OpenFiberSeg. To independently validate that the segmentation tool produces the correct assessment of porosity, the total density of each SFRP specimen is calculated, and compared to the measured experimental value of density. Detailed calculations are presented in Supplementary Materials (Appendix B).

As shown in Figure 5.11a, there is generally good agreements between fiber volume fractions as predicted from the segmentation output and those obtained by the mass fractions. The results from the segmentation output are overestimated by at most 4% for some filling fractions. This variation can be explained considering how different are the morphologies from low to high filling fractions (with porosity ranging from 10% to 40%), and the fact that no tweaking of parameters is done to process them.

As shown in Figure 5.11b, the two methods of determining density are in high agreement (mean error of <2%), which would only happen if all the volume fractions were correctly estimated, particularly c_p^v, which has a larger effect on density, as pores occupy space but contribute no mass. Any remaining deviation between the two density measurements can be explained by sampling error: the tomographs encompass a volume of 1 mm^3, while the specimen used for the pycnometer measurement is ~200× larger. The scanned region might possibly have a local phase distributions slightly different from the average. The much higher porosity (39%) of the 10 wt.% CF specimen explains the large departure of it's density from the general trend. It can also explain the largest discrepancy between both methods, at 4.9% error: possibly some helium leaks into the unusually large pores, leading to an

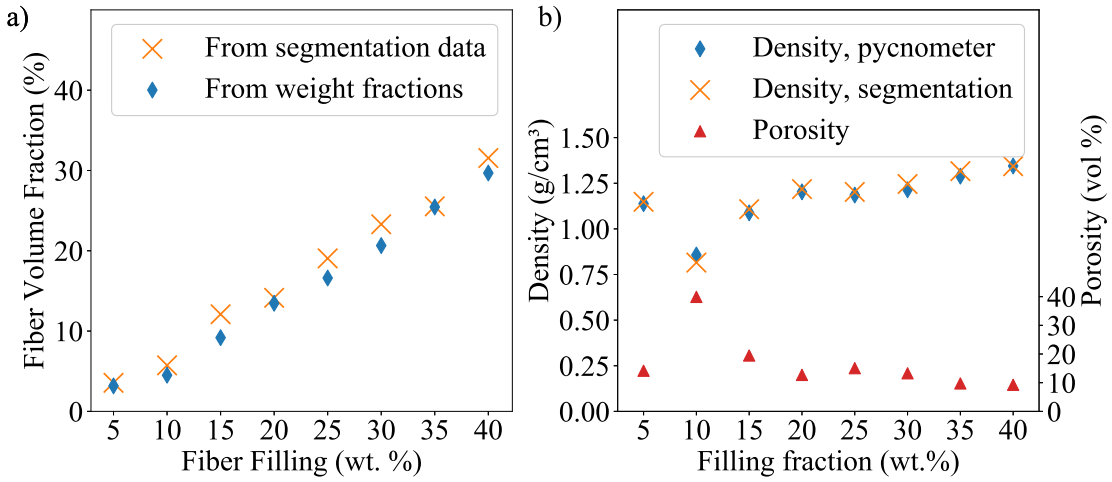

Figure 5.11 Experimental validation: a) Comparison of fiber volume fraction obtained directly from the segmentation output, vs. calculated from the known densities of matrix and reinforcement materials, as a function of fiber filling fraction. The difference between the two is at most 4% (meaning if one method gives 10%, the other can give at most 14%). b) Comparison of specimen density, as calculated from the segmentation output and the density measured directly with the help of a gas pycnometer. Very high agreement (mean error <2%) between the two indicates the proportions of matrix, fiber and porosity as predicted by the segmentation are a reliable indicator of the proportions in the real material.

overestimation of density from the instrument. Ning *et al.* also reported an uncommonly high value of porosity for 10 wt.% CF filled acrylonitrile butadiene styrene (ABS) (9.04% whereas specimen with 0-15% filling averaged at 2%) [128].

It remains possible however that the volume fractions are accurate on average, but only due to the number of missed fiber detections being cancelled by false detections. To ascertain how reliable the output at the pixel level, the following method is used. On a slice-by-slice basis, we can superimpose the segmentation output onto the raw data. This visualization is presented in Figure 5.12 for two different material composition: in a) PEEK with 15 wt.% CF and in b) PEEK with 40 wt.% CF. A different colormap was used to show which reference direction each fiber was detected from. For both these materials, it is clearly visible that the vast majority of fibers present are identified, with only a few missed fibers or false detections. Also, nearly full cross-section of each fiber is captured rather than a portion of it. And while there are more false detections in the in-plane directions (as shown in Figure 5.12d), the fibers with strong inclination (near-tangent to the $x - y$ plane) are also successfully captured. To assess the segmentation precision, a slice-by-slice analysis is presented in Video 5.13 for the specimen with 25 wt.% CF. For each studied slice, we compared the fibers detected by OpenFiberSeg against the original data, and labelled false fibers or single true

fibers fragmented into segments as false positives (FP) and missed fibers or separate true fibers combined into one as false negative (FN). This annotation is performed at 7 separate locations (2D slices) in the data, encompassing 3945 individual fiber detections. Precision for this specimen (defined as the voxel ratio of TP/(TP+FP)) is computed to 95.6%, with rates of FP of 4.4% and FN of 1.6% (average across all filling ratios: precision: 93.1%, FP: 6.9%, FN: 1.5%). The majority of FP are in the vicinity of pores, and are for short fibers (< 20 μm). Overall, there is <1% occurence of fiber fragmentation or false combination.

5.6.2 Discussion

For each material specimen, we obtain a set of individual fibers, complete with their position in space, orientation vector and length. In order to study the correlated distribution of lengths and orientations, and to compare them across material composition, we produce the following visualization. In Figure 5.14, a 2D-histogram is presented for the fibers present in a PEEK specimen with 40 wt.% CF. The lengths and deviation angle are both discretized into 256 bins, and the color of each pixel represents the density (amount/bin) for that combination of length and deviation angle. A logarithmic scale is used for the colormap, so that both high and low density regions are appreciable. Single-variable histograms for lengths and deviation angle are also shown, making explicit the relation between bin count and the pixel color mapping. The correlated histogram allows us to assert the inverse relation between fiber length and deviation: longer fibers tend to be better aligned, and shorter fibers can deviate more (although the bulk of the distribution is always at <30°). The extent of shear-induced alignment during the extrusion process is thus revealed, which could not have been inferred from the single-variable histograms alone.

The same visualization allows us to compare the specimen between them: in Figure 5.15, all 8 specimen types are juxtaposed, in order of increasing filling ratio. Fiber counts and processing times on a workstation with an Intel™ i9-10940X CPU, and 64GB of RAM are presented for each dataset. Here we can see that the shear-induced alignment is present even at low fiber concentrations. This indicates it is attributable to fibers aligning with the flow direction, more than interactions between fibers which are less frequent at low filling fraction. Also, for higher ratios, the most noticeable increase (regions in red) is in the < 100 μm, <30° range, suggesting more fiber breakage at these ratios, as the proportion of fibers 100 μm and longer are essentially the same for 30 wt.% CF and above. The unusually large proportion of short fibers at large deviations for the 40 wt.% CF also suggest more breakage for higher filling ratios. Additionally, the lower fiber count at 35 wt.% compared to 30 wt.% suggests there is less fiber breakage at this filling ratio.

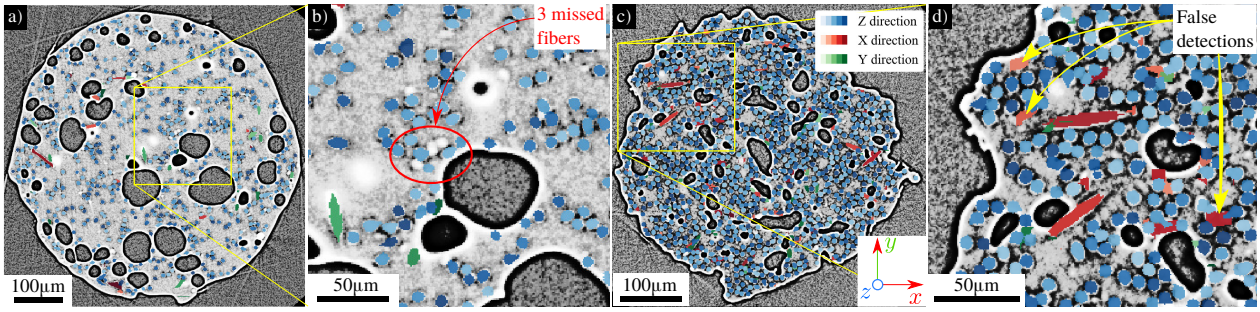

Figure 5.12 Output of segmentation for 2 material compositions: a) PEEK with 15 wt.% CF and c) with 40 wt.% CF. Different color maps are used to represent in which reference direction the fiber was detected. The majority of fibers are detected in the out-of-place (z direction), and some in the in-plane directions x and y. In b), a closer look shows examples of missed detections, and in d), we can observe that more false detections are present in the x direction, but the strongly inclined fibers are also successfully captured.

The degree to which shear-induced alignment is more pronounced for longer fibers is illustrated in Figure 5.16. Here, for each dataset, only the fibers of a certain length are selected (centered at 20 and 100 μm) and the histograms of the deviation angles are compared. Clearly, the general tendency is that fibers tend to align with the flow direction (the bulk of the distribution is always at $>30°$) but this phenomenon is markedly more prominent as longer fibers are considered. One dataset (10 wt.% CF) doesn't follow this trend, which can be explained by inordinately large porosity for this specimen, probably changing the flow characteristics. The highest peak for long (100 μm) fibers being for the 35 wt.% also indicates less fiber breakage at this filling ratio.

5.7 Conclusion

In this work, we presented OpenFiberSeg, a tool for fiber tracking and segmentation of individual fibers in tomographic scans of SFRPs. Combining elements from several techniques, we propose original improvements such as retroactive correction of labelling based on fiber reconstruction, as well as a detailed heuristic for stitching fibers from partially detected segments. The method is shown to be robust and satisfactorily reproduces the results of 2 independent studies on continuous fiber reinforced composites. When applied to FFF SFRP with non-negligible porosity, it can be used to corroborate the experimental measurement of porosity and fiber filling fraction, and produce a detailed portrait of the correlated fiber lengths and orientation distributions for vastly dissimilar specimen composition (5-40 wt.% filling ratio), yielding an average segmentation precision of 93.1% on a per-voxel basis. This tool can serve as a central characterization and diagnostic method for the development of

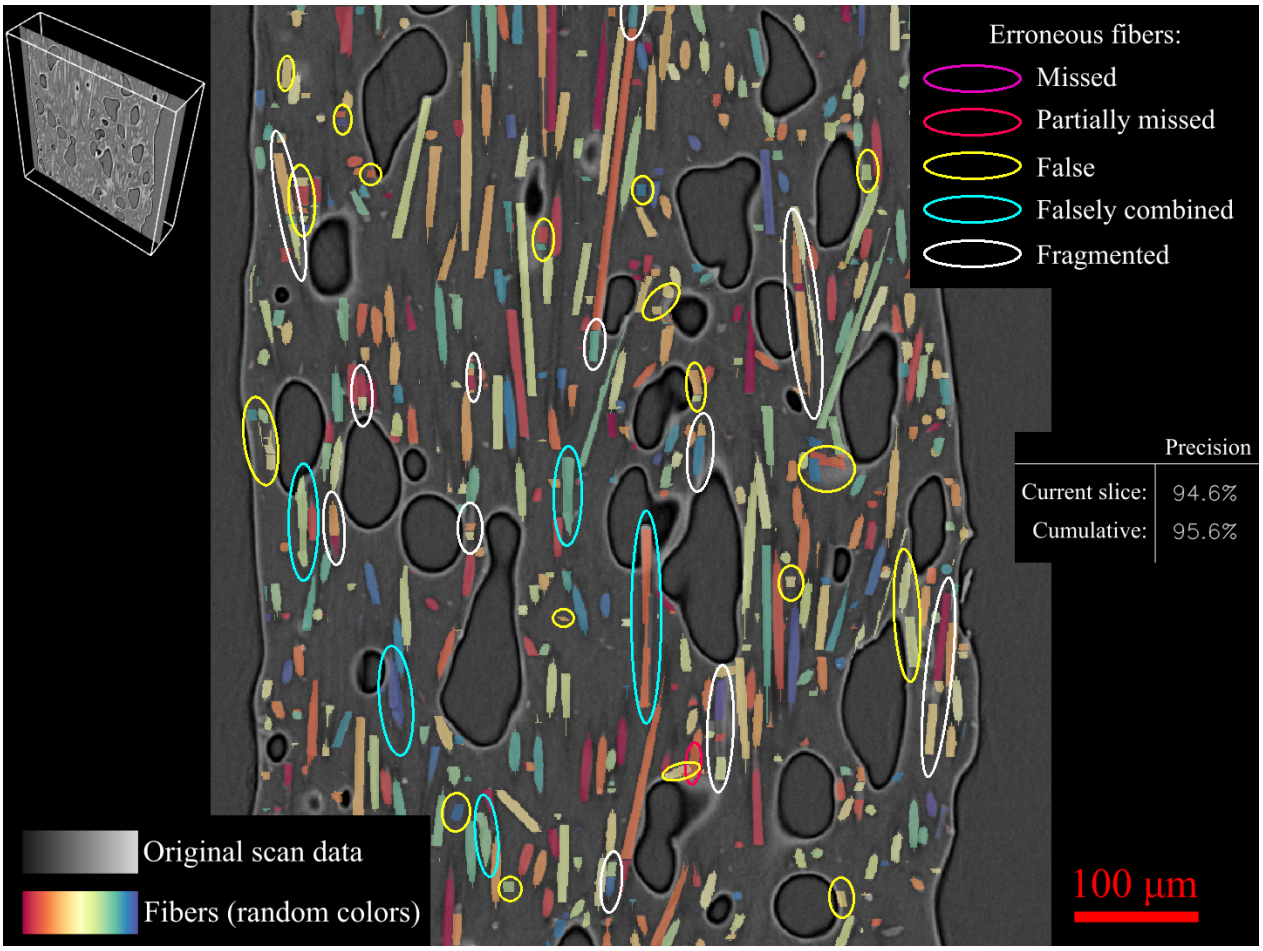

Figure 5.13 Slice-by-slice analysis of segmentation accuracy: PEEK 25 wt.% CF. The porosity and perimeter detection are shown to be nearly perfect. The fiber extraction precision is measured at 95.6% for this specimen. Animated sweep of fibers colorized first by length and then deviation highlight the trend by which longer fibers are better aligned and vice-versa. Link to video.

FFF SFRP materials and processes. However, it is not designed for fibers with significant curvature, as fibers are represented by line segments, and up to 1% of fibers can be fragmented or combined with another with which they are well aligned and in close proximity. By divulging the source code, this project can reduce development time for other research groups, and be applied to a variety of use cases, such as other types of SFRP, reinforced ceramics, concrete, etc. The precise knowledge of reinforcement and pore size and position will be invaluable for the development of models involving elasticity, viscoelasticity, fracture dynamics, and transport phenomena.

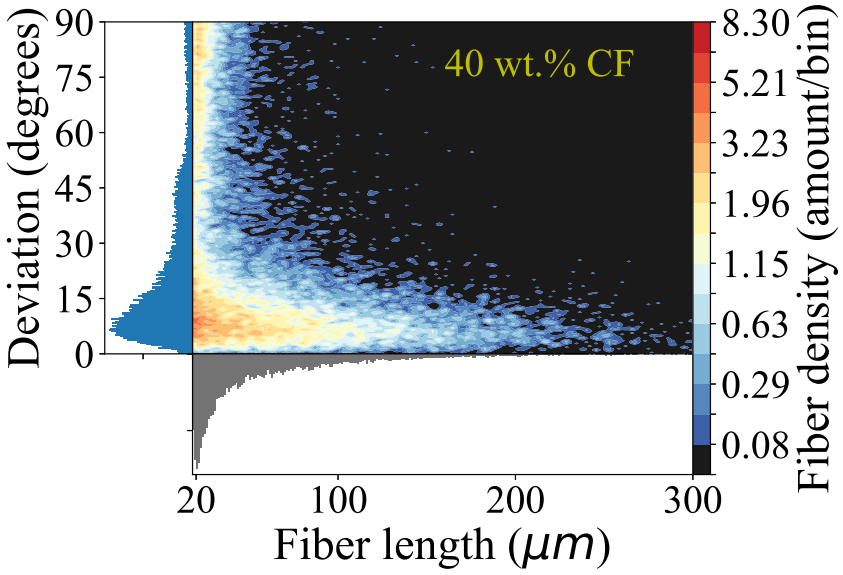

Figure 5.14 2D histogram representation of the correlated lengths and angle of deviation from tracking direction (z) for fibers present in a PEEK specimen with 40 wt.% CF filling ratio. Single-variable histograms are juxtaposed on the left-hand and lower side, to highlight the relationship between the counts for each variable and the correlated density values.

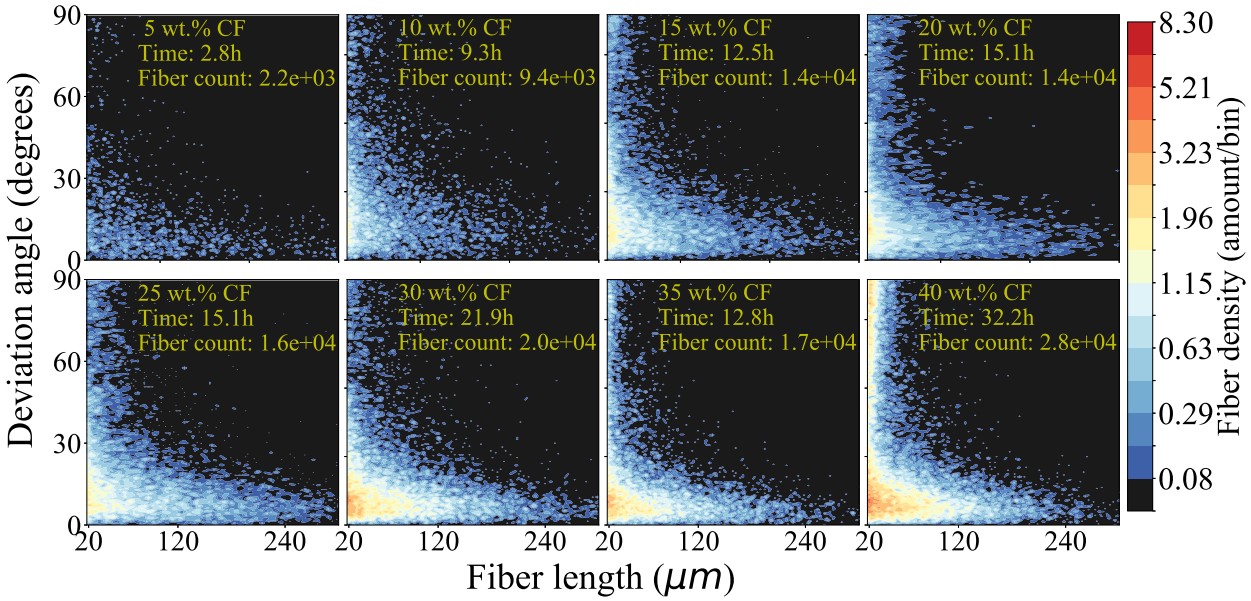

Figure 5.15 Correlated lengths and deviation histograms for PEEK SFRP with filling ratios of 5-40 wt.% CF. For all levels of filling, there exists an inverse correlation between fiber length and deviation: longer fibers will be more aligned with the extrusion direction. Processing time is given, along with fiber count for each scan.

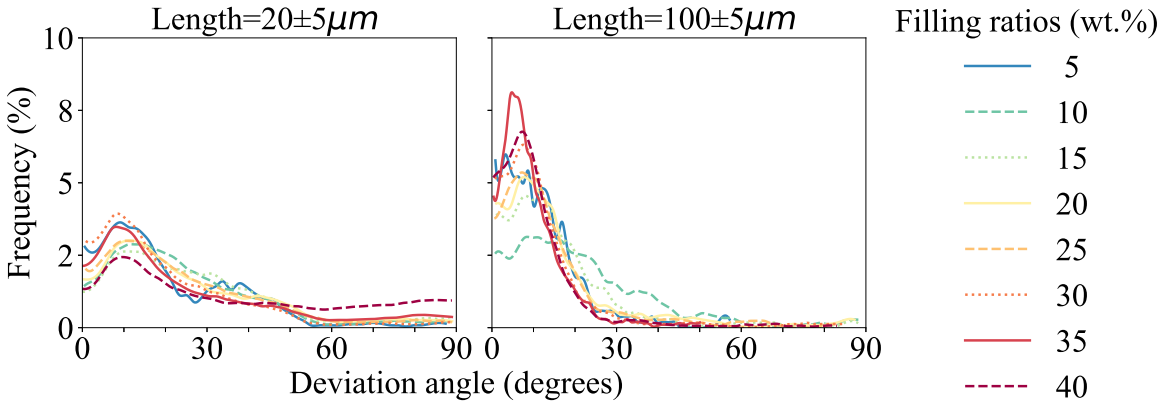

Figure 5.16 Histograms of deviation angles for 2 different ranges of fiber lengths, centered at 20 and 100 μm, by specimen filling fraction. Shear-induced alignment is present for all specimen, as evidenced by the bulk of the distribution being below 30° for specimen. This effect is more pronounced for longer fibers for all filling ratios, except 10 wt.%, which can be explained by unusually high porosity.

5.8 Source code and data repository

The full source code repository along with original tomographic data used in this work are available at `https://github.com/lm2-poly/OpenFiberSeg`.

Acknowledgements

This research project is made possible by financial and technical support from Safran S.A. (FACMO Research Chair), as well as financial support from the Natural Sciences and Engineering Research Council of Canada (Alexander Graham Bell Canada Graduate Scholarship program, and the Collaborative Research and Development program, grant no CRDPJ514761). Computational resources were made available by Calcul Québec (`www.calculquebec.ca`) and Compute Canada (`www.computecanada.ca`). Research data used for validating the accuracy of our method was shared with us by Pr. Czabaj at the University of Utah.

CHAPTER 6 ARTICLE 2: Multiscale Fast Fourier Transform homogenization of additively manufactured fiber reinforced composites from component-wise description of morphology

Sosa-Rey, F., Vella, C., Lingua, L., Pierre, J., Piccirelli, N., Therriault, D. & Lévesque, M. Submitted to *Composites Science and Technology* on January 19th 2023.

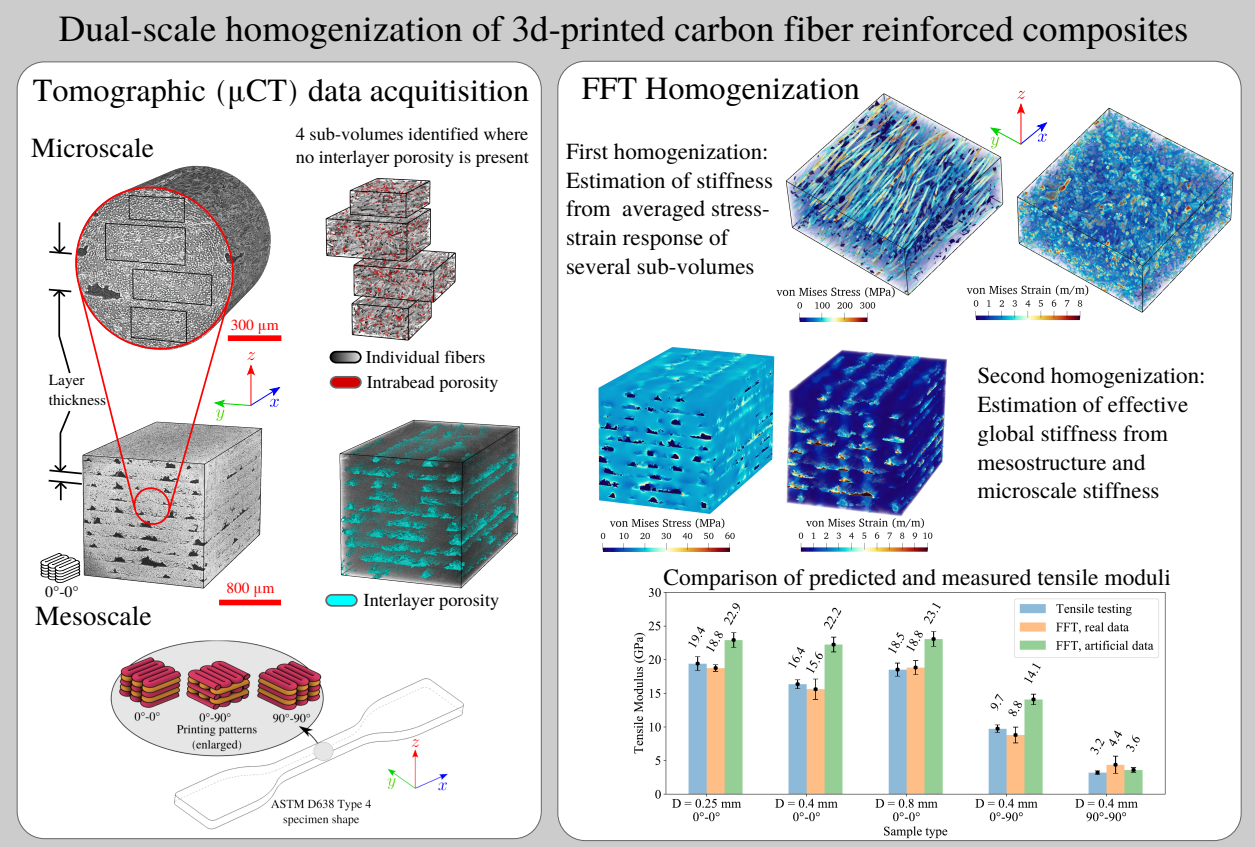

Figure 6.1 Graphical Abstract: Multiscale homogenization

6.1 Abstract

The process-structure-property relationship in short-fiber reinforced composites made in Fused Filament Fabrication (FFF) remains inadequately understood, much trial-and-error and extensive testing is required to use these materials for load-bearing applications. As a consequence, the largely empirical design process has hindered the adoption of this technology, notably due to the lack of reliable structural analysis capability. In order to surpass the

limitations of mechanical property prediction using simplified artificial microstructures, this work demonstrates the decisive advantage of using geometries obtained directly from imaging of printed specimen instead. The analysis of μCT images is performed via a purpose-built extraction tool called OpenFiberSeg, yielding profound insight into the process-structure relation. The use of real microstructures is shown to considerably improve the mechanical behavior prediction capability via dual-scale FFT-based homogenization, bringing relative error margins below 5%, for full anisotropic description. It also becomes possible to investigate the effect of processing parameters such as nozzle diameter and printing pattern on morphological properties and on mechanical behavior, revealing the magnitude of the spatial variation of local properties. The combination of experimental and simulation enables insight that is not accessible to either alone. Original imaging data and source code are made publicly available.

6.2 Introduction

Fused filament fabrication (FFF) is an additive manufacturing (AM) method by which complex parts are built layer-by-layer by the deposition of semi-molten polymer filaments through numerical control. As opposed to injection or compression molding, the process requires no molds or tooling, which leads to fewer design restrictions, low cost per unit in small batches, customizability and simplicity of manufacturing [4, 11, 15, 62]. By employing short fiber reinforced polymer (SFRPs) filaments made from high-performance polymers such as poly ether-ether-ketone (PEEK) mixed with short carbon fibers (CFs), parts made through FFF exhibit weight-specific properties giving them the potential of replacing metallic components in fields like the aerospace or automotive industries [15, 51, 62]. In addition, by controlling the orientation of reinforcements, the mechanical, thermal and electrical properties of parts can be engineered for specific purposes [11, 62, 67]. However, before FFF parts can be used for load-bearing applications, structural analysis tools must be significantly improved [11, 61, 65]. The lack of understanding of the relation between processing parameters and mechanical properties makes existing tools insufficiently reliable [61, 62, 154], rendering the design process largely empirical [11, 155]. The main problem resides in the fact that morphological characteristics are influenced first by the properties of the base materials and the processing parameters [13, 50, 62, 63], which lead to localized gradients in material properties and contribute to suboptimal part consistency [103, 156–158]. Fiber length and orientation distributions, local fiber volume fractions and the formation of porosity are all affected by processing conditions, and exhibit local variation within parts [50, 63–67,]. In addition, parts made by FFF exhibit structural features at several distinct length scales [61, 62],

some of which are absent in molded parts [13]. Understanding the link between these microstructural features and the resulting mechanical properties is a crucial, and yet-unsolved, challenge [11, 64, 148, 154, 155, 159].

Generally, three distinct scales are relevant in the context of SFRPs manufactured by FFF. The microscale is where the constituents (matrix, fibers, intra-bead voids) are explicitly considered [61, 63]. Then, the part geometry scale, or macroscale, is always present and is the main focus of mechanical design. Lastly, the FFF process imparts an intermediate, or mesoscale, level of structuring that is determined by the printing infill pattern selected, and the characteristics of the exterior part shell. Even with the simplest of infill patterns, i.e., all passes aligned with each other, and 100% volume occupation, each bead being round at the nozzle tip and forced into a rectangular section leaves voids at the corner of this rectangle, which form a periodic array of neatly aligned cavities throughout the part [62, 148, 160], contributing to part anisotropy [12, 13, 161, 162]. All these scales must be encompassed by an attempt to account for the morphology-property relation of AM SFRPs [61].

6.3 Background

6.3.1 Morphological characterization: fiber properties

Predicting the mechanical stiffness of SFRPs requires a description of their microstructure, often generated from statistical observations of real materials. Fiber length and orientation distributions are commonly obtained as follows. The elliptical cross-section of individual fibers can be obtained from scanning electron microscopy (SEM) images of polished samples. The orientation of individual fibers in three-dimensional (3D) space are computed by measuring the angle those ellipses make with the printing direction and their ratio of minor to major axis [18, 63, 68]. Fiber lengths can be measured under optical microscopy or SEM after they are separated from the matrix, either though pyrolysis [4, 63] or dissolution [18]. However, those procedures are time-consuming and suffer from repeatability issues [68], and accuracy is reduced for fibers almost perpendicular to the image plane [163]. Further, SEM images are two-dimensional (2D) rather than volumetric, and thus cannot account for property variation at different depths in the material. In addition, the lengths and orientations aren't measured at once on the same fibers, therefore the SEM images method does not produce a full-field description including positions in 3D space, and the correlation between length and orientation is unknown [68]. Some studies have measured this correlation, more so for carbon fibers than for glass fibers because of their higher average aspect ratio [63, 71, 164]. It is possible to obtain data at several depths, by repeatedly polishing the specimen to produce

a 3D rendering [68, 70], or use confocal microscopy to image beyond the surface [69].

These statistics can be used directly in analytical modelling [18, 64, 75, 165] or artificial geometries can be tailored to have similar average properties [4, 45, 63, 90, 104, 166]. These geometrical descriptions, or representative volume elements (RVEs), are a volume description of a sample of the microstructure which is small enough so modelling is achievable, but rich and complex enough to be representative of the variability of the real morphology (for strict definitions, see [99, 100]). The generation of such RVEs is complex and computationally costly, especially when large fiber aspect ratios and volume filling fractions v_f are required [4, 45, 63, 167]. As a consequence, the v_f considered only rarely reach 25% [104], whereas the v_f in SFRPs are commercially available at 30% and can reach as much as 40% [10, 164]. A commonly used method of microstructure generation is random sequential adsorption (RSA) [103–105, 168, 169], in which inclusions (fibers and/or pores) are seeded into a volume one at a time, checking for interference with existing inclusions, and randomly repositioned in case of interference, until the desired volume fraction is reached. Fiber segments that extend beyond volume boundaries are repeated on opposite faces of the volume, ensuring geometric periodicity [104, 167]. Notably for large aspect ratios, this method has been modified in several ways to enable higher volume fractions [63,105,154]. Other methods draw from molecular dynamics modeling, in which fibers have velocities and collide with each other while increasing in volume, until the desired v_f is reached [167,170,171]. A few studies attempted generating artificial microstructures with a specific set of orientation and lengths distributions, in addition to infill fractions. Tian et al. proposed a fiber growth method by which they were able to reach 25% of infill [103, 105], but only 19% was achieved with an aspect ratio of 10 [104]. Tang et al. achieved $v_f = 38\%$ at a mean aspect ratio of 15, but only for random orientations [154]. Using a modification of the RSA algorithm, they generated microstructures (including fibers and voids) in which fibers conformed to an orientation tensor obtained from a computed micro-tomography (μCT) scan of a real CF polyamide-12 (PA12) specimen. By generating RVEs with varying characteristics, they demonstrated that fiber alignment has a pronounced effect on tensile properties: an RVE with an average deviation of 18° shows a tensile modulus 2.67 larger than one with random orientation.

Nasirov et al. [4] used artificially generated RVEs with v_f up to 10% with a constant fiber length of 60 μm, with either uniform (random) orientations or aligned with the print direction. This microstructure was homogenized first, then embedded in a mesotructure of unidirectional or 0°-90° printing pattern (each layer has aligned beads, and subsequent layers are perpendicular to each other). For their mesostructure description, the authors considered *ideal* RVEs of beads modelled as rounded rectangles and *actual* RVEs, generated according to mesotructures observed in microscope images of physical specimens. They compared the

tensile moduli predicted by simulation to tensile testing measurements performed on carbon fiber reinforced polylactic acid (PLA), and encounter up to 20% error in unidirectional configuration, and up to 40% error for 0°-90°, using actual mesotructure RVEs (error was higher for ideal mesotructures). Another study from the same group considered aligned carbon fibers in polycarbonate (PC), and an ideal mesostructure, and reported 3.5% to 36% error in tensile modulus prediction [160]. These studies suggest the mesoscale porosity has a significant influence on effective properties, notably in making the material anisotropic, even when considering a pure (non-reinforced) isotropic polymer [13]. They also highlight the fact that real microstructures are not perfectly aligned, which has a decisive impact on effective properties. The non-uniform nature of real mesoscale porosity and the probable spatial variation in microscale properties can also cause discrepancies between those models and reality. The correlation between those attributes is also not accounted for. Those factors explain the rather large error encountered when comparing predictions to experimentally measured tensile moduli.

Volumetric characterization based on imaging methods such as μCT has also been reported for SFRPs [65, 66, 68, 76, 77, 85, 164]. Obtaining microstructures this way is technically challenging, requiring specialized post-processing that is computationally costly, but the microstructures produced are detailed and high fidelity to physical specimen can be achieved [68, 85, 164]. To the authors' knowledge, however, material data produced in this manner has only rarely [87] been utilized directly for mechanical properties prediction.

6.3.2 Effect of processing on microstructure

The rheological phenomena by which fiber alignment and lengths are affected by processing has been studied from modelling and expeximental perspectives. Using flow simulations, most studies [165, 172] utilize a so-called weakly coupled approach, in which fluid flow is solved first without considering the presence of fibers. Then, a fiber orientation tensor is inferred from flow profiles via the Advani and Tucker's equations [173]. The weakly coupled assumption is considered valid for $v_f < 10\%$, beyond which fiber-fiber and fiber-matrix interactions induce strong coupling. These models predict a change of fiber alignment at nozzle tip. Lewicki et al. [67] performed flow simulations using discretely modelled fibers and epoxy resin, with a $v_f = 6\%$ and aspect ratio of 50. They found that alignment is promoted during the extrusion phase, most notably close to the walls. Zhang et al. [155] performed a coupled fluids/discrete fiber modelling of extrusion in FFF to study the phenomena of nozzle clogging. They used their modelling and μCT data of CF filled PA6 to propose nozzle geometries and fiber characteristic to prevent nozzle clogging and promote fiber alignment.

On the experimental front, Chacón et al. [174] studied the effect of nozzle diameter on the tensile and strength properties of CF reinforced polyamide-6 (CF-PA6) specimens, along with porosity generation and geometric accuracy. They found that mechanical properties increased with a larger nozzle diameter, and that porosity is lowest for large diameter nozzles (measured up to 0.8 mm). However, to the author' knowledge, there hasn't been numerical prediction of mechanical properties taking nozzle diameter as a variable. Extrusion of SFRPs is known to cause fiber breakage, which attenuates their mechanical properties [50, 67, 175]. Limited data exists on this phenomenon, whether experimental [50, 164] or simulated [155], as the computational requirements to model this phenomenon would be prohibitive [11].

6.3.3 Mechanical property prediction: homogenization

Homogenization is the process of estimating the effective properties of a heterogeneous solid. There are generally two families of methods by which this process is carried out: mean-field and full-field methods. Mean-field, or analytical, methods use statistics about the size and orientation of inclusions along with their material properties to estimate those of the composite solid. Such methods include the Mori-Tanaka [176, 177], the self-consistent scheme [178], Lielen [179] and others, see [166]. These methods all assume ellipsoidal inclusion shapes and uniform spatial distribution of orientations, sizes and local density [180]. Further, the interaction between inclusions is possible only to a limited extent (usually for $v_f < 15\%$) [166, 180]. It has been suggested that these simplifications make mean-field methods unsuitable for modelling complex microstructures such as high-v_f SFRP [104], notably at high property contrasts and aspect ratios [166].

Recent progress in full-field or volumetric approaches have produced more accurate predictions [4, 45, 63, 166, 180], though at a much higher computational cost. In full-field methods, a unit cell representing the microstructure (the RVE) is subjected to external strain, and the local stress response is computed at each point in space by numerical resolution of the constitutive laws. The effective response is obtained by volume averaging of the local responses [64] (see Appendix 6.8 for details). The chosen boundary conditions (BCs) directly affect the convergence rate towards true effective properties [100, 105], with periodic BCs converging the fastest [99].

The most well-known of full-field methods is the Finite Element (FE) method, which has had some success in the context of homogenization of SFRPs [63, 87, 103–105]. However, the FE method requires a suitable mesh representing the microstructure geometry, whose construction becomes increasingly challenging and computationally costly with high v_f [63, 104]. For high fiber content and aspect ratios, the meshing can fail altogether due to numerous

contact points between fibers [103,181]. Mesh-free methods offer a means to circumvent this problem.

One such method was developed by Moulinec and Suquet [110], where the elasticity equation is expressed in a so-called Lippman-Schwinger form, and resolved iteratively with the help of the Fast Fourier Transform operation (FFT) (see Appendix 6.9 for details). In the FFT method, the microstructure is described by an orthogonal grid (a 3D array), which means this method has the decisive advantage of being able to use data from 3D-imaging techniques directly [159]. The absence of meshing also lowers the memory requirements, which combined with the computational efficiency of the FFT method, enables the resolution of large and realistic microstuctures [180,182]. Recent developments have extended the original Moulinec and Suquet method to allow convergence in presence of infinite phase contrast (as for porous materials), which was a limitation of the original formulation [183]. The AMITEX software implements the FFT method with these improvements, along with distributed computing techniques that allow performance gains on multi-CPU architectures [184,185].

When a material exhibits structuring phenomena at dissimilar length scales, such as in SFRPs made by FFF, attempting to consider the smallest features at the largest scale is often unfeasible [159,186]. Sommireddy et al. [87] attempted it for predicting tensile properties, using a single RVE with a simplified description of both micro and mesostructure, with error margins of 16 to 26%, depending on load direction. Multiscale techniques are used instead, where the constitutive equations at the macroscale are substituted by the output of the boundary value problem computed at the microscale. Doing so allows the combination of different methods for each scale, drawing on the strengths of each. For instance, the efficiency of FFT method applied to the microscale can be combined by the ability of FE at the macroscale to account for arbitrary part geometry and BCs [180,182]. For the multiscale method to be valid, however, a sufficient scale separation must exist between the each scale: the typical length at which the smallest features vary, or l_n, must be small when compared to the RVE size used to homogenize those features, or L_n. That RVE size must also be small when compared to the features at the scale above it, or l_{n+1}, and the RVE size used to model those, or L_{n+1} [187]. This can be expressed as $l_n << L_n << l_{n+1} << L_{n+1}$.

6.4 Methods and materials

We investigated the process-structure-property relationship of SFRPs made by FFF. As shown in Figure 6.2, specimens of CF reinforced PEEK were manufactured using unidirectional (0°-0°), 0°-90° and 90°-90° patterns and an intermediate nozzle diameter. Unidirectional specimens were also fabricated for 2 additional nozzle diameters, one smaller and one

larger. As shown in Figure 6.3, for each scenario, both the microscale and mesoscale morphologies were characterized through μCT imaging. Component extraction was then performed using OpenFiberSeg, a special-purpose tool developed by the authors [164]. This tool enables the identification of individual fibers, as well as the intra-bead (microscale) and inter-layer (mesoscale) porosity. Sub-volumes where no mesoscale features are present are located, which serve as representation of the intra-bead microstructure itself. This microscale description $\mathbf{C}(\boldsymbol{x})$ (stiffness as a function of position in space) was then processed with the AMITEX software to obtain an homogenized effective stiffness at the microscale, $\tilde{\mathbf{C}}_{\text{micro}}$, which was used in turn to obtain the homogenized stiffness at the mesoscale, or $\tilde{\mathbf{C}}_{\text{meso}}$. The stiffness predicted by dual-scale homogenization was then validated by comparing with experimental data and contrasted with predictions made with simplified artificial microstructures.

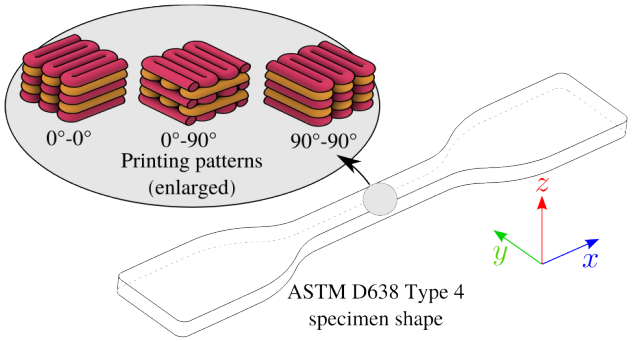

Figure 6.2 Schematic representation of the printing patterns used to produce the test specimens. For all nozzle diameters, the 0°-0° or unidirectional along the longitudinal axis was studied. For the 0.4 mm nozzle, additional specimens using the 0°-90° and 90°-90° pattern were also considered.

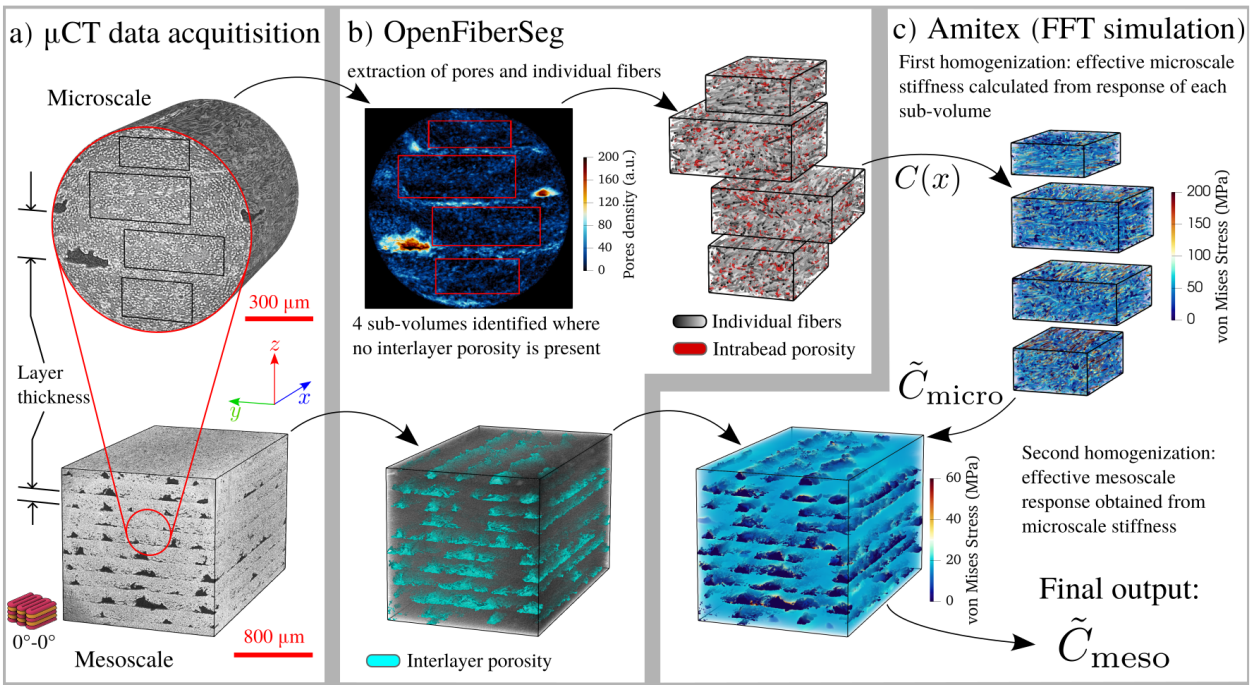

Figure 6.3 Schematic flowchart of the dual-scale FFT-homogenization. a) μCT imaging data of physical specimen, performed with large field of view for the mesoscale, and at high resolution for the microscale. b) Constituent extraction using specialized software OpenFiberSeg. c) The result of FFT-homogenization at the microscale serves as input for the mesoscale homogenization.

6.4.1 ASTM D638 Type 4 specimen preparation

Commercial filament Tecafil™ PEEK VX 30CF from Ensinger was placed in a vaccum oven for 24 h at 60°C and 17 kPa. Figure 6.2 shows an ASTM D638 Type 4 dogbone specimen that was printed in an AON3D™ Mark 2 industrial 3D printer using 3 different nozzle diameters (Volcano model from E3D, diameters $D = 0.25$, 0.4 and 0.8 mm). The slicing parameters utilized in the Simplify3D™ slicer are shown in Table 6.1. The layer height and extrusion multiplier were set empirically by attempting to minimize inter-layer porosity, with a printing speed of 30 mm/s. In addition, the following temperature settings were common to all specimens: nozzle temperature: 410°C, bed temperature: 180°C, and chamber temperature: 120°C (maximum allowable in AON Mark 2). A total of 6 specimens were produced for each nozzle diameter, using longitudinal or 0°-0° (all passes are along the longitudinal axis of the specimen, i.e., the 0° direction). Using the 0.4 mm nozzle, 6 additional dogbones were made using a 0°-90° pattern (layers alternate printing passes along the long and short axis) and a 90°-90° pattern (all passes perpendicular to the dogbone axis). Filaments spools were kept

in the heated chamber for the duration of printing.

Table 6.1 Printing parameters used for each specimen type

D, **nozzle diameter (mm)**	**Layer height (mm)**	**Extrusion width (mm)**	**Extrusion multiplier**	**Printing pattern**
0.25	0.10	0.22	0.95	0°-0°
0.40	0.20	0.42	1.10	0°-0°, 0°-90°, 90°-90°
0.80	0.25	0.80	1.01	0°-0°

Additionally, for each of the nozzle diameters considered, 3 specimens were made by extrusion in free-space, meaning the printhead is not pressed against the table. These specimens enable the characterization of the microstructure at the bead scale, excluding all phenomena related to the deposition onto a part.

6.4.2 Tensile testing

The specimens were loaded at a rate of 5 mm/min using a MTS Insight Material Testing system and a MTS uniaxial extensometer model 634_25F-25. For each loading sequence, the strain was obtained directly from the calibrated extensometer readings, and the stress was computed by dividing the loading force by the specimen cross-section area (measured from the average of 4 caliper measurements along the narrow section of the dogbone). The linearly elastic range for each specimen was identified in the following manner. A first-degree polynomial was fitted by the least-square method to the entire stress-strain data. The fit was then performed iteratively, each time removing the point at the highest stress from the data, until the relative error between the fitted line and the experimental curve reached 1%. This segment of the data was considered within the linear regime, and the tensile modulus for each specimen is the slope of the fitted line.

6.4.3 Volumetric characterization

Tomographic data acquisition

Using a specimen of roughly the same physical dimensions as the scanning field of view (FoV) minimizes the noise contributed by material outside the FoV and helps achieve the highest quality imaging data. To ensure that individual fibers are differentiated and tracked, at least 10 pixels [65, 164] for the typical fiber diameter of $7 - 10$ μm are required for carbon fibers, which leads to a pixel size of $0.7 - 1.0$ μm. The Zeiss XRadia™ 520 micro-tomographic scanner has a cylindrical FoV with a diameter and height of ~ 1000 pixels, which at that pixel

size allows for a diameter and height of $0.7 - 1.0$ mm of physical specimen volume. In each specimen, a roughly cylindrical section of diameter $1 - 1.5$ mm was manually carved from the narrow part of the dogbones and mounted on the specimen holder. The following scanning parameters were used: source power: 7 W, source voltage 80 kV, distance from source to specimen: 9.1 mm, distance from detector to specimen: 23.0 mm, optical magnification: 10×, exposition time: 1.25 s, number of projections: 3200, and no filter (i.e., using air attenuation). This configuration yields a pixel size of 0.764 μm, and a total scan time of 2 h 20 m per specimen. Two separate FoVs were chosen inside each specimen to account for local variations in properties. In total, 4 FoVs were scanned at high resolution for each printing configuration: 2 FoV per specimen and 2 specimens per configuration. The free-space specimens, along with a section of feedstock 1.75 mm filament, were also scanned in this manner.

Except when using the nozzle with $D = 0.25$ mm, the grid-like printing pattern is larger than the diameter of the high resolution scans. To enable the analysis of those mesoscale features, rectangular sections measuring ~ 4 mm on one side were also produced and scanned at a larger FoV (meaning at a lower resolution). Here, the scan resolution was reduced considerably since we are mainly interested in the larger mesoscale porosity, not the small intra-bead pores, nor the fibers. The parameters used are the same as above, except for: distance from source to specimen: 21.1 mm, distance from detector to specimen: 9.0 mm, optical magnification 4×, exposition time: 0.4 s, number of projections: 1600. This yielded a pixel size of 4.69 μm and a total scan time of 40 min. One such FoV was produced for each nozzle diameter and print configuration. As the specimen preparation for μCT scanning is destructive (a small section is carved from the dogbones) all imaging was performed after tensile testing.

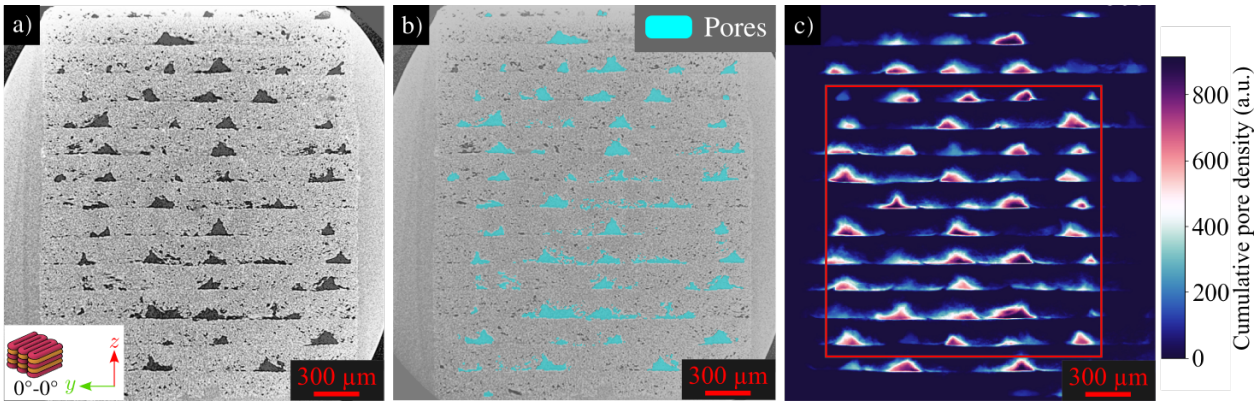

Figure 6.4 Segmentation of mesoscale porosity and definition of subvolume for homogenization. a) Slice of tomographic data showing a rectangular specimen printed according to the 0°-0° pattern and a 0.4 mm nozzle. Horizontal printing layers are visible, leaving mesoscale porosity in dark. b) The inter-layer porosity identified by OpenFiberSeg is highlighted in light blue. c) Cumulative sum of all porosity voxels in the out-of-plane direction. The grid-like arrangement of printing passes is revealed in sharp contrast. The red rectangle is the chosen subvolume for homogenization.

Component extraction (OpenFiberSeg)

The tomographic scans were processed with the help of OpenFiberSeg, an open-source software built for the purpose of identifying the constituents in the volume (matrix, pores and individual fibers). With this software, the user first manually labels a small patch of data to identify the constituents. This labelling is then fed to a machine learning algorithm to identify the remaining pixels in the entire dataset. On a slice-by-slice basis, the pixels containing fibers are automatically grouped into connected regions, and the centroids of those regions are tracked across 3D space to form neatly aligned chains, which are used to infer the presence of individual fibers. Thanks to this extraction, it is possible to build a voxel-based (regularly-spaced volume elements) representation of the microstructure for a specific specimen. Porosity is labelled using classical image processing methods such as the Canny edge detection algorithm. As can be seen in Figure 6.4 a), at this length scale, the large pores belonging to the mesostructure and the smaller intra-bead pores can be discriminated according to their size. Each pore size is estimated by the number of connected pixels it contains, then a size threshold ($\sim 1\%$ of total FoV volume) was chosen such that only mesoscale porosity is kept. Examination of Figure 6.4 b), in which the pores above the threshold are in shown in light blue serves to ascertain that all the mesoscale porosity has been labelled.

Subvolume definition, micro and mesoscale

For the purpose of homogenization, one or more rectangular subvolumes inside the cylindrical FoV need to be identified. These combined subvolumes form the RVE for a particular printing configuration. The FoV must be cropped for several reasons. First, the rectangular subvolume must lie entirely within the material. Then, for the case of mesoscale homogenization, the subvolume dimensions should respect the periodic structure formed by the evenly spaced printing layers and extrusion beads, since only a handful of periods is included. Lastly, for the purpose of dual-scale homogenization, the microscale structure containing fibers/matrix/intra-bead pores must be isolated from the mesoscale pores, to not skew the results by including those twice.

The shape and size of porosity made by the priting pattern is irregular and the grid-like pattern is not readily visible on a single slice. To reveal this pattern more clearly and to identify suitable subvolumes within a FoV, the following method was used. Across the entire volume, the pixels containing pores were assigned the value 1, and all other pixels the value 0. Then, we took the cumulative sum of all 2D slices in the volume along a reference direction (for instance, the out-of-plane direction in the Figure 6.4 b), creating a 2D map with high values where the mesoscale porosity in concentrated, and low values otherwise, as shown in Figure 6.4 c). Here, the mesoscale porosity is revealed unambiguously for the entire volume. A subvolume that is inscribed in the natural periodicity of the mesostructure is thus identified: the red rectangle in Figure 6.4 c) encompasses an integer number of layers (starts and ends at mid-layer in the vertical direction) and of passes (starts and ends at bead centers).

The same projection procedure was repeated for the case of microstructure homogenization, on the high-resolution imaging data, as shown in Figure 6.5 for the nozzle with $D = 0.4$ mm and a specimen made with a 0°-0° pattern. In Figure 6.5 a), the input imaging data is shown, with the corresponding material labelling in Figure 6.5 b). In Figure 6.5 c), the subvolumes identified are the largest possible such that they contain only microscale porosity.

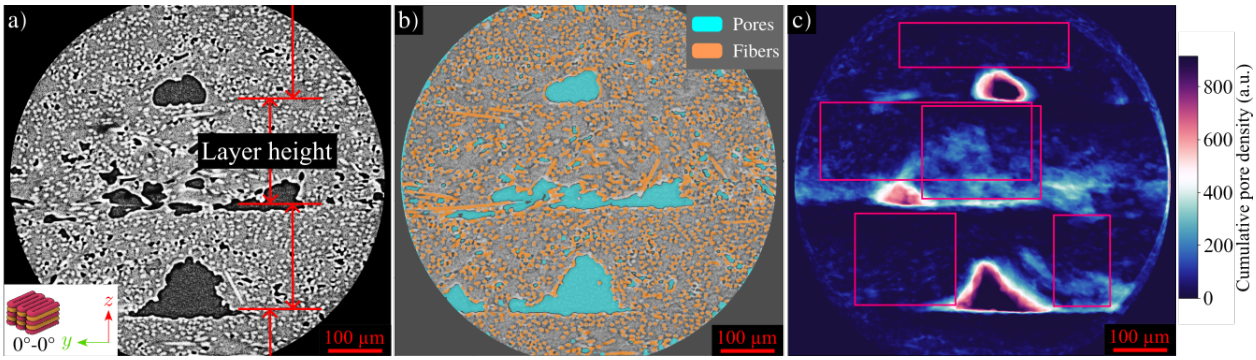

Figure 6.5 Segmentation of fibers and microscale porosity and definition of subvolumes for homogenization. a) Slice of tomographic data of a specimen printed according to the 0°-0° pattern with a 0.4 mm nozzle, showing horizontal printing layers. b) Fibers and porosity found by OpenFiberSeg highlighted in orange and light blue, respectively. c) Cumulative sum of porosity voxels in the out-of-plane direction. The location of mesostructure porosity across the volume is made obvious, relatively to the single-slice rendering in b). The red rectangles are chosen for homogenization, selected to the maximum size while avoiding mesoscale porosity.

6.4.4 Dual-scale homogenization

Under the condition of scale separation, the microscale morphology (including fibers, matrix, and the small, inter-layer porosity) can be homogenized by itself if the scale at which this homogenization occurs (a single pass) is large when compared to the dimension of constituent phase change (the size of fibers and pores). Using many subvolumes across several different scans enables the estimates given by homogenization to be representative of the variability in the real material.

The AMITEX software accepts as inputs a volumetric description containing a number of different materials, which can be the organized in zones, for instance for fibers or grains with different orientations. For the problem at hand, the isotropic matrix is described by tensile modulus E and Poisson's ratio ν. If the axis of the transverse isotropy is $\vec{e}_1$, and the transverse plane is $\vec{e}_2 \times \vec{e}_3$, the fibers are described by longitudinal (along $\vec{e}_1$) and transverse (along $\vec{e}_2$ or $\vec{e}_3$) moduli E_l and E_t, respectively, Poisson's ratios between axes ($\vec{e}_1$,$\vec{e}_2$) and ($\vec{e}_2$,$\vec{e}_3$), i.e. ν_l and ν_t respectively, and the shear modulus between axes ($\vec{e}_1$,$\vec{e}_2$), i.e. G_l. The matrix properties were obtained from manufacturer datasheets on Victrex 450G PEEK [1]. The precise carbon fiber type is not disclosed, but the most likely candidate are the so-called standard modulus fibers, of which Toray T300 carbon is the most common and cost-effective [188]. The material properties for T300 fibers are taken from [2, 3]. Property values are given in Table 6.2.

Table 6.2 Material properties for base constituents, see [1–3].

Polymer	E (GPa)	ν			
Victrex 450G PEEK	4.0	0.3855			
Carbon fibers	E_l (GPa)	E_t (GPa)	ν_l	ν_t	G_l (GPa)
Toray T300	230	13.4	0.256	0.3	27.3

Whereas all matrix and porosity voxels can share the same default zone (they are isotropic), the different fiber orientations are represented using zone descriptors at each voxel, which include a rotated reference frame onto which the stiffness tensor is projected. The implementation of the AMITEX software has the number of zones limited to $2^{15} = 32768$. For large subvolumes containing more fibers than this limit, the orientation angles ϕ and θ (spherical coordinates) are rounded to the nearest integer, and fibers with common angle pairs are grouped under the same zone identifier, with negligible effect on homogenization output (this was tested on subvolumes below the fiber count limit, for which it is possible to not round the angle values).

The homogenized stiffness tensor for an equivalent solid is obtained by subsequently applying the uniaxial strains in the 3 references directions, and the 3 pure shear strains to a given microstructure. For each load case, the volume-averaged stress response of the entire solid yields one column vector in the homogenized stiffness tensor for this material (see Appendix 6.8 for more details). For each printing configuration, each subvolume is processed through AMITEX in this manner, and the stiffness tensors for each realization were averaged. This averaged tensor represents the composite made of matrix-fiber-microscale pores, which is then used in mesoscale homogenization, where the RVE contains this composite and the grid-like porosity pattern due to the printing procedure. For the 0°-90° printing pattern, the microscale was homogenized separately for beads containing only 0° or 90° subvolumes, and the two resulting $\tilde{\mathbf{C}}_{\text{micro}}$ were averaged together to represent the 0°-90° pattern. Only then was inserted into the mesostructure RVE. The output of this last stage is the effective stiffness for each printing configuration.

The specimen made with the $D = 0.25$ mm nozzle has a printing pattern with layer height $\times$ extrusion width of 0.1 mm$\times$0.2 mm. As such, a single high-resolution scan volume of diameter $\approx$0.75 mm contains several printing passes, so in this case only single-scale homogenization is required.

6.4.5 Alternative approach: artificial microstructures

The approach based on high-resolution tomographic imaging is restrictive in many respects. It requires access to expensive equipment and technical expertise, and extensive post-processing of the imaging data. To benchmark the quality of our modelling approach against those found in the literature [4, 160], and quantify its added value, the following approach is also presented. Producing an artificial geometry with the full orientation and lengths distribution of real materials, at high v_f is technically challenging, and beyond the scope of this work. Much like the approach used in [4, 160], a simplified set of artificial geometries can be used instead. Based on the work of Ghossein et al. [167], microstructures can be created using an algorithm based on molecular dynamics modelling, in which ellipsoidal fibers are generated at a fixed aspect ratio (AR), with near-ideal alignment (some fibers rotate during the generation process due to collisions), up to a desired v_f. Spherical pores, occupying a specified volume fraction $v_p =$ are also produced. To determine which AR is representative of a real physical specimen, the following method was used. In Figure 6.6 a), the distribution of lenghts and deviation angles θ as seen in real physical specimens is shown. Longer fibers contribute more to the effective stiffness than shorter fibers, therefore simply using the mean length as seen in a real specimen will not capture the outsized effect of longer fibers. An estimation of the effect of AR on effective properties was gained by performing Mori-Tanaka simulations on aligned microstructures, for AR ranging from 1 to 100.

In Figure 6.6 b), the relative effect (or weight) of a fiber's AR is shown: by keeping v_f constant, the tensile modulus predicted by the Mori-Tanaka model is normalized by the modulus for $AR = 1$. The value obtained is an indication of the effect each AR has on the effective moduli: an AR=10 was a weight of 3, meaning it has 3× the effect on effective stiffness than a fiber of AR=1. Using these weights, a weighted mean can be computed, which accounts for the larger effect of longer fibers. For instance, instead of one fiber with AR=1 and one with AR=10 giving a mean AR of 5.5, we consider the fiber with AR=10 to be duplicated 3 times, according to its weight, therefore the weighted mean becomes $(10 * 3 + 1)/4 = 7.8$. Therefore, a Mori-Tanaka estimate using two fibers with AR=1,10 is equivalent to one with a single fiber of AR=7.8, keeping total v_f constant. The weighted mean procedure is done on the distribution of ARs in a real specimen, duplicating each fiber by the integer amount of its weight. The weighted and unweighted mean obtained are presented in Figure 6.6 a), with values of 32 μm ($AR = 4.2$) and 60 μm ($AR = 8.0$), respectively.

The latter value of AR is used to generate artificial microstructures, along with $v_f = 23.8\%$ and $v_p = 2\%$, and a deviation value $\theta \approx 0°$. As these microstructures are costly to generate for large fiber counts, 20 subvolumes with 300 fibers and 8 pores were used instead. An

example of such a microstructure is presented in figure 6.6 c), with fibers identified in different shades of grey, and pores shown in red. Keeping the same dual-scale FFT-homogenization approach, these artificial geometries are used as a stand-in for the microscale description from real materials. The averaged output of this homogenization ($\tilde{\mathbf{C}}_{\text{micro}}$) was then inserted into the same mesoscale RVE obtained from μCT imaging of each specimen type, to evaluate the relevance of using high-resolution imaging and individual fiber tracking. The alternate approach uses only the low-resolution μCT images for the mesoscale, and the much simpler labelling of mesoscale porosity, along with idealized microstructure description.

6.5 Results and discussion

6.5.1 Tensile testing results

Figure 6.7 contains the stress-strain curves as measured during tensile testing, as well as the line segments that represent the estimated linear domain for each test. In general, considerable variability is observed between specimens of the same printing configuration.

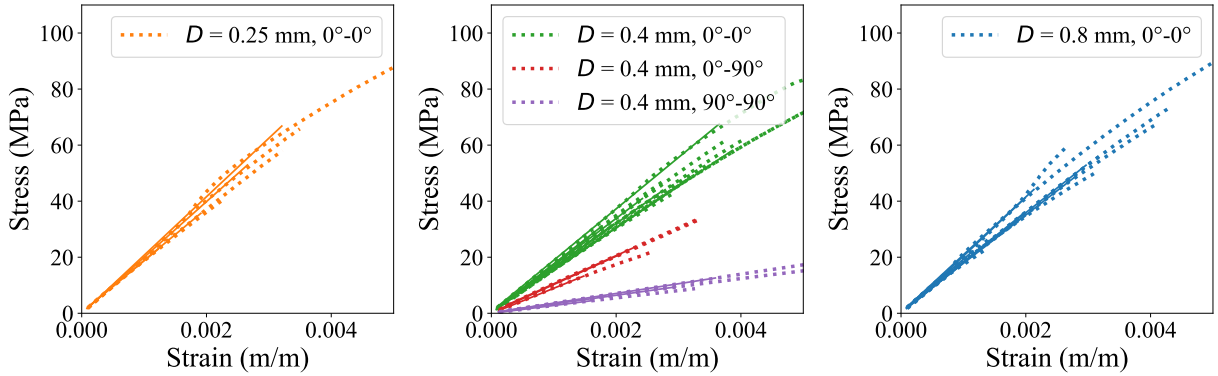

Figure 6.7 Stress-strain curves for each specimen, for all 5 printing configurations. Solid lines segments represent the estimation of the linear elastic domain for each curve, from which the tensile modulus is calculated.

The averaged modulus for each specimen category is presented in Table 6.3. Among the specimen made with the 0°-0° print pattern, those made with the $D = 0.4$ mm nozzle have a stiffness 14% lower than the average of specimens made with the $D = 0.25$ and 0.8 mm nozzles. The specimens made with the 90°-90° pattern have the lowest tensile modulus, since the fibers are mainly oriented in the direction perpendicular to the testing direction, and the specimens at 0°-90° exhibit an intermediate modulus.

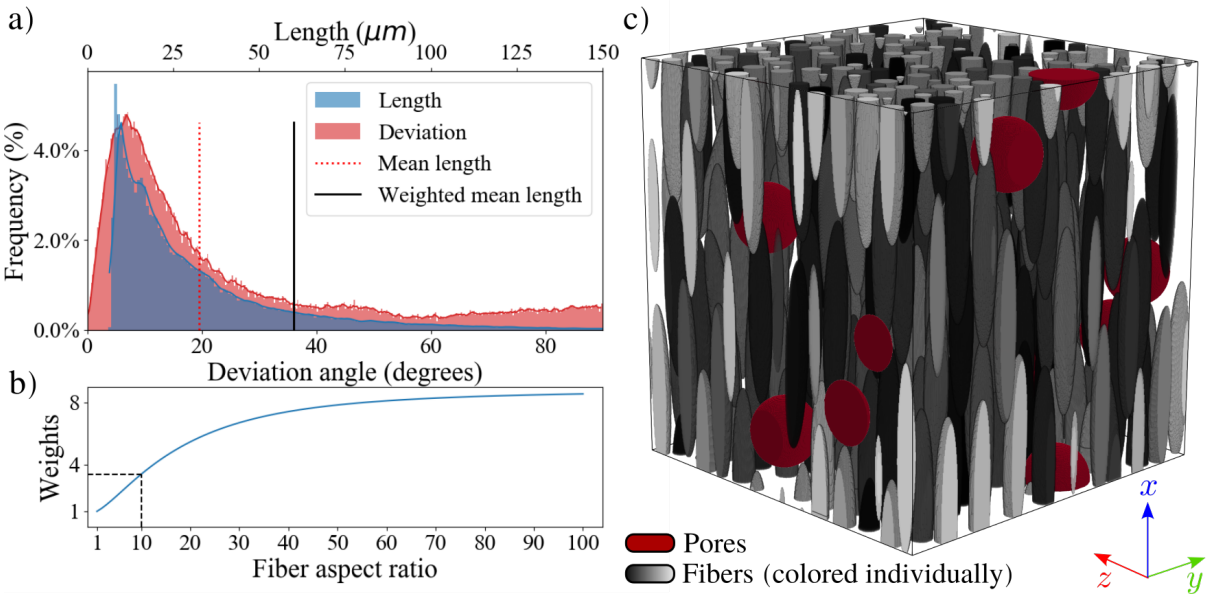

Figure 6.6 Generation of representative simplified artificial microstructure. In a) the fiber lengths and deviations in all physical specimen is shown. In b) the Mori-Tanaka model is used to give a weight to each fiber according to its aspect ratio, and its relative impact on effective tensile properties. c) Example of a microstructure, with constant aspect ratio $AR = 8$, corresponding to the weighted mean in b), and near-ideal alignment. This RVE was used to compare against the prediction accuracy of the homogenization procedure using imaging data. Fibers occupy $v_f = 23.1\%$, and pores occupy $v_p = 2\%$, which is consistent with real material microstructures.

Table 6.3 Measured averaged modulus for each specimen type, with 95% confidence intervals

D, **nozzle diameter (mm)**	**Printing pattern**	**Averaged modulus (GPa)**
0.25	$0° - 0°$	19.4 ± 1.0
0.40	$0° - 0°$	16.4 ± 0.7
0.80	$0° - 0°$	18.5 ± 1.0
0.40	$0° - 90°$	9.7 ± 0.6
0.40	$90° - 90°$	3.2 ± 0.3

6.5.2 Effect of nozzle diameter

The probability density functions (PDF) of fiber lengths and deviation angles from the extracted fiber properties pertaining to the free-space extrudates and the segment of 1.75 mm filament feedstock are shown in Figure 6.8. In Figure 6.8 a) the extent of fiber breakage is revealed: for all 3 nozzles, the proportion of fibers shorter than 20 μm increased by nearly a third, when compared to that of the 1.75 mm filament, with no large distinction between nozzle diameters. In Figure 6.8 b), the effect of extrusion on fiber alignment is appreciated, as measured by the peak locations (θ_{max}) on each curves and the measure of full width at half maximum (FWHM). Although the position of peaks is nearly unchanged, there is more dispersion surrounding the peak in all extruded specimens. Though these variations are small, their magnitude had not been measured before. Having these distributions along with the corresponding 3D renderings of the fibers as they present in each bead could be valuable for future rheology modelling efforts of the extrusion of SFRPs.

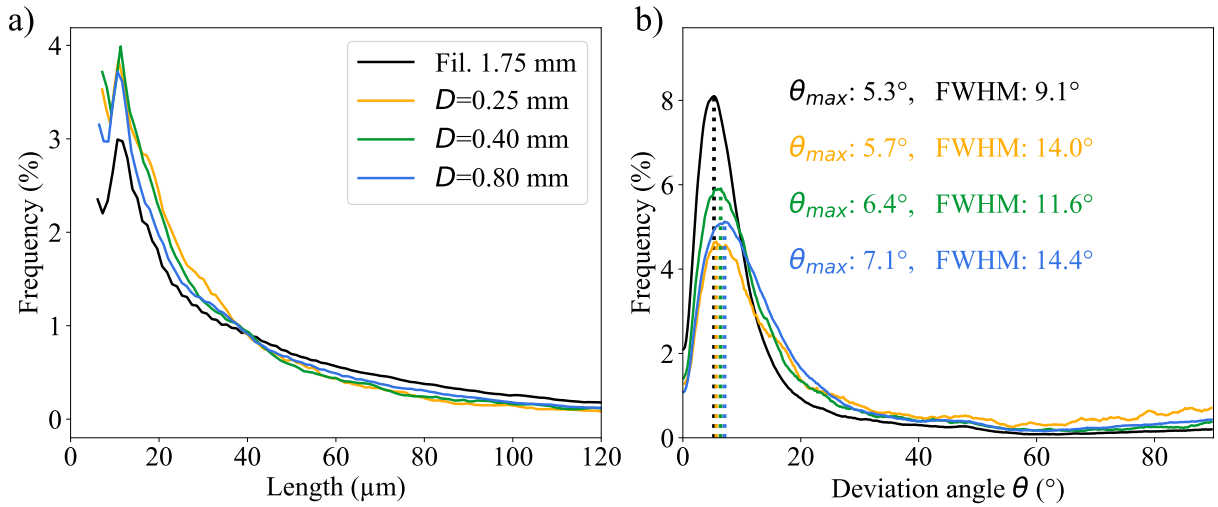

Figure 6.8 Probability density functions (PDFs) of a) fiber lengths and b) fiber deviation angles relative to printing direction (θ), for each nozzle diameter D. In a), the comparison to the PDF in the feedstock filament (diameter=1.75 mm) shows that fiber breakage occurs for all nozzle diameters to roughly the same degree. The peak locations (θ_{max}) on each curve and the full width at half maximum (FWHM) in b) reveal the effect of extrusion on fiber alignment. The drops in peak heights in b) could be explained by fiber breakage: the short segments produced by breaks are more likely to be misaligned. This effect is particularly prevalent in the 0.25 mm nozzle.

6.5.3 Local property variation

The same cumulative sum procedure described in Section 6.4.3 was used to visually analyze the microstructure for each printed configuration. As presented in the Video in Supplementary Materials (Appendix C), in addition to computing the cumulative sum of pixels containing fibers or pores, here each pixel is also given the value of a property: first fiber length, then fiber alignment with the 0° print direction. As a reminder, x and y are the 0° and 90° printing direction, respectively, the $x-y$ plane is the printing bed plane, and z is the vertical direction. Cumulative sums are taken along both x and y, enabling the study of gradients in material property, that is not easily seen on a slice-by-slice basis.

Figure 6.9 presents the cumulative sums of fiber alignment with the 0° print direction, fiber length, fiber and pore densities, for specimens printed with nozzle $D = 0.4$ mm, and the 0°-0° printing pattern. Three whole layers are visible, and one partially at the bottom. In Figure 6.9 a), we can see that there are pockets of stronger and weaker alignment (pale blue patches) that are of a size comparable to the layer height. This degree of non-uniformity is one possible explanation to the variability observed in tensile properties: these variations

are not always present depending on which specimen or scan location is considered. If more patches of weak alignment are present in a specimen, it would lead to lower macroscopic modulus in that direction. In addition, there is noticeable decrease in both fiber length and fiber density at the layer interfaces (Figure 6.9 b anc c). This effect is subtle, but indicative that different rheological characteristics are found at the interface. In Figure 6.9 d), we also observe a vertical gradient in the distribution of intra-bead porosity, which accumulate towards the bottom of each layer. These phenomena offers an interpretation to the known deviation of tensile and fracture properties at the inter-layer region.

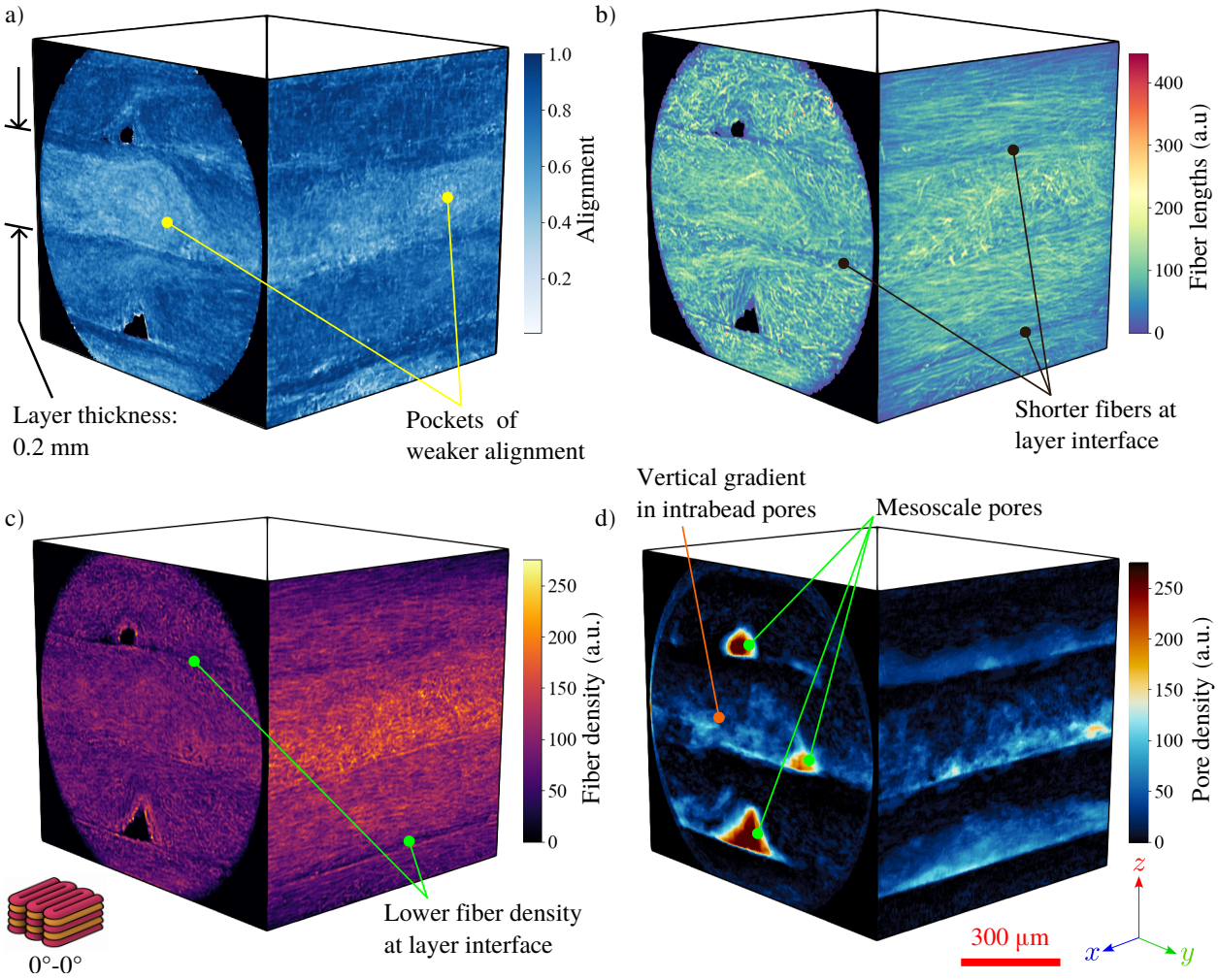

Figure 6.9 Morphology visualization: 0°-0° pattern, nozzle diameter $D = 0.4$ mm. Cumulative sum of per-voxel properties along x and y directions. a) Alignment with 0° print direction x (1.0 is perfect alignment ($\theta = 0°$), 0.0 is perpendicular ($\theta = 90°$)). b) Length of fibers. c) Fiber density. d) Pore density.

Figure 6.10 depicts the same cumulative sums, for specimens of nozzle $D = 0.4$ mm, and the

0°-90° printing pattern. From top to bottom, 4 layers are distinguished, namely 0°-90°-0°-90°. The alignment color code in Figure 6.10 a) is with direction x, therefore the white parts in the 90° layers are those with the strongest alignment with y. Again, regions of weaker alignment are perceptible in both the 0° and 90° passes, although in this case they are in the shape of elongated streaks. In addition, the $x - z$ (left-hand side) and $y - z$ (right-hand side) cumulative sums plots are not mirror images: the right-hand side shows much more pronounced waves. There are also noticeably longer fibers present in the center of those deeper indentations, as visible in Figure 6.10 b). We surmise this is due to the different cooling duration between the 0° pass and the 90° pass: the central part of the dogbone specimen has a long aspect ratio. Therefore, the print head travels 115 mm for the 0° pass and only 6 mm for the 90° pass, a difference of 19 times. As a consequence, for each 90° bead much less cooling has occurred when the adjacent one is applied, therefore local base layer temperature is higher. More remelting of the base layer can thus occur, forming deeper indentations. We corroborate this explanation by scanning and analyzing a specimen made from a square plate (aspect ratio of 1, dimensions $20 \times 20 \times 4$ mm) printed in the 0°-90° configuration, also with the $D = 0.4$ mm nozzle. In Figure 6.10 e), the resulting cumulative sum visualization for fiber alignment in such a specimen is presented. In this scenario, the indentations left on the preceding layer are of similar severity for the passes in both directions. This effect suggests that feature aspect ratio is a source of microstructure orthotropy: the fiber alignment and length distribution is less symmetrical when part aspect ratio is high, leading to a different moduli in the x, y and z directions.

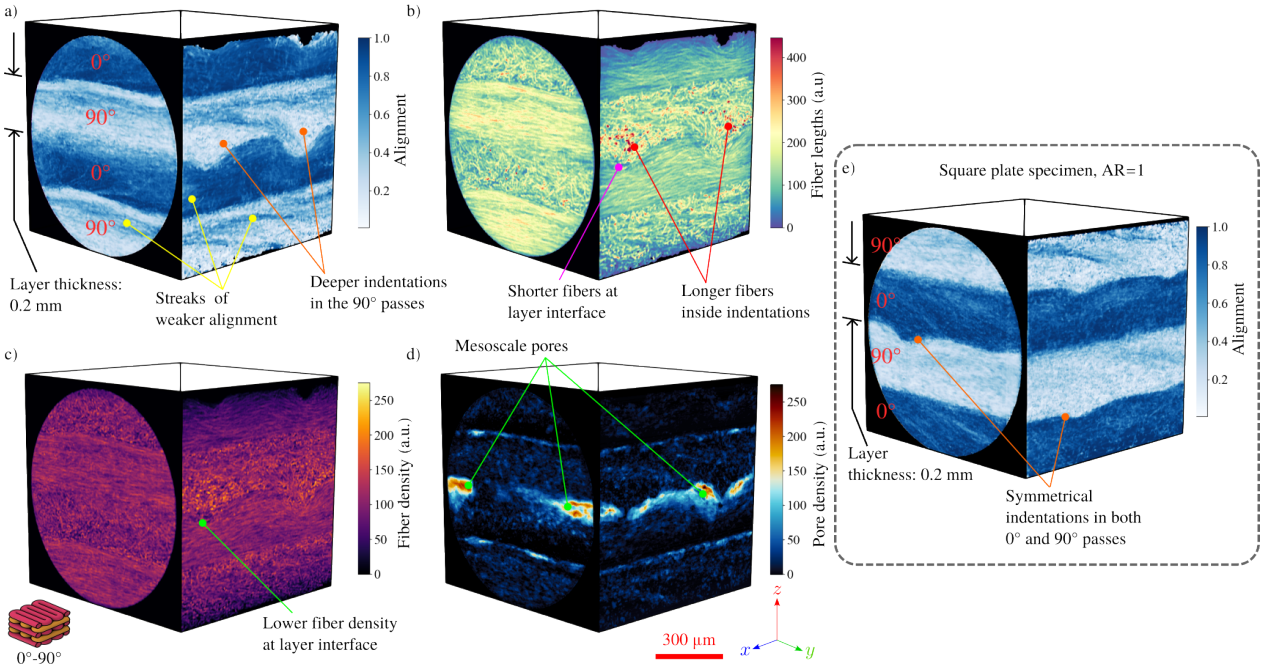

Figure 6.10 Morphology visualization: 0°-90° pattern, nozzle diameter $D = 0.4$ mm. Cumulative sum of per-voxel properties along x and y directions. a) Alignment with 0° print direction x (1.0 is perfect alignment ($\theta = 0°$), 0.0 is perpendicular ($\theta = 90°$)). b) Length of fibers. c) Fiber density. d) Pore density. e) Fiber alignment, using alternative square-shaped specimen (part aspect ratio of 1, dimensions $20 \times 20 \times 4$ mm). The indentations left on previous layers are of similar extent for print passes in both directions.

The reader is referred to the Supplementary Materials (Appendix C) for the renderings of data from the nozzles with $D = 0.25$ mm and $D = 0.8$ mm mm. All these local variations highlight the need for using several FoVs across many specimens, as this is the only way to reach a true RVE for each printing configuration for this class of material.

6.5.4 Microscale orthotropy

It is expected that the presence of fibers in SFRP introduces transverse isotropy, i.e. the material's stiffness is symmetric with respect to rotation along one axis, here the printing direction x. However, the degree to which the microstructure by itself is orthotropic rather than transversely isotropic is not clear, meaning that the tensile moduli along directions y and z are also different from each other, which breaks the rotational symmetry along x. This effect is hard to disentangle from global orthotropy, to which the mesoscale printing pattern is a known contributor [12,13,161,162,]. Having a detailed description of the microstructure allows us to investigate this feature. As shown in Figure 6.11, each fiber in a microstructure

can be represented in polar coordinates, in the following manner. The angle θ the fiber makes with the printing direction x is the radial coordinate, and the azimuthal angle in the $y-z$ plane is the angular coordinate. Doing so, a two-dimensional histogram can be generated, by binning all the fibers in a specimen by θ and ϕ. In addition, just as in artificial microstructure generation, the histogram is weighted to account for longer fibers' estimated effect on effective stiffness (see Section 6.4.5). Figure 6.12 presents the resulting histograms for nozzles with $D = 0.25$, 0.4 and 0.8 mm. The degree of alignment with print direction is higher for nozzle $D = 0.25$ and 0.8 mm, as seen in Figure 6.12 a) and c). The cumulative distribution function in Figure 6.12 d) shows that, for those specimen categories, 56% of all fibers have $\theta < 15°$, whereas for the $D = 0.4$ mm specimen the proportion is 29%. This explains the drop in tensile modulus observed in experiments, as presented in Table 6.3, where the $D = 0.4$ mm specimen is 14% less stiff in the x direction that the average of the $D = 0.25$ and 0.8 mm specimens. Furthermore, the more elongated and horizontally aligned red regions in Figure 6.12 b) indicate that the $D = 0.4$ mm specimen has a higher ratio of fibers aligned with the y direction against the z direction. This is not correlated with the extrusion cross-section (layer height/extrusion width, see Table 6.1), as the $D = 0.25$ and 0.4 mm specimen have a cross-section aspect ratio of 2, and the $D = 0.8$ mm specimen has an aspect ratio of 3. Nonetheless, this phenomenon deserves further investigation, as $D = 0.4$ mm nozzle offers a good trade-off between geometric print resolution and printing speed, but the drop in tensile properties is deleterious. Whereas the experimental measurement of microscale orthotropy, separately from the mesoscale contribution is not feasible, the degree of orthotropy can be gauged from the homogenized stiffness tensors at the microscale, $\tilde{\mathbf{C}}_{\text{micro}}$. The degree of congruence with either transverse isotropy or orthotropy can be measured by projecting $\tilde{\mathbf{C}}_{\text{micro}}$ to either space, i.e. rebuilding the tensor from the extracted independent parameters for each symmetry class, and measuring the $L2$ norm of the difference between the two. For instance the distance e of the projection into orthotropic space is: $e = \left|\tilde{\mathbf{C}}_{\text{micro}} - \tilde{\mathbf{C}}^{\text{ortho}}_{\text{micro}}\right|_{L2}$. The distances for all nozzle diameters are presented in Table 6.4, along with the ratio of tensile moduli along each of the reference directions. While the distance for the the $D = 0.25$ and 0.8 mm specimens are nearly identical for both symmetry classes, the one for the $D = 0.4$ mm specimen has a value 50% larger for transverse isotropy than orthotropy. The same effect is noticeable with the E_z/E_y which is further from unit for the latter specimen, and the moduli perpendicular to the printing direction E_z/E_x and E_y/E_x are also relatively larger.

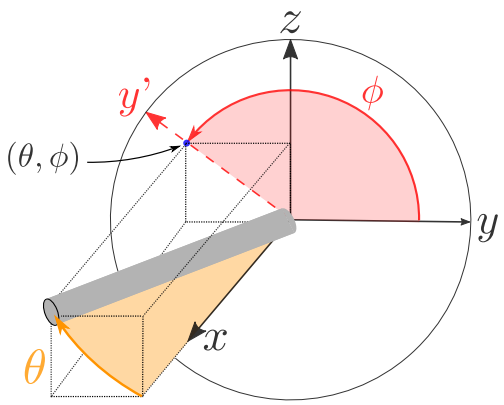

Figure 6.11 Polar representation of a fiber by its deviation angle θ and azimuthal angle ϕ. The angle θ the fiber makes with the printing direction x becomes the radial coordinate, and the angular coordinate ϕ is the angle made by the $x - y'$ plane containing the fiber and the $x - y$ print bed plane.

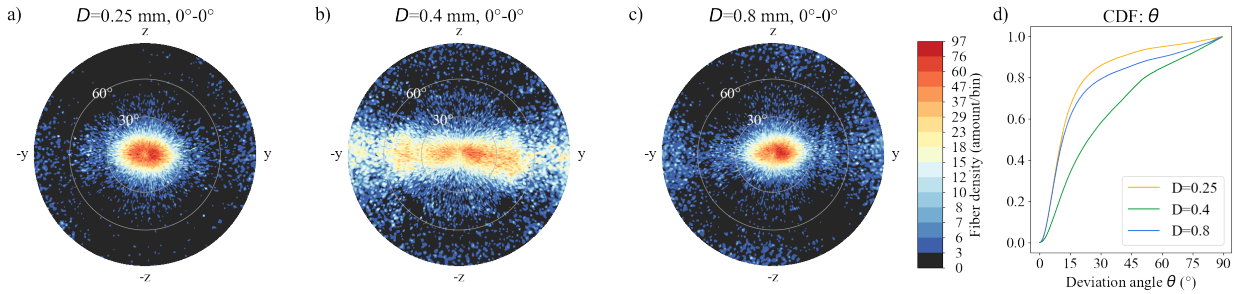

Figure 6.12 Histogram of fibers angular distributions, for the 0°-0° specimen made with: a) nozzles $D = 0.25$ mm, b) $D = 0.4$ mm and c) $D = 0.8$ mm, including $\sim 10^5$ individual fibers each. The radial coordinate is the deviation angle θ, and the angular coordinate is the azimuthal angle ϕ. As the cumulative distribution function of θ for each nozzle diameter showns in d), the specimens made with 0.25 and 0.8 mm nozzles have their fibers much more aligned with the print direction, with 56% of fibers with $\theta < 15°$, when compared to 29% for the $D = 0.4$ mm nozzle, which explains lower axial tensile properties for the latter. In addition, the specimen made with $D = 0.4$ mm nozzle exhibits a preferential alignment in the y direction (ratio between y-alignment and z-alignment of 74:26 instead of 61:39 for $D = 0.25$ and 0.8 mm).

Table 6.4 Remainder of $\tilde{\mathbf{C}}_{\text{micro}}$ after projection to transversely isotropic and orthotropic space. Ratios of tensile moduli along x, y and z.

D, **nozzle diameter (mm)**	**Printing pattern**	**Distance Trans. iso**	**Distance Orthotropy**	E_z/E_y	E_z/E_x	E_y/E_x
0.25	$0° - 0°$	1.15	1.07	0.97	0.26	0.27
0.40	$0° - 0°$	3.02	1.86	0.84	0.33	0.40
0.80	$0° - 0°$	2.08	2.02	0.96	0.24	0.25
0.40	$0° - 90°$	8.88	1.71	0.42	0.63	1.52
0.40 (plate)	$0° - 90°$	5.53	0.70	0.52	0.54	1.04
0.40	$90° - 90°$	1.26	1.19	1.02	0.25	0.24

However, in many applications, having an isotropic response is preferable, for which the 0°-90° printing pattern is better suited. In Figure 6.13, the histograms for the $D = 0.4$ mm nozzle are presented, first by separating the fibers in the 0° and the 90° passes in Figures 6.13 a) and b), then by showing both passes together in Figure 6.13 c). Note that the 90° pass is made in the y direction, therefore most fibers in that pass have values of $\theta \sim 90$ and $\phi \sim 0, 180$, where the two red regions in Figure 6.13 b) are located. However, much as was observed in the morphological visualizations in Figure 6.10, the two directions show salient asymmetry. As can be observed visually, no red region is present in Figure 6.13 a), meaning the concentration of fibers aligned with x is lower. In addition, the ratio of fibers better aligned with y to those aligned with x is 57:43, suggesting the different thermal conditions seen by the 90° pass are more favorable to fiber alignment in that direction. The difference in alignment between the two passes suggests tensile properties are inferior in the x direction (0°) than the y direction (90°), likely due to part aspect ratio. That prediction is corroborated in the homogenization output, as seen in Table 6.4: just as the alignment profile was asymetrical in the dogbone specimen vs. the square plate, the $\tilde{\mathbf{C}}_{\text{micro}}$ is also far more symmetrical for the plate specimen, with a ratio of E_y/E_x=1.04, against 1.52 in the dogbone specimen.

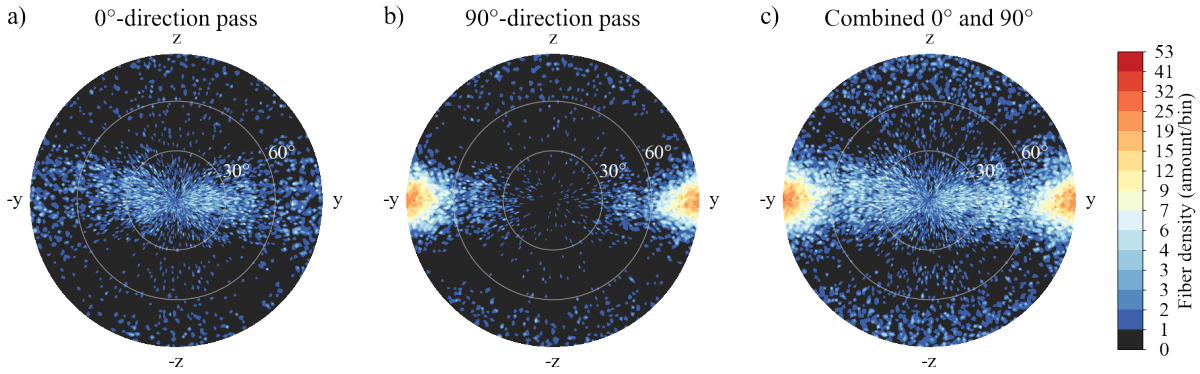

Figure 6.13 Histogram of fibers angular distributions, for the 0°-90° specimen made with the $D = 0.4$ mm nozzle. The fibers are separated as belonging to: a) the 0° pass, b) the 90° pass, and c) both 0° and 90° passes combined. More fibers are aligned with the y direction than with the x direction, with a ratio of 53:47, introducing orthotropy, attributable to part aspect ratio of 19 in ASTM D638 Type 4 dogbones.

6.5.5 FFT Homogenization results

Using the fully detailed description of the microstructure for elastic homogenization allows the study of the stress-strain fields that develop inside the material. In Figure 6.14, a slice oriented in the printing bed plane inside one of the subvolumes used for homogenization for a specimen printed with the 0°-0° pattern and the $D = 0.25$ mm nozzle is presented. For this nozzle, the micro and mesoscale homogenization are made in a single step as the printing pattern is present at a length scale close that of the individual fibers. In Figure 6.14 a), the tomographic data is depicted, where the fibers are distinguished in white, the matrix in grey, and the pores in dark. The printing pattern is also discernible, with the extrusion width annotated in red. In Figure 6.14 b) and c), the von Mises strain and stress fields computed with the help of AMITEX are presented. The fibers being the phase with the highest stiffness, most of the stress concentrates inside them, and they exhibit very little strain. The opposite is true for the pores: they have no stiffness, therefore they develop no stress, and the maximum values of strain are inside them, as they deform freely (contrary to what is done in the FE method, in FFT-homogenization the nodes are regularly-spaced, meaning the inside of pores is also solved for).Inside the matrix phase, we can observe stress concentration near the tip of fibers, or where pores have sharp corners. Those locations are likely to be damage initiation sites.

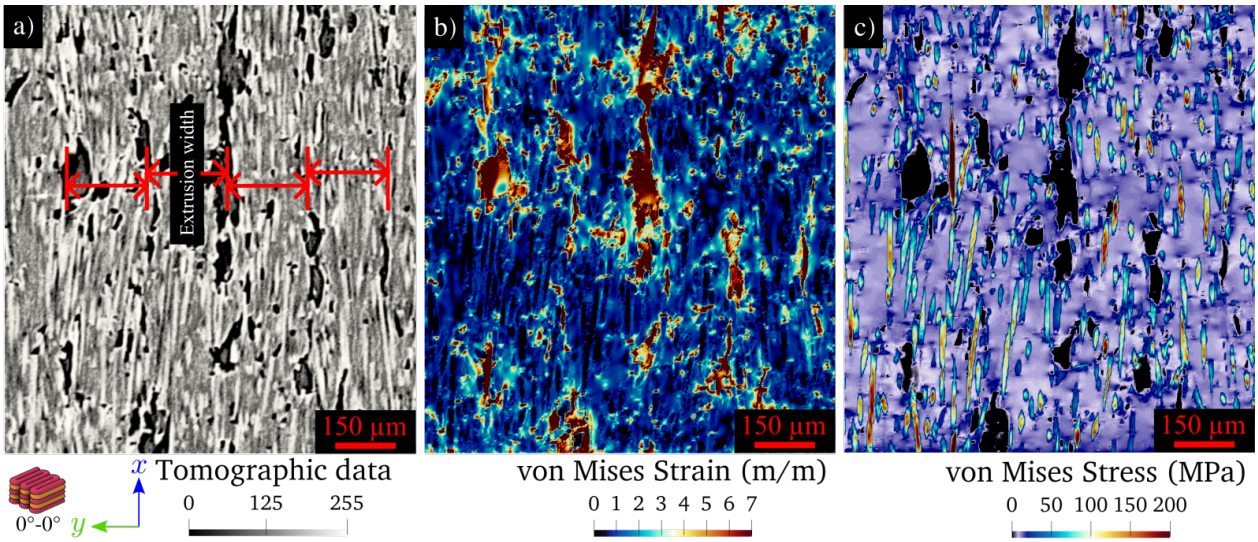

Figure 6.14 Result of the FFT homogenization procedure on a subvolume of a specimen made with the $D = 0.25$ mm nozzle and the 0°-0° printing pattern. a) Tomographic data in the plane of the printing bed. b) Von Mises strain field, mainly present in pores. c) Von Mises stress field, concentrating inside fibers.

In Figure 6.15, the mesoscale homogenization results for the specimen made with the 0°-0° printing pattern and the $D = 0.4$ mm nozzle are presented. In this case, only two phases are homogenized: the mesoscale porosity and the solid phase described by the $\tilde{\mathbf{C}}_{\text{micro}}$ stiffness tensor obtained at the microscale homogenization step. In Figure 6.15 b), the strain field is again maximal inside pores, however the strain also forms bands in the vertical direction. In Figure 6.15 c), the stress field shows that stress concentrates where the mesoscale pores form small radii.

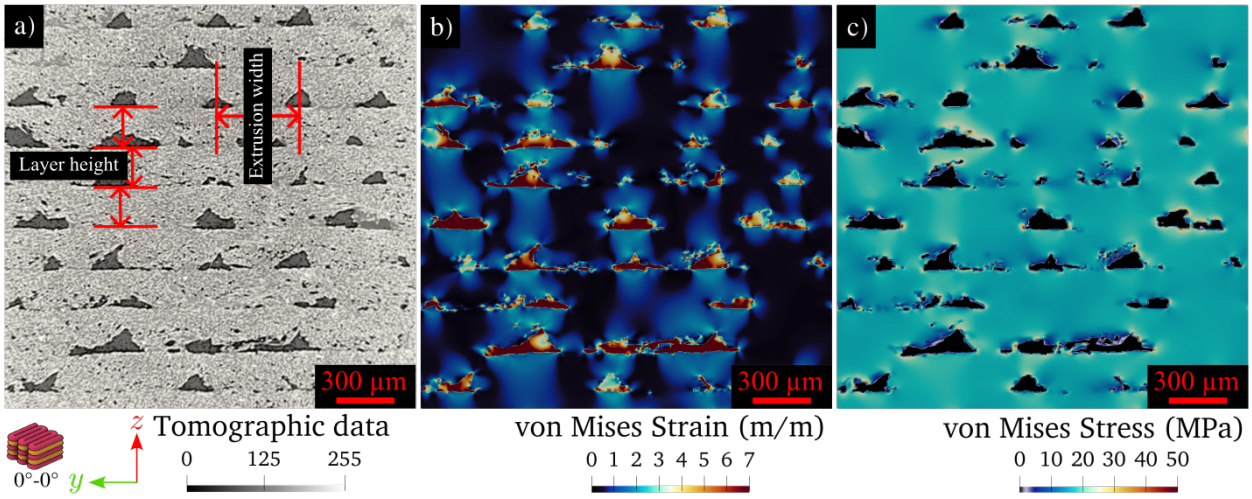

Figure 6.15 Resulting stress-strain fields for the mesoscale FFT homogenization procedure on a subvolume of a specimen made with the $D = 0.4$ mm nozzle and the 0°-0° printing pattern (0° is out-of-plane). a) Tomographic data. b) Von Mises strain field. c) Von Mises stress field.

6.5.6 Simulation vs experimental results

Table 6.5 FFT-simulation results, microscale only ($\tilde{\mathbf{C}}_{\text{micro}}$)

D, nozzle diameter (mm)	Pattern	E_x (GPa)	E_y (GPa)	E_z (GPa)
0.25	$0° - 0°$	20.30	5.53	5.37
0.40	$0° - 0°$	18.32	7.27	6.13
0.80	$0° - 0°$	21.37	5.30	5.10
0.40	$0° - 90°$	10.07	15.26	6.34
0.40 (plate)	$0° - 90°$	11.25	11.75	6.07
0.40	$90° - 90°$	5.59	23.21	5.73

Table 6.6 FFT-simulation results, dual-scale homogenization ($\tilde{\mathbf{C}}_{\text{meso}}$). For the $D = 0.25$ mm nozzle, both the separate and simultaneous dual-scale outputs are shown.

D, nozzle diameter (mm)	Printing pattern	E_x (GPa)	E_y (GPa)	E_z (GPa)	Exper. E_x (GPa)	Relative error (%)
0.25 (simult.)	$0° - 0°$	18.76	5.02	4.60	19.4 ± 1.0	3.37
0.25 (sep.)	$0° - 0°$	17.67	4.64	4.17	19.4 ± 0.7	8.98
0.40	$0° - 0°$	15.60	5.69	3.49	16.4 ± 0.7	4.60
0.80	$0° - 0°$	18.82	4.63	4.31	18.5 ± 1.0	1.63
0.40	$0° - 90°$	8.80	13.30	4.25	9.7 ± 0.6	9.63
0.40	$90° - 90°$	4.37	19.55	3.23	3.2 ± 0.3	36.23

In Tables 6.5 and 6.6, the homogenization results for each specimen type are presented, for the microscale and the mesoscale, respectively. The relative errors between the tensile testing values and the prediction for FFT-homogenization using real data are all below 5%, except for the 90°-90° specimen with the 0.4 mm nozzle which has a 36% error. For the $D = 0.25$ mm nozzle, the relevance of using simultaneous dual-scale instead of separating them as for the rest of the specimen types is demonstrated: the relative error is nearly halved by doing simultaneous dual-scale homogenization, as the scale separation is insufficient in this case to successfully account for $\tilde{\mathbf{C}}_{\text{micro}}$ alone.

In Figure 6.16, the final output of the dual-scale FFT-homogenization procedure for each specimen type is presented, along with the tensile testing measurements, and the results of the alternate method using artificial microstructures for the microscale step. The confidence intervals in the simulated results are calculated from the dispersion of results for each sub-volumes in each of the simulated cases. The relative errors between the tensile testing values and the predictions made with artificial data are all in excess of 19%. Even though the artificial microstructures used are simplified, the recourse to fully detailed mesostructures makes the prediction quality somewhat improved, when compared to similar methods in the literature [4, 160]. Nonetheless, using real microstructures is considerably more reliable, and the prediction quality is within or near the confidence interval for the experimental measurements. A few sources of error that affect the result quality bear mentioning. First, the material variability due to the manufacturing process is considerable, as witnessed by the width of the confidence intervals in tensile properties themselves. Then, local morphological properties can vary within and between specimens, which affects both physical specimens as well as homogenization prediction quality. Then, the FFT method assumes periodic boundary conditions. When generating artificial microstructures, both RSA or molecular dynamics methods enforce geometrical periodicity by repeating fiber segments that exceed the unit-cell boundary on the opposite side, which isn't the case in microstructures based on real (non-periodic) imaging data. Also, the matrix-fiber interface is considered ideal in our method, which is likely not true in real materials [18], and were this included, the homogenization prediction would be somewhat lower. However, the quality of these results for such a broad range of morphological configurations leaves no doubt that using rich microstructures from actual specimen is a decisive advantage over relying on artificial geometries. Note that the simplification made in some studies considering isotropic CFs [4] is not advisable: when our simulations were done with isotropic CFs, the estimated moduli were in excess of 20% above experiment. Using transversely isotropic CFs, while requiring more analysis to differentiate individual fibers, is also a determining factor for successful homogenization. In addition, the number of fibers that encompass the RVEs are in the order of 10^4, much higher than the

customary $10 - 200$. Each of the predictions in Figure 6.16 requires $\approx$ 10 h in combined processing on AMITEX, using 24 CPUs and 90GB of RAM. This is on top of the $\approx$ 20 h of extraction done on OpenFiberSeg for each FoV.

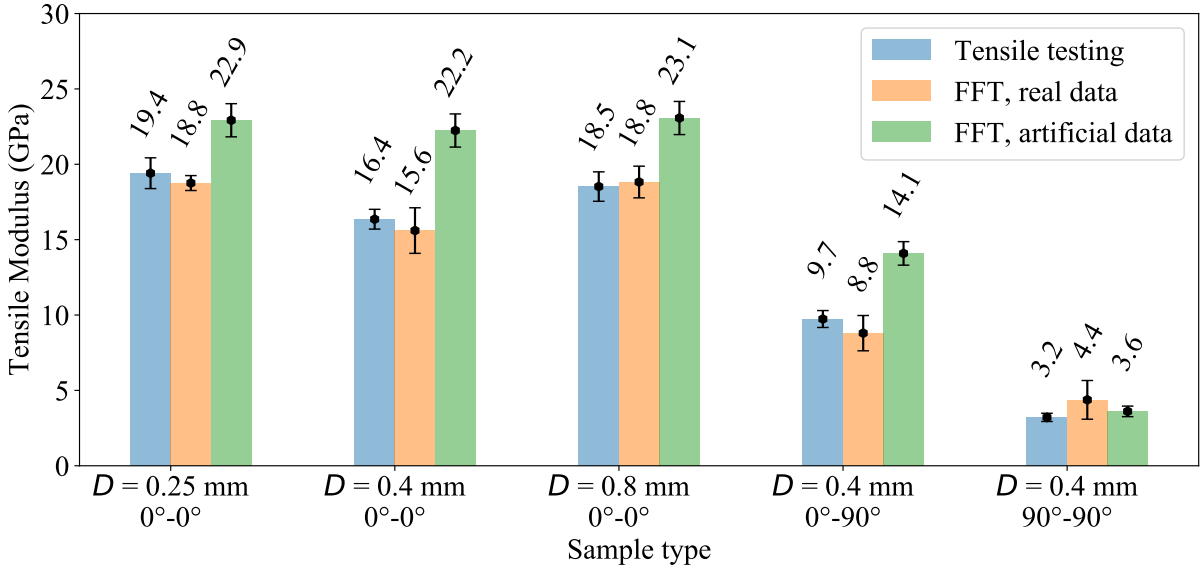

Figure 6.16 Comparison of tensile moduli as predicted from FFT-homogenization and as measured experimentally. Values are averaged for at least 4 subvolumes in each configuration. The error bars indicate 95% confidence intervals. The variation in the simulation output is representative of the spread of values encountered for the subvolumes that makeup the RVE for each configuration.

6.6 Conclusion

In this work, the process-structure-property relationship for FFF SFRPs is investigated, including the effect of using three nozzle diameters, and three different printing patterns. Physical specimens were produced and comprehensively characterized, using μCT imaging and individual component extraction, both in free-space extrusion (no contact with print bed) or in standard tensile testing specimen. Dual-scale homogenization was employed to successfully predict the tensile properties of 5 different print configurations, and it was demonstrated that the relative errors are reduced by a factor of 4, when compared to using simplified artificial microstructure descriptions. Variations in local morphology and in angular deviations between specimens were exposed, which provides insight into the variability in tensile properties between specimen. For instance, the large angular dispersion in specimens made with a $D = 0.4$ mm nozzle explain the lower tensile moduli. In addition, the impact of part

aspect ratio on the microscopic morphology is revealed, which is an important phenomena for predicting part behavior for real applications. Future work on this topic would include a more rigorous handling of the size of representative volume element (RVE), an exploration of inter-layer properties, the application of this method to fracture modelling, the use of imperfect matrix-fiber interfaces, and mechanical modelling using parts of more complex geometry, infill pattern and loading scenarios. The FFT homogenization method can also be applied to FFF SFRPs to study other material behavior laws, including thermal and electrical conductivity, thermal expansion, viscoelasticity and piezoelectricity.

6.7 Source code and data repository

The full source code repository and selected original tomographic data including processed results are available at `https://github.com/lm2-poly/OpenFiberSeg`.

CRediT authorship contribution statement

Facundo Sosa-Rey: Conceptualization, Methodology, Formal analysis, Software, Validation, Writing - Original Draft. **Clément Vella:** Software, Validation. **Alessandra Lingua:** Experimental investigation. **Juliette Pierre:** Experimental investigation. **Nicola Piccirelli:** Project administration. **Daniel Therriault:** Supervision, Writing - Review & Editing. **Martin Lévesque:** Supervision, Writing - Review & Editing.

Acknowledgements

This project was supported financially and conducted with the technical and financial support of Safran S.A. (FACMO Research Chair). Financial support was also granted by the Natural Sciences and Engineering Research Council of Canada (Alexander Graham Bell Canada Graduate Scholarship program, and the Collaborative Research and Development program, grant no CRDPJ514761). Further funding was obtained through the Simulation-based Engineering Science program funded through the CREATE program. High performance computing ressources were made available by Calcul Québec (`calculquebec.ca`) and the Digital Research Alliance of Canada (`alliancecan.ca`).

6.8 Appendix: Deriving effective properties of a microstructure

Notation and conventions used

In the following discussions, unless otherwise specified scalars are represented by lowercase letters (a, b, α, β), vectors by lowercase latin bold letters ($\mathbf{a}$,$\mathbf{b}$), 2^{nd}-order tensors by lowercase bold greek letters: $(\boldsymbol{\varepsilon}, \boldsymbol{\sigma})$, 4^{th}-order tensors by uppercase bold Latin letters: $(\mathbf{C}, \mathbf{S})$. Einstein summation convention is adopted, which reads for the singly contracted product:

$$\mathbf{a} \cdot \mathbf{b} = a_i b_i = \sum_i a_i b_i = \ c \text{ (a scalar)} \tag{6.8.1}$$

$$\boldsymbol{\alpha} \cdot \boldsymbol{\beta} = \alpha_{ij}\beta_{jk} = \sum_j \alpha_{ij}\beta_{jk} = \ \delta_{ik} = \boldsymbol{\delta} \text{ (a } 2^{nd}\text{-order tensor)} \tag{6.8.2}$$

The doubly-contracted tensor product is denoted: $A_{ijkl}x_{jl} = b_{ik}$, or $\mathbf{A} : \boldsymbol{x} = \mathbf{b}$. The spatial averaging operation is denoted $\bar{b} = \langle b(\boldsymbol{x}) \rangle$ (with b being a scalar or tensor of any order).

The 4^{th} rank tensors that are of relevance to continuum mechanics generally present minor and major symmetries, and can be represented concisely in the so-called modified Voigt notation. A $4^{th}-$order tensor $\boldsymbol{A}$ takes the following modified Voigt notation:

$$\boldsymbol{A}_{ijkl} = \begin{bmatrix} A_{1111} & A_{1122} & A_{1133} & \sqrt{2}A_{1123} & \sqrt{2}A_{1131} & \sqrt{2}A_{1112} \\ A_{2211} & A_{2222} & A_{2233} & \sqrt{2}A_{2223} & \sqrt{2}A_{2231} & \sqrt{2}A_{2212} \\ A_{3311} & A_{3322} & A_{3333} & \sqrt{2}A_{3323} & \sqrt{2}A_{3331} & \sqrt{2}A_{3312} \\ \sqrt{2}A_{2311} & \sqrt{2}A_{2322} & \sqrt{2}A_{2333} & 2A_{2323} & 2A_{2331} & 2A_{2312} \\ \sqrt{2}A_{3111} & \sqrt{2}A_{3122} & \sqrt{2}A_{3133} & 2A_{3123} & 2A_{3131} & 2A_{3112} \\ \sqrt{2}A_{1211} & \sqrt{2}A_{1222} & \sqrt{2}A_{1233} & 2A_{1223} & 2A_{1231} & 2A_{1212} \end{bmatrix}. \tag{6.8.3}$$

Writing $\boldsymbol{A}_{IJ}$ refers to the I$^{\text{th}}$ row and J$^{\text{th}}$ column in the modified Voigt representation.

Homogenization

For any given microstructure described by $\mathbf{C}(\boldsymbol{x})$, an equivalent homogeneous $\tilde{\mathbf{C}}$ tensor can be derived. With the help of a numerical scheme (FE, FFT, etc), a solution for $\boldsymbol{\sigma}(\boldsymbol{x}) = \mathbf{C}(\boldsymbol{x}) : \boldsymbol{\varepsilon}(\boldsymbol{x})$ can be found for any average applied strain $\bar{\boldsymbol{\varepsilon}} = \langle \boldsymbol{\varepsilon}(\boldsymbol{x}) \rangle$. By applying a pure uniaxial strain such as $\bar{\boldsymbol{\varepsilon}} = [1, 0, 0, 0, 0, 0]^T$, we thus obtain the corresponding $\boldsymbol{\sigma}(\boldsymbol{x})$ given $\mathbf{C}(\boldsymbol{x})$, and

the volume averaged equation $\langle \boldsymbol{\sigma}(\boldsymbol{x}) \rangle = \tilde{\mathbf{C}} \ : \ \langle \boldsymbol{\varepsilon}(\boldsymbol{x}) \rangle$ is then:

$$\begin{bmatrix} \Sigma_{11} \\ \Sigma_{22} \\ \Sigma_{33} \\ \sqrt{2}\Sigma_{23} \\ \sqrt{2}\Sigma_{13} \\ \sqrt{2}\Sigma_{12} \end{bmatrix} = \begin{bmatrix} C_{11} & \# & \# & \# & \# & \# \\ C_{21} & \# & \# & \# & \# & \# \\ C_{31} & \# & \# & \# & \# & \# \\ \sqrt{2}C_{41} & \# & \# & \# & \# & \# \\ \sqrt{2}C_{51} & \# & \# & \# & \# & \# \\ \sqrt{2}C_{61} & \# & \# & \# & \# & \# \end{bmatrix} \cdot \begin{bmatrix} 1 \\ 0 \\ 0 \\ 0 \\ 0 \\ 0 \end{bmatrix} \tag{6.8.4}$$

(The symbol # denotes irrelevant values). The first column in $\tilde{\mathbf{C}}$ is then inferred from the average stress $\langle \boldsymbol{\sigma}(\boldsymbol{x}) \rangle$ as :

$$\Big[C_{11}, C_{21}, C_{31}, C_{41}, C_{61}, C_{51}\Big]^T = \Big[\Sigma_{11}, \Sigma_{22}, \Sigma_{33}, \Sigma_{23}, \Sigma_{13}, \Sigma_{12}\Big]^T \tag{6.8.5}$$

Performing this procedure for the 3 uniaxial loadings and the 3 pure shear yields the entire $\tilde{\mathbf{C}}$ tensor for the microstructure at hand.

6.9 Appendix: Moulinec's algorithm

The local deformation can be written as the sum of a constant term $\mathbf{E}$, and a fluctuating term $\boldsymbol{\varepsilon}(\boldsymbol{u}^*(\boldsymbol{x}))$, as: $\boldsymbol{\varepsilon}(\boldsymbol{u}(\boldsymbol{x})) = \boldsymbol{\varepsilon}(\boldsymbol{u}^*(\boldsymbol{x})) + \mathbf{E}$, or equivalently: $\boldsymbol{u}(\boldsymbol{x}) = \boldsymbol{u}^*(\boldsymbol{x}) + \mathbf{E} \cdot \boldsymbol{x}$. Here $\boldsymbol{u}^*$ is considered periodic, and the stress term $\boldsymbol{\sigma}$ is antiperiodic: $\boldsymbol{\sigma}(L) \cdot \mathbf{n} = -\boldsymbol{\sigma}(-L) \cdot \mathbf{n}$ so that the traction term $\boldsymbol{\sigma} \cdot \mathbf{n} = \mathbf{0}$ at the boundary (equilibrium condition). $\mathbf{n}$ is the vector normal to the boundary, and the unit cell has side of length $2L$.

The classical elasticity equation becomes:

$$\begin{cases} \boldsymbol{\sigma}(\boldsymbol{x}) = \mathbf{C}(\boldsymbol{x}) : \Big(\boldsymbol{\varepsilon}(\boldsymbol{u}^*(\boldsymbol{x})) + \mathbf{E}\Big) & \forall \ \boldsymbol{x} \in V \\ \nabla \cdot \boldsymbol{\sigma}(\boldsymbol{x}) = \mathbf{0} & \forall \ \boldsymbol{x} \in V \end{cases} \tag{6.9.1}$$

We pose a reference media with stiffness $\mathbf{C}_0$ and define $\delta_{\mathbf{C}(\boldsymbol{x})} = \mathbf{C}(\boldsymbol{x}) - \mathbf{C}_0$. Inserting $\delta_{\mathbf{C}(\boldsymbol{x})}$ into equation (6.9.1) gives:

$$\boldsymbol{\sigma}(\boldsymbol{x}) = (\delta_{\mathbf{C}(\boldsymbol{x})} + \mathbf{C}_0) : \boldsymbol{\varepsilon}(\boldsymbol{u}(\boldsymbol{x})) \tag{6.9.2}$$

$$= \mathbf{C}_0 : \boldsymbol{\varepsilon}(\boldsymbol{u}(\boldsymbol{x})) + \delta_{\mathbf{C}(\boldsymbol{x})} : \boldsymbol{\varepsilon}(\boldsymbol{u}(\boldsymbol{x})). \tag{6.9.3}$$

$$\text{We define: } \tau(\boldsymbol{x}) = \delta_{\mathbf{C}(\boldsymbol{x})} : \boldsymbol{\varepsilon}(\boldsymbol{u}(\boldsymbol{x})), \tag{6.9.4}$$

called the *polarization*, which contains the position-dependent stiffness through $\delta_{\mathbf{C}(\boldsymbol{x})}$, and the "random" component of deformation through $\boldsymbol{\varepsilon}(\boldsymbol{u}(\boldsymbol{x}))$. This formulation is termed the periodic Lippmann-Schwinger equation [111]. The Moulinec algorithm iteratively solves for this $\tau(\boldsymbol{x})$ through a fixed-point scheme.

Expessing equation (6.9.3) in the Fourier domain, it is possible to write the solution as:

$$\boldsymbol{\varepsilon}(\boldsymbol{u}^*(\boldsymbol{x})) = -\boldsymbol{\Gamma}^0 * \tau(\boldsymbol{x}) \tag{6.9.5}$$

where $\boldsymbol{\Gamma}^0$ is the Green operator corresponding to the reference media $\mathbf{C}_0$, and $*$ denotes a convolution product. In the Fourier domain, $\boldsymbol{\Gamma}^0$ can be derived explicitly, and takes the following form for isotropic symmetries [110, 112]:

$$\hat{\boldsymbol{\Gamma}}^0_{khij}(\boldsymbol{\xi}) = \frac{1}{4\mu_0|\boldsymbol{\xi}|^2}\Big(\delta_{ki}\xi_h\xi_j + \delta_{hi}\xi_k\xi_j + \delta_{kj}\xi_h\xi_i + \delta_{hj}\xi_k\xi_i\Big) - \frac{\lambda_0+\mu_0}{\mu_0(\lambda_0+2\mu_0)}\frac{\xi_i\xi_j\xi_k\xi_h}{|\boldsymbol{\xi}|^4} \tag{6.9.6}$$

where δ_{ij} is the Kroeneker delta, $\boldsymbol{\xi}$ are the frequency domain variables and μ_0 and λ_0 are the Lamé coefficients of the reference material. The work of Mura [112] details the derivation of the Green operator for other material symmetries.

The principle behind the Moulinec algorithm is to use equations (6.9.4-6.9.5), respectively in the real and Fourier space, to iteratively solve equation (6.9.3). A constant deformation $\mathbf{E}$ is applied, and the stiffness tensors $\mathbf{C}(\boldsymbol{x})$ and $\mathbf{C}_0$ are known. we start by computing $\boldsymbol{\sigma}$ and $\tau(\boldsymbol{x})$ from $\mathbf{C}(\boldsymbol{x})$ and $\mathbf{E}$ (equations (6.9.9-6.9.10)). This initial $\tau(\boldsymbol{x})$ will not be accurate, as it only accounts for the average displacement $\mathbf{E}$. It can be used to arrive at a better estimate of $\hat{\boldsymbol{\varepsilon}}$ (equation (6.9.13)), which in turn yields a better estimate of $\boldsymbol{\sigma}$ (equation (6.9.15). The entire algorithm is repeated until the solution has converged (equation 6.9.12), meaning the estimated error is inferior to a prescribed value. The error at iteration i is defined as:

$$e^i = \frac{\Big(\Big\langle|\nabla\cdot\boldsymbol{\sigma}^i|^2\Big\rangle\Big)^{1/2}}{\Big\langle|\boldsymbol{\sigma}^i|\Big\rangle} = \frac{\Big(\Big\langle|\boldsymbol{\xi}\cdot\hat{\boldsymbol{\sigma}}^i|^2\Big\rangle\Big)^{1/2}}{\Big\langle|\hat{\boldsymbol{\sigma}}^i|\Big\rangle}, \tag{6.9.7}$$

where $|\cdot|$ is the Euclidean norm, and $\langle\cdot\rangle$ is the spatial average. A typical value of stopping

criteria is $e \leq 10^{-4}$. The main algorithm is as follows:

Initialization (step i=0)

$$\boldsymbol{\varepsilon}^0(\boldsymbol{x}) = E \quad \forall \boldsymbol{x} \in V \tag{6.9.8}$$

$$\boldsymbol{\sigma}^0(\boldsymbol{x}) = \mathbf{C}(\boldsymbol{x}) : \boldsymbol{\varepsilon}(\boldsymbol{x})^0 \quad \forall \boldsymbol{x} \in V \tag{6.9.9}$$

Iteration (step i+1)

$$a)\ \tau^i(\boldsymbol{x}) = \boldsymbol{\sigma}^i(\boldsymbol{x}) - \mathbf{C}_0 : \boldsymbol{\varepsilon}^i(\boldsymbol{x}) \tag{6.9.10}$$

$$b)\ \hat{\tau}^i(\boldsymbol{\xi}) = \mathcal{F}(\tau(\boldsymbol{x})^i) \tag{6.9.11}$$

$$c)\ \text{Convergence test} \tag{6.9.12}$$

$$d)\ \hat{\boldsymbol{\varepsilon}}^{i+1}(\boldsymbol{\xi}) = -\hat{\boldsymbol{\Gamma}}^0(\boldsymbol{\xi}) : \hat{\tau}(\boldsymbol{x})^i(\boldsymbol{\xi}) \quad \forall \boldsymbol{\xi} \neq 0, \text{ and } \hat{\boldsymbol{\varepsilon}}^{i+1}(0) = E \tag{6.9.13}$$

$$e)\ \boldsymbol{\xi}^{i+1} = \mathcal{F}^{-1}(\hat{\boldsymbol{\varepsilon}}^{i+1}) \tag{6.9.14}$$

$$f)\ \boldsymbol{\sigma}^{i+1}(\boldsymbol{x}) = \mathbf{C}(\boldsymbol{x}) : \boldsymbol{\varepsilon}^{i+1}(\boldsymbol{x}) \tag{6.9.15}$$

Once an equilibrium condition has been reached, if the applied strain $\mathbf{E}$ was chosen to be uniaxial and unitary, one column of the homogenized stiffness tensor $\tilde{\mathbf{C}}$ is obtained directly from $<\boldsymbol{\sigma}(\boldsymbol{x})>$ (see Appendix 6.8).

The Moulinec basic algorithm is known to have poor convergence for the cases of high property contrasts, and in the presence of voids (infinite contrasts), as the number of iterations required is proportional to the contrast between phases [90, 189]. To deal with this problem, Eyre and Milton [189] proposed a modification to deal with the cases of high contrasts.

CHAPTER 7 ARTICLE 3: Thermo-viscoelastic multiscale homogenization of additively manufactured short fiber reinforced polymers from direct microstructure characterization

Sosa-Rey, F., Lingua, L., Piccirelli, N., Therriault, D. & Lévesque, M. Submitted to *International Journal of Solids and Structures* on Febuary 22$^{\text{th}}$ 2023.

7.1 Abstract

Short fiber reinforced polymers (SFRPs) processed by Fused Filament Fabrication (FFF) show great promise for applications requiring high weight-specific mechanical properties, such as aerospace. However, the unique morphology created by the printing process and the relationship between processing parameters and part behavior is not sufficiently well understood, making structural analysis a largely empirical task. The limited ability to predict the effective viscoelastic properties and their thermal dependence is a problem from a mechanical design standpoint and is an obstacle to the widespread adoption of SFRPs made by FFF. In this work, those properties are evaluated using high-resolution imaging of physical samples, enabling the accurate prediction of time-dependent stress-strain relations across different temperatures. Multiscale homogenization is performed considering individual components (fibers, pores, matrix) at the microscale, and the regular pattern created by the printing process at the mesoscale. The efficiency of the Fast Fourier Transform (FFT) based homogenization procedure is leveraged to allow for large Representative Volume Element (RVE) sizes, which are required due to the complexity of real microstructures. The predicted thermo-viscoelastic behavior is validated against creep-recovery data of specimens printed from 30 wt.% short carbon fiber reinforced poly-ether-ether ketone (PEEK), and the experimental data can be predicted within 3% mean relative error for axial loading, both at 21° and 120°C. Imaging data and pre-processed RVEs as well as original source code are made publicly available.

7.2 Introduction

Fused Filament Fabrication (FFF) is an additive manufacturing method in which parts are constructed out of thermoplastic polymer filaments by depositing them layer-by-layer in a molten state through computer control. When compared to injection molding, the process is more cost-effective for small part count, can achieve intricate interior geometries, and

produces complex parts in a single step, with minimal material waste [4, 11, 15, 40, 62]. The addition of short fiber reinforcements to the feedstock filaments yields printed parts featuring higher elastic and viscoelastic stiffness, when compared to those of the matrices alone, mainly along the print direction. The presence of short carbon fibers also reduces warpage during cooldown via higher thermal conductivity, and part design can be optimized by purposeful positioning of fibers in the directions of expected in-service stresses [11, 62, 67]. Short-fiber reinforced polymers (SFRPs) thus have relatively high specific mechanical properties, which are sought in automotive and aerospace applications in which weight reductions translate into reduced fuel consumption [15, 40, 51, 62], and have been used as an alternative to metals for certain components [21]. Short fibers are more economical and easier to process than continuous fibers, and retain the increased performance given that fiber aspect ratio is high enough to enable efficient load transfer to the fibers [93, 190, 191]. Due to their viscoelastic matrix, SFRPs have a vibration damping effect which is higher than metals, which is of considerable interest in many applications [24, 192–194]. The viscoelastic behavior of SFRPs made by FFF has been less studied than their elastic or fracture properties [93], and the interplay between processing parameters, morphology and mechanical properties has scarcely been explored [195].

The viscoelastic properties of SFRPs made by FFF are anisotropic due to several factors. Firstly, reinforcements are preferentially aligned with the printing direction, which induces the highest stiffness to be along that axis. Secondly, reinforcements such as carbon fibers (CF) are themselves transversely isotropic [34, 194] (glass fibers are considered isotropic [28, 45]). Anisotropy makes both modelling and experimental investigations more complex: the former must be done with a larger set of independent time-dependent coefficients [24, 196], and the latter requires specialized equipment and is more time-consuming [24, 25, 194]. However, if anisotropy is not precisely accounted for, mechanical designers are forced to use the most compliant value in all directions, thus restricting the performance advantage of using this class of materials and leading to approximate mechanical behavior prediction.

Given the multiscale nature of these solids, successful modelling depends on correctly accounting for microstructural features at all relevant scales. However, considering the smallest features at the largest scale would be impractical computationally. Instead, multiscale methods have been developed to exploit the scale separation between structural features and make the modelling much more efficient by computing only the amount of detail necessary to correctly describe each scale separately [27, 37, 93, 190, 197–200]. For fiber reinforced composites in general (continuous or short), many authors consider the smallest scale as one represented by a cubic or hexagonal unit-cell with a single or a few fibers [93,190,198,200,201], that, when repeated periodically, generate a regular arrangement of fibers. In the case of

SFRPs, the complex nature of the microstructure requires a much more detailed microstructure description. To date, studies on viscoelasticity of SFRPs have been performed by accounting for a number of fibers ranging from a dozen to several hundreds [45, 190, 196, 202]. For thermo-viscoelasticity, the only studies where the scale above the microstructure is accounted for focus on the pattern made by weaved continuous fibers [37, 197, 198]. However, for SFRPs made by FFF, modelling efforts of elastic properties have shown that considering the mesoscale pattern created by the printing process is essential [4, 160, 203]. From those studies, it can be inferred that the mesoscale likely affects the effective viscoelastic response. In addition, those studies also highlight that using microstructure descriptions derived from imaging data, where individual components are identified, lead to more accurate predictions than when artificial microstructures are used.

In this work, a dual-scale homogenization model is developed using micro- and meso-structure descriptions made by constituent extraction in imaging data from printed specimen. The model is used to generate an anisotropic constitutive behavior law for the time-temperature dependence of SFRPs made by FFF. The size of the microstructure description used are several orders of magnitude larger than what is often encountered in the field of viscoelastic homogenization, as measured by the number of represented fibers. In addition, multi-axis experimental data is used for two purposes. First, the constitutive law parameters are inferred from the characterization of the pure polymer in its 3D-printed form, at 21 and 120°C. Second, the predictions of the homogenization model are validated against creep-recovery curves of 3D-printed composite specimens. This close relationship between model and experiment proves to be a decisive advantage in the prediction of thermo-viscoelasticity of SFRPs made by FFF.

7.3 Background

Homogenization is the process by which effective mechanical properties are predicted, given a specific microstructure description and the properties of each constituent. There are generally two classes of homogenization procedures for viscoelasticity: those based on the Laplace-Carson transform, and those that perform homogenization in the time-domain [195, 204]. The former exploits the so-called elastic-viscoelastic correspondence principle to transpose viscoelastic constitutive equations into a form analogous to elasticity, via the Laplace-Carson transform [24, 32, 196, 205–207]. By doing so, the analytical homogenization methods developed for linear elasticity (such as the Mori-Tanaka model, Lielen's model, the Self-consistent scheme among others), are applied directly in the Laplace-Carson domain, and the results can be used to predict the frequency-dependent viscoelastic properties [34, 196, 204]. While being

the subject of recent theoretical and practical studies [34, 193, 208], these analytical methods have intrinsic limitations. For high reinforcement volume fractions, the fiber interactions as a function of their spatial distribution are not captured accurately [109, 194]. Furthermore, the conversion back from the Laplace-Carson domain requires specialized optimization methods and is not forthcoming in many cases [32, 209–212].

In the second class of methods, homogenization is performed directly in the temporal domain, via full-field numerical methods: the constitutive laws for a multi-phase solid are integrated numerically with the help of internal variables [27, 195, 213–215]. The complexity of interconversion is avoided entirely, at the additional cost of being more computationally intensive, and dependent on having a geometrically explicit microstructure description, the so-called Representative Volume Element (RVE). Authors that have studied the viscoelastic behavior of SFRPs given a particular fiber length and orientation distributions have done so using RVEs generated artificially from statistical observations [28, 45, 104, 216]. It is also possible to create RVEs directly from volumetric imaging data of real specimens. To the authors' knowledge, however, that method has only been used for elasticity modelling of SFRPs made by FFF. In those works, the authors show that this approach is required due to the complexity of the morphology seen in those materials [4, 14, 87, 203]. Due to the poorly understood relation between processing parameters and morphology, approaches using direct description of microstructure are likely to surpass the prediction accuracy of methods using only a few statistical features such as fiber lengths and orientation distributions.

In numerical homogenization, the stress-strain constitutive relations are first solved at the local level for a particular microstructure and material properties. The effective global response is obtained by averaging the stress and strain fields. Most homogenization efforts of viscoelastic properties of FRPs are done using the Finite Element (FE) method [20, 29, 33, 36, 106]. However, resolving the constitutive law via the FE method is cumbersome for high fiber volume fraction and non-ideal fiber alignment, as the RVE required is large and achieving a mesh description which conforms to all individual components is challenging [63, 104]. This is especially true for anisotropic fibers, where knowledge of the material's axes for each fiber is required, contrary to isotropic fibers [100]. The continued reliance on FE is explained by the fact that many studies use simplified models for the microstructure, e.g., single fiber RVEs or a handful of perfectly aligned continuous fibers [37, 93, 190, 197, 198, 200, 201]. Those models are well-suited for woven composites, in which the spatial arrangement of (continuous) fibers is regular and predictable, and the warp and weft structure is usually handled at a second homogenization step [37, 197, 198]. Furthermore, for viscoelasticity, the evaluation of constitutive equations is performed at several time increments, rather than for a single one in elasticity, making the CPU and memory requirements of the FE method impractical for

RVEs featuring $\sim 10^3 - 10^4$ fibers. To circumvent those issues, mesh-free methods have been developed, which have recently been extended to the case of SFRPs made by FFF, notably in [45, 203]. A leading example of mesh-free methods is that developed by Moulinec and Suquet [110, 183, 189, 217]. In this method, the constitutive relations are transposed in the Fourier domain and solved iteratively via the Fast Fourier transform, hence it is called the FFT method. It has been demonstrated to produce more accurate predictions than analytical methods [45, 166], and has lower computational requirements than the FE method [26].

To date, few studies have been performed on the thermo-viscoelasticity of SFRPs made by FFF, but the topic is well developed for fiber-reinforced polymers more generally, be it continuous fibers or molded short fibers composites. Models that explicitly consider temperature and time-dependent materials, with anisotropic relaxation or creep tensors include: Halpin and Pagano [218], Poon and Ahmad [38], Yi et al. [33], Taylor et al. [20], and Petterman and DeSimone [29]. Extensions to nonlinear viscoelasticity (using the Shapery model [219]) include Yi et al. [33], Lévesque et al [220], and numerical implementation details and an alternative Finite Differences formulation are discussed in Crochon et al. [221]. Thermo-rheologically complex anisotropic materials are discussed in Sawant and Muliana [36]. An important limitation of many of those studies is that they often lack experimental data to inform or validate the constitutive laws presented, and many are validated against other numerical implementations.

7.3.1 Linear thermo-viscoelastic constitutive relation

The Generalized Maxwell Model (GMM) [23–28, 32, 36] expresses the relationship between the stress and strain histories as:

$$\boldsymbol{\sigma}(t) = \mathbf{C}^{(\infty)} : \boldsymbol{\varepsilon}(t) + \int_0^t \sum_{i=1}^{N} \mathbf{C}^{(i)} \left(e^{-\omega_i (t-\tau)} \right) : \frac{\mathrm{d}\boldsymbol{\varepsilon}(\tau)}{\mathrm{d}\tau} \mathrm{d}\tau = \int_0^t \mathbf{C}(t-\tau) : \frac{\mathrm{d}\boldsymbol{\varepsilon}(\tau)}{\mathrm{d}\tau} \mathrm{d}\tau \qquad (7.3.1)$$

or, the strain history as a function of the stress history as:

$$\boldsymbol{\varepsilon}(t) = \mathbf{S}^{(0)} : \boldsymbol{\sigma}(t) + \int_0^t \sum_{i=1}^{N} \mathbf{S}^{(i)} \left(1 - e^{-\lambda_i (t-\tau)} \right) : \frac{d\sigma}{\mathrm{d}\tau} \mathrm{d}\tau. \qquad (7.3.2)$$

Here, $\boldsymbol{\sigma}(t)$ and $\boldsymbol{\varepsilon}(t)$ are the time-dependent stress and strain, respectively. $\mathbf{C}(t)$ and $\mathbf{S}(t)$ are the time-dependent stiffness and compliance, which are composed of $i+1$ individual tensors $\mathbf{C}^{(i)}$ and $\mathbf{S}^{(i)}$, which can be of any material symmetry class (positive semi-definite, symmetric

tensors), and are related to i relaxation times ω_i or $\lambda_i > 0$.

For thermo-rheologically simple materials, temperature-dependence is described through the concept of internal time [21, 34] by the time-temperature superposition principle, in which real time t is adjusted by a shift factor function a_T, which depends on temperature T such that:

$$\mathbf{C}(t, T) = \mathbf{C}\left(\frac{t}{a_T(T)}\right). \tag{7.3.3}$$

Below the glass transition temperature (T_g) of the polymer, the a_T function can be expressed by the Arrhenius relationship as per [35]:

$$\log(a_T) = \frac{E_a}{\ln(10)R}\left(\frac{1}{T} - \frac{1}{T_0}\right), \tag{7.3.4}$$

where E_a is the polymer's relaxation activation energy, R is the ideal gas constant and T_0 is a reference temperature. Once $\mathbf{C}(t, T)$ is known for the polymer matrix, it can be used in conjunction with the fiber stiffness $\mathbf{C}_f$ in analytical or numerical homogenization schemes to predict the overall viscoelastic properties of a composite.

7.3.2 Homogenization models

Several studies focus on short or continuous fibers use either regular (periodic) or randomly arranged aligned fibers. A non-exhaustive list includes the following authors. Pathan et al. considered a 2D description of randomly spaced, aligned fibers. They considered linearly elastic, isotropic fibers and linearly viscoelastic isotropic matrix. The resulting composite was transversely isotropic due to perfect fiber alignment. They compared the prediction of several analytical estimates for all five independent transversely isotropic coefficient estimates against those of numerical homogenization, and found that Mori-Tanaka and Lielen's model were the most accurate. They also conducted a RVE size analysis, as measured by fiber count. They found the axial tensile modulus E_l to be RVE size-independent (it is fiber-dominated) and the numerical homogenization predictions coincided exactly with any of the mean-field methods employed. Across all five transversely isotropic coefficients, the authors concluded that, for this microstructure, a RVE size of 12 fiber radii, including 30 realizations, was sufficient to produce a prediction accuracy of $\pm 5\%$.

In a series of recent studies, Cruz-González et al. [190, 199, 200] proposed a model in which asymptotic homogenization was used in which the scale separation between the smallest

features and the macroscale that encompasses a regular arrangement of fiber was exploited to diminish the computational workload. To expand the method to non-continuous fibers for which closed-form solutions are not known, the FE method was employed on unit-cells containing a single short fiber. The FE resolution was made in the Laplace-Carson domain at a number of evaluations of p, the time variable in the Laplace-Carson domain. They compared their method to experimental data on continuous fibers for oblique loading at several angles and reported relative error between 3 and 7%. They demonstrated that their method could be used for short, aligned fibers which could be all be rotated by a fixed angle, though no experimental comparison was made for that case.

Studies that are concerned with the response to a cyclical loading can take advantage of the correspondence principle and avoid the interconversion back to the time-domain. Considerable success was achieved for simple morphologies, notably for isotropic matrix and fibers, with either perfect alignment [194–196] or following a particular orientation distribution [196]. Conejos et al. [198] used a dual-scale approach to model the thermo-viscoelastic response of fiber reinforced aluminium under cyclical loads at various frequencies and temperatures, using a full-field FE method both at the microscale and the scale of woven fibers.

Gusev studied analytical homogenization methods applied to fiber-reinforced viscoelastic materials [196]. The Monte-Carlo method was used to produce either aligned ellipsoidal inclusions, aligned spherocylindrical inclusions, or spherocylindrical inclusions with a specified fiber orientation distribution and constant aspect ratio. He studied the dependence of viscoelastic compliance on fiber aspect ratio and filling fraction. The viscoelastic behavior was modelled with the storage and loss moduli used in dynamic mechanical analysis and fibers were considered isotropic (glass fibers). He then compared each scenario by homogenization in the viscoelastic regime for either Mori-Tanaka, the self-consistent scheme, or the Advani Tucker orientation averaging procedure for non-ideal fiber orientation distribution. He found that Mori-Tanaka's model yielded the most accurate prediction for spherocylindrical inclusions, which is surprising because it is derived using the ellipsoidal Eshelby tensor description. He did not however consider the transverse isotropy of inclusions, as his target material was isotropic glass fiber reinforced polymers.

An et al. [27] created RVEs by arranging unidirectional fibers in regular arrays, such as a rectangular or hexagonal grid, and produced an `ABAQUS` plugin to help user define their own UMAT (user-defined material) subroutine for anisotropic viscoelastic behavior of composites with the specified material inputs and geometries. They compared the predictions of these UMATs against data from the asymptotic homogenization procedure (see [190]) and found good agreement (within 1%).

Wang et al. [93] studied the effect of fiber volume fraction and fiber aspect ratio on the homogenized creep compliance of discontinuous aligned fibers, in a elementary unit-cell RVE, and for several packing geometries. They confirmed that fibers have the most notable effect on the direction of alignment, and that fiber aspect ratio amplifies this effect: longer fibers increase stiffness.

Chen et al. [205] developed a constitutive model of linearly viscoelastic behavior for finite (large) deformations. They implemented this model in unidirectional randomly spaced continuous fibers and found good agreement between FE modelling of the finite strains and their constitutive model, with $< 1\%$ error in the axial direction and up to 5.12% error in the transverse direction. Their RVE relied on 12 continuous aligned fibers, no porosity, and regular spatial distribution.

Anoop et al. [25] and Luo et al. [222] investigated the behavior of 3D-printed polylactic acid (PLA), both through modelling and experimental characterization, and demonstrated that the printing pattern makes the viscoelastic properties orthotropic, with the highest stiffness along the print direction, even in the absence of reinforcements.

To the author's knowledge, the thermo-viscoelastic behavior of the specific morphology of SFRPs made by FFF has only been studied in [45], using artificial microstructures generated from imaging data. The fact that, in elasticity modelling, the best results are obtained when imaging data is used to directly create geometrical descriptions for the purpose of homogenization, makes us believe that using that approach in thermo-viscoelasticity will also yield more accurate results.

7.4 Methods and materials

Figure 7.1 presents a schematic of the entire modelling approach. The homogenization procedure requires material properties characterization of the neat (pure) polymer, in its 3D printed form, as well as the CF stiffness data. A viscoelastic material law for the polymer matrix was generated using experimental creep-recovery data. The microstructure description was achieved via analysis of µCT imaging data, in which porosity and individual fibers were identified. The AMITEX FFT homogenization software was then used to produce an effective relaxation curve, at the 2 temperatures at which the experimental characterization was performed. These relaxation curves were then used to fit a temperature-dependent anisotropic viscoelastic law, which is encapsulated in a UMAT subroutine. The second homogenization step was then performed using AMITEX, with the UMAT behavior law representing the microstructure response of the fiber-matrix composite and a mesostructure description

including mesoscale porosity. The output of this homogenization was a set of simulated creep-recovery curves, created under the same loading conditions as those obtained experimentally for the CF-reinforced specimens. The simulated and experimental data were then compared to validate the method.

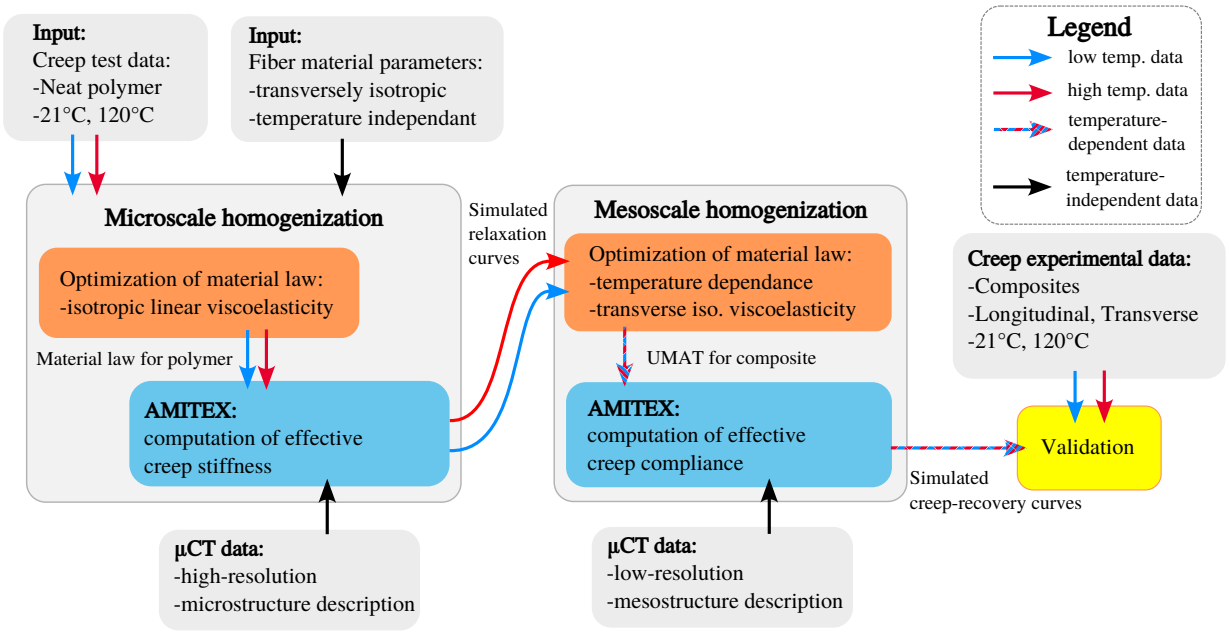

Figure 7.1 Schematic of the dual scale homogenization procedure. The first homogenization was done using a polymer material law derived from experimental data and a microstructure description extracted from µCT imaging. The output of the first homogenization was used to create a temperature-dependent anisotropic material law which, along with a mesostructure description, was homogenized again to create simulated creep-recovery curves. These are compared with experimental data on reinforced polymer to validate the approach.

7.4.1 Specimen preparation

As presented in Figure 7.2, standard ASTM D638 Type 1 dogbone specimens were manufactured in an AON3D™ Mark 2 3D printer for the purpose of viscoelastic characterization. Using neat PEEK filament (Tecafil™ PEEK VX Natural from Ensinger) and the corresponding 30 wt.% CF reinforced variant (Tecafil™ PEEK VX 30CF), 4 specimens for each of the following material/printing pattern configuration were made: neat filament/0° (all print passes in the long axis of the specimen), reinforced filament/0°, reinforced filament/90° (all print passes in the perpendicular direction). The printing parameters used were as follows: nozzle diameter: 0.4 mm, layer height: 0.2 mm, extrusion width: 0.42 mm, extrusion multiplier: 0.95, speed: 30 mm/s, infill: 100%, nozzle temperature: 410°C (neat polymer) and

440°C (reinforced polymer), chamber temperature: 120°C, bed temperature: 180°C.

7.4.2 Creep-recovery tensile testing

The composite's axial creep compliance was measured for specimens printed at 0°, and the transverse compliance for those printed at 90°. Only measurements on 0° specimens are required for the neat polymer, as the creep compliance of PEEK resin is considered isotropic [28, 216]. As per the ASTM D2990 standard, for materials exhibiting linearly viscoelastic behavior, each specimen was subjected to at least three loading levels within the linear range. Using a MTS Insight Material Testing system, the loading was applied in less than 5 seconds, then kept at this loading level for a fixed time t_0, then released for a recovery time at no load of $4t_0$ before a new loading was applied. The axial and transverse strain data was recorded with an MTS biaxial extensometer model number 634.25F-25, as shown in Figure 7.2b). The linearly viscoelastic range was ascertained by applying progressively higher loads, then normalizing each strain response as a function of time by the applied stress. By taking the lowest loading level as a reference point, with axial strain $\varepsilon_o(t)$ and stress σ_o, the mean relative error quantifying deviation from linear behavior is defined as:

$$e_i = \frac{\sum_{n=1}^{N} \left| \frac{\varepsilon_i(t_n)}{\sigma^i} - \frac{\varepsilon_o(t_n)}{\sigma_o} \right|}{N} \tag{7.4.1}$$

where e_i is the error associated with loading level i, $\varepsilon_i(t)$ is the axial strain and σ^i is the (constant) applied stress for loading i, n it the index in the time-series, and N are the total number of data points for a given stress level. In this work, a maximum relative error of less than 0.5% was chosen to define the linear regime. Once the threshold for linear viscoelasticity was known, all specimens were subjected to at least 3 loading levels below it.

To characterize temperature dependence, the procedure is done once at room temperature (21°C) and at 120°C, using a Thermcraft™ LBO-series laboratory oven. As per the ASTM 2990 standard, specimens were pre-conditioned at the target temperature for at least 48 hours before starting the creep-recovery testing procedure.

7.4.3 Tomographic data acquisition and analysis

The scanning procedure used here has been described in detail in [164,203], and is summarized here. To achieve a microstructure description of sufficient quality, a high-resolution scan was performed on a small piece (cylinder of $\sim$ 1.5 mm diameter and height) carved from the central region of the composite dogbone specimens, in a Zeiss XRadia™ 520 micro-

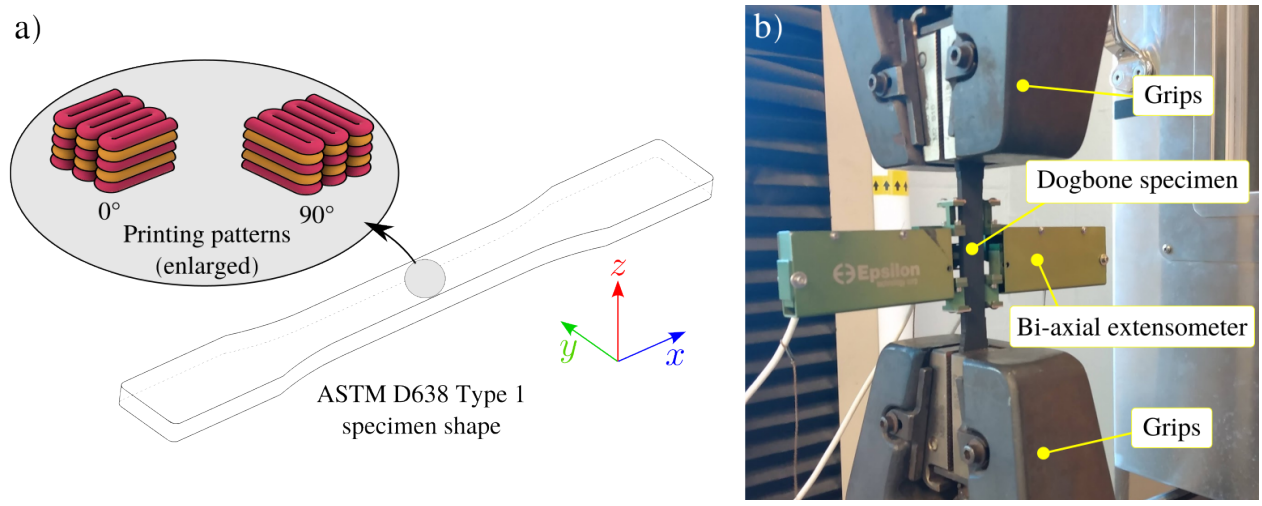

Figure 7.2 Specimen geometry and tensile testing setup. a) Schematic representation of the printing patterns used to produce the ASTM 638 Type 1 specimens. Two printing patterns were considered, either with all print passes aligned with the long axis (0° pattern, along the x-direction) or with passes along the y-direction, or 90° pattern. b) Specimen mounted in tensile testing machine, with extensometer attached.

tomographic scanner. As presented in Figure 7.3a), a series of 4 scans in a 2×2 grid pattern were made on samples extracted from 2 separate dogbone specimens. The scanning parameters for each scan were: source power: 7 W, source voltage 80 kV, distance from source to specimen: 9.0 mm, distance from detector to specimen: 23.0 mm, optical magnification: 10×, exposition time: 1.5 s, using 3200 projections. This configuration yields a pixel size of 0.758 μm, and a total acquisition time of 2 h 20 m for each of the 4 scans.

A low-resolution scan at a larger field of view (FoV) is also required to enable the mesoscale analysis. To that end, a cubic sample of 5 mm side was cut from a dogbone specimen, and scanned with the same acquisition parameters as above, except for the detector distance, now set to 9.0 mm, with optical magnification of 4×, 0.25 s exposition time and 1600 projections. This yielded a pixel size of 3.34 μm and a total scan time of 55 m.

7.4.4 Component extraction (OpenFiberSeg)

For both the micro and mesoscale scans, the imaging data was processed through an open-source software created by the authors called OpenFiberSeg [164], which was developed for the purpose of component (fiber, matrix and pores) identification and fiber tracking. In Figure 7.3a), the high-resolution imaging data for microstructure characterization is presented, and in Figure 7.3b) the result of the extraction procedure with OpenFiberSeg is presented. Once the component extraction and fiber tracking are performed, the density of pores can

be visualized using the following method. In the volume of data, each pixel is replaced with the value 1 where a pore is present, and 0 otherwise. Afterwards, the cumulative sum of 2D slices along the print direction is taken. This allows to appreciate the density variations in porosity, as presented in Figure 7.3c). The subvolumes required for the microstructure homogenization were then identified by selecting regions inside each print bead, avoiding the mesoscale porosity, as shown in colored rectangles in Figure 7.3c).

The same procedure was performed on the mesoscale imaging scan, as presented in Figure 7.4. At this resolution, the fibers cannot be identified, only the mesoscale pores are clearly visible in Figure 7.4a). The labelling of porosity obtained by OpenFiberSeg is presented in light blue in Figure 7.4b). Here, the subvolume definition for the mesoscale homogenization should respect the natural periodicity produced by the printing pattern, so that volume made from periodic repetitions of the RVE has the same grid-like pattern as the real solid [4]. As represented by the red rectangle in Figure 7.4c), the subvolume definition spans 4 layer widths and 8 layer heights.

7.4.5 Identification of polymer viscoelastic parameters

A linearly isotropic viscoelastic constitutive law for the polymer matrix is required to be used as an input for the microscale homogenization. The procedure detailed in Appendix 7.8 was used to derive this law from the creep-recovery curves obtained experimentally. The relaxation times λ_i were chosen to be evenly distributed on a logarithmic range from $[1, 10^4]$ seconds (which is $10\times$ more than the load duration in the experimental test data), with 2 values per decade, as per:

$$\lambda = \left\{ 1, \frac{1}{10^{\frac{1}{2}}}, \frac{1}{10^{1}}, \frac{1}{10^{\frac{3}{2}}}, \frac{1}{10^{2}}, \frac{1}{10^{\frac{5}{2}}}, \frac{1}{10^{3}}, \frac{1}{10^{\frac{7}{2}}}, \frac{1}{10^{4}} \right\}. \tag{7.4.2}$$

For each relaxation time ω_i, the corresponding $\mathbf{C}^{(i)}$ isotropic tensor identified was decomposed into its isostatic and shear moduli, respectively denoted κ_i and μ_i.

In addition, the fitted constitutive law must be representative of the neat polymer in the absence of porosity, as the inter and intrabead porosity is considered at the micro and mesoscale homogenization step, respectively. Therefore, the experimental data pertaining to the neat polymer must first be compensated for the porosity. Considering that the mesoscale porosity forms neatly aligned structures along the print direction, the Voigt mixture law was used to infer the properties of the neat matrix by itself. An estimate of the total porosity was obtained in the following way. By measuring the dimensions of each specimen, and comput-

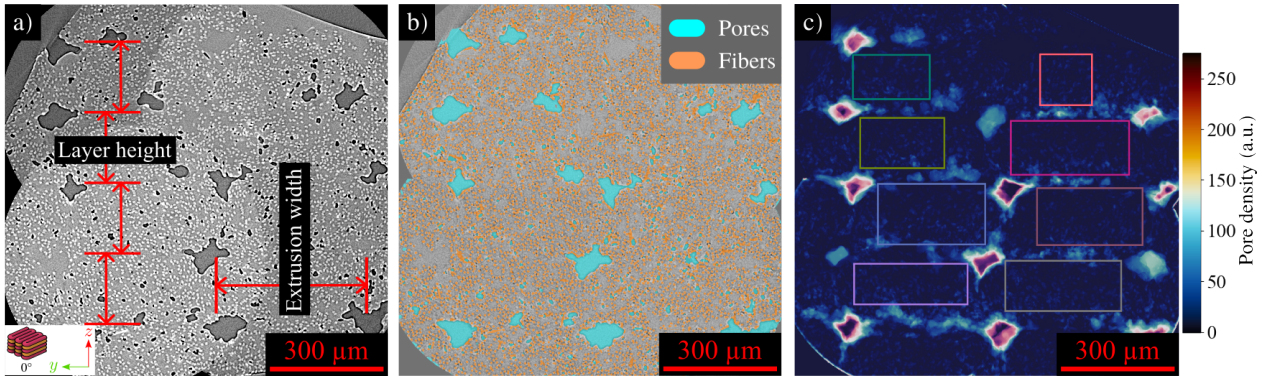

Figure 7.3 Tomographic data acquisition and microscale component extraction. a) Imaging data in a 2×2 grid. b) Visualization of fiber density. c) Visualization of pore density. Colored rectangles are the subvolumes selected for microstructure homogenization, avoiding the mesoscale porosity.

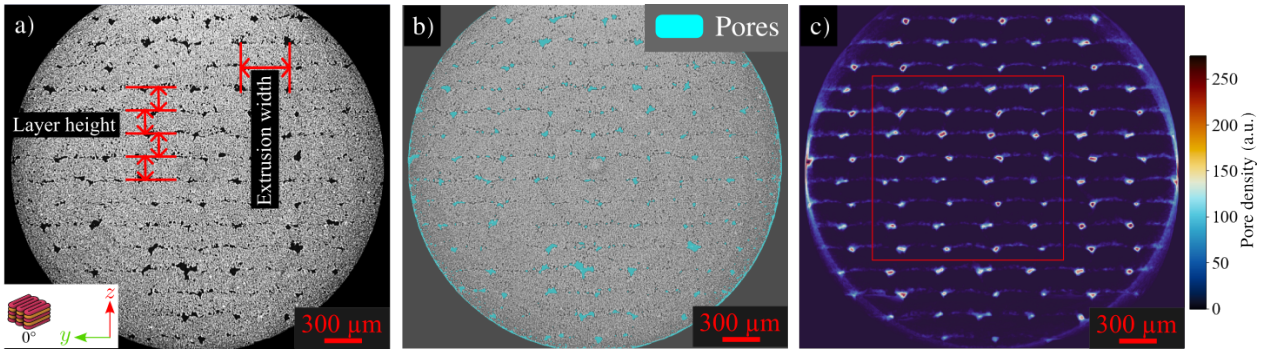

Figure 7.4 Tomographic data acquisition and mesoscale component extraction. a) Imaging data spanning $\approx$ 14 full layers. b) Labelling of mesoscale porosity. c) Visualization of mesoscale pore density. Red rectangle is the subvolume selected for mesostructure homogenization. The dimensions of the subvolume respect the natural periodicity created by the printing pattern, by having the boundaries in the middle of layers and in the center of printing beads.

ing its volume, its ideal mass m_{ideal} with zero porosity was computed using the density of the pure polymer as provided in the manufacturer datasheet [1]. Each specimen was then weighed, and the measured mass $m_{measured}$ was used to derive the porosity of each specimen as: $v_p = 1 - \frac{m_{measured}}{m_{ideal}}$. Then, each specimen cross-section measurement was compensated by this porosity factor, i.e., $A_{actual} = A_{external}(1 - v_p)$ and the true stress was obtained from the loading, as per $\boldsymbol{\sigma}(t) = F(t)/A_{actual}$, where $F(t)$ is the applied force at time t. A different set of $\mathbf{S}^{(i)}$ values were obtained for each of the temperatures used for experimental testing.

7.4.6 Homogenization

The micro and mesoscale homogenizations were performed with the help of the AMITEX software which implements the FFT homogenization method. The inputs to the software are the subvolumes as described in Section 7.4.4, along with the orientation of each individual fiber, which AMITEX interprets to rotate the fiber stiffness tensor accordingly. For microscale homogenization, the matrix material was described using the parameters produced by the optimization procedure described in Section 7.4.5, i.e., a series of $\mathbf{C}^{(i)}$ and corresponding ω_i. The conversion from $\mathbf{S}^{(i)}$ and λ_i was performed using the procedure described in [223]. The fibers were considered to be linearly elastic, with transversely isotropic symmetry. The set of parameters used correspond to Toray T300 fibers, which are reported in [2, 3]. If $\vec{e}_1$ is the axis of transverse isotropy, and $\vec{e}_2 \times \vec{e}_3$ the transverse plane, then the longitudinal modulus (along $\vec{e}_1$) is $E_l = 230$GPa, the transverse modulus is $E_t = 13.4$GPa, the Poisson's ratio between directions $\vec{e}_1$ and $\vec{e}_2$ is $\nu_l = 0.256$, the ratio between $\vec{e}_2$ and $\vec{e}_3$ is $\nu_t = 0.3$, and the shear modulus between axis $\vec{e}_1$ and $\vec{e}_2$ is $G_l = 27.3$GPa. Using AMITEX, relaxation curves were obtained for all the subvolumes pertaining to the microscale, using the matrix material parameters for both 21°C and 120°C, by prescribing a unit strain in all 3 reference directions, and in the 3 pure shear modes, and integrating the stress for $\Delta t = 40$ min for each loading case. At each time-step, the time-dependent stiffness tensor was constructed column-by-column, from the averaged stress field for each of the loading cases. These curves were used as the output of the microscale homogenization step.

Before the mesoscale homogenization can be performed, a material behavior law for the microstructure must be derived using these relaxation curves. To that end, an optimization procedure developed by Trofimov et al. [37] was used. In that method, the relaxation curves at several temperatures are used to optimize a material law of arbitrary symmetry, which includes temperature-dependence under the time-temperature superposition principle. The procedure is based on the NOMAD algorithm [224], and seeks a set of $\mathbf{C}^{(i)}$ and ω_i such that the distance between the relaxation curves obtained numerically and the input data is minimized

across all temperatures. Once convergence is reached, this material law representing the microscale behavior is encoded in a UMAT subroutine, which was then utilized inside AMITEX along with the mesoscale description (see Figure 7.4), to create simulated creep-recovery data at a specified temperature and loading profile. The output of the dual-scale homogenization procedure was validated by comparing it with the experimental creep-recovery curves for the reinforced specimens, at both 21°C and 120°C, when loading them in the axial direction, as well as in the transverse direction.

7.5 Results and discussion

An example of experimental stress-strain history curves, which are the starting point of the optimization procedure, are presented in Figure 7.5, for a neat polymer specimen printed longitudinally (0° print pattern). The subsequent stress levels σ_{axial} are shown (as compensated for actual specimen cross-section, see Section 7.4.5), along with the corresponding axial and transverse strain responses, or ε_{axial} and $\varepsilon_{transverse}$, respectively. The normalized ε_{axial} responses are also presented, where the lowest loading level was not considered for the material properties identification, as it can possibly be affected by initial play in the testing setup.

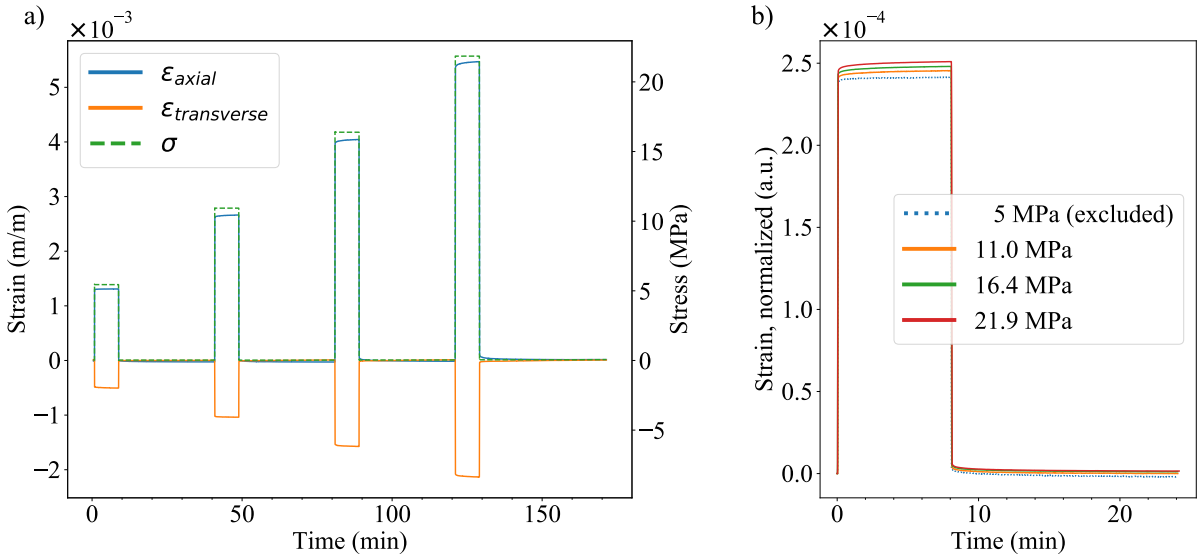

Figure 7.5 Example of stress-strain history curves for creep parameter identification, longitudinally (0°) printed specimen, neat PEEK polymer, at 21°C. a) Sequence of 8 min loadings, with 32 min recovery. b) Superposition of axial strain curves when normalized by loading level.

The pure polymer constitutive law numerical values (κ_i and μ_i) are presented in Table 7.1

and Table 7.2, for the low and high temperature inputs, respectively.

In Figure 7.6, the relaxation curves obtained from the microscale homogenization step and the resulting fit obtained with the method developed by Trofimov et al. are presented, for both 21°C and 120°C temperatures. It can be observed that the microstructure homogenization procedure produces relaxation curves that do not perfectly satisfy the transverse isotropy symmetry but show some degree of orthotropy. Under transverse isotropy, with the principal axis in direction $\vec{e}_1$, the components of the stiffness tensor involving $\vec{e}_2$ and $\vec{e}_3$ are identical. This is visible in the tensor expression, where elements $C_{22} = C_{33} \neq C_{11}$, and analogously for the shear terms: $C_{55} = C_{66} \neq C_{44}$. In these data, however, for all time steps both $C_{22} \neq C_{33}$ and $C_{55} \neq C_{66}$, which is indicative of orthotropic symmetry.

The following method was used to quantify the degree of conformity to either symmetry class. The distance to that representation type was measured by projecting the stiffness tensors at each timestep into the transverse isotropic space and the orthotropic space, i.e., by extracting the independent parameters for each and using those to re-construct the tensor. If $\mathbf{C}$ is a tensor of arbitrary symmetry, and $\mathbf{C}_{proj}$ is the reconstruction in either the transversely isotropic or orthotropic space, then the distance for each time point $d(t)$ is defined as:

$$d(t) = \frac{\|\mathbf{C}(t) - \mathbf{C}_{proj}(t)\|_{L2}}{\|\mathbf{C}(t)\|_{L2}}, \tag{7.5.1}$$

where $\| \, . \, \|_{L2}$ denotes the L2-norm (sum of squared elements). In Figure 7.7, the distances from both the microscale homogenization step and the final dual-scale homogenization are presented. In all cases, the distance to orthotropic symmetry is lower by a considerable margin ($\approx$ 70%). This indicates that the microscale morphology itself is orthotric. For both symmetry classes, the second homogenization step further breaks the symmetry, i.e., the distance to a perfect transversely isotropic or orthotropic material is larger. This means that although the printing pattern is regular, and orthogonal, the local variability in porosity

Table 7.1 Constitutive law parameters identified for the pure PEEK polymer specimens, at 21°C. Only the terms within 3 orders of magnitude of the largest values are kept.

i	κ_i (MPa)	μ_i (MPa)	ω_i (s)
0	6221	1185	$--$
1	2171	668	10^{0}
2	54	12	$10^{-\frac{1}{2}}$
3	0	9	10^{-2}
4	0	43	$10^{-\frac{7}{2}}$
5	239	242	$10^{-\frac{9}{2}}$

Table 7.2 Constitutive law parameters identified for the pure PEEK polymer specimens, at 120°C. Only the terms within 3 orders of magnitude of the largest values are kept.

i	κ_i (MPa)	μ_i (MPa)	ω_i (s)
0	5700	640	$--$
1	0	458	10^{0}
2	139	20	$10^{-\frac{1}{2}}$
3	6	9	$10^{-\frac{3}{2}}$
4	0	19	$10^{-\frac{5}{2}}$
5	729	649	$10^{-\frac{9}{2}}$

creates anisotropy in the most general sense. This global effect is small however, and for most applications considering transversely isotropic behavior rather than orthotropy would be sufficient.

Once a UMAT law was obtained for the composite material in the 3D printed form, a simulated creep-recovery test was done, under the same conditions as the experimental data for composite dogbones. In Figure 7.8, the resulting comparison for an axial loading on a longitudinally printed (0° pattern) dogbone and the axial loading on a perpendicular (90° pattern) are presented. The average prediction error over all N time steps is defined as:

$$e = \frac{\sum_{n=0}^{N} \left| \frac{\varepsilon_{exp}(t_n) - \varepsilon_{sim}(t_n)}{\varepsilon_{exp}(t_n)} \right|}{N}, \tag{7.5.2}$$

where ε_{exp} and ε_{sim} are the experimentally measured and simulated strains at time t, respectively, and $|.|$ denotes the absolute value operation. The computed error values for each scenario are presented in Table 7.3 For the longitudinal printing pattern, the match between simulation and experiment is within 3%. For the perpendicular printing pattern, the match is far less accurate, with a maximal error reaching nearly 25% for the axial strain. However, the transverse strain, which in this configuration (90° printing pattern) is the strain along the stiff axis, remains within 3% mean relative error, suggesting the error originates from the load transfer from polymer to fibers in the transverse direction. Several phenomena were considered to possibly close this gap, however each strategy encountered only partial results. As the fiber type is not known with certainty, it is possible that the material properties used are not correct. If the transverse modulus E_t or the shear modulus G_l were lower, the compliance across the transverse direction would be larger. However, even when these values are reduced to a degree that is not physically realistic (e.g., 10% of the values stated in Section 7.4.6), the compliance obtained is only increased by a small margin, insufficient to reach the experimental values. The impact of fiber-matrix interface was also considered.

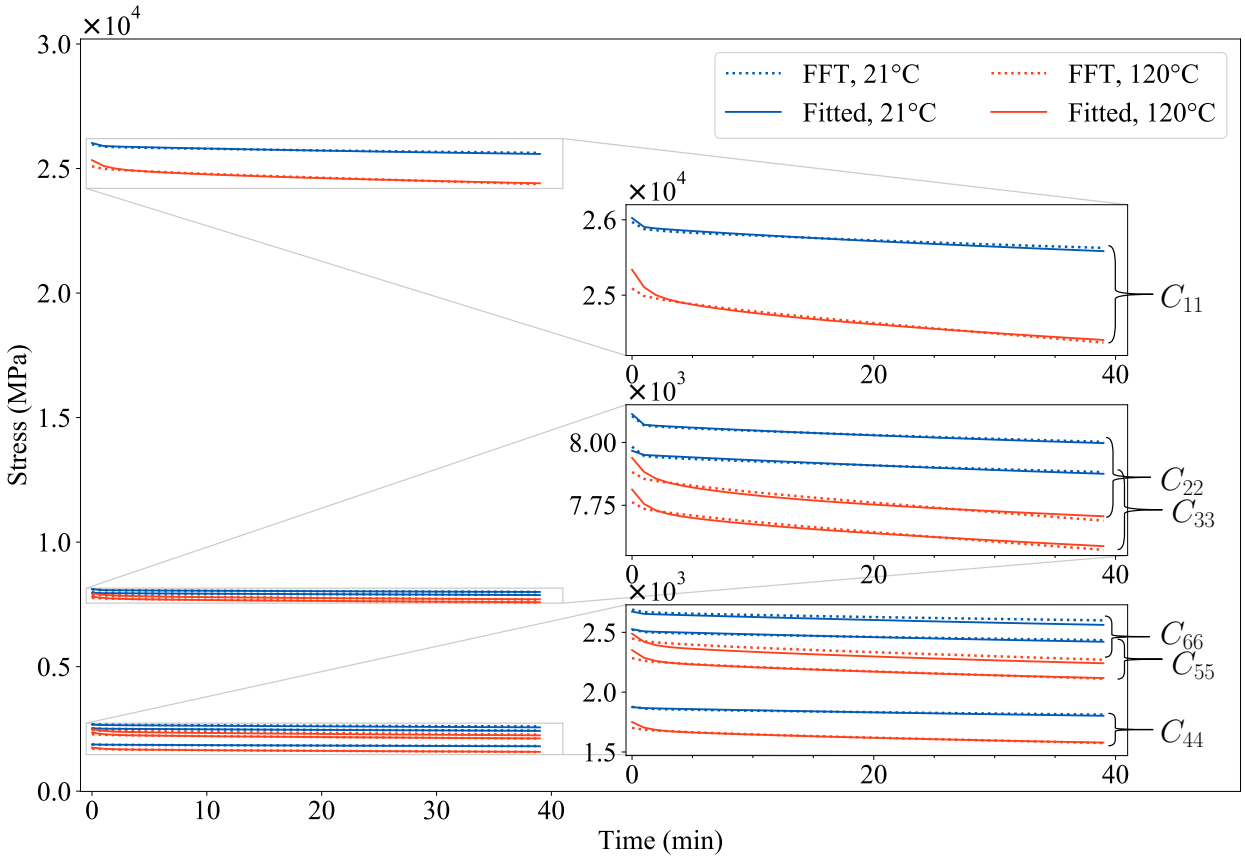

Figure 7.6 Output of the microscale homogenization: the dotted lines are the relaxation curves produced with the FFT method, considering the microscale description, the fitted parameters for the matrix behavior, and the fiber properties. The full lines are the result of the optimization of parameter for the composite behavior, given these relaxation curves.

As a first approximation, the pixels immediately in contact with each fiber perimeter were labelled as interface. Then, to allow for the possibility that the wetting and therefore the load transfer from matrix to fiber is only partial, the interface pixels were assigned a set of penalized properties, relative to the matrix values. However, this method also only encountered partial success at compensating for the transverse compliance, and values that had a significant effect on the transverse behavior also negatively affected the axial behavior. Further investigation of the creep response to transverse loading is left for future studies.

7.6 Conclusion

The thermo-viscoelastic properties of SFRPs were investigated from a modelling standpoint using dual-scale homogenization, and from an experimental and material characterization

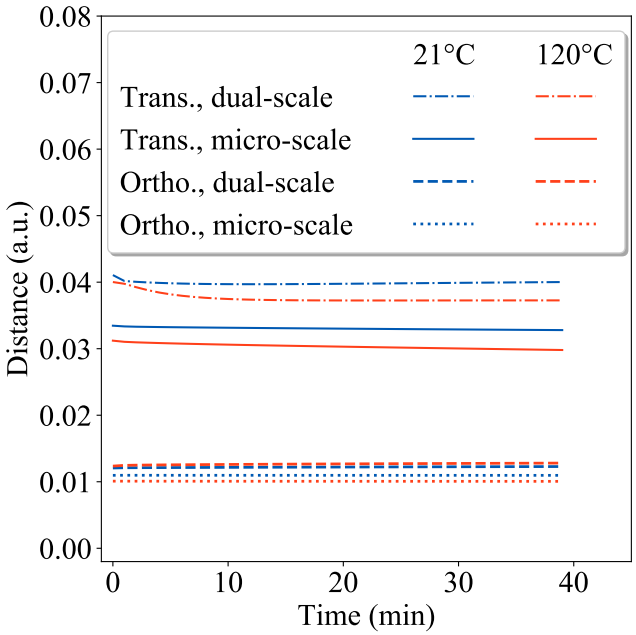

Figure 7.7 Homogenized tensors distance to transverse isotropy and orthotropy projections, at each time-step of a simulated relaxation test, at both the initial (microscale only) step and the final (dual-scale) result. The blue lines are for low temperature (21°C) and the red lines are for high temperature (120°C). In all cases the projection to orthotropic representation has a $\approx 70\%$ lower error value.

perspective. This holistic approach allows the inference of material properties such as orthotropy and the degree of thermal and temporal dependence of each independent material parameter. The use of RVEs obtained from imaging of physical specimens is proven to be necessary in the process of obtaining constitutive laws which account for the morphology seen in SFRPs made by FFF. The scale separation was exploited, such that the microscale behavior was homogenized first, then a material law was optimized for it, which was then used to homogenize the mesoscale structure. The computational advantage of this dual-scale procedure is clear, as the pixel size necessary to differentiate fibers is small, and using it for the mesoscale would produce an RVE of impractical size. This approach opens the door to a more advanced series of studies on the matter of SFRPs, as the RVE obtained through volumetric imaging and specialized processing are published alongside this study: both source code and processed volumes spanning 10^6 differentiated fibers are available. While the prediction of axial viscoelastic behavior as a function of temperature is demonstrated to be highly accurate (3% mean relative error between simulated and experimental results), the same material constitutive law submitted to transverse loading produces predictions that

Table 7.3 Relative error between the experimental strains (ε_{axial} and $\varepsilon_{transverse}$) and the strain predicted by the dual scale homogenization method.

	21°C		120°C	
Printing pattern	ε_{axial}	$\varepsilon_{transverse}$	ε_{axial}	$\varepsilon_{transverse}$
Longitudinal (0°)	0.39%	0.97%	1.51%	2.38%
Transverse (90°)	24.5%	3.14%	24.3%	3.31%

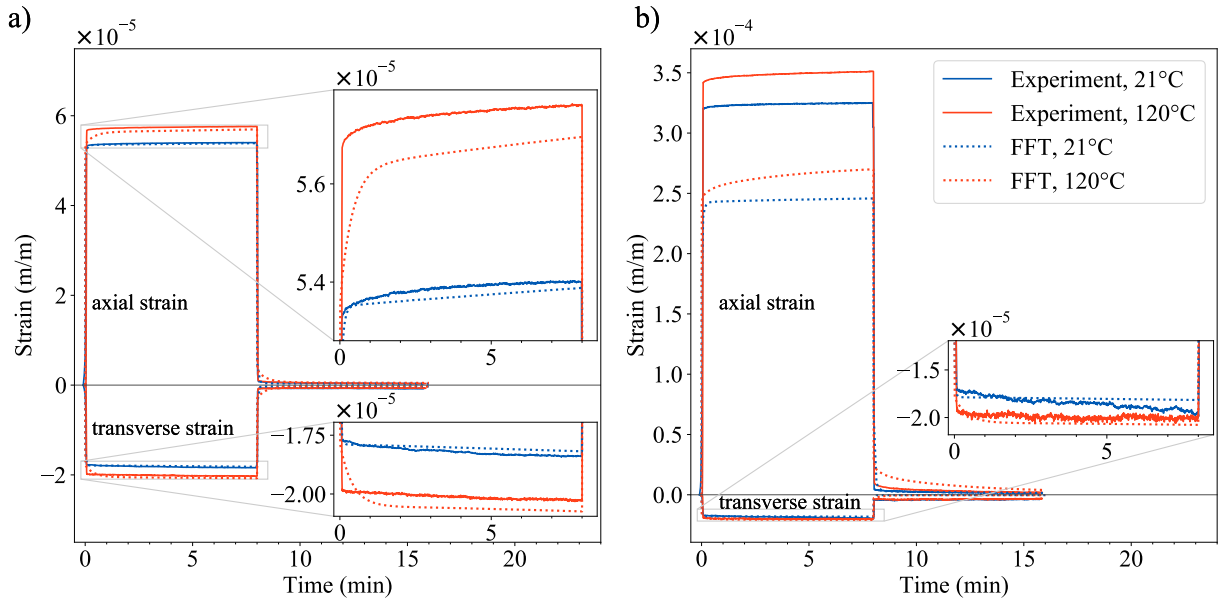

Figure 7.8 Output of dual-scale homogenization compared with averaged experimental creep-recovery curves on fiber-reinforced dogbone specimens. Axial and transverse strain are shown, for both the low (21°C) and high (120°C) conditions. a) Longitudinal (0°) printing pattern. b) Perpendicular (90°) printing pattern.

overestimate the stiffness by a considerable margin (25% mean relative error). Future work related to this topic include the extension to other fiber-matrix combinations, more elaborate printing patterns, and the consideration of other physical transport phenomena such as thermal and electrical conductivity, thermal expansion, and the aging of polymer matrix.

7.7 Source code and data repository

The component extraction code (OpenFiberSeg), along with the implementation of AMITEX using the microstructure description obtained with it are available at `https://github.com/lm2-poly/OpenFiberSeg`. The imaging datasets are also released, along with fully processed RVEs. While the anisotropic optimization procedure is not published due to confidentiality

agreements with our industrial partner, this work has been described in detail in previous publications [37].

CRediT authorship contribution statement

Facundo Sosa-Rey: Conceptualization, Methodology, Formal analysis, Software, Validation, Writing - Original Draft. **Alessandra Lingua:** Experimental investigation. **Nicola Piccirelli:** Project administration. **Daniel Therriault:** Supervision, Writing - Review & Editing. **Martin Lévesque:** Supervision, Writing - Review & Editing.

Acknowledgements

This research is supported financially and made with the scientific collaboration of Safran S.A. (FACMO Research Chair). Funding is also provided by the Natural Sciences and Engineering Research Council of Canada (Alexander Graham Bell Canada Graduate Scholarship program, and the Collaborative Research and Development program, grant no CRDPJ514761). Further funding was obtained through the Génie Par la Simulation (GPS) program. Computational resources were made available by Calcul Québec (`calculquebec.ca`) and the Digital Research Alliance of Canada (`alliancecan.ca`).

7.8 Appendix: Fit of isotropic constitutive law parameters

The load profile for each creep-recovery test was modelled by:

$$\boldsymbol{\sigma}(t) = H(t)\left(\frac{\sigma_o t}{t_1}\right) + H(t-t_1)\left(-\frac{\sigma_o t}{t_1} + \sigma_o\right) + H(t-t_2)\left(-\sigma_o - \frac{\sigma_o t}{t_3 - t_2}\right) + H(t-t_3)\left(\frac{\sigma_o t}{t_3 - t_2}\right) \tag{7.8.1}$$

where t is the time variable, $H(t)$ is the Heaviside step function and σ_o is the applied (axial) stress. $t = 0$ is the initial load application time, t_1 is when full loading is reached, t_2 is the load release time, and t_3 the time at which load returns to 0. By inserting Equation (7.8.1) into the constitutive law (7.3.2), we obtain:

$$\begin{aligned}\boldsymbol{\varepsilon}(t) = \mathbf{S}^{(0)}\boldsymbol{\sigma}(t) + \sum_{i=1}^{N}\mathbf{S}^{(i)}\frac{\sigma_o}{t_1}\left(t - \frac{1}{\lambda_i}(1-e^{-\lambda_i(t)})\right)H(t) \\ -\mathbf{S}^{(i)}\frac{\sigma_o}{t_1}\left(t - t_1 - \frac{1}{\lambda_i}(1-e^{-\lambda_i(t-t_1)})\right)H(t-t_1) \\ -\mathbf{S}^{(i)}\frac{\sigma_o}{t_3-t_2}\left(t - t_2 - \frac{1}{\lambda_i}(1-e^{-\lambda_i(t-t_2)})\right)H(t-t_2) \\ +\mathbf{S}^{(i)}\frac{\sigma_o}{t_3-t_2}\left(t - t_3 - \frac{1}{\lambda_i}(1-e^{-\lambda_i(t-t_3)})\right)H(t-t_2).\end{aligned} \tag{7.8.2}$$

The experimental values of $\boldsymbol{\varepsilon}(t)$ was used to infer the $\mathbf{S}^{(i)}$ and λ_i such that the difference between the $\boldsymbol{\varepsilon}(t)$ obtained with Equation (7.8.2) and the experimental data is minimized. To reduce the complexity of the optimization problem, the following variable change was made. Each isotropic tensor can be written as $\mathbf{S}^{(i)} = \alpha_i\mathbf{J} + \beta_i\mathbf{K}$, where $\mathbf{J}$ is the hydrostatic and $\mathbf{K}$ the deviatoric 4th-order tensors [225]. Using the definitions $\mathbf{J}$ and $\mathbf{K}$, equation (7.3.2) can be expressed as:

$$3\boldsymbol{\varepsilon}_1(t) = (\alpha_o + 2\beta_o)\boldsymbol{\sigma}(t) + \int_o^t \sum_{i=1}^{N}(\alpha_i + 2\beta_i)\left(1 - e^{-\lambda_i(t-\tau)} : \frac{d\sigma}{\mathrm{d}\tau}\right) \tag{7.8.3}$$

$$3\boldsymbol{\varepsilon}_2(t) = (\alpha_o - \beta_o)\boldsymbol{\sigma}(t) + \int_o^t \sum_{i=1}^{N}(\alpha_i - \beta_i)\left(1 - e^{-\lambda_i(t-\tau)} : \frac{d\sigma}{\mathrm{d}\tau}\right). \tag{7.8.4}$$

Then, by taking:

$$\begin{aligned}\boldsymbol{\varepsilon}^{\dagger}(t) &= \check{\boldsymbol{\varepsilon}}_1(t) - \check{\boldsymbol{\varepsilon}}_2(t) \\ \boldsymbol{\varepsilon}^{\dagger\dagger}(t) &= \check{\boldsymbol{\varepsilon}}_1(t) + 2\check{\boldsymbol{\varepsilon}}_2(t)\end{aligned} \tag{7.8.5}$$

with $\check{\boldsymbol{\varepsilon}}_j$ the experimental strain along direction $j = 1, 2$ (axial and transverse, respectively), variables $\boldsymbol{\varepsilon}^{\dagger}(t)$ and $\boldsymbol{\varepsilon}^{\dagger\dagger}(t)$ allow the fit of parameters α_i and β_i to be done independently, using at once the axial and the transverse experimental data. The non-negative condition on α_i and β_i was removed by optimizing instead for x_i and y_i such that $\alpha_i = x_i^2$ and $\beta_i = y_i^2$, which makes the optimization problem unconstrained. To optimize the parameters, the Levenberg-Marquardt algorithm in Matlab™ lsqnonlin was used, defining the residual using the averaged stress-strain time series as:

$$\begin{aligned}\mathrm{res}_{\alpha} &= \boldsymbol{\varepsilon}_{\alpha}^{LM} - \boldsymbol{\varepsilon}^{\dagger\dagger}(t) \\ \mathrm{res}_{\beta} &= \boldsymbol{\varepsilon}_{\beta}^{LM} - \boldsymbol{\varepsilon}^{\dagger}(t)\end{aligned} \tag{7.8.6}$$

where $\boldsymbol{\varepsilon}_{\alpha}^{LM}$ and $\boldsymbol{\varepsilon}_{\beta}^{LM}$ are the strains given via the coefficients found via Levenberg-Marquardt.

The interconversion between the identified $\mathbf{S}^{(i)}$ into $\mathbf{C}^{(i)}$ was then performed with the procedure explained in [223].

CHAPTER 8 COMPLEMENTARY WORK: RVE size convergence study using realistic microstrutures

The advantage of using imaging data from printed specimens for homogenization has been demonstrated in Chapters 6 and 7. Having the ability to produce large datasets with explicitly identified constituents presents with the opportunity to carry out a rigorous evaluation of the RVE size for SFRPs made by FFF. In addition, the effect of morphological factors such as fiber and pore volume fraction, fiber's average length and orientation on estimated mechanical properties such as E_l and E_t can be analyzed separately, as each subvolume can be treated as a statistical sample of the material.

8.1 Creation of large microstructure description

As presented in Figure 8.1, a similar procedure as that used in Sections 6.4.3 and 7.4.4 was used to create a larger dataset from multiple individual scans. An ASTM D638 type 1 dogbone specimen was printed from reinforced PEEK (using commercial filament Tecafil™ VX 30CF) with the 0.4 mm nozzle with the 0°-0° pattern (see Section 7.4.1 for details on processing parameters). A segment of $\approx$ 1.5 mm diameter was then carved from it. A low-resolution (large FoV) scan of the carved segment is presented in Figure 8.1 a). Then, the same segment was repeatedly scanned at high resolution, with each FoV carefully placed in a 3×3 grid, in such a manner that FoVs overlap to completely cover a wider volume, as shown in Figure 8.1 b). Once the data was acquired, each of the 9 datasets were juxtaposed by manually adjusting the coordinates so that fibers and pores that cross the boundary between neighboring scans are correctly aligned, as shown in Figure 8.1 c). In this Figure, the 9 individual scans are given an intensity offset in a checkered pattern, so that continuity across boundaries can be visually assessed. The combined tomographic dataset was then processed using OpenFiberSeg in the same manner as for individual FoV, on a compute server with enough memory capacity ($\approx$ 200 GB) for the task. Three such datasets were produced and processed in this manner. The processing for those datasets took 20 days using 32 CPUs, identifying $\approx 10^6$ individual fibers. The result of the segmentation is presented in Figure 8.1 d) and e), showing the fiber and the pores density, respectively. The fiber density is nearly homogeneous except at the locations of mesotructure porosity (there are no fibers inside pores). The pore density concentrates at the corners of each print bead, and between print layers.

Under the hypothesis that a volume of this size is larger than the minimum RVE size for this

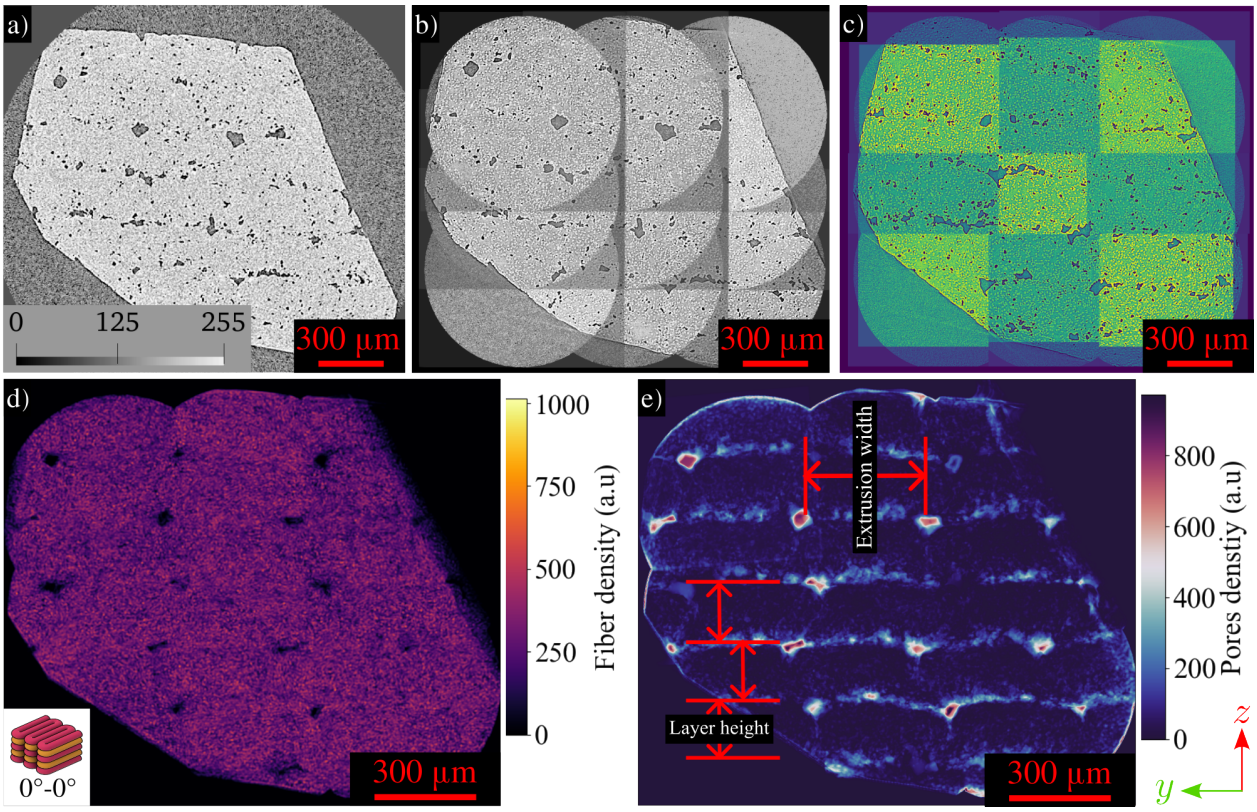

Figure 8.1 Creation and processing of a large dataset from a specimen printed with the 0°-0° pattern. a) Low-resolution scan with large FoV. b) 9 high-resolution scans, in a grid pattern. c) Manual cropping and juxtaposition. OpenFiberSeg results: d) fiber density and e) pore density, revealing the printing pattern.

microstructure, elasticity homogenization is performed using first the largest subvolume that respects the natural periodicity of the printing pattern, as shown in Figure 8.3. The largest rectangle encompassing the 4 smaller ones starts and ends in the middle of a layer, and at the center of a bead. The largest volume is then partitioned by dividing in each direction by a power of 2. There are therefore $2^3 = 8$ subdivisions in the first set (as presented in Figure 8.2), $4^3 = 64$ in the second and $8^3 = 512$ in the third. For each of these subdivisions, FFT homogenization is performed in the way presented in Section 6.4.4. The results of those simulations are presented in the following sections.

8.2 Homogenization results

For each realization processed through AMITEX, the five transversely isotropic parameters were extracted from their homogenized stiffness tensors. The longitudinal and transverse tensile moduli, respectively E_l and E_t, obtained for each subdivision are presented in Figure 8.4

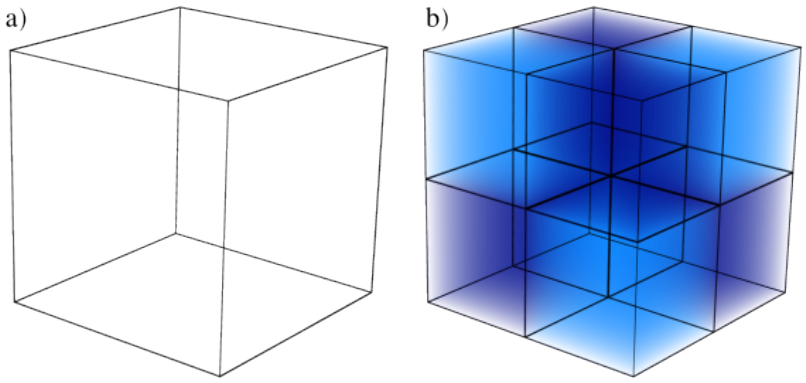

Figure 8.2 Subdivision process of data volume. a) Single, whole volume before any subdivision. b) Grid of $2 \times 2 \times 2 = 8$ sudvisions of the volume at the first level of subdivisions.

as a function of fiber count. The longitudinal shear moduli G_l, and the longitudinal and transverse Poisson's ratio, ν_l and ν_t are presented in Figure 8.6. From the dotted trend lines connecting the average values for each subdivision level, out of the 5 transversely isotropic parameters, the values which converge the slowest among those are E_l.

In Figure 8.5, the mean values of E_l for each subdivision level is presented, along with the total CPU time required to process those microstructures through AMITEX. The value for E_l estimated at the subdivision level 64 (near 10^3 fibers) is within 5% of the asymptotic value, but the processing time required is more than 40 times lower.

Using these data, the influence of factors that are generally thought to influence mechanical properties can be examined in isolation. In Figure 8.7, the longitudinal modulus E_l is presented as a function of mean fiber length and mean fiber deviation in each of the subdividions. E_l shows a moderate positive correlation (computed at 0.37) with mean fiber lengths, and a moderate negative correlation with mean fiber deviation (computed at -0.4). These observations are consistent with expectation, though they had not been quantified previously.

In Figure 8.8, the dependence of E_l on the fiber and pore volume fraction is presented. Surprisingly, the correlation with fiber volume fraction is weak, measured at 0.2. This suggests that fiber fraction by itself is not a sufficient indicator of overall stiffness, but rather it's combination with alignment and low porosity for instance. The correlation with pores fraction is negative and stronger, measured at -0.6. This is in line with expectation, as pores have a negative effect on stiffness.

The Kanit method presented here is usually performed on artificially generated microstructures. However, reaching high volume fractions and aspect ratios with predominant alignment is a long-standing problem in the field [4, 45, 63, 98, 167]. The use of imaging data instead

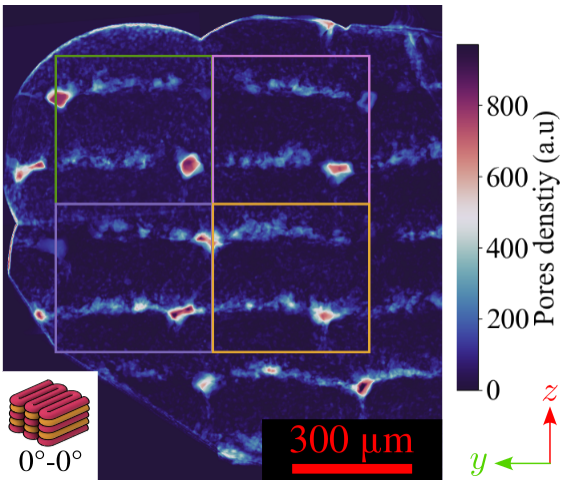

Figure 8.3 Definition of subvolume inscribed in the natural periodicity of the printing pattern. The largest volume is then divided by 2 along each dimension as shown. Here 4 squares are visible, out of the 8 cubes formed by the subdivision process.

allows the method to be applied in those regimes. Observing the convergence of properties in data obtained experimentally is a strong validation that the Kanit method is applicable in materials showing these morphological features.

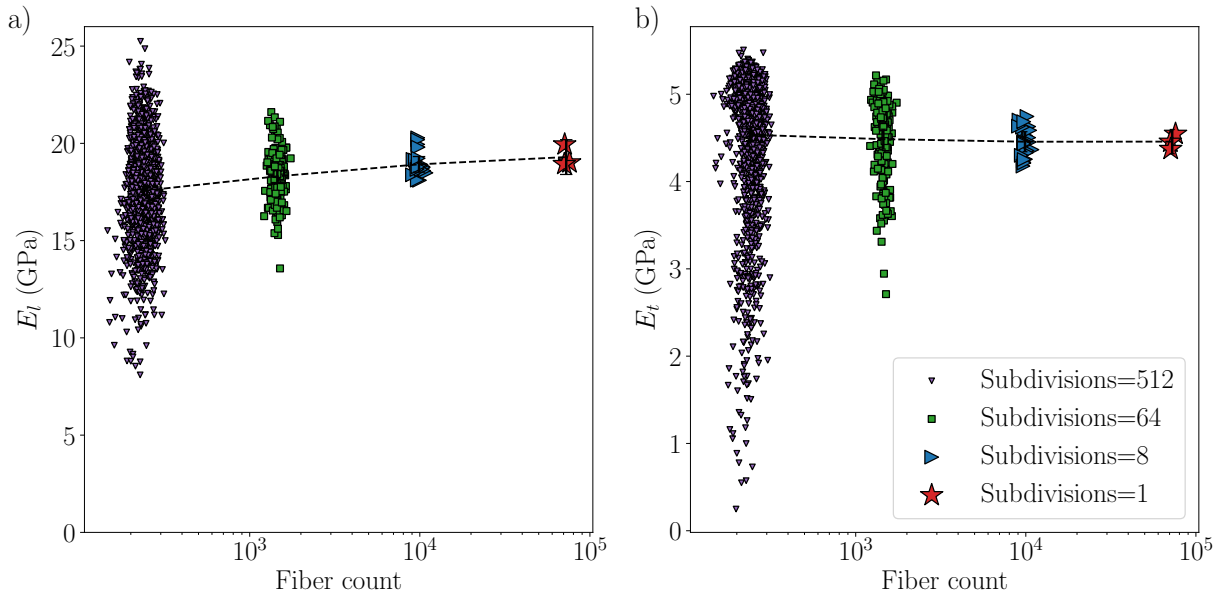

Figure 8.4 Longitudinal and transverse tensile moduli (E_l and E_t, respectively) of each realization as a function of fiber count

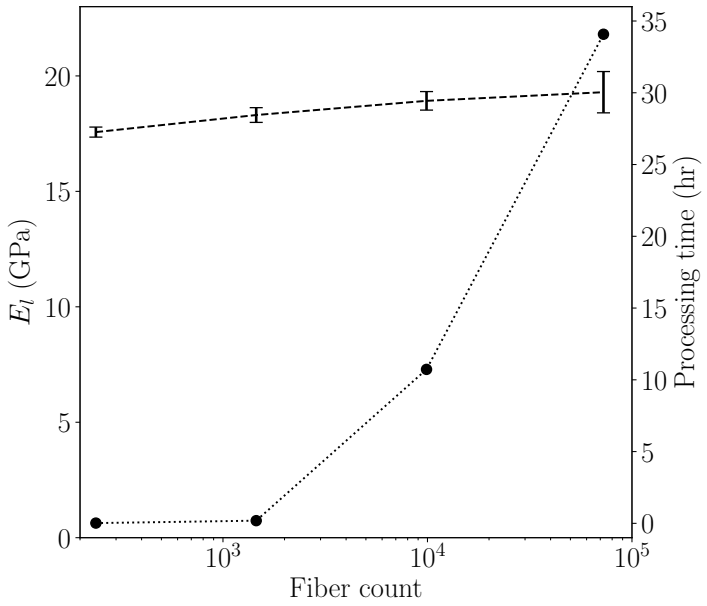

Figure 8.5 Mean longitudinal tensile moduli E_l of each realization as a function of fiber count, with 95% confidence intervals. Total processing time for each subdivision level.

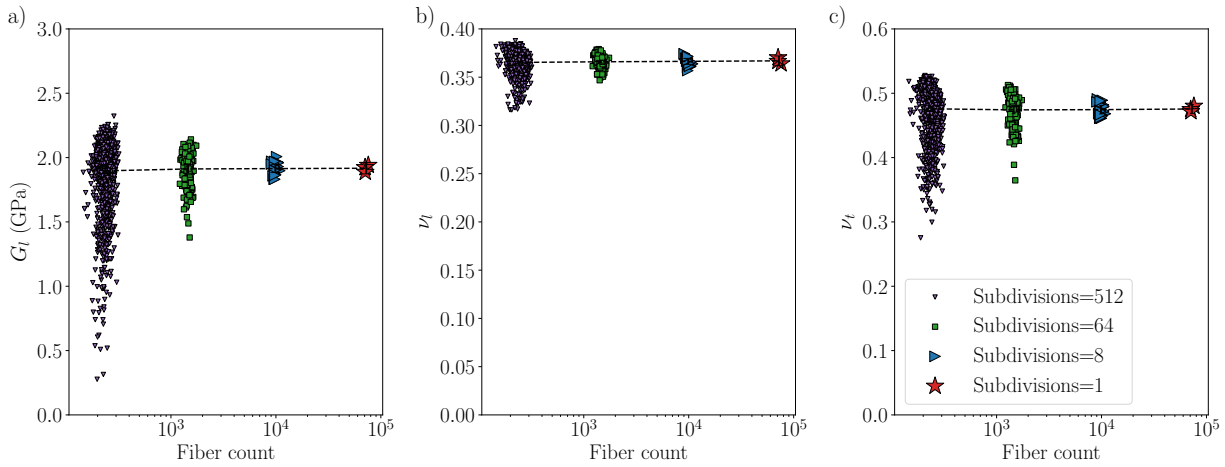

Figure 8.6 Longitudinal shear modulus G_l and Poisson's ratio ν_l, transverse Poisson's ratio ν_t of each realization as a function of fiber count

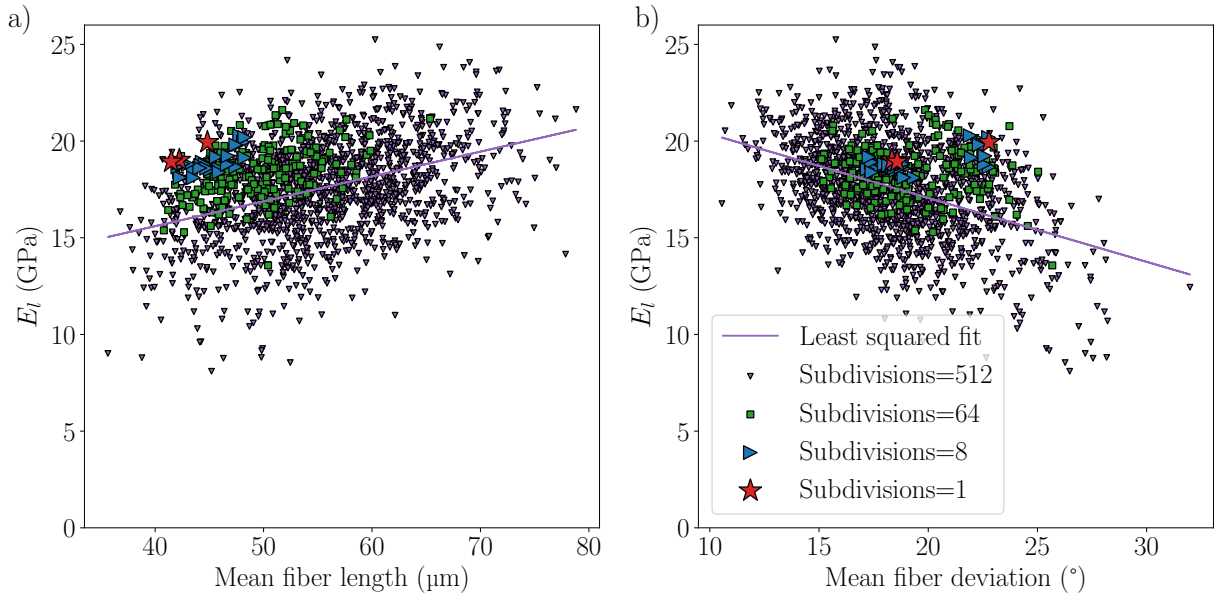

Figure 8.7 Longitudinal tensile modulus E_l for each realization, showing the dependence on mean fiber length and mean fiber deviation from printing direction

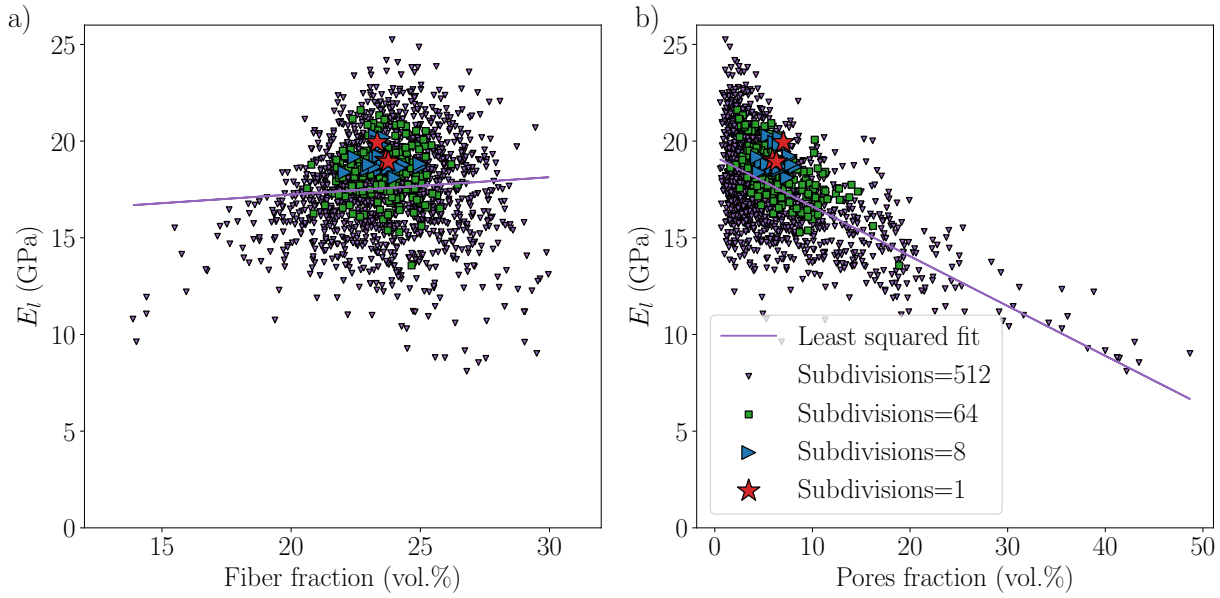

Figure 8.8 Longitudinal tensile modulus for each realization, showing the dependence on fiber volume fraction and pore volume fraction in each.

CHAPTER 9 GENERAL DISCUSSION

9.1 Generalization of the method presented

Two variants of CF-reinforced PEEK were studied in this thesis. In Chapter 5, a custom mixture of Victrex 90G PEEK and chopped Panex 35 CF was used, at various infill levels, produced at LM2. In Chapters 6 and 7, the commercial product Tecafil™ VX 30CF by Ensinger was used. In both cases, the polymer used is a high-performance polymer with high melting temperature and high viscosity, which is challenging to successfully form into filament spools while minimizing porosity. The reliance on a commercially available product for the characterization efforts undertaken increases the usefulness and potential reproducibility of the results presented. However, the morphological attributes observed in the previous chapters are likely to be somewhat unique to the combination of materials studied, and the additives and other industrial secrets that are involved in its processing, which are not disclosed by the manufacturer.

In order to extend this work and generalize it, it would be of great utility to have the ability to estimate the properties of other combinations of polymer and reinforcements, without having to manufacture them first. However, several factors make such an endeavor difficult. For instance, through the work pertaining to Chapter 5, specimens were also fabricated using Poly-Ether-Imide (PEI) resin, and PEEK reinforced with milled CFs. In Figure 9.1, the experimentally measured tensile modulus, tensile strength and porosity of several samples at each level of CF filling fraction is presented (see Sections 5.6.1 and 6.4.2 for details on the experimental procedures). While the dependence of tensile modulus on CF filling fraction is simply understood, as it roughly follows a linear law (except for a filling of 10%, where the porosity is high), the strength and porosity data are much less regular. These data illustrate an important point: knowledge of the material properties given one particular combination and ratio of constituents cannot reliably be used to predict the properties for significantly different ratios. For instance, the tensile strength of chopped CF-PEEK increases for high filling fractions, above the levels for the neat resin. This is not the case for milled CF-PEEK or chopped CF-PEI, for which the tensile strength remains below that for neat resin at all filling ratios.

Nonetheless, the microstructural features observed in Chapter 5 for a variety of CF filling fractions can be used as a starting point for material system design which could possibly include other polymer matrices such as PEI, polyamide-6 (PA6), polycarbonate (PC), different grades of CF, and other reinforcement materials such as glass fibers or natural fibers like

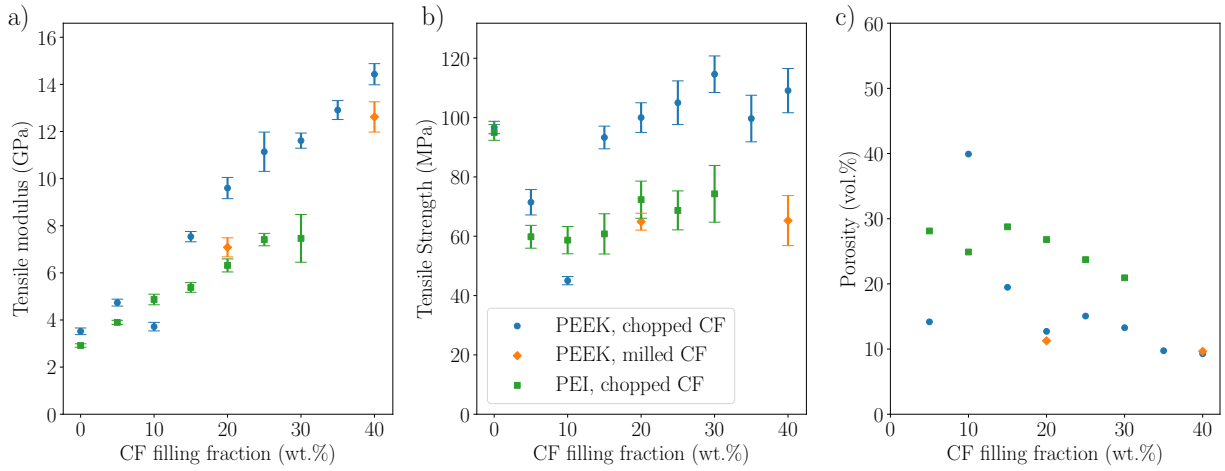

Figure 9.1 Experimental measurements of a) tensile modulus, b) tensile strength and c) porosity for specimen made with Victrex 90G PEEK mixed with chopped and milled CFs, and Ultem1010 PEI mixed with chopped CFs, at several fiber volume fractions.

hemp or wood. Mechanical properties could be estimated using the microstructures found in our specimen data, but the accuracy of such estimates remains to be demonstrated, especially with polymers which have vastly different rheological properties to PEEK, in which case the morphology as a function of processing parameters could be significantly different.

In addition to nozzle diameter and the few printing patterns considered in this thesis, there are many more process parameters which all work in concert to produce unique morphological attributes. First, the filament production step is complex and has many adjustable parameters, then arriving at general rules of thumb to optimize the 3D printing process itself across various material systems is notoriously difficult. For the work on commercial filaments presented here, the parameter search (speed, bed temperature, nozzle temperature, chamber temperature, layer height, extrusion width, extrusion multiplier) was done by a trial-and-error process, and the first pass of optimization was performed on the basis of quality of printing assessed visually. Once parameters were narrowed, µCT observations were used to gauge the level of internal porosity and layer adhesion, to determine final print settings. Some of the parameters chosen were a limitation of our equipment, as the manufacturer recommends 250°C for the chamber temperature when printing with PEEK, but the AON3D MK2 printer can only reach 135°C. The high viscosity of CF-reinforced PEEK means the flow through the nozzle can settle into metastable states such as oscillations, as presented in Figure 9.2. In Figure 9.2 a), the visualization of length distribution features flow patterns which are not in perfect alignment with extrusion direction. In Figure 9.2 c), the somewhat wavy nature of the flow is revealed, as the flow trendline is not straight but oscillating. The

non-aligned nature of the flow is corroborated by visualizing the alignment with a direction perpendicular to the extrusion direction, which is labelled y in Figure 9.3. In this figure, a light color indicates stronger alignment with the vertical direction in the image, and a darker green color is away from it. The same pocket of flow identified in Figure 9.2 a) can be seen here as better aligned with y. To the extent that such flow structures are common, they could be the source of some of the spatial variability and local gradients observed in printed specimens in Chapter 6.

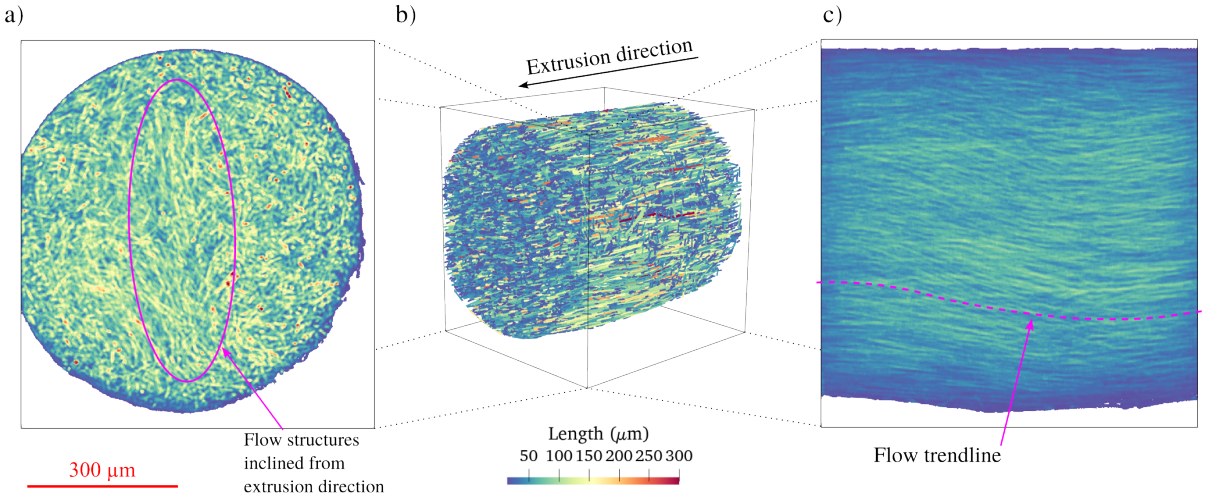

Figure 9.2 Morphological visualization: Oscillations observed in free-space extrusion using nozzle diameter 0.8 mm. a) Cumulative sum of the lengths in the FoV, in the plane normal to extrusion direction. b) 3D-rendering of the fibers in the FoV, colored by length. c) Cumulative sum of the lengths in the FoV, in a plane parallel to the extrusion direction.

Again, it is possible that these observations and other morphological properties discussed are unique to the particular polymer and reinforcement under study, and the processing parameters used. The question of whether some of the insights are generalizable to other polymer/reinforcement combinations is quite relevant, and can only be answered by future studies on the topic, some of which are already underway at LM^2. But while the finely resolved features like spatial variation in local properties and the differential concentration of fibers at interface regions may differ from one material system to another, there are coarser features that can be generalized with more confidence.

For instance, the microstructures as observed in Chapter 5 (at several fiber volume fractions, see Figure 5.15) can be inserted into the mesostructures as presented in Chapters 6 and 7 (see Figures 6.4 and 7.4), and the homogenization procedure could predict with high confidence the tensile properties of materials created from those fiber volume fractions using a particular nozzle and printing patterns. As demonstrated in Section 6.5.6, the majority of the variation

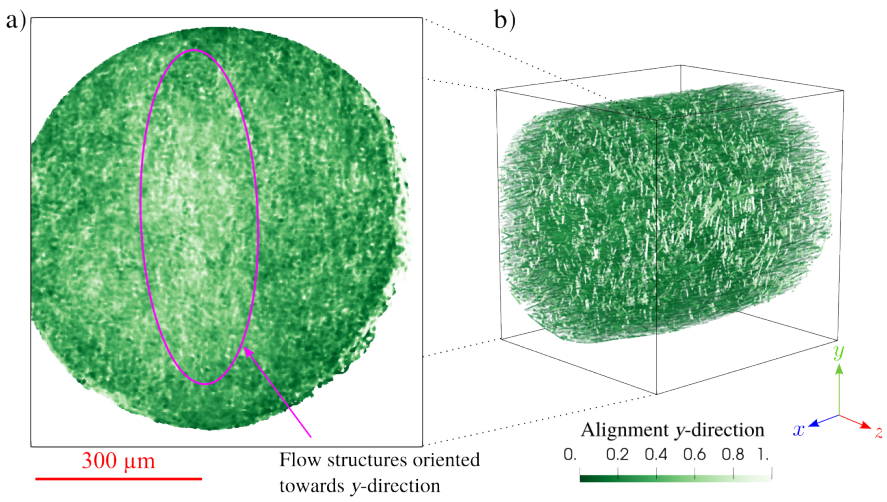

Figure 9.3 Morphological visualization: Alignment with the y-direction. a) Cumulative sum of the alignment in the FoV, in the plane normal to the extrusion direction. b) 3D-rendering of the fibers in the FoV, colored by length.

between specimen configuration is attributed to the microscale features, not the mesoscale. Therefore, using a generic mesoscale description for other microstructure types should leave the prediction accuracy largely unaffected.

9.2 Investigation of interlayer properties

In FFF, the deposition of material in layers creates an interlayer region, where the welding of beads occurs. It is often mentioned that the different mechanical properties at the interlayer region are responsible for much of the observable differences between printed and injected parts, especially in terms of tensile strength. The extensive characterization performed now enables the discussion of how the morphological features at the interface diverge from those of the bulk material. Using the data presented in Section 8.1, and the visualization of morphological properties by 2D cumulative sum, a further reduction of the data is performed, as presented in Figure 9.4. The 2D mappings in each subfigure is averaged along the vertical direction (excluding positions where no data exists, such as pores), and this averaged data is normalized by its maximum value. The data thus created represents the variation of a property as a function of a single coordinate, in this case the z-direction, which is the direction normal to the bed plane. The resulting values for each property, which vary between $0 - 1$ are plotted in red on top of the 2D cumulative sums they pertain to. In Figure 9.4 b), the fiber density is seen to have little dependence on the z position, though it has noticeable dips at the interlayer regions. In Figure 9.4 c), the average length is shown to have a much

larger dependence, as the average value drops by 20% in the interlayer region. In Figure 9.4 d), e) and f), the average alignments with directions x (the printing direction), y (the other in-plane direction), and z is shown. In the interlayer regions, the alignement with the print direction x drops, and more dispersion in y and z is noticeable. Therefore, this data reveals that the interlayer regions have lower than average fiber lengths, and the alignment with the printing direction is lower than in the bulk of the material. In addition to the partial polymer welding that exists in this region, those morphological attributes contribute to explain the consistently lower strength values in the direction normal to the layer plane.

9.3 Sensitivity of homogenization to extraction parameters

In Chapter 5, the image analysis and fiber extraction tool make use of parameters which have been optimized to yield results that are as accurate as possible for the materials under consideration, as evaluated by visual inspection (see Section 5.4 for details). It is reasonable to expect that the precise parameter selection influences the mechanical prediction quality performed in Chapters 6 and 7 as well. For instance, the volume fraction in the extracted volume will be affected by the sensitivity of the machine learning-based voxel-wise identification. Successfully identifying the fiber boundaries is still an outstanding problem, as those are not readily identifiable in visual inspection, and the sharpness of the boundary is affected by the scan quality and the tomographic reconstruction parameters. Future work would be required to investigate the precise relationship that exists between those parameters and the predicted mechanical properties. One effect of relevance occurs at the location of contact between fibers. If there are pixels that are identified as belonging to different fibers that are immediately adjacent, there would exist a perfect load communication at those locations, which is not what we expect in real materials. This effect is a possible explanation for the over-estimation of transverse creep stiffness in the mechanical simulations in Chapter 7.

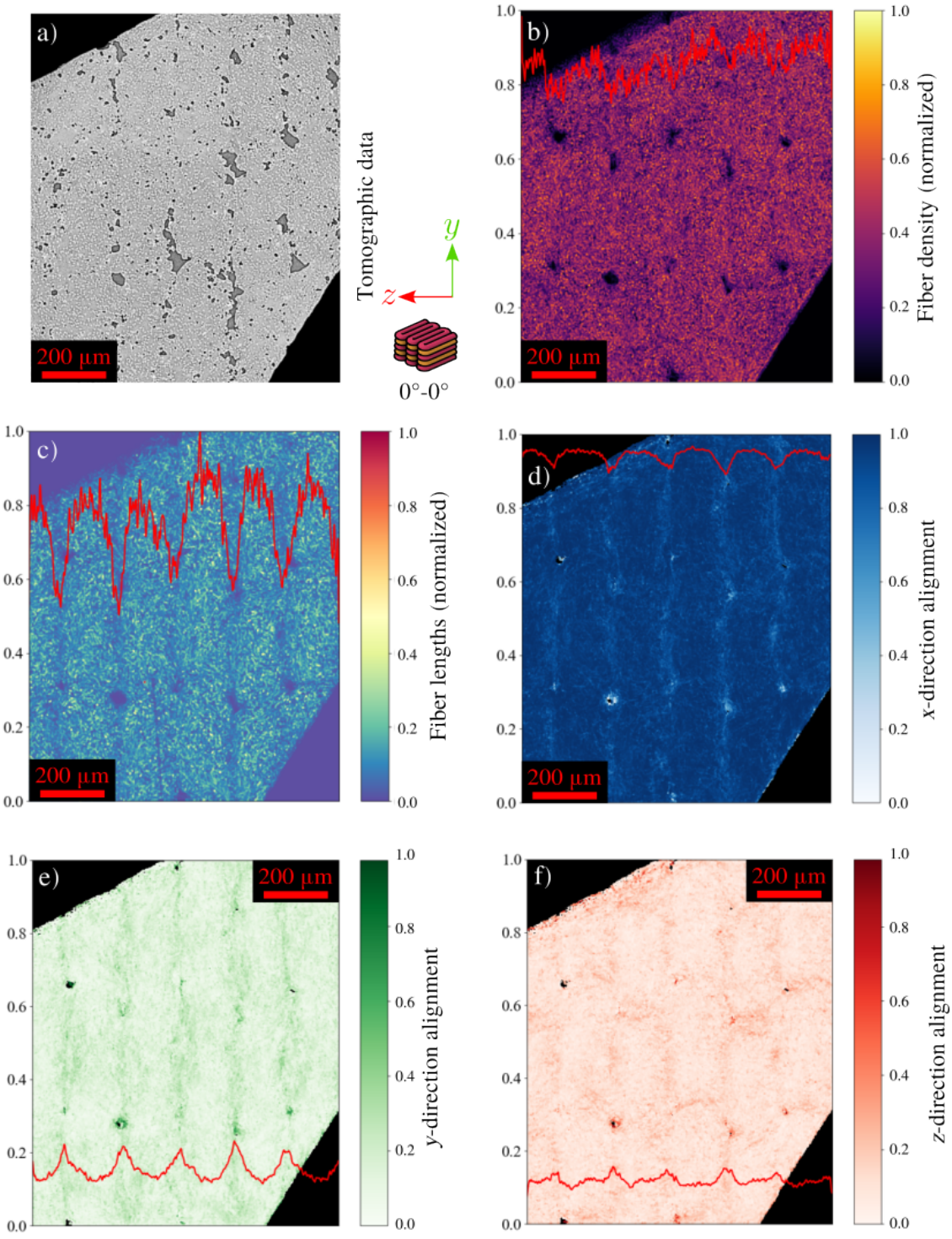

Figure 9.4 Interface property variation as a function of position in the z-direction (normal to the print bed). Specimen printed with 0.4 mm nozzle, in the 0°-0° printing pattern. a) Slice of the tomographic data, where the print direction is out of the page. b) Cumulative sum of the fiber density in the volume. c) Cumulative sum of the fiber lengths.) d) Cumulative sum of the alignment with the x-direction (print direction). e) Cumulative sum of the alignment with the y-direction. f) Cumulative sum of the alignment with the z-direction. For each case, the red line is the average value over the vertical direction, giving a estimation of the variation of the property in question along the position in z.

CHAPTER 10 CONCLUSION AND RECOMMENDATIONS

In this work, the process-structure-property relationship of SFRPs made by FFF was investigated, and a methodology for relating microstructure characterization of printed specimens to effective properties was developed and validated. An automated tool called OpenFiberSeg was developed for the purpose of extracting individual components from µCT imaging data. With this tool, a volume of data is segmented (classified) into either fiber, pore or polymer matrix in a pixel-wise manner using machine learning (K-nearest neighbors method) and classical image processing (Canny edge detection and morphological operations). Then the regions containing fibers are grouped and differentiated using a special-purpose heuristic in which partial detections serve to inform on possible missing segments, enabling the reconstruction of entire fibers in an efficient manner, with little to no human input. The tool is validated by reproducing the results of two independent publications, and by visual inspection of the output when used on SFRPs with different levels of fiber volume fraction, which yields 93.1% accuracy on a per-voxel basis. The output was also validated globally by using it to calculate the density of the specimens directly from the tomographic data and comparing the estimate with experimental measurements.

OpenFiberSeg being fully automated, it can be used to process large quantities of data from several types of specimens without introducing user error or other types of experimental bias, though the quality of the segmentation is markedly dependent on the resolution and contrasts in the tomographic data used as input. Having a tool specifically designed for the type of morphological features found in SFRPs made by FFF has greatly facilitated the analysis of the process-structure relationship in those materials.

The process-structure-property relationship was then investigated, by producing specimen made with different nozzle diameters and printing patterns, in a total of five different configurations. Several tomographs were taken for each configuration, both at high resolution to characterize the microstructure, i.e., the individual fibers and small intra-bead pores, and at low resolution to analyze the mesostructure, i.e., the regular array of beads and larger porosity left by the printing pattern. The relationship between process parameters such as nozzle diameter and fiber lengths and orientation distribution were revealed experimentally for the first time, enabling the quantification of phenomena like fiber breakage and shear-induced fiber alignment during extrusion. The extraction of individual fibers in a volume of specimen also allows the analysis of variation of local properties such as fiber or pore density, degree of alignment, and lengths distribution. Up to now, localized gradients such as those were

suspected but had not been measured.

The advantage of using such a highly detailed characterization for tensile property prediction was demonstrated, by implementing a dual-scale FFT homogenization method based on imaging data, which reduces the relative error on tensile testing predictions by a factor of 4 compared to homogenization procedures using artificially generated micro and mesostructures.

Furthermore, the dual-scale homogenization method was extended to the thermo-viscoelastic domain. A procedure was devised, by which the parameters for the isotropic constitutive law pertaining to the neat polymer is identified from experimental creep-recovery data, then used in conjunction with detailed microstructure descriptions to create simulated relaxation curves. These curves were used to obtain an anisotropic, temperature-dependent constitutive law describing the creep behavior of the SFRPs at the microscale. Using this constitutive law and a mesostructure description, the macroscopic creep response to an arbitrary loading as a function of temperature can be predicted. The quality of these predictions was evaluated by using the behavior law produced to simulate creep-recovery tests on the SFRPs, which were compared against experimental multi-axis measurements on composite specimens. In the case of axial loading (0° printing pattern), the mean relative error of the predicted creep strain to the measured one was $< 3\%$ for both 21°C and 120°C. In the case of transverse loading (90° printing pattern), the error is much larger, reaching nearly 25% mean relative error. This is the first study to attempt to compare the predicted multi-axis response to experimental data for a homogenization model on SFRPs, and the general accuracy in axial loading is on par with leading methods in the field.

Limitations and recommendations for future studies This thesis centered on the modelling of effective properties of CF-reinforced PEEK, in the morphology produced by FFF. The definition of the scope of the work is such that several limitations can be mentioned.

In addition to the many other thermoplastics suitable for FFF, there are other types of reinforcements such as glass or natural fibers, for which the tracking procedure nor the homogenization models have not been tested. The tracking procedure as implemented assumes that each fiber can be considered straight. For longer fibers, such as those used in some injection molding applications, this assumption does not hold, and a more complex representation of fibers would be required that includes curvature, such as splines for instance. Such a description would considerably complicate the stitching heuristic, as the missing segments would also have curvature, making the identification and ranking of candidate matches much more demanding algorithmically. However, using OpenFiberSeg for SFRPs made by injec-

tion molding is already possible, which could help ascertain how FFF and injection affect morphological features differently.

The work presented in this thesis focusses on stiffness, either elastic or viscoelastic. However, stiffness is not the only mechanical attribute that is relevant to mechanical design: for many applications the tensile strength, elastic limit, fracture toughness, or impact hardness can be the main design criterion. For the study and prediction of all those features, having a highly resolved microstructure description is certainly an advantage. For instance, the degree of stress concentration at the microscale near fiber tips or at points of contact between fibers, which can be observed in the full-field solutions presented in Section 6.5.5, can be used as a starting point for fracture toughness evaluation. The influence of different properties at the fiber-matrix interface is also of great research interest, as they have been shown to affect elastic and fracture properties but are cumbersome to study, as the interface properties cannot be measured directly. The insertion of an interphase region in the immediate surrounding or fibers would provide a means of investigating those properties with inverse methods for instance. On the topic of temperature-dependent properties, the behavior law produced can accommodate temperature variations during loading. This feature was not tested numerically or experimentally, but that would be of considerable interest, as anisotropic thermal expansion is a non-trivial concern for mechanical designers. Another advantage of the encapsulation of the behavior law in a UMAT subroutine is that it can be used with any mechanical modelling software that accepts UMATs, not necessarily the AMITEX implementation presented here.

In addition, other types of physical laws can also be studied with a similar methodology as presented here. For instance, linear thermal or electrical conductivity has essentially the same mathematical expression as Hooke's law, therefore those properties pertaining to SFRPs could be evaluated using the dual-scale homogenization method, without modification. It would be interesting to compare those estimations with experiment, particularly anisotropic features. Anisotropic thermal conductivity and thermal expansion are of considerable technological interest, as tooling used in resin transfer molding technique, which require high temperature resistance could be manufactured using CF-reinforced PEEK or PEI by FFF instead of machined steel. In such cases, the tool warpage attributed to anisotropic thermal expansion change must be predictable to a high level of precision.

Finally, an area of research that was only touched on is the study of infill patterns, for which FFF offers great flexibility and potential for optimization. The emerging field of architected materials is becoming much more accessible thanks to low-cost FFF equipment, and the creation of functionally graded infill patterns is of great interest for technological

applications [226]. The ability to predict the macroscale properties of any arbitrary infill pattern increases the potential for computational optimization of such materials.

REFERENCES

[1] Victrex PLC, "Victrex peek 450g," November 2019. [Online]. Available: https://www.victrex.com/en/downloads/datasheets/victrex-peek-450g

[2] Toray Composite Materials America, Inc, "T300 datasheet," November 2022. [Online]. Available: https://www.toraycma.com/wp-content/uploads/T300-Technical-Data-Sheet-1.pdf.pdf

[3] H. Miyagawa, T. Mase, C. Sato, E. Drown, L. T. Drzal, and K. Ikegami, "Comparison of experimental and theoretical transverse elastic modulus of carbon fibers," *Carbon*, vol. 44, no. 10, pp. 2002–2008, 2006.

[4] A. Nasirov, A. Gupta, S. Hasanov, and I. Fidan, "Three-scale asymptotic homogenization of short fiber reinforced additively manufactured polymer composites," *Composites Part B: Engineering*, vol. 202, p. 108269, 2020.

[5] P. Wang, B. Zou, S. Ding, C. Huang, Z. Shi, Y. Ma, and P. Yao, "Preparation of short cf/gf reinforced peek composite filaments and their comprehensive properties evaluation for fdm-3d printing," *Composites Part B: Engineering*, vol. 198, p. 108175, 2020.

[6] Laminated Plastics, "Technical data sheet ultem (pei)," June 2022. [Online]. Available: https://laminatedplastics.com/ultem.pdf

[7] X. Y. Chen, A. Romero, A. Paton-Carrero, M. P. Lavin-Lopez, L. Sanchez-Silva, J. L. Valverde, S. Kaliaguine, and D. Rodrigue, "Functionalized graphene–reinforced foams based on polymer matrices: processing and applications," in *Functionalized Graphene Nanocomposites and their Derivatives*. Elsevier, 2019, pp. 121–155.

[8] Stratasys, "Ultem 1010 resin," May 2018. [Online]. Available: https://www.stratasys.com/siteassets/materials/materials-catalog/fdm-materials/ultem1010/mds_fdm_ultem-1010-resin_0921a.pdf?v=48e257

[9] X. Xiao, C. Hiel, and A. Cardon, "Characterization and modeling of nonlinear viscoelastic response of peek resin and peek composites," *Composites Engineering*, vol. 4, no. 7, pp. 681–702, 1994.

[10] A. Diouf-Lewis, R. D. Farahani, F. Iervolino, J. Pierre, Y. Abderrafai, M. Lévesque, N. Piccirelli, and D. Therriault, "Design and characterization of carbon fiber-reinforced

peek/pei blends for fused filament fabrication additive manufacturing," *Materials Today Communications*, vol. 31, p. 103445, 2022.

[11] B. Brenken, E. Barocio, A. Favaloro, V. Kunc, and R. B. Pipes, "Fused filament fabrication of fiber-reinforced polymers: A review," *Additive Manufacturing*, vol. 21, pp. 1–16, 2018.

[12] M. Domingo-Espin, J. M. Puigoriol-Forcada, A.-A. Garcia-Granada, J. Llumà, S. Borros, and G. Reyes, "Mechanical property characterization and simulation of fused deposition modeling polycarbonate parts," *Materials & Design*, vol. 83, pp. 670–677, 2015.

[13] P. Biswas, S. Guessasma, and J. Li, "Numerical prediction of orthotropic elastic properties of 3d-printed materials using micro-ct and representative volume element," *Acta Mechanica*, vol. 231, no. 2, pp. 503–516, 2020.

[14] A. Gupta, I. Fidan, S. Hasanov, and A. Nasirov, "Processing, mechanical characterization, and micrography of 3d-printed short carbon fiber reinforced polycarbonate polymer matrix composite material," *The International Journal of Advanced Manufacturing Technology*, vol. 107, no. 7, pp. 3185–3205, 2020.

[15] P. Wang, B. Zou, H. Xiao, S. Ding, and C. Huang, "Effects of printing parameters of fused deposition modeling on mechanical properties, surface quality, and microstructure of peek," *Journal of Materials Processing Technology*, vol. 271, pp. 62–74, 2019.

[16] L. J. Love, V. Kunc, O. Rios, C. E. Duty, A. M. Elliott, B. K. Post, R. J. Smith, and C. A. Blue, "The importance of carbon fiber to polymer additive manufacturing," *Journal of Materials Research*, vol. 29, no. 17, pp. 1893–1898, 2014.

[17] Victrex PLC, "Victrex peek 90g," July 2017. [Online]. Available: https://www.victrex.com/en/downloads/datasheets/victrex-peek-90g

[18] Y. Abderrafai, M. H. Mahdavi, F. Sosa-Rey, C. Hérard, I. O. Navas, N. Piccirelli, M. Lévesque, and D. Therriault, "Additive manufacturing of short carbon fiber-reinforced polyamide composites by fused filament fabrication: Formulation, manufacturing and characterization," *Materials & Design*, vol. 214, p. 110358, 2022.

[19] J. D. Ferry, *Viscoelastic properties of polymers*. John Wiley & Sons, 1980.

[20] Z. A. Taylor, O. Comas, M. Cheng, J. Passenger, D. J. Hawkes, D. Atkinson, and S. Ourselin, "On modelling of anisotropic viscoelasticity for soft tissue simulation: Numerical solution and gpu execution," *Medical image analysis*, vol. 13, no. 2, pp. 234–244, 2009.

[21] R. Song, M. Morak, and A. Muliana, "A thermo-viscoelastic model of anisotropic polyamide glass fiber composites," *Composite Structures*, p. 115850, 2022.

[22] J. R. White, "Polymer ageing: physics, chemistry or engineering? time to reflect," *Comptes Rendus Chimie*, vol. 9, no. 11-12, pp. 1396–1408, 2006.

[23] N. Zobeiry, S. Malek, R. Vaziri, and A. Poursartip, "A differential approach to finite element modelling of isotropic and transversely isotropic viscoelastic materials," *Mechanics of Materials*, vol. 97, pp. 76–91, 2016.

[24] M. Pathan, V. Tagarielli, and S. Patsias, "Numerical predictions of the anisotropic viscoelastic response of uni-directional fibre composites," *Composites Part A: Applied Science and Manufacturing*, vol. 93, pp. 18–32, 2017.

[25] M. Anoop, P. Senthil, and V. Sooraj, "An investigation on viscoelastic characteristics of 3d-printed fdm components using rve numerical analysis," *Journal of the Brazilian Society of Mechanical Sciences and Engineering*, vol. 43, no. 1, pp. 1–13, 2021.

[26] V. Šmilauer and Z. P. Bažant, "Identification of viscoelastic csh behavior in mature cement paste by fft-based homogenization method," *Cement and Concrete Research*, vol. 40, no. 2, pp. 197–207, 2010.

[27] N. An, Q. Jia, H. Jin, X. Ma, and J. Zhou, "Multiscale modeling of viscoelastic behavior of unidirectional composite laminates and deployable structures," *Materials & Design*, p. 110754, 2022.

[28] B. Burgarella, A. Maurel-Pantel, N. Lahellec, J.-L. Bouvard, and N. Billon, "Modeling the effective viscoelastic properties of peek matrix reinforced by arbitrary oriented short glass fibers," *Mechanics of Time-Dependent Materials*, pp. 1–29, 2020.

[29] H. E. Pettermann and A. DeSimone, "An anisotropic linear thermo-viscoelastic constitutive law," *Mechanics of time-dependent materials*, vol. 22, no. 4, pp. 421–433, 2018.

[30] R. S. Lakes, *Viscoelastic solids*. CRC press, 2017.

[31] G. Youssef, *Applied mechanics of polymers: properties, processing, and behavior*. Elsevier, 2021.

[32] I. Sevostianov, V. Levin, and E. Radi, "Effective viscoelastic properties of short-fiber reinforced composites," *International Journal of Engineering Science*, vol. 100, pp. 61–73, 2016.

[33] S. Yi, H. H. Hilton, and M. F. Ahmad, "Nonlinear thermo-viscoelastic analysis of interlaminar stresses in laminated composites," *Transactions of the ASME*, vol. 63, no. 1, pp. 218–224, 1996.

[34] Y. Yang, Q. He, Y.-N. Rao, and H.-L. Dai, "Estimation of dynamic thermo viscoelastic moduli of short fiber-reinforced polymers based on a micromechanical model considering interphases/interfaces conditions," *Polymer Composites*, vol. 41, no. 2, pp. 788–803, 2020.

[35] Y. Shangguan, F. Chen, E. Jia, Y. Lin, J. Hu, and Q. Zheng, "New insight into time-temperature correlation for polymer relaxations ranging from secondary relaxation to terminal flow: Application of a universal and developed wlf equation," *Polymers*, vol. 9, no. 11, p. 567, 2017.

[36] S. Sawant and A. Muliana, "A thermo-mechanical viscoelastic analysis of orthotropic materials," *Composite Structures*, vol. 83, no. 1, pp. 61–72, 2008.

[37] A. Trofimov, J. Le-Pavic, C. Ravey, W. Albouy, D. Therriault, and M. Levesque, "Multi-scale modeling of distortion in the non-flat 3d woven composite part manufactured using resin transfer molding," *Composites Part A: Applied Science and Manufacturing*, vol. 140, p. 106145, 2021.

[38] H. Poon and M. Ahmad, "A material point time integration procedure for anisotropic, thermo rheologically simple, viscoelastic solids," *Computational Mechanics*, vol. 21, no. 3, pp. 236–242, 1998.

[39] R. Dua, Z. Rashad, J. Spears, G. Dunn, and M. Maxwell, "Applications of 3d-printed peek via fused filament fabrication: A systematic review," *Polymers*, vol. 13, no. 22, p. 4046, 2021.

[40] S. C. Joshi and A. A. Sheikh, "3d printing in aerospace and its long-term sustainability," *Virtual and Physical Prototyping*, vol. 10, no. 4, pp. 175–185, 2015.

[41] W. Wu, P. Geng, J. Zhao, Y. Zhang, D. Rosen, and H. Zhang, "Manufacture and thermal deformation analysis of semicrystalline polymer polyether ether ketone by 3d printing," *Materials Research Innovations*, vol. 18, no. sup5, pp. S5–12, 2014.

[42] A. Stepashkin, D. Chukov, F. Senatov, A. Salimon, A. Korsunsky, and S. Kaloshkin, "3d-printed peek-carbon fiber (cf) composites: Structure and thermal properties," *Composites Science and Technology*, vol. 164, pp. 319–326, 2018.

[43] R. Gao, J. Xie, J. Yang, C. Zhuo, J. Fu, and P. Zhao, "Research on the fused deposition modeling of polyether ether ketone," *Polymers*, vol. 13, no. 14, p. 2344, 2021.

[44] W. Zhong, F. Li, Z. Zhang, L. Song, and Z. Li, "Short fiber reinforced composites for fused deposition modeling," *Materials Science and Engineering: A*, vol. 301, no. 2, pp. 125–130, 2001.

[45] C. Suarez-Afanador, R. Cornaggia, N. Lahellec, A. Maurel-Pantel, D. Boussaa, H. Moulinec, and S. P.-A. Bordas, "Effective thermo-viscoelastic behavior of short fiber reinforced thermo-rheologically simple polymers: An application to high temperature fiber reinforced additive manufacturing," *European Journal of Mechanics-A/Solids*, p. 104701, 2022.

[46] S. K. Adapa, "Prospects of natural fiber-reinforced polymer composites for additive manufacturing applications: A review," *JOM*, pp. 1–21, 2023.

[47] K. Boparai, R. Singh, and H. Singh, "Comparison of tribological behaviour for nylon6-al-al2o3 and abs parts fabricated by fused deposition modelling: This paper reports a low cost composite material that is more wear-resistant than conventional abs," *Virtual and Physical Prototyping*, vol. 10, no. 2, pp. 59–66, 2015.

[48] Z. Liu, Q. Lei, and S. Xing, "Mechanical characteristics of wood, ceramic, metal and carbon fiber-based pla composites fabricated by fdm," *Journal of Materials Research and Technology*, vol. 8, no. 5, pp. 3741–3751, 2019.

[49] C. Sauder, J. Lamon, and R. Pailler, "The tensile behavior of carbon fibers at high temperatures up to 2400 c," *Carbon*, vol. 42, no. 4, pp. 715–725, 2004.

[50] H. L. Tekinalp, V. Kunc, G. M. Velez-Garcia, C. E. Duty, L. J. Love, A. K. Naskar, C. A. Blue, and S. Ozcan, "Highly oriented carbon fiber–polymer composites via additive manufacturing," *Composites Science and Technology*, vol. 105, pp. 144–150, 2014.

[51] M. Rinaldi, F. Cecchini, L. Pigliaru, T. Ghidini, F. Lumaca, and F. Nanni, "Additive manufacturing of polyether ether ketone (peek) for space applications: A nanosat polymeric structure," *Polymers*, vol. 13, no. 1, p. 11, 2021.

[52] L. Pigliaru, M. Rinaldi, L. Ciccacci, A. Norman, T. Rohr, T. Ghidini, and F. Nanni, "3d printing of high performance polymer-bonded peek-ndfeb magnetic composite materials," *Functional Composite Materials*, vol. 1, pp. 1–17, 2020.

[53] A. Arzak, J. Eguiazábal, and J. Nazábal, "Mechanical performance of directly injection-molded peek/pei blends at room and high temperature," *Journal of Macromolecular Science, Part B: Physics*, vol. 36, no. 2, pp. 233–246, 1997.

[54] H.-L. Chen and R. S. Porter, "Phase and crystallization behavior of solution-blended poly (ether ether ketone) and poly (ether imide)," *Polymer Engineering & Science*, vol. 32, no. 24, pp. 1870–1875, 1992.

[55] J. M. Margolis, *Engineering thermoplastics: properties and applications*. Taylor & Francis, 1985, vol. 8.

[56] S. Kumar, R. K. Mishra, and T. Nandi, "Experimental and theoretical investigations of the high performance blends of peek/pei," *Journal of Polymer Engineering*, vol. 38, no. 4, pp. 351–361, 2018.

[57] D. Blundell, J. Chalmers, M. Mackenzie, and W. Gaskin, "Crystalline morphology of the matrix of peek-carbon fiber aromatic polymer composites. i. assessment of crystallinity," *Sampe Quarterly*, vol. 16, no. 4, pp. 22–30, 1985.

[58] R. D. Maksimov and J. Kubat, "Time and temperature dependent deformation of poly (ether ether ketone)(peek)," *Mechanics of composite materials*, vol. 33, no. 6, pp. 517–525, 1997.

[59] M. Katouzian, O. Bruller, and A. Horoschenkoff, "On the effect of temperature on the creep behavior of neat and carbon fiber reinforced peek and epoxy resin," *Journal of Composite Materials*, vol. 29, no. 3, pp. 372–387, 1995.

[60] Y. Guo and R. D. Bradshaw, "Isothermal physical aging characterization of polyether-ether-ketone (peek) and polyphenylene sulfide (pps) films by creep and stress relaxation," *Mechanics of Time-Dependent Materials*, vol. 11, no. 1, pp. 61–89, 2007.

[61] X. Liu and V. Shapiro, "Homogenization of material properties in additively manufactured structures," *Computer-Aided Design*, vol. 78, pp. 71–82, 2016.

[62] P. Parandoush and D. Lin, "A review on additive manufacturing of polymer-fiber composites," *Composite Structures*, vol. 182, pp. 36–53, 2017.

[63] F.-L. Guo, J.-M. Hu, T. Guan, Y.-T. Fu, C.-Y. Huang, Y.-Q. Li, and S.-Y. Fu, "Modeling and characterizations of mechanical behaviors of short carbon fiber and short glass fiber reinforced polyetherimide composites," *Composites Science and Technology*, p. 109685, 2022.

[64] V. Müller, M. Kabel, H. Andrä, and T. Böhlke, "Homogenization of linear elastic properties of short-fiber reinforced composites–a comparison of mean field and voxel-based methods," *International Journal of Solids and Structures*, vol. 67, pp. 56–70, 2015.

[65] T. Baranowski, D. Dobrovolskij, K. Dremel, A. Hölzing, G. Lohfink, K. Schladitz, and S. Zabler, "Local fiber orientation from x-ray region-of-interest computed tomography of large fiber reinforced composite components," *Composites Science and Technology*, vol. 183, p. 107786, 2019.

[66] P. A. Hessman, T. Riedel, F. Welschinger, K. Hornberger, and T. Böhlke, "Microstructural analysis of short glass fiber reinforced thermoplastics based on x-ray micro-computed tomography," *Composites Science and Technology*, vol. 183, p. 107752, 2019.

[67] J. P. Lewicki, J. N. Rodriguez, C. Zhu, M. A. Worsley, A. S. Wu, Y. Kanarska, J. D. Horn, E. B. Duoss, J. M. Ortega, W. Elmer *et al.*, "3d-printing of meso-structurally ordered carbon fiber/polymer composites with unprecedented orthotropic physical properties," *Scientific reports*, vol. 7, no. 1, pp. 1–14, 2017.

[68] I. Hanhan, R. Agyei, X. Xiao, and M. D. Sangid, "Comparing non-destructive 3d x-ray computed tomography with destructive optical microscopy for microstructural characterization of fiber reinforced composites," *Composites Science and Technology*, vol. 184, p. 107843, 2019.

[69] C. Eberhardt and A. Clarke, "Fibre-orientation measurements in short-glass-fibre composites. part i: automated, high-angular-resolution measurement by confocal microscopy," *Composites Science and Technology*, vol. 61, no. 10, pp. 1389–1400, 2001.

[70] N. Davidson, A. Clarke, and G. Archenhold, "Large-area, high-resolution image analysis of composite materials," *Journal of Microscopy*, vol. 185, no. 2, pp. 233–242, 1997.

[71] V. Müller, B. Brylka, F. Dillenberger, R. Glöckner, S. Kolling, and T. Böhlke, "Homogenization of elastic properties of short-fiber reinforced composites based on measured microstructure data," *Journal of Composite Materials*, vol. 50, no. 3, pp. 297–312, 2016.

[72] A. Badran, D. Marshall, Z. Legault, R. Makovetsky, B. Provencher, N. Piché, and M. Marsh, "Automated segmentation of computed tomography images of fiber-reinforced composites by deep learning," *Journal of Materials Science*, vol. 55, no. 34, pp. 16 273–16 289, 2020.

[73] J. M. Sietins, J. C. Sun, and D. B. K. Jr, "Fiber orientation quantification utilizing x-ray micro-computed tomography," *Journal of Composite Materials*, vol. 55, no. 8, pp. 1109–1118, 2021.

[74] C. Aguilar, I. A. Hanhan, R. F. Agyei, M. D. Sangid, and M. Comer, "Void detection and fiber extraction for statistical characterization of fiber-reinforced polymers," *Electronic Imaging*, vol. 2020, no. 14, pp. 250–1, 2020.

[75] T. Mishurova, N. Rachmatulin, P. Fontana, T. Oesch, G. Bruno, E. Radi, and I. Sevostianov, "Evaluation of the probability density of inhomogeneous fiber orientations by computed tomography and its application to the calculation of the effective properties of a fiber-reinforced composite," *International Journal of Engineering Science*, vol. 122, pp. 14–29, 2018.

[76] M. W. Czabaj, M. L. Riccio, and W. W. Whitacre, "Numerical reconstruction of graphite/epoxy composite microstructure based on sub-micron resolution x-ray computed tomography," *Composites Science and Technology*, vol. 105, pp. 174–182, 2014.

[77] P. J. Creveling, W. W. Whitacre, and M. W. Czabaj, "A fiber-segmentation algorithm for composites imaged using x-ray microtomography: Development and validation," *Composites Part A: Applied Science and Manufacturing*, vol. 126, p. 105606, 2019.

[78] S. Yu, Y. H. Hwang, J. Y. Hwang, and S. H. Hong, "Analytical study on the 3d-printed structure and mechanical properties of basalt fiber-reinforced pla composites using x-ray microscopy," *Composites Science and Technology*, vol. 175, pp. 18–27, 2019.

[79] M. J. Emerson, K. M. Jespersen, A. B. Dahl, K. Conradsen, and L. P. Mikkelsen, "Individual fibre segmentation from 3d x-ray computed tomography for characterising the fibre orientation in unidirectional composite materials," *Composites Part A: Applied Science and Manufacturing*, vol. 97, pp. 83–92, 2017.

[80] D. Salaberger, K. A. Kannappan, J. Kastner, J. Reussner, and T. Auinger, "Evaluation of computed tomography data from fibre reinforced polymers to determine fibre length distribution," *International Polymer Processing*, vol. 26, no. 3, pp. 283–291, 2011.

[81] J. P. Chiverton, A. Kao, M. Roldo, and G. Tozzi, "Automatic diameter and orientation distribution determination of fibrous materials in micro x-ray ct imaging data," *Journal of microscopy*, vol. 272, no. 3, pp. 180–195, 2018.

[82] S. Goris and T. A. Osswald, "Fiber orientation measurements using a novel image processing algorithm for micro-computed tomography scans," in *Proceedings of Society of Plastics Engineers, 15th Annual Automotive Composites Conference and Exhibition*, 2015.

[83] F. De Pascalis and M. Nacucchi, "Volume orientation: A practical solution to analyse the orientation of fibres in composite materials," *Journal of Microscopy*, vol. 276, no. 1, pp. 27–38, 2019.

[84] L. Schöttl, D. Dörr, P. Pinter, K. A. Weidenmann, P. Elsner, and L. Kärger, "A novel approach for segmenting and mapping of local fiber orientation of continuous fiber-reinforced composite laminates based on volumetric images," *NDT & E International*, vol. 110, p. 102194, 2020.

[85] R. F. Agyei and M. D. Sangid, "A supervised iterative approach to 3d microstructure reconstruction from acquired tomographic data of heterogeneous fibrous systems," *Composite Structures*, vol. 206, pp. 234–246, 2018.

[86] S. Pei, K. Wang, J. Li, Y. Li, D. Zeng, X. Su, X. Xiao, and H. Yang, "Mechanical properties prediction of injection molded short/long carbon fiber reinforced polymer composites using micro x-ray computed tomography," *Composites Part A: Applied Science and Manufacturing*, vol. 130, p. 105732, 2020.

[87] M. Somireddy and A. Czekanski, "Computational modeling of constitutive behaviour of 3d printed composite structures," *Journal of Materials Research and Technology*, vol. 11, pp. 1710–1718, 2021.

[88] Z. Hashin, "Analysis of composite materials—a survey," *Journal of Applied Mechanics*, vol. 50, no. 3, pp. 481–505, 1983.

[89] A. Zaoui, "Continuum micromechanics: survey," *Journal of Engineering Mechanics*, vol. 128, no. 8, pp. 808–816, 2002.

[90] E. Ghossein, "Numerical validation of analytical homogenization models for the case of randomly distributed and oriented ellipsoidal fibers reinforced composites," Ph.D. dissertation, École polytechnique de Montréal, 2014.

[91] E. Ghossein and M. Lévesque, "A comprehensive validation of analytical homogenization models: The case of ellipsoidal particles reinforced composites," *Mechanics of Materials*, vol. 75, pp. 135–150, 2014.

[92] A. A. Gusev, "Representative volume element size for elastic composites: a numerical study," *Journal of the Mechanics and Physics of Solids*, vol. 45, no. 9, pp. 1449–1459, 1997.

[93] Z. Wang and D. E. Smith, "Numerical analysis on viscoelastic creep responses of aligned short fiber reinforced composites," *Composite Structures*, vol. 229, p. 111394, 2019.

[94] M. Ostoja-Starzewski, "Microstructural randomness versus representative volume element in thermomechanics," *Journal of Applied Mechanics*, vol. 69, no. 1, pp. 25–35, 2002.

[95] R. Hill, "Elastic properties of reinforced solids: some theoretical principles," *Journal of the Mechanics and Physics of Solids*, vol. 11, no. 5, pp. 357–372, 1963.

[96] K. Sab, "On the homogenization and the simulation of random materials," *Eur. J. Mech,. A/Solids*, no. 5, pp. 585–607, 1992.

[97] W. J. Drugan and J. R. Willis, "A micromechanics-based nonlocal constitutive equation and estimates of representative volume element size for elastic composites," *Journal of the Mechanics and Physics of Solids*, vol. 44, no. 4, pp. 497–524, 1996.

[98] H. Moussaddy, "A new definition of the representative volument element in numerical homogenization problems and its application to the performance evaluation of analytical homogenization models." Ph.D. dissertation, École Polytechnique de Montréal, 2013.

[99] T. Kanit, S. Forest, I. Galliet, V. Mounoury, and D. Jeulin, "Determination of the size of the representative volume element for random composites: statistical and numerical approach," *International Journal of solids and structures*, vol. 40, no. 13-14, pp. 3647–3679, 2003.

[100] J. Dirrenberger, S. Forest, and D. Jeulin, "Towards gigantic rve sizes for 3d stochastic fibrous networks," *International Journal of Solids and Structures*, vol. 51, no. 2, pp. 359–376, 2014.

[101] C. Huet, "Application of variational concepts to size effects in elastic heterogeneous bodies," *Journal of the Mechanics and Physics of Solids*, vol. 38, no. 6, pp. 813–841, 1990.

[102] A. Denisiewicz, M. Kuczma, K. Kula, and T. Socha, "Influence of boundary conditions on numerical homogenization of high performance concrete," *Materials*, vol. 14, no. 4, p. 1009, 2021.

[103] W. Tian, L. Qi, J. Zhou, J. Liang, and Y. Ma, "Representative volume element for composites reinforced by spatially randomly distributed discontinuous fibers and its applications," *Composite Structures*, vol. 131, pp. 366–373, 2015.

[104] L. Chen, B. Gu, J. Zhou, and J. Tao, "Study of the effectiveness of the rves for random short fiber reinforced elastomer composites," *Fibers and Polymers*, vol. 20, no. 7, pp. 1467–1479, 2019.

[105] L. Qi, W. Tian, and J. Zhou, "Numerical evaluation of effective elastic properties of composites reinforced by spatially randomly distributed short fibers with certain aspect ratio," *Composite Structures*, vol. 131, pp. 843–851, 2015.

[106] M. Zocher, S. Groves, and D. H. Allen, "A three-dimensional finite element formulation for thermoviscoelastic orthotropic media," *International Journal for Numerical Methods in Engineering*, vol. 40, no. 12, pp. 2267–2288, 1997.

[107] A. Fortin and A. Garon, "Les éléments finis: de la théorie à la pratique," *Université Laval*, 2011.

[108] Y. Pan, L. Iorga, and A. A. Pelegri, "Analysis of 3d random chopped fiber reinforced composites using fem and random sequential adsorption," *Computational Materials Science*, vol. 43, no. 3, pp. 450–461, 2008.

[109] S. Brisard and L. Dormieux, "Fft-based methods for the mechanics of composites: A general variational framework," *Computational Materials Science*, vol. 49, no. 3, pp. 663–671, 2010.

[110] H. Moulinec and P. Suquet, "A numerical method for computing the overall response of nonlinear composites with complex microstructure," *Computer methods in applied mechanics and engineering*, vol. 157, no. 1-2, pp. 69–94, 1998.

[111] B. A. Lippmann and J. Schwinger, "Variational principles for scattering processes. i," *Physical Review*, vol. 79, no. 3, p. 469, 1950.

[112] T. Mura, *Micromechanics of defects in solids*. Springer Science & Business Media, 2013.

[113] A. Rovinelli, H. Proudhon, R. A. Lebensohn, and M. D. Sangid, "Assessing the reliability of fast fourier transform-based crystal plasticity simulations of a polycrystalline material near a crack tip," *International Journal of Solids and Structures*, vol. 184, pp. 153–166, 2020.

[114] A. Haleem and M. Javaid, "Polyether ether ketone (peek) and its manufacturing of customised 3d printed dentistry parts using additive manufacturing," *Clinical Epidemiology and Global Health*, vol. 7, no. 4, pp. 654–660, 2019.

[115] L. Ding, W. Lu, J. Zhang, C. Yang, and G. Wu, "Preparation and performance evaluation of duotone 3d-printed polyetheretherketone as oral prosthetic materials: A proof-of-concept study," *Polymers*, vol. 13, no. 12, p. 1949, 2021.

[116] M. Luo, X. Tian, J. Shang, W. Zhu, D. Li, and Y. Qin, "Impregnation and interlayer bonding behaviours of 3d-printed continuous carbon-fiber-reinforced poly-ether-ether-ketone composites," *Composites Part A: Applied Science and Manufacturing*, vol. 121, pp. 130–138, 2019.

[117] Q. Li, W. Zhao, Y. Li, W. Yang, and G. Wang, "Flexural properties and fracture behavior of cf/peek in orthogonal building orientation by fdm: Microstructure and mechanism," *Polymers*, vol. 11, no. 4, p. 656, 2019.

[118] S. Sommacal, A. Matschinski, K. Drechsler, and P. Compston, "Characterisation of void and fiber distribution in 3d printed carbon-fiber/peek using x-ray computed tomography," *Composites Part A: Applied Science and Manufacturing*, p. 106487, 2021.

[119] S. Garzon-Hernandez, A. Arias, and D. Garcia-Gonzalez, "A continuum constitutive model for fdm 3d printed thermoplastics," *Composites Part B: Engineering*, vol. 201, p. 108373, 2020.

[120] W. Gao, Y. Zhang, D. Ramanujan, K. Ramani, Y. Chen, C. B. Williams, C. C. Wang, Y. C. Shin, S. Zhang, and P. D. Zavattieri, "The status, challenges, and future of additive manufacturing in engineering," *Computer-Aided Design*, vol. 69, pp. 65–89, 2015.

[121] M. Talagani, S. DorMohammadi, R. Dutton, C. Godines, H. Baid, F. Abdi, V. Kunc, B. Compton, S. Simunovic, C. Duty *et al.*, "Numerical simulation of big area additive manufacturing (3d printing) of a full size car," *Sampe Journal*, vol. 51, no. 4, pp. 27–36, 2015.

[122] M. Teßmann, S. Mohr, S. Gayetskyy, U. Haßler, R. Hanke, and G. Greiner, "Automatic determination of fiber-length distribution in composite material using 3d ct data," *EURASIP journal on advances in signal processing*, vol. 2010, pp. 1–9, 2010.

[123] H. Shen, S. Nutt, and D. Hull, "Direct observation and measurement of fiber architecture in short fiber-polymer composite foam through micro-ct imaging," *Composites science and technology*, vol. 64, no. 13-14, pp. 2113–2120, 2004.

[124] S.-Y. Fu and B. Lauke, "Effects of fiber length and fiber orientation distributions on the tensile strength of short-fiber-reinforced polymers," *Composites Science and Technology*, vol. 56, no. 10, pp. 1179–1190, 1996.

[125] S. K. Kugler, A. P. Dey, S. Saad, C. Cruz, A. Kech, and T. Osswald, "A flow-dependent fiber orientation model," *Journal of Composites Science*, vol. 4, no. 3, p. 96, 2020.

[126] G. D. Goh, Y. L. Yap, S. Agarwala, and W. Y. Yeong, "Recent progress in additive manufacturing of fiber reinforced polymer composite," *Advanced Materials Technologies*, vol. 4, no. 1, p. 1800271, 2019.

[127] S. Ding, B. Zou, P. Wang, and H. Ding, "Effects of nozzle temperature and building orientation on mechanical properties and microstructure of peek and pei printed by 3d-fdm," *Polymer Testing*, vol. 78, p. 105948, 2019.

[128] F. Ning, W. Cong, J. Qiu, J. Wei, and S. Wang, "Additive manufacturing of carbon fiber reinforced thermoplastic composites using fused deposition modeling," *Composites Part B: Engineering*, vol. 80, pp. 369–378, 2015.

[129] C. Meola and C. Toscano, "Flash thermography to evaluate porosity in carbon fiber reinforced polymer (cfrps)," *Materials*, vol. 7, no. 3, pp. 1483–1501, 2014.

[130] T. Mulholland, S. Goris, J. Boxleitner, T. A. Osswald, and N. Rudolph, "Process-induced fiber orientation in fused filament fabrication," *Journal of Composites Science*, vol. 2, no. 3, p. 45, 2018.

[131] M. P. Starmans, S. R. van der Voort, J. M. C. Tovar, J. F. Veenland, S. Klein, and W. J. Niessen, "Radiomics: Data mining using quantitative medical image features," in *Handbook of medical image computing and computer assisted intervention*. Elsevier, 2020, pp. 429–456.

[132] F. Chen, Y. Chen, and H. D. Tagare, "A new framework of multiphase segmentation and its application to partial volume segmentation," *Applied Computational Intelligence and Soft Computing*, vol. 2011, 2011.

[133] S. Evsevleev, S. Paciornik, and G. Bruno, "Advanced deep learning-based 3d microstructural characterization of multiphase metal matrix composites," *Advanced Engineering Materials*, vol. 22, no. 4, p. 1901197, 2020.

[134] R. Lorenzoni, I. Curosu, S. Paciornik, V. Mechtcherine, M. Oppermann, and F. Silva, "Semantic segmentation of the micro-structure of strain-hardening cement-based composites (shcc) by applying deep learning on micro-computed tomography scans," *Cement and Concrete Composites*, vol. 108, p. 103551, 2020.

[135] T. Li, M. Comer, and J. Zerubia, "A connected-tube mpp model for object detection with application to materials and remotely-sensed images," in *2018 25th IEEE International Conference on Image Processing (ICIP)*. IEEE, 2018, pp. 1323–1327.

[136] C. Aguilar and M. Comer, "A marked point process model incorporating active contours boundary energy," *Electronic Imaging*, vol. 2018, no. 15, pp. 230–1, 2018.

[137] B. Mlekusch, E. Lehner, and W. Geymayer, "Fibre orientation in short-fibre-reinforced thermoplastics i. contrast enhancement for image analysis," *Composites science and technology*, vol. 59, no. 4, pp. 543–545, 1999.

[138] Y. Sinchuk, P. Kibleur, J. Aelterman, M. N. Boone, and W. Van Paepegem, "Variational and deep learning segmentation of very-low-contrast x-ray computed tomography images of carbon/epoxy woven composites," *Materials*, vol. 13, no. 4, p. 936, 2020.

[139] M. J. Emerson, V. A. Dahl, K. Conradsen, L. P. Mikkelsen, and A. B. Dahl, "Statistical validation of individual fibre segmentation from tomograms and microscopy," *Composites Science and Technology*, vol. 160, pp. 208–215, 2018.

[140] V. A. Dahl, M. J. Emerson, C. H. Trinderup, and A. B. Dahl, "Content-based propagation of user markings for interactive segmentation of patterned images," in *Proceedings of the IEEE/CVF Conference on Computer Vision and Pattern Recognition Workshops*, 2020, pp. 994–995.

[141] K. Kamnitsas, C. Ledig, V. F. Newcombe, J. P. Simpson, A. D. Kane, D. K. Menon, D. Rueckert, and B. Glocker, "Efficient multi-scale 3d cnn with fully connected crf for accurate brain lesion segmentation," *Medical image analysis*, vol. 36, pp. 61–78, 2017.

[142] A. Prasoon, K. Petersen, C. Igel, F. Lauze, E. Dam, and M. Nielsen, "Deep feature learning for knee cartilage segmentation using a triplanar convolutional neural network," in *International conference on medical image computing and computer-assisted intervention*. Springer, 2013, pp. 246–253.

[143] W. Whitacre and M. Czabaj, "Automated 3d digital reconstruction of fiber reinforced polymer composites," in *AIAA Guidance, Navigation, and Control Conference*, 2015, p. 0342.

[144] H. Altendorf, "3d morphological analysis and modeling of random fiber networks: applied on glass fiber reinforced composites," Ph.D. dissertation, Paris, ENMP, 2011.

[145] K. Breuer and M. Stommel, "Rve modelling of short fiber reinforced thermoplastics with discrete fiber orientation and fiber length distribution," *SN applied Sciences*, vol. 2, no. 1, pp. 1–13, 2020.

[146] L. Wang, G. Nygren, R. L. Karkkainen, and Q. Yang, "A multiscale approach for virtual testing of highly aligned short carbon fiber composites," *Composite Structures*, vol. 230, p. 111462, 2019.

[147] M. J. Emerson, K. M. Jespersen, Y. Wang, P. J. Withers, V. A. Dahl, K. Conradsen, L. P. Mikkelsen, and A. B. Dahl, "Insegt fibre: A powerful segmentation tool for quantifying fibre architecture in composites," in *Int. Conf. Tomography of Materials & Structures. Cairns, Australia*, 2019.

[148] A. Nasirov and I. Fidan, "Prediction of mechanical properties of fused filament fabricated structures via asymptotic homogenization," *Mechanics of Materials*, vol. 145, p. 103372, 2020.

[149] S. Wilkins, T. E. Gureyev, D. Gao, A. Pogany, and A. Stevenson, "Phase-contrast imaging using polychromatic hard x-rays," *Nature*, vol. 384, no. 6607, pp. 335–338, 1996.

[150] S. Van der Walt, J. L. Schönberger, J. Nunez-Iglesias, F. Boulogne, J. D. Warner, N. Yager, E. Gouillart, and T. Yu, "scikit-image: image processing in python," *PeerJ*, vol. 2, p. e453, 2014.

[151] S. R. Biswal, T. Sahoo, and S. Sahoo, "Prediction of grain boundary of a composite microstructure using digital image processing: A comparative study," *Materials Today: Proceedings*, vol. 41, pp. 357–362, 2021.

[152] P. Virtanen, R. Gommers, T. E. Oliphant, M. Haberland, T. Reddy, D. Cournapeau, E. Burovski, P. Peterson, W. Weckesser, J. Bright, S. J. van der Walt, M. Brett, J. Wilson, K. J. Millman, N. Mayorov, A. R. J. Nelson, E. Jones, R. Kern, E. Larson, C. J. Carey, İ. Polat, Y. Feng, E. W. Moore, J. VanderPlas, D. Laxalde, J. Perktold,

R. Cimrman, I. Henriksen, E. A. Quintero, C. R. Harris, A. M. Archibald, A. H. Ribeiro, F. Pedregosa, P. van Mulbregt, and SciPy 1.0 Contributors, "SciPy 1.0: Fundamental Algorithms for Scientific Computing in Python," *Nature Methods*, vol. 17, pp. 261–272, 2020.

[153] "The opencv reference manual: Image segmentation with watershed algorithm," Itseez, April 2014. [Online]. Available: https://docs.opencv.org/4.x/d3/db4/tutorial_py_watershed.html

[154] H. Tang, H. Chen, Q. Sun, Z. Chen, and W. Yan, "Experimental and computational analysis of structure-property relationship in carbon fiber reinforced polymer composites fabricated by selective laser sintering," *Composites Part B: Engineering*, vol. 204, p. 108499, 2021.

[155] H. Zhang, L. Zhang, H. Zhang, J. Wu, X. An, and D. Yang, "Fibre bridging and nozzle clogging in 3d printing of discontinuous carbon fibre-reinforced polymer composites: Coupled cfd-dem modelling," *The International Journal of Advanced Manufacturing Technology*, vol. 117, no. 11, pp. 3549–3562, 2021.

[156] P. Feraboli, T. Cleveland, P. Stickler, and J. Halpin, "Stochastic laminate analogy for simulating the variability in modulus of discontinuous composite materials," *Composites Part A: Applied Science and Manufacturing*, vol. 41, no. 4, pp. 557–570, 2010.

[157] K. Wang, S. Pei, Y. Li, J. Li, D. Zeng, X. Su, X. Xiao, and N. Chen, "In-situ 3d fracture propagation of short carbon fiber reinforced polymer composites," *Composites Science and Technology*, vol. 182, p. 107788, 2019.

[158] E. Bertevas, J. Férec, B. C. Khoo, G. Ausias, and N. Phan-Thien, "Smoothed particle hydrodynamics (sph) modeling of fiber orientation in a 3d printing process," *Physics of Fluids*, vol. 30, no. 10, p. 103103, 2018.

[159] C. Gierden, J. Kochmann, J. Waimann, B. Svendsen, and S. Reese, "A review of fe-fft-based two-scale methods for computational modeling of microstructure evolution and macroscopic material behavior," *Archives of Computational Methods in Engineering*, pp. 1–21, 2022.

[160] A. Gupta, S. Hasanov, I. Fidan, and Z. Zhang, "Homogenized modeling approach for effective property prediction of 3d-printed short fibers reinforced polymer matrix composite material," *The International Journal of Advanced Manufacturing Technology*, pp. 1–18, 2021.

[161] A. Bellini and S. Güçeri, "Mechanical characterization of parts fabricated using fused deposition modeling," *Rapid Prototyping Journal*, 2003.

[162] S. Dai, Z. C. Deng, Y. J. Yu, K. Zhang, S. H. Wang, and J. Ye, "Orthotropic elastic behaviors and yield strength of fused deposition modeling materials: Theory and experiments," *Polymer Testing*, vol. 87, p. 106520, 2020.

[163] A. Bernasconi, F. Cosmi, and P. Hine, "Analysis of fibre orientation distribution in short fibre reinforced polymers: A comparison between optical and tomographic methods," *Composites Science and Technology*, vol. 72, no. 16, pp. 2002–2008, 2012.

[164] F. Sosa-Rey, Y. Abderrafai, A. D. Lewis, D. Therriault, N. Piccirelli, and M. Lévesque, "Openfiberseg: Open-source segmentation of individual fibers and porosity in tomographic scans of additively manufactured short fiber reinforced composites," *Composites Science and Technology*, p. 109497, 2022.

[165] Z. Wang, D. E. Smith, and D. A. Jack, "A statistical homogenization approach for incorporating fiber aspect ratio distribution in large area polymer composite deposition additive manufacturing property predictions," *Additive Manufacturing*, vol. 43, p. 102006, 2021.

[166] E. Ghossein and M. Lévesque, "Homogenization models for predicting local field statistics in ellipsoidal particles reinforced composites: Comparisons and validations," *International Journal of Solids and Structures*, vol. 58, pp. 91–105, 2015.

[167] ——, "Random generation of periodic hard ellipsoids based on molecular dynamics: A computationally-efficient algorithm," *Journal of Computational Physics*, vol. 253, pp. 471–490, 2013.

[168] J. Feder, "Random sequential adsorption," *Journal of Theoretical Biology*, vol. 87, no. 2, pp. 237–254, 1980.

[169] J. Talbot, P. Schaaf, and G. Tarjus, "Random sequential addition of hard spheres," *Molecular Physics*, vol. 72, no. 6, pp. 1397–1406, 1991.

[170] B. D. Lubachevsky and F. H. Stillinger, "Geometric properties of random disk packings," *Journal of statistical Physics*, vol. 60, no. 5, pp. 561–583, 1990.

[171] A. Donev, S. Torquato, and F. H. Stillinger, "Neighbor list collision-driven molecular dynamics simulation for nonspherical hard particles. i. algorithmic details," *Journal of computational physics*, vol. 202, no. 2, pp. 737–764, 2005.

[172] B. P. Heller, D. E. Smith, and D. A. Jack, "Effects of extrudate swell and nozzle geometry on fiber orientation in fused filament fabrication nozzle flow," *Additive Manufacturing*, vol. 12, pp. 252–264, 2016.

[173] S. G. Advani and C. L. Tucker III, "The use of tensors to describe and predict fiber orientation in short fiber composites," *Journal of rheology*, vol. 31, no. 8, pp. 751–784, 1987.

[174] J. M. Chacón, M. Á. Caminero, P. J. Núñez, E. García-Plaza, and J. P. Bécar, "Effect of nozzle diameter on mechanical and geometric performance of 3d printed carbon fibre-reinforced composites manufactured by fused filament fabrication," *Rapid Prototyping Journal*, vol. 27, no. 4, pp. 769–784, 2021.

[175] B. Hausnerova, N. Honkova, A. Lengalova, T. Kitano, and P. Saha, "Rheology and fiber degradation during shear flow of carbon-fiber-reinforced polypropylenes," *Polymer Science Series A*, vol. 48, no. 9, pp. 951–960, 2006.

[176] T. Mori and K. Tanaka, "Average stress in matrix and average elastic energy of materials with misfitting inclusions," *Acta metallurgica*, vol. 21, no. 5, pp. 571–574, 1973.

[177] Y. Benveniste, "A new approach to the application of mori-tanaka's theory in composite materials," *Mechanics of materials*, vol. 6, no. 2, pp. 147–157, 1987.

[178] R. Christensen and K. Lo, "Solutions for effective shear properties in three phase sphere and cylinder models," *Journal of the Mechanics and Physics of Solids*, vol. 27, no. 4, pp. 315–330, 1979.

[179] G. Lielens, P. Pirotte, A. Couniot, F. Dupret, and R. Keunings, "Prediction of thermo-mechanical properties for compression moulded composites," *Composites Part A: Applied Science and Manufacturing*, vol. 29, no. 1-2, pp. 63–70, 1998.

[180] J. Spahn, H. Andrä, M. Kabel, and R. Müller, "A multiscale approach for modeling progressive damage of composite materials using fast fourier transforms," *Computer Methods in Applied Mechanics and Engineering*, vol. 268, pp. 871–883, 2014.

[181] M. G. Pike and C. Oskay, "Three-dimensional modeling of short fiber-reinforced composites with extended finite-element method," *Journal of Engineering Mechanics*, vol. 142, no. 11, p. 04016087, 2016.

[182] S. Lucarini, M. V. Upadhyay, and J. Segurado, "Fft based approaches in micromechanics: fundamentals, methods and applications," *Modelling and Simulation in Materials Science and Engineering*, 2021.

[183] H. Moulinec and F. Silva, "Comparison of three accelerated fft-based schemes for computing the mechanical response of composite materials," *International Journal for Numerical Methods in Engineering*, vol. 97, no. 13, pp. 960–985, 2014.

[184] L. Gélébart and J. Derouillat, "Amitex_fftp website," Commissariat à l'énergie atomique, 2020. [Online]. Available: https://amitexfftp.github.io/AMITEX/index.html

[185] L. Gélébart and R. Mondon-Cancel, "Non-linear extension of fft-based methods accelerated by conjugate gradients to evaluate the mechanical behavior of composite materials," *Computational Materials Science*, vol. 77, pp. 430–439, 2013.

[186] P. Bhattacharya, Q. Li, D. Lacroix, V. Kadirkamanathan, and M. Viceconti, "A systematic approach to the scale separation problem in the development of multiscale models," *PloS one*, vol. 16, no. 5, p. e0251297, 2021.

[187] C. Boutin, J.-L. Auriault, and C. Geindreau, *Homogenization of coupled phenomena in heterogenous media*. John Wiley & Sons, 2010, vol. 149.

[188] Jinjiuyi, Carbon fiber sheets professional supplier, "What's the difference between t300 t700 and t800 carbon fiber?" July 2020. [Online]. Available: https://www.jinjiuyi.net/news/difference-between-t300-t700-and-t800-carbon-fiber.html

[189] D. J. Eyre and G. W. Milton, "A fast numerical scheme for computing the response of composites using grid refinement," *The European Physical Journal-Applied Physics*, vol. 6, no. 1, pp. 41–47, 1999.

[190] O. Cruz-González, A. Ramírez-Torres, R. Rodríguez-Ramos, J. Otero, R. Penta, and F. Lebon, "Effective behavior of long and short fiber-reinforced viscoelastic composites," *Applications in Engineering Science*, vol. 6, p. 100037, 2021.

[191] H.-B. Huang and Z.-M. Huang, "Micromechanical prediction of elastic-plastic behavior of a short fiber or particle reinforced composite," *Composites Part A: Applied Science and Manufacturing*, vol. 134, p. 105889, 2020.

[192] M. L. Dunn, "Viscoelastic damping of particle and fiber reinforced composite materials," *The Journal of the Acoustical Society of America*, vol. 98, no. 6, pp. 3360–3374, 1995.

[193] S. Liu, Y. Cheng, B. Liang, H. Cheng, B. Luo, and K. Zhang, "Sequential homogenization in laplace domain for viscoelastic properties of composites with functionally graded interphase," *Composite Structures*, vol. 260, p. 113266, 2021.

[194] W. V. Liebig, A. Jackstadt, V. Sessner, K. A. Weidenmann, and L. Kärger, "Frequency domain modelling of transversely isotropic viscoelastic fibre-reinforced plastics," *Composites Science and Technology*, vol. 180, pp. 101–110, 2019.

[195] P. Yang, Y. Chen, Z. Guo, N. Hu, and W. Sun, "Modeling the effective elastic and viscoelastic properties of randomly distributed short fiber reinforced composites," *Composites Communications*, p. 101341, 2022.

[196] A. A. Gusev, "Finite element estimates of viscoelastic stiffness of short glass fiber reinforced composites," *Composite Structures*, vol. 171, pp. 53–62, 2017.

[197] A. Courtois, L. Marcin, M. Benavente, E. Ruiz, and M. Lévesque, "Numerical multiscale homogenization approach for linearly viscoelastic 3d interlock woven composites," *International Journal of Solids and Structures*, vol. 163, pp. 61–74, 2019.

[198] F. Conejos, E. Balmes, B. Tranquart, E. Monteiro, and G. Martin, "Viscoelastic homogenization of 3d woven composites with damping validation in temperature and verification of scale separation," *Composite Structures*, vol. 275, p. 114375, 2021.

[199] O. Cruz-González, R. Rodríguez-Ramos, J. Otero, A. Ramírez-Torres, R. Penta, and F. Lebon, "On the effective behavior of viscoelastic composites in three dimensions," *International Journal of Engineering Science*, vol. 157, p. 103377, 2020.

[200] T. D. Pallicity, O. Cruz-González, J. Otero, and R. Rodríguez-Ramos, "Effective behavior of viscoelastic composites: comparison of laplace–carson and time-domain mean-field approach," *Archive of Applied Mechanics*, vol. 92, no. 8, pp. 2371–2395, 2022.

[201] K.-h. Kaku, M. Arai, T. Fukuoka, and T. Matsuda, "Evaluation of thermo-viscoelastic property of cfrp laminate based on a homogenization theory," *Acta mechanica*, vol. 214, no. 1, pp. 111–121, 2010.

[202] E. Marks, G. Requena, H.-P. Degischer, and E. Boller, "Microtomography and creep modeling of a short fiber reinforced aluminum piston alloy," *Advanced Engineering Materials*, vol. 13, no. 3, pp. 199–207, 2011.

[203] F. Sosa-Rey, C. Vella, A. Lingua, J. Pierre, N. Piccirelli, D. Therriault, and M. Lévesque, "Multiscale fast fourier transform homogenization of additively manufactured fiber reinforced composites from component-wise description of morphology," *Composites Science and Technology*, p. 123456, 2023.

[204] Y. Chen, P. Yang, Y. Zhou, Z. Guo, L. Dong, and E. P. Busso, "A micromechanics-based constitutive model for linear viscoelastic particle-reinforced composites," *Mechanics of Materials*, vol. 140, p. 103228, 2020.

[205] Y. Chen, Z. Guo, X.-L. Gao, L. Dong, and Z. Zhong, "Constitutive modeling of viscoelastic fiber-reinforced composites at finite deformations," *Mechanics of Materials*, vol. 131, pp. 102–112, 2019.

[206] K. Li, X.-L. Gao, and A. Roy, "Micromechanical modeling of viscoelastic properties of carbon nanotube-reinforced polymer composites," *Mechanics of Advanced Materials and Structures*, vol. 13, no. 4, pp. 317–328, 2006.

[207] R. Masson, R. Brenner, and O. Castelnau, "Incremental homogenization approach for ageing viscoelastic polycrystals," *Comptes Rendus Mécanique*, vol. 340, no. 4-5, pp. 378–386, 2012.

[208] E. Vilchevskaya, V. Levin, S. Seyedkavoosi, and I. Sevostianov, "Replacement relations for a viscoelastic material containing multiple inhomogeneities," *International journal of engineering science*, vol. 136, pp. 26–37, 2019.

[209] S. Park and R. Schapery, "Methods of interconversion between linear viscoelastic material functions. part i—a numerical method based on prony series," *International journal of solids and structures*, vol. 36, no. 11, pp. 1653–1675, 1999.

[210] Y.-M. Yi, S.-H. Park, and S.-K. Youn, "Asymptotic homogenization of viscoelastic composites with periodic microstructures," *International Journal of Solids and Structures*, vol. 35, no. 17, pp. 2039–2055, 1998.

[211] R. Brenner, R. Masson, O. Castelnau, and A. Zaoui, "A "quasi-elastic" affine formulation for the homogenised behaviour of nonlinear viscoelastic polycrystals and composites," *European Journal of Mechanics-A/Solids*, vol. 21, no. 6, pp. 943–960, 2002.

[212] M. Lévesque, M. D. Gilchrist, N. Bouleau, K. Derrien, and D. Baptiste, "Numerical inversion of the laplace–carson transform applied to homogenization of randomly reinforced linear viscoelastic media," *Computational mechanics*, vol. 40, no. 4, pp. 771–789, 2007.

[213] N. Lahellec and P. Suquet, "Effective behavior of linear viscoelastic composites: a time-integration approach," *International Journal of Solids and Structures*, vol. 44, no. 2, pp. 507–529, 2007.

[214] J.-M. Ricaud and R. Masson, "Effective properties of linear viscoelastic heterogeneous media: Internal variables formulation and extension to ageing behaviours," *International Journal of Solids and Structures*, vol. 46, no. 7-8, pp. 1599–1606, 2009.

[215] C. Mareau and S. Berbenni, "An affine formulation for the self-consistent modeling of elasto-viscoplastic heterogeneous materials based on the translated field method," *International journal of Plasticity*, vol. 64, pp. 134–150, 2015.

[216] B. Burgarella, A. Maurel-Pantel, N. Lahellec, J.-L. Bouvard, N. Billon, H. Moulinec, and F. Lebon, "Effective viscoelastic behavior of short fibers composites using virtual dma experiments," *Mechanics of Time-Dependent Materials*, vol. 23, no. 3, pp. 337–360, 2019.

[217] J. Michel, H. Moulinec, and P. Suquet, "A computational method based on augmented lagrangians and fast fourier transforms for composites with high contrast," *CMES(Computer Modelling in Engineering & Sciences)*, vol. 1, no. 2, pp. 79–88, 2000.

[218] J. C. Halpin and N. J. Pagano, "Observations on linear anisotropic viscoelasticity," *Journal of Composite Materials*, vol. 2, no. 1, pp. 68–80, 1968.

[219] R. A. Schapery, "Nonlinear viscoelastic and viscoplastic constitutive equations based on thermodynamics," *Mechanics of Time-Dependent Materials*, vol. 1, no. 2, pp. 209–240, 1997.

[220] M. Lévesque, K. Derrien, D. Baptiste, and M. D. Gilchrist, "On the development and parameter identification of schapery-type constitutive theories," *Mechanics of Time-Dependent Materials*, vol. 12, no. 2, pp. 95–127, 2008.

[221] T. Crochon, T. Schönherr, C. Li, and M. Lévesque, "On finite-element implementation strategies of schapery-type constitutive theories," *Mechanics of Time-Dependent Materials*, vol. 14, no. 4, pp. 359–387, 2010.

[222] J. Luo, Q. Luo, G. Zhang, Q. Li, and G. Sun, "On strain rate and temperature dependent mechanical properties and constitutive models for additively manufactured polylactic acid (pla) materials," *Thin-Walled Structures*, vol. 179, p. 109624, 2022.

[223] J. Luk-Cyr, T. Crochon, C. Li, and M. Lévesque, "Interconversion of linearly viscoelastic material functions expressed as prony series: a closure," *Mechanics of Time-Dependent Materials*, vol. 17, no. 1, pp. 53–82, 2013.

[224] C. Audet, S. Le Digabel, V. Rochon Montplaisir, and C. Tribes, "Algorithm 1027: NOMAD version 4: Nonlinear optimization with the MADS algorithm," *ACM Transactions on Mathematical Software*, vol. 48, no. 3, pp. 35:1–35:22, 2022. [Online]. Available: https://dx.doi.org/10.1145/3544489

[225] W. J. Parnell, "The eshelby, hill, moment and concentration tensors for ellipsoidal inhomogeneities in the newtonian potential problem and linear elastostatics," *Journal of Elasticity*, vol. 125, no. 2, pp. 231–294, 2016.

[226] S. Hasanov, A. Gupta, A. Nasirov, and I. Fidan, "Mechanical characterization of functionally graded materials produced by the fused filament fabrication process," *Journal of Manufacturing Processes*, vol. 58, pp. 923–935, 2020.

APPENDIX A GREEN'S TENSOR FOR ISOTROPIC SYMMETRIES

The following derivation is adapted from [110, 112]. Hooke's law, re-expressed using the polarization term $\tau(\boldsymbol{x})$ reads:

$$\boldsymbol{\sigma}(\boldsymbol{x}) = \mathbf{C}_0 : \boldsymbol{\varepsilon}(\boldsymbol{u}(\boldsymbol{x})) + \tau(\boldsymbol{x}). \tag{A.0.1}$$

Considering

$$\boldsymbol{\varepsilon}(u_{ij}(x)) = \frac{1}{2}\left(\frac{du_i}{dx_j} + \frac{du_j}{dx_i}\right), \tag{A.0.2}$$

and the fact that $\mathcal{F}(\frac{\partial u_k}{\partial x_h}) = i\xi_h\hat{u}_k$ and $\mathcal{F}(\frac{\partial u_h}{\partial x_k}) = i\xi_k\hat{u}_h$, this equation in the Fourier domain reads:

$$\hat{\varepsilon}_{hk} = \frac{1}{2}i\left(\xi_h\hat{u}_k + \xi_k\hat{u}_h\right). \tag{A.0.3}$$

By definition we have $\varepsilon_{ij} = \varepsilon_{ji}$, which implies $\hat{\varepsilon}_{hk} = \hat{\varepsilon}_{kh}$, and therefore $\hat{\varepsilon}_{hk} = i\xi_h\hat{u}_k$, and hence Hooke's law in the Fourier domain is expressed as:

$$\hat{\sigma}_{ij}(\boldsymbol{\xi}) = iC^o_{ijkl}\xi_h\hat{u}_k(\boldsymbol{\xi}) + \hat{\tau}_{ij}(\boldsymbol{\xi}) \tag{A.0.4}$$

Furthermore, the condition $\nabla\cdot\sigma(x) = 0, \quad \forall x \in V$ allows us to write $\mathcal{F}(\nabla\cdot\sigma) = i\xi_j\sigma_{ij}(\boldsymbol{\xi}) = 0$ (since $\nabla\cdot\sigma = \frac{d\sigma_{ij}}{dx_j}$) so (A.0.4) simplifies to

$$K^0_{ik}\hat{u}_k(\boldsymbol{\xi}) = C^o_{ijkh}\xi_h\xi_j\hat{u}_k(\boldsymbol{\xi}) = i\xi_j\hat{\tau}_{ij}(\boldsymbol{\xi}), \tag{A.0.5}$$

where $K^0_{ik}(\vec{\xi}) = C^0_{ijkh}\xi_h\xi_j$. We isolate $\hat{u}(\boldsymbol{\xi}) = iN^0_{ki}\hat{\tau}_{ij}(\vec{\xi})\xi_j$, where $N^0 = \frac{1}{K^0}$, and use the symmetry of τ, i.e. $\tau_{ij} = \tau_{ji}$, to write:

$$\hat{u}_k(\boldsymbol{\xi}) = \frac{i}{2}\left(N^0_{ki}\hat{\tau}_{ij}(\boldsymbol{\xi})\xi_j + N^0_{kj}\hat{\tau}_{ji}(\boldsymbol{\xi})\xi_i\right) \tag{A.0.6}$$

$$= \frac{i}{2}\left(N^0_{ki}\xi_j + N^0_{kj}\xi_i\right)\hat{\tau}_{ij}(\boldsymbol{\xi}). \tag{A.0.7}$$

Then, by virtue of: $\hat{\boldsymbol{\varepsilon}}_{hk} = \frac{i}{2}\Big(\xi_h \hat{u}_k + \xi_k \hat{u}_h\Big)$, we find:

$$\hat{\boldsymbol{\varepsilon}}_{hk} = -\frac{1}{4}\Big(N^0_{ki}\xi_j\xi_h + N^0_{kj}\xi_i\xi_h + N^0_{hi}\xi_j\xi_k + N^0_{hj}\xi_i\xi_k\Big)\hat{\tau}_{ij} \tag{A.0.8}$$

$$= -\Gamma^0 : \hat{\boldsymbol{\tau}}, \tag{A.0.9}$$

where Γ^0 is the Green tensor. If the material is isotropic with Lamé coefficients κ_0 and μ_0 $\mathbf{C}^0$, we have:

$$C^0_{ijkh} = \kappa_0\delta_{ij}\delta_{kh} + \mu_0\left(\delta_{ik}\delta_{jh} + \delta_{ih}\delta_{jk}\right) \tag{A.0.10}$$

$$\text{therefore:} \qquad K^0_{ik}(\boldsymbol{\xi}) = (\kappa_0 + \mu_0)\xi_i\xi_k + \mu_o|\boldsymbol{\xi}|^2\delta_{ik} \tag{A.0.11}$$

$$\text{and} \qquad N^0_{ik}(\boldsymbol{\xi}) = \frac{1}{\mu_0|\boldsymbol{\xi}|^2}\left(\delta_{ik} - \frac{\xi_i\xi_k}{|\boldsymbol{\xi}|^2}\frac{\kappa_0 + \mu_0}{\kappa_0 + 2\mu_0}\right), \tag{A.0.12}$$

so the Green tensor for isotropic symmetries is:

$$\hat{\boldsymbol{\Gamma}}^0_{khij}(\boldsymbol{\xi}) = \frac{1}{4\mu_0|\boldsymbol{\xi}|^2}\Big(\delta_{ki}\xi_h\xi_j + \delta_{hi}\xi_k\xi_j + \delta_{kj}\xi_h\xi_i + \delta_{hj}\xi_k\xi_i\Big) - \frac{\lambda_0 + \mu_0}{\mu_0(\lambda_0 + 2\mu_0)}\frac{\xi_i\xi_j\xi_k\xi_h}{|\boldsymbol{\xi}|^4} \tag{A.0.13}$$

APPENDIX B SUPPLEMENTARY MATERIAL: ARTICLE: OPEN-SOURCE SEGMENTATION OF SHORT FIBER REINFORCED COMPOSITES

Extension of incomplete detection of fiber regions

In scans of specimen with low filling fraction ($\leq$15wt.%), the following difficulty was encountered: radiometric artifacts are more prominent in the comparatively large regions occupied by matrix, and are more often confused by InSegt as fiber voxels. To prevent many false detections, the probability threshold had to be kept relatively high, which has the side effect of not capturing each fiber region entirely and yields an underestimation of total fiber volume fraction. The following procedure was applied to be able to extend these regions into the actual space occupied by each fiber without introducing false detections.

The probability field produced by InSegt was first smoothed (with cv.GaussianBlur) and then the Laplacian of the field was taken (with cv.Laplacian), shown in Figure B.1 a). The Laplacian of probability field inside fibers is low (< 500), which does not occur where there are radiometric artifacts. To identify these regions in an adaptive manner, which is invariant to scan quality and intensity, the threshold is empirically set at 1.5 standard deviations below the mean of the Laplacian. This mask, shown in Figure B.1 b), delimits a larger region around each fiber detection. The threshold was set on the basis of the size of these expanded regions compared with visual inspection of the input data. Computing it in this manner successfully found nearly all fiber regions, without introducing false detections at the location of radiometric artifacts, regardless of scan characteristics. The watershed algorithm is then used, taking the initial detections as seeds, and the mask as the boundaries. Although the mask does feature regions where no fibers are present, since they also contain no "seed" values, they will not introduce false detections. The output of the watershed algorithm is shown in Figure B.1 c), overlaid on the raw data alongside the output from InSegt for a PEEK specimen with 5 wt.% CF. If the blue regions were absent from the detection, each fiber would be under-represented by 15-25%, which in turn would yield incorrect estimates of fiber volume fraction and density, and ultimately mechanical properties in general.

Calculation of fiber volume fraction and material density

Using the number of voxels labelled as fibers, matrix or pores (respectively marked as v_f, v_m and v_p) the fiber volume fraction c_f^v can be predicted from the segmentation output, as per:

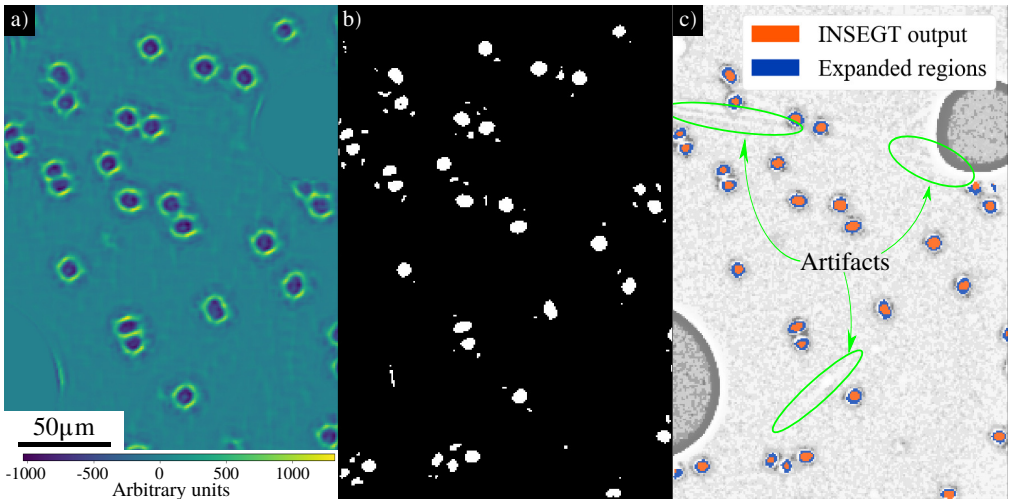

Figure B.1 Expansion of fiber regions for low fiber filling fraction specimen (PEEK with 5 wt.% CF): a) Laplacian of the probability field provided by InSegt, b) binary mask, thresholding on the Laplacian values, c) initial fiber regions (orange) serving as seeds for the watershed algorithm, expanding them into areas delimited by the binary mask (blue). This method allows the inference of the entirety of fiber cross sections without introducing false detections where artifacts are present.

$$c_f^v = \frac{v_f}{v_f + v_m + v_p}. \tag{B.0.1}$$

On the other hand, the volume fraction can be computed from the fiber mass filling fractions, c_f^m with which the specimen were manufactured, as per:

$$c_m^m = 1 - c_f^m \tag{B.0.2}$$

$$v = v_f + v_m + v_p \tag{B.0.3}$$

$$v_p = c_p^v v, \tag{B.0.4}$$

where c_m^m is the mass fraction of matrix, and v is the total volume of the specimen. By positing a total mass m of 1 gram, we can obtain v_f and v_m directly from the mass fractions and the densities ρ, as per:

$$v_f = \frac{m c_v^m}{\rho_f}, \tag{B.0.5}$$

and similarly for v_m. We then combine (B.0.3) and (B.0.4) and obtain v_p as:

$$v_p = c_p^v \left(\frac{v_f + v_m}{1 - c_p^v} \right). \tag{B.0.6}$$

Knowing all partial volumes allows us to use (B.0.1) to compute the c_f^v directly from the known density data for matrix and fibers and the mass fractions.

To validate that the segmentation tool produces the correct assessment of porosity, the total density of each SFRP specimen can be measured directly with the help of a helium pycnometer (AccuPyc II 1340 from Micromeritics). The density is obtained from the volume fractions obtained by the segmentation tool by:

$$\rho = \frac{m}{v_m + v_f + v_p}. \tag{B.0.7}$$

APPENDIX C SUPPLEMENTARY MATERIALS: ARTICLE: MULTISCALE FFT-HOMOGENIZATION OF AM FIBER REINFORCED COMPOSITES FROM COMPONENT-WISE DESCRIPTION OF MORPHOLOGY

Effect of processing on microstructure: radial dependence of fiber properties

The non-uniform distribution of fiber properties through an extrusion bead has been suggested by several modelling-based studies. These models predict a radial variation of fiber alignment at nozzle tip. Heller et al. [172] found it is maximized at the periphery for CF filled ABS, $v_f = 15\%$, with aspect ratio of 15, using a nozzle diameter $D = 0.35$ mm. Wang et al. [165] found that alignment is maximized at the center of the bead for a large (3 mm) nozzle used in Large Area Additive Manufacturing (LAAM), using a realistic length distribution of fibers in 13% Acrylonitrile Butadiene Styrene (ABS). Lewicki et al. [67] performed flow simulations using discretely modelled fibers and epoxy resin (a thermosetting polymer), with a $v_f = 6\%$ and aspect ratio of 50. They found that alignment is promoted during the extrusion phase, most notably close to the walls. Bertevas et al. studied the impact of fiber aspect ratio and v_f on the flow-induced orientations, finding that printing beads exhibit skin-core alignment differential, also predicting higher alignment at perimeter for fiber-filled PLA [158]. They comment on the lack of rich experimental data to corroborate their findings against. Wang et al. used a fully coupled model in which the effect of fiber presence on the flow characteristic is accounted for, and compare with a weakly-couple approach, in the context of large nozzles used in LAAM [165,]. They found that both models predict increased alignment at the walls, and decreased alignment at the center, but less so in the fully coupled model.

Experimental measurements of radial dependence

By knowing the position of each fiber or pore relatively to the axis of each cylindrical extrudate specimen, the radial dependence of fiber alignment, fiber length and fiber and pore densities can be computed. Those statistics are presented in Figure C.1. Contrary to what was predicted in the literature [67, 165, 172], only some curves show some radial dependence, notably the higher fiber lengths at the periphery of the $D = 0.4$ mm nozzle and its more centralized porosity distribution. The porosity is higher for that nozzle as well, and is much more lateralized for both the $D = 0.25$ mm and $D = 0.8$ mm extrudates. We do not have a

clear explanation for this observation at this stage, given that the input filament has evenly distributed porosity and that the extrusion speeds and temperatures used are all identical. However, the effect is seen consistently across many specimens.

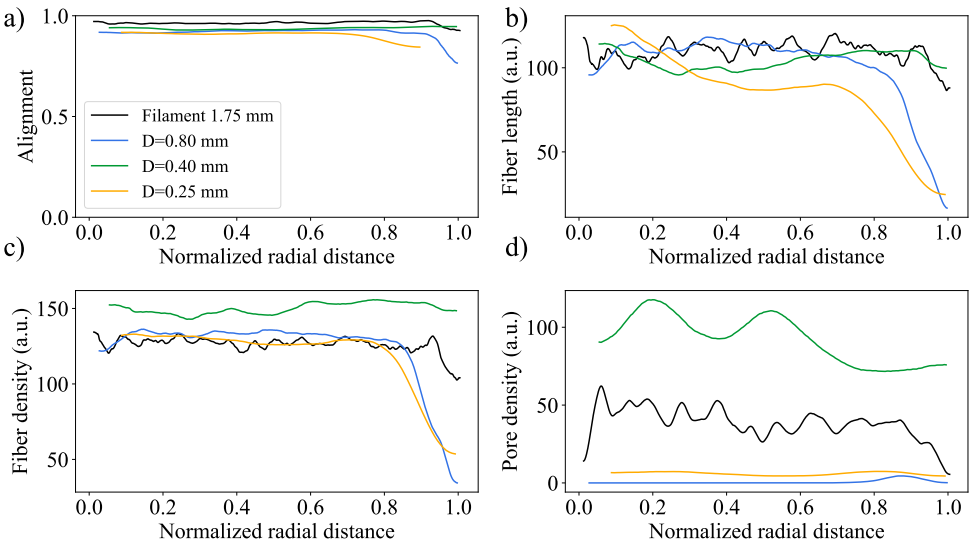

Figure C.1 Variation of fiber characteristic as a function of radial position in free-space extrusion, for 3 nozzle diameters D, and the feedstock filament. a) Alignment with print direction (1.0 is perfect alignment ($\theta = 0°$), 0.0 is perpendicular ($\theta = 90°$)) is highest in the 1.75 mm filament, and has no appreciable radial dependence in any of the 4 cases. b) Fiber lengths has little radial dependence: is slightly higher at the periphery in the $D = 0.4$ mm nozzle, and slightly lower at the periphery in the $D = 0.8$ mm nozzle. c) Fiber density is evenly distributed for all nozzle diameters. d) Pore density is slightly more centralized in feedstock filament and the $D = 0.4$ mm nozzle, and much lower and more lateralized for nozzles of $D = 0.25$ mm and $D = 0.8$ mm

Cumulative sum of morphological properties

Once the properties of each fiber have been extracted, the spatial variations of fiber properties can be investigated with the following method, as shown in Video C.2. For the volume under consideration, the numerical value of the property of each fiber (e.g. fiber length or alignment with the x direction) is inserted at the location where that fiber is present (or NaN where matrix or porosity is present). Then, the cumulative sum of those properties all 2D slice across the volume along one of the reference directions is taken, and for each column of pixels along that direction, the sum is divided by the number of pixels containing fiber in that column of voxels. This is so that the value isn't skewed by the absence of fibers in some regions, for instance where mesoscale porosity is dominant. As a reminder, x and y are the

0° and 90° printing direction, respectively, the $x - y$ plane is the printing bed plane, and z is the vertical direction. This procedure is illustrated in Video C.2

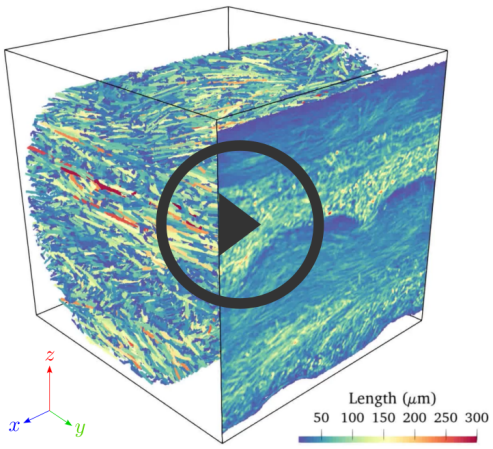

Figure C.2 Material property visualization by taking cumulative sum along x and y direction, for a specimen printed with the 0°-90° pattern and the $D = 0.4$ mm nozzle. Local property variability is exposed. Link to video.